SYNTHESIS, CHARACTERIZATION AND REDOX BEHAVIOUR OF 1,2,4-DITHIAZOLIUM SALTS AND THEIR RADICALS.

IBUKUN SHOTONWA
B.Sc., University of Ibadan, Nigeria, 2000

A Thesis
Submitted to the School of Graduate Studies
of the University of Lethbridge
in Partial Fulfilment of the
Requirement for the Degree

MASTER OF SCIENCE

Department of Chemistry and Biochemistry
University of Lethbridge
LETHBRIDGE, ALBERTA, CANADA

SYNTHESIS, CHARACTERIZATION AND REDOX BEHAVIOUR OF 1,2,4-DITHIAZOLIUM SALTS AND THEIR RADICALS.

IBUKUN SHOTONWA

Approved:

Signature	Rank	(Highest Degree)	Date
	Professor	Ph.D.	

René T. Boeré
Supervisor

	Professor	Ph.D.	

David Naylor
Thesis Examination
Committee Member

	Professor	Ph.D.	

Michael Gerken
Thesis Examination
Committee Member

	Professor	Ph.D.	

Ignacio Vargas-Baca
External Examiner

	Associate Professor	Ph.D.	

Ute Wieden-Kothe
Chair, Thesis
Examination Committee

Abstract

This thesis describes the synthesis, characterization and redox behaviour of three potential candidates for molecular conductors with the aim of determining whether or not a stable neutral species is accessible. The target compounds are 3,5-diphenyl-1,2,4-dithiazolium perchlorate salt $\mathbf{3}^+$, 3-diethylamino-5-phenyl-1,2,4-dithiazolium perchlorate salts $\mathbf{1}^+$ and 3,3,5,5-tetramethyl-1,2,4-dithiazolium hexafluorophosphate salt $\mathbf{14}^+$. Crystals of $\mathbf{3}^+$ are monoclinic, space group $P2_1/c$**,** a = 8.9194 (11) Å, b = 10.8047 (14) Å, c = 15.422 (2) Å, β = 102.91 (2) º, V = 1448.67 (3) $Å^3$, Z = 4 and R = 6.79 %. Crystals of $\mathbf{1}^+$ are monoclinic, space group $P2_1/n$**,** a = 7.4531 (9) Å, b = 12.0752 (15) Å, c = 17.09 (2) Å, β = 102.5 (10) º, V = 1501.6 (3) $Å^3$, Z = 4 and R = 2.9 %. Crystals of $\mathbf{14}^+$ are monoclinic, space group $P2_1/c$**,** a = 9.344 (3) Å, b = 19.100 (7) Å, c = 7.383 (3) Å, β = 101.815 (5) º, V = 1289.74 (8) $Å^3$, Z = 4 and R = 12.1 %. They all possess flat central NC_2S_2 rings with almost coplanar aryl and alkylamino substituents. The redox-active properties of these compounds were investigated via cyclic voltammetry and rotating disk electrode (RDE) voltammetry in CH_2Cl_2 and CH_3CN solutions containing 0.4 and 0.1 M $[^nBu_4N][PF_6]$ on platinum and glassy carbon electrodes. Cyclic voltammetry revealed the three compounds to show uniform behaviour with chemically and electrochemically irreversible 0/+1 reduction processes with strong offset reoxidation waves that show dependence on scan rates, solvents and substituent size. Diffusion coefficients were estimated by RDE voltammetry in CH_3CN/0.1 M $[^nBu_4N][PF_6]$: **3,** $8.48(2) \times 10^{-6}$ cm^2/s; **1,** $4.51(4) \times 10^{-5}$ cm^2/s; **14,** $4.30(2) \times 10^{-5}$ cm^2/s. The electronic structures of cationic, neutral, anionic and dianionic species of **3**, **1**, and **14** are herein discussed in the light of density functional theory (DFT) calculations. Digital simulations of experimental CVs detected an E_1E_2C mechanism (open anion model) that displayed slow electron transfer rates for both the reductive and offset oxidation processes coupled with the determination of rate constants for the follow up first order homogenous chemical step. An alternate mechanism is the $E_1C_2E_2C_2$· (dimer model) wherein the neutral radicals act as "spectator" molecules in the electrochemical-chemical cycle without having any

effect on the equilibrium. Both mechanisms had very common parameters ($E^0, k_s, k_f \ and \ K_{eq}$) extracted from them in addition to giving clues for the non-detection of neutral radicals via SEEPR experiments. On the basis of energy requirements, the open anion model is favoured while on the basis of extent of fits between theoretical and experimental CVs, the dimer model is better favoured.

Acknowledgements

First and foremost, I would like to say a big "Thank you" to my supervisor, Professor René Boeré whose motivation and positive criticism helped in the completion of this thesis.

I also say thank you to my supervisory and advisory committee members; Professors Michael Gerken, Marc Roussel and David Naylor for their guidance and advice towards bringing the best out of my Masters programme at the University of Lethbridge. I appreciate the efforts of Professors Michael Gerken and Hans-Joachim Wieden in the interpretation of journals from German to English and also Dr. Johnson for elemental analysis of my compounds. I appreciate the effort of Dr. Roemmele for designing the SEEPR cell used in the Boeré lab and also the mass spectrometric analysis of my compounds.

My appreciation would be incomplete without mentioning the efforts of Professor Peter W. Dibble who treats graduate students as far as I know as though he was their supervisor. It has been pleasant working in the lab of "geniuses". To all members of the Boere and Dibble lab, I say thank you for your assistance and team spirit. You all made my stay in the lab a very interesting one. To Dr. Greg Patenaude, I say thank you for the advice and help rendered during the pursuit of this degree at the University of Lethbridge.

I thank the entire members of the Shotonwa family for their prayers and staunch support and to my Lethbridge friends, I am grateful for the "love and care" showered on me.

To my wife (Inumidun) and my lovely son (Oluwapamilerin), your love and understanding were all I needed to drive me on till this very end. "I LOVE YOU BOTH"

To Inumidun and Oluwapamilerin

Table of Contents

List of Tables

List of Figures

List of schemes

Abbreviations and Symbols

Å	Angstrom
AsF_6^-	Hexafluoroarsenate (V)
Ag/Ag^+	Silver/silver ion reference electrode
Bu_4NPF_6	Tetrabutylammonium hexafluorophosphate (V)
Bu_4NBF_4	Tetrabutylammonium tetrafluoroborate (III)
$n\text{-}Bu_4NClO_4$	Tetrabutylammonium perchlorate (VII)
BF_4^-	Tetrafluoroborate (III)
B3LYP	Becke, three-parameter, Lee-Yang-Parr
cm^{-1}	Wavenumber
CF_3	Trifluoromethyl
Cl-O	Chlorine-oxygen (perchlorate anion)
C-N	Carbon-nitrogen
CV	Cyclic voltammogram
CH_2Cl_2	Dichloromethane
DFT	Density functional theory
eV	Electron volt
E_p	Peak potential
E_a	Anodic peak potential
E_{cell}	Cell potential
e^-	Electron
EPR	Electron paramagnetic resonance
F_c	Ferrocene
GHz	Gigahertz
G	Gauss
HOMO	Highest occupied molecular orbital

HCl	Hydrochloric acid
H_2O_2	Hydrogen peroxide
IR	Infrared
IUPAC	International Union of Pure and Applied Chemistry
KCl	Potassium chloride
MHz	Megahertz
Me	Methyl
MeCN	Acetonitrile
mT	MilliTesla
μA	MicroAmpere
M	Molar
mVs^{-1}	Millivolt per second
MNDO	Modified neglect of diatomic orbitals (Semi-empirical)
N	Nitrogen
N-H	Nitrogen-hydrogen
2(N)I+1	Number of coupling equivalent nuclei
NMe_2	Dimethylamino
n	Number of electrons transferred
NRCs	Neutral radical conductors
^oC	Degree Celsius
PF_6^-	Hexafluorophospate anion
ppm	Parts per million
Pt	platinum
Ph	Phenyl
RC	Alkyl-carbon
R	Alkyl

RICs	Radical ion conductors
RB3LYP	Restricted Becke, three-parameter, Lee-Yang-Parr
RDE	Rotating disk electrode
SCN^-	Thiocyanate anion
SOMO	Singly occupied molecular orbital
S-N	Sulphur-nitrogen
SCE	Saturated Calomel electrode
S••••S	Sulphur-sulphur contact
TPSS	Tao, Perdew, Staroverov & Scuseria exchange functionals
UV	Ultraviolet
UB3LYP	Unrestricted Becke, three-parameter, Lee-Yang-Parr
V	Volt
σ*	Sigma antibonding
π*	Pi antibonding
π	Pi bonding
σ_p	Hammett substituent constant
ρ	Reaction constant
^oC	Degree Celcius

List of Compounds

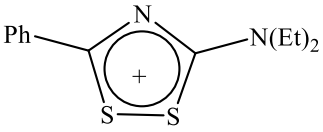

1

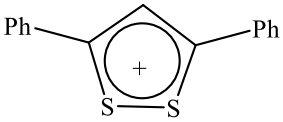

2

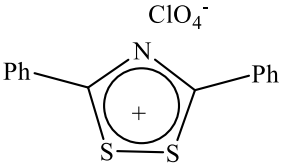

3

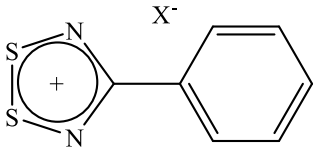

4 X = (a)PF_6, (b)AsF_6

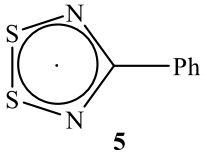

5

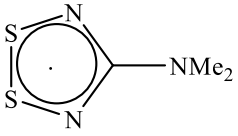

6

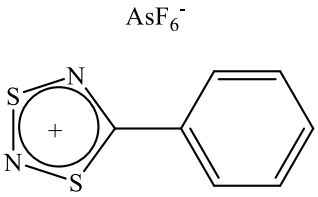

7

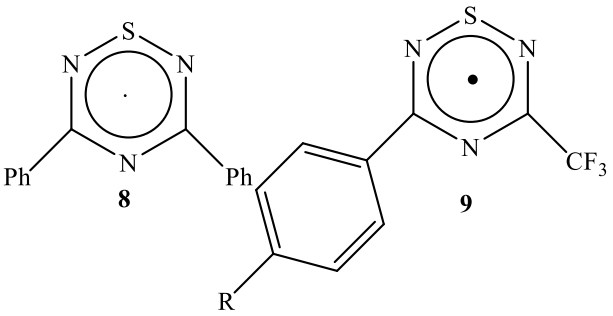

8 **9**

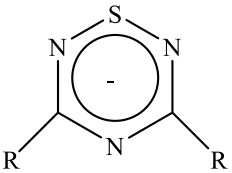

10

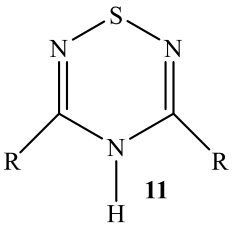

11

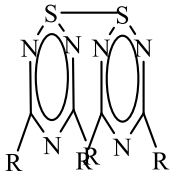

12

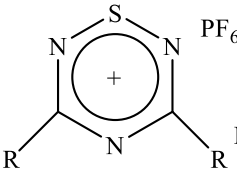

13

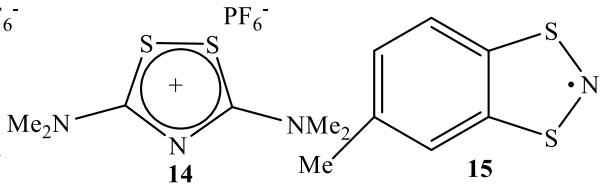

14 **15**

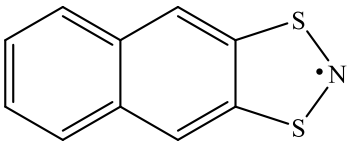

16

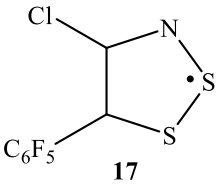

17

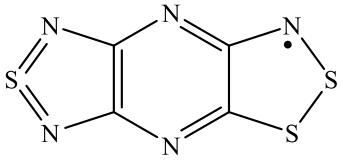

18

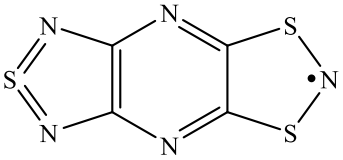

19

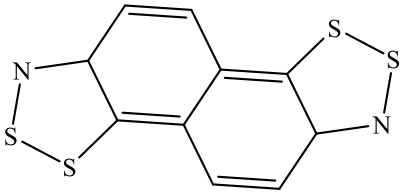

20

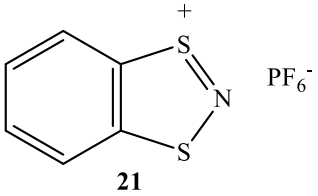

21

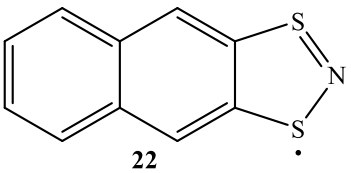

22

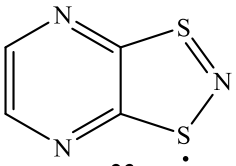

23

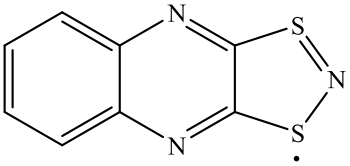

24

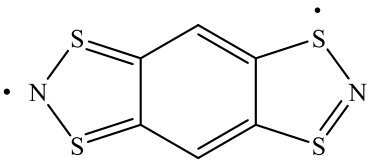

25

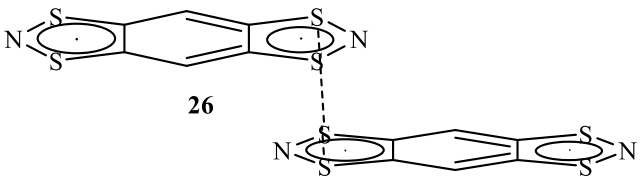

26

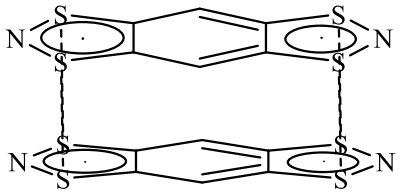

27

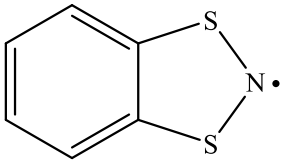

28

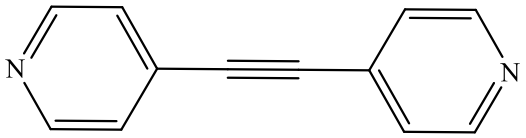

29 (a, c, d)

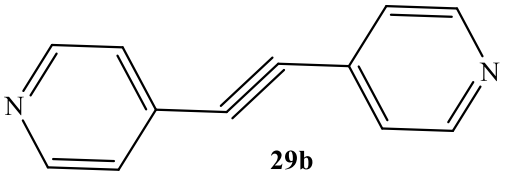

29b

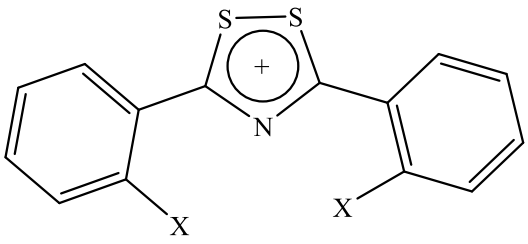

30

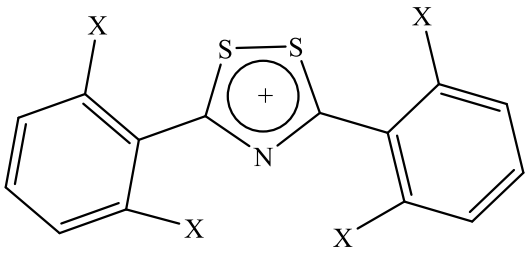

31

X = CH_3, C_2H_5, $CH(CH_3)_2$, -NHR, NR_2, -OH, -OR, CF_3, halogens, -CN, $-NO_2$
R = alkyl, (ethyl, isopropyl, t-butyl)

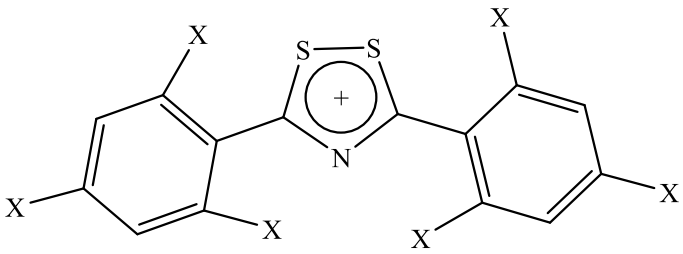

32

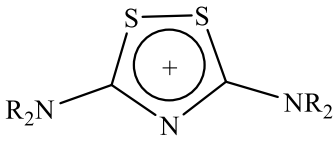

33

Chapter One

1.1 Introduction to binary sulphur-nitrogen and carbon-nitrogen-chalcogen ring systems.

The unprecedented growth and development of S-N chemistry began with considerable rise of scientific interest at the discovery of their metallic and superconducting properties.[1-2] Quite a large number of these ring systems have been made and diverse reports have ascertained their relevance in the field of nanotechnology,[3] electrical and electronics engineering,[4-6] medicine,[5] industrial and military applications.[5] Experimental scientists began to focus more on S-N chemistry[7] when planar unsaturated S_xN_y rings were proposed by Bannister to belong to a category of electron rich aromatics that conform to the Hückel (4n+2)π-electron rule.[8] One factor that has favoured S-N ring compounds is the strong π-electron delocalization pattern of -S=N- units which is driven by efficient overlap of pπ orbitals of S and N coupled with the high electronegativities of nitrogen and sulphur.[9] The aforementioned factor spurred the discoveries of theoretical chemists[10] to come up with electronic factors that explained thermodynamic[7] and kinetic[11] responses from S-N containing ring systems which have resulted in unrivaled magnetic[12] and conducting properties.[13]

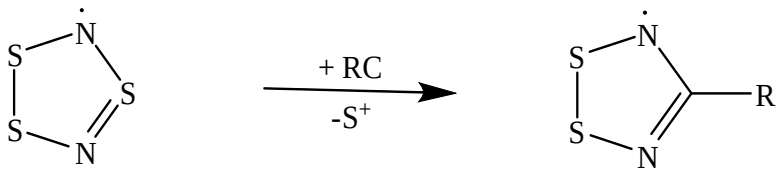

Scheme 1.1 Derivation of C-N-E rings via substitution

The study of binary S-N rings received greater scientific recognition when the incorporation of a carbon into the rings to form C-N-S (some selenium and tellurium analogues are known too) led to better thermal stability. Most C-N-E (E = chalcogens) rings are derived by substitution of R-C for isolobal S^+ or N in a S-N binary system (Scheme 1.1).[9, 12] This form of substitution is possible since the molecular fragments possess similar number of electrons in their frontier orbitals, symmetry properties, approximate energy and shape of frontier orbitals. The substitution induces great stability to the rings and also provides the platform for comparison

between benzenoid compounds and these inorganic heterocycles.[9] The substitution was inspired by the theoretical prediction that polymeric units $(RCNSN)_x$ will possess similar conducting characteristics as the SN_x polymer.[10] Subsequently, the study of C-N-S heterocycles as potential precursors for polymeric units $(RCNSN)_x$ has led to the emergence of a new era of dithiadiazolyl $[RCN_2S_2]^{\bullet}$ radical chemistry and a host of other related radical systems.[14] Oakley and co-workers have utilized these radical systems coupled with their selenium analogues as building blocks for constructing organic conductors[13] while Rawson and co-workers focused on these ring systems as building blocks for organic magnets.[12]

1.1.1 Electrochemical behaviour of redox-active S-N containing ring systems

S-N containing ring compounds possess very fascinating properties and the most promising of all these is their ability to be redox-active; an interplay between conducting and magnetic properties.[9] Redox-active heterocycles are candidates for catalysis[15-16] and material science,[17] sensing[18-19] and optical materials.[20] In the presence of substituents of different sizes and orientations, the redox potentials of S-N containing rings and other ring systems are tuned within a certain redox potential window,[21-26] resulting in enhanced electron transfer rates, redox potentials[27] and other related parameters such as activation energy[28] by appreciable factors. Moreover, the importance of substituent effects in the stabilization of ring systems incorporating sulphur-nitrogen and other main group elements to prevent dimer formation are extremely invaluable.[29-33]

There have been quite a number of reports on redox heterocyclic, radical ring systems that are neutral (neutral radical conductors [NRC])[13, 34] or charged (radical ion conductors [RIC] [35] and whose applications are directed towards the construction of molecular conductors. The factors that control the design of these conductors will be addressed in this review.

First and foremost, a low disproportionation energy based on the forward reaction of the reversible reaction below (Eqn. 1.1) is required to design neutral radical conductors.

$$2\,radical \rightleftharpoons cation^{+} + anion^{-} \qquad eqn.\,1.1$$

This energy measurement is connected to the molecular orbitals (highest occupied molecular orbitals and lowest unoccupied molecular orbitals) energy gap (HOMO-LUMO). Theoretically, information on molecular orbitals could be obtained from computational studies but they have been shown to share close numerical affinities with E_{cell} values obtained from solution electrochemistry. Reports have it that electrochemical experiments on certain S-N compounds revealed remarkably high disproportionation energies which in turn affected their effectiveness as molecular metals.[26] The backward reaction termed comproportionation reaction is one other factor that determines the design of conductors. Electrochemical irreversibility which is attributed to rapid comproportionation reaction in solution[36] has led to emphasizing the importance of the neutral species of the redox triad as the chemical source for electrochemical experiments. This has led to the use of neutral species, as the bulk material for electrochemical experiments prevents comproportionation reactions and aids the attainment of a stable triad of redox states. This is why in some cases cations from salts are first converted into neutral radicals chemically before use in electrochemical experiments.[12, 37]

Second, the nature of the singly occupied molecular orbital (SOMO) is a determinant of whether an emerging conductor is NRC or RIC. It has been established from computational studies that NRCs are more likely if the SOMO possessed a node at its carbon centre which hinders communication between π-electrons of the carbocyclic backbone and heterocycles.[38-41] RICs typically possess SOMOs with no node making it possible for π-electron communication between the carbocyclic backbone and heterocycles.[42-43]

A lot of thiazyl compounds have been studied via electrochemical methods especially cyclic voltammetry alongside spectroscopic methods such as electron paramagnetic resonance spectroscopy (EPR) and Ultraviolet-Visible photoelectron spectroscopy (UV-PES) in order to probe their potentials as molecular conductors. Some notable examples are 1,2,3- and 1,2,5-thiadiazoles, 1,2,3- and 1,3,2- dithiazoles, 1,2,3,5- and 1,3,2,4-dithiadiazoles and 1,2,4,6-thiatriazines.[44] This thesis is based upon using electrochemical methods such as squarewave,

cyclic and rotating disk electrode voltammetries coupled with spectroelectrochemical methods such as electron paramagnetic resonance spectroscopy (EPR) to look into how 1,2,4-dithiazolylium salts fit in as NRCs or RICs. Digital simulation has been shown to interprete complex cyclic voltammetric responses and will be used to have a mechanistic understanding of the redox behaviour of the salts in solution.

1.2 Steric, electronic and redox studies of 1,2,4-dithiazoles

1,2,4-dithiazolylium salts possess a well delocalised π-electron system. They possess extra stabilization as a result of the delocalization of positive charge in the cation on all the sulphur and carbon atoms in the ring and also on electron donating substituents.[45]

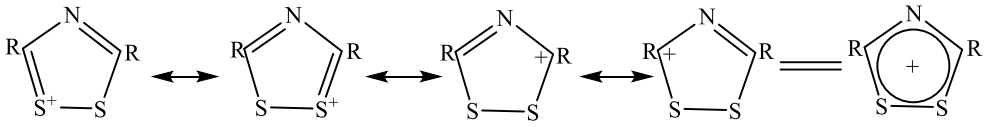

Figure 1.1 Delocalization of positive charge over resonance structures of 1,2,4-dithiazolylium rings.

Several methods have been used to prepare these salts[46-61] and quite a number of these methods were employed in the synthetic details reported in this thesis. They have been characterized by IR, NMR and UV-visible spectroscopies.[48, 52, 58, 62-63] They have been reported to show interesting activity such as insect chemosterilants,[59] antimicrobial,[64] and fungicidal.[65]

The electrochemical behaviour of 1,2,4-dithiazolylium salts have not been explored thoroughly except for two salts that were reported independently by Hartung *et al*.[66] and Uemachi *et al*.[67] Also, closely related rings in terms of size, electronic structure and substituents type will be reviewed relative to the 1,2,4-dithiazole ring systems.

1.2.1 3-diethylamino-5-phenyl-1,2,4-dithiazolium salts

Hartung and co-workers[66] reported the cyclic voltammetry experiments on 3-diethylamino-5-phenyl-1,2,4-dithiazolium salts **1**$^+$ (with $CuCl_4^{2-}$, $Cu_2Cl_6^{2-}$, $CuBr_4^{2-}$, $CoCl_4^{2-}$, $NiCl_4^{2-}$ and ClO_4^- anions) wherein it gave irreversible processes that were attributed to single $2e^-$ transfer reactions (Scheme 1.2) and coupled chemical steps. They were of the opinion that the

anion formed via the $2e^-$ transfer resulting in the rapid S-S bond cleavage which makes the process to be electrochemically irreversible with chemical reversibility. This means that the rate of electron transfer between the working electrode and the solution redox species is slow due to complications imposed by significant thermodynamic barriers. Chemical reversibility on the hand refers to the stability of the electrochemically generated anion to the homogenous chemical reaction that follows the electron transfer steps (see section 2.1.1.3 for full explanation of electrochemical and chemical steps). His claim that the chemical step is reversible is determined by a low or zero chemical rate constant k_f for the observed chemical couple. There is the possibility that the cleavage of the S-S bond is in agreement with occupation of the strong S-S σ* molecular orbitals. This is a major type of behaviour in solution that requires further investigation such as simulation to ascertain the mechanism behind the redox behaviour of the salt.[66]

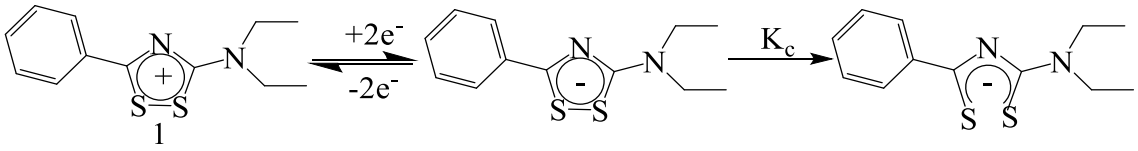

Scheme 1.2 A $2e^-$ electrochemical reduction of 1 forming the anion followed by a chemical step.

1.2.2 3,5-diaryl-1,2-dithiolylium cations

Stable organic 1,2-dithiole radicals were first reported by Bechgaard *et al.*[23] to have been prepared from the cathodic reduction of the corresponding 1,2-dithiolylium cations at room temperature. The cyclic voltammetric experiment (Fig. 1.2) on 3,5-diaryl-1,2-dithiolylium ions **2** which was carried out in pure oxygen-free acetonitrile (CH_3CN) containing 0.1 M sodium perchlorate and at a scan rate of 150 mV/s gave a quasi-reversible process with peak difference of 60 mV. This was confirmed by coulometric experiment to be a one-electron reduction of the cation to the neutral free radical. The EPR spectrum of the radical in acetonitrile revealed approximately twenty-six distinct lines at 8 ^oC while at a low temperature of -35 ^oC, the intensity of the lines became weak only to reappear on warming up. The change in the intensity of the

signal at the two extreme temperatures is an indication of equilibrium between the radical and a non-radical species that is suspected to be the dimer of the neutral radicals.

This same group carried out the reduction of 5-p-anisyl-3-phenyl-, 3,5-di-p-anisyl-, and 5-p-dimethylaminophenyl-3-phenyl-1,2-dithiolylium cations to form stable radicals in a manner similar to that of 2 whereas the reduction of 3,4-diaryl-1,2-dithiolylium cations resulted in dimers. This is an indication that the presence of bulky groups at the 3,5-positions are determinants of whether the radical or the dimer formation is favoured. Apart from the 3,4-diaryl-1,2-dithiolylium cations that got reduced to dimers, this group proved that an aryl and methyl substituents or methyl substituents at the 3,5-positions were not bulky enough to prevent dimerization.[68]

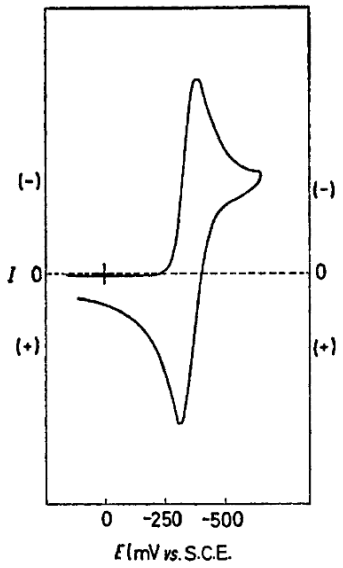

Figure 1.2 Cyclic voltammogram for the formation of **2**$^{\bullet}$ in CH_3CN containing 0.1 M sodium perchlorate at a scan rate of 150 mV/s. "Adapted from Pedersen, C. T.; Bechgaard, K.; Parker, V. D., *J. Chem. Soc., Chem. Commun.* **1972,** 430-431 with permission of The Royal Society of Chemistry".

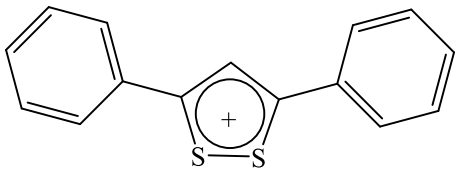

2

About nine months later, a repetition of the cyclic voltammetry was reported, first, for **2** followed by other 3,5-disubstituted dithiolylium ions in acetonitrile and dichloromethane containing 0.2 M tetra-n-butylammonium tetrafluoroborate at a platinum electrode.[23] Just like in the previous report,[68] the ions undergo quasi-reversible one-electron reduction process $\mathbf{R_1}$-$\mathbf{O_1}$ with peak separation of 60 mV coupled with the ratio of the peak currents being close to unity.

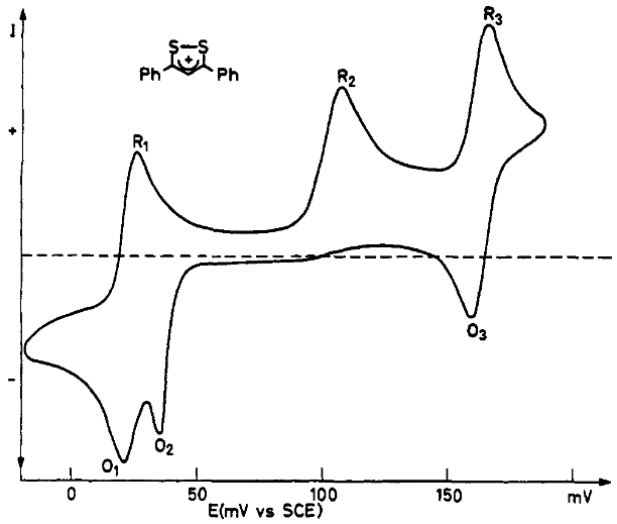

Figure 1.3 Steady-state cyclic voltammograms for cation 2 in CH_3CN containing 0.2 M Bu_4NBF_4 at a scan rate of 300 mV/s. "Adapted with permission from (Bechgaard, K.; Parker, V. D.; Pedersen, C. T., *J. Am. Chem. Soc.* **1973,** *95*, 4373.). Copyright (1977) American Chemical Society."

On scanning deep into the negative potential, a second irreversible process $\mathbf{R_2}$ identified as the anion though having an offset reoxidation process O_2 and a third reversible $\mathbf{R_3}$-$\mathbf{O_3}$ processes corresponding to the dianion were observed. The cyclic voltammetry on the neutral radical in acetonitrile gave identical peaks as the CV of the cation. Coulometric redox processes coupled with UV-visible absorption spectrometry confirmed the stabilities of the intermediates and the electrochemical irreversibility with chemical reversibility of the second couple. Though the dianionic process $\mathbf{R_3}$-$\mathbf{O_3}$ appears to be quite stable within the time-scale of the cyclic voltammetry, the product is short lived on the time-scale of coulometry. It is also in agreement with the added electron occupying the S-S antibonding σ-orbital. In dichloromethane (DCM), the dianion couple seems to occur beyond the cathodic limit of the solvent and so was not observed.

On cooling the DCM solution to -80 ^{o}C, the distinct lines from the EPR spectrum disappeared and reappeared on warming showing similar temperature dependence as reported nine months earlier to be a reversible monomeric radical-dimer equilibrium. An in-depth study of the thermodynamic properties of these experiments clearly shows that there is a strong competition between steric and electronic effects in determining the direction (equilibrium shift to the left or right) of the radical-dimer equilibria. At 25 ^{o}C, the ratio of the peak currents observed for reduction of 2^{+} and the reoxidation of $2^{\bullet}$ was observed to be very close to 1.0. This yielded an equilibrium that favoured radical formation to dimer formation in the ratio of approximately 40%:60% respectively. The percentage allotted to the radical is a result of the rapid dissociation of the dimer as the radical is oxidized, while the dimer formation is attributed to less bulky groups such as phenyl-methyl or methyl-methyl not possessing enough driving force to achieve dissociation reaction. Moreover, the changes in entropy for the dimers formed from $2^{\bullet}$ and 1,2-dithiolyl radical with *tert*-butyl groups at the 3,5-positions were the same, but the difference in equilibrium constant is proportional to the strength of the bond in their dimers. The much smaller equilibrium constant for 1,2-dithiolyl radical with *tert*-butyl groups at the 3,5-positions is an indication that steric repulsion of the substituents was able to overcome the stabilization energy from the phenyl groups of $2^{\bullet}$ showing that the bulkiness of the substituents is a major determinant of equilibrium constant.[23]

1.2.3 3,5-diphenyl-1,2,4-dithiazolium perchlorate salt

Uemachi and co-workers[67] carried out cyclic voltammetry on 3,5-diphenyl-1,2,4-dithiazolium perchlorate salt $\mathbf{3}^{+}$ with the aim of determining their efficiency as a charge storage material in lithium secondary batteries. Three redox peaks were reported for the experiment (Fig. 1.4); a reversible 0/+1 (one-electron reduction of 1,2,4-dithiazolylium ring to neutral species at -0.15 and -0.06 V) and two irreversible -1/0 and -2/-1 processes at -1.07 V and -1.53 V and their offset oxidation processes at -0.45 V and -1.32 V respectively representing scission and reformation of the S-S bond). Molecular orbital calculations show that the S-S bond in the 1,2,4-

dithiazolylium ring is responsible for the narrowing of the HOMO-LUMO gap; a phenomenon that is in agreement with electrochemical experiments.

Sugimoto and co-workers[69] synthesized 3,5-diphenyl-1,2,4-dithiazol-l-ium iodide through the oxidation of thiobenzamide with iodine in benzene under reflux. This method was in accordance with previous methods reported by Hofmann.[70] After recrystallization from acetonitrile, two crystal habits were discovered: dark-brown brick shaped crystals and needle shaped crystals. All the molecules in the two crystals were identified as 3,5-diphenyl-1,2,4-dithiazol-l-ium cation and iodide anion via single-crystal X-ray structure analysis using the synchrotron X-ray.[69] In addition to the two crystal habits, they discovered that the dark-brown shaped crystals further contain neutral cyclo S_6 molecules as cocrystals enclosed by the cation and anion. This cocrystallization pattern is similar to cyclosulphur of S_n in zeolites and sodalites which is an indication of the contribution to the stabilization of cyclo- S_6 molecules. This characteristics has been used to improve utilization of crystals by controlling the activity of sulphur coupled with stability via crystal engineering of cocrystals.

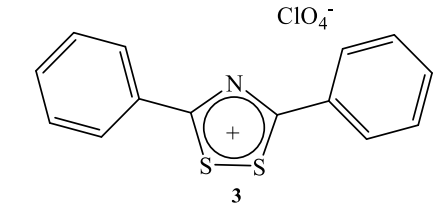

3

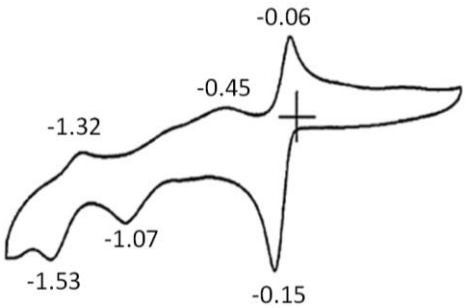

Figure 1.4. Cyclic voltammograms of **3** in CH_3CN solution (0.1 M $[^nBu_4N][ClO_4]$ at a scan rate of 100 mVs^{-1}. "Reprinted from Electrochimica Acta, 46 (15), H Uemachi, Y Iwasa, T Mitani, © 2001, with permission from Elsevier."

1.3 Ring systems related to 1,2,4-dithiazoles

1.3.1 1,2,3,5-Dithiadiazoles

1,2,3,5-Dithiadiazolium salts of PF_6^- [71] **4a** and AsF_6^- [72] **4b** with aryl groups at the 4-position were subjected to electrochemistry. The former gave a reversible one-electron reduction at room temperature to form the neutral radical coupled with an irreversible process that points at the dithiadiazolide anion. The irreversibility could be a result of the rapid quenching by the cationic species in the bulk solution.[36] The latter on the other hand gave a quasi-reversible one-electron reduction at -10°C to form the neutral radical. The neutral species **5** was subjected to

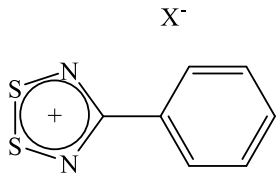

4 X = (a)PF_6, (b)AsF_6

electrochemical studies in both CH_3CN and DCM (Tables 1.1, 1.2, and 1.3). They both displayed very close -1/0 processes (-0.83 V and -0.82 V) in CH_3CN and DCM, respectively. On the contrary, they gave reversible 0/+1 processes at room temperature with the potential in CH_3CN being more cathodic (+0.60 V) than in DCM (+0.78 V). For the 1,2,3,5-dithiadiazole radical with a dimethylamino substituent at the 4- position **6**, -1/0 and 0/+1 processes were evident in CH_3CN and DCM. They were all reversible at room temperature except for the -1/0 process in DCM that was quasi-reversible at room temperature.

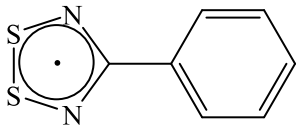

5

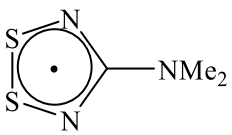

6

The two -1/0 processes are close (-0.96 V to -0.95 V) in CH_3CN and DCM, respectively, but the 0/+1 processes are far apart with the potential in CH_3CN being more cathodic than the potential in DCM.[26]

Table 1.1 Voltammetric data for 1,2,3,5-dithiadiazoles

	E_{cell} (V)	
Solvent	CH_3CN	DCM
NMe_2	-1.31	-1.45
Phenyl	-1.43	-1.60
Δ^a	0.12	0.15

[a]Shift in E_{cell} as substituents change from NMe_2 to phenyl

Table 1.2 Redox potentials of dimethylamino and phenyl dithiadiazoles in CH_3CN

	Oxidation $E_{1/2}$ (V)	Reduction $E_{1/2}$ (V)	Oxidation E_{cell} (V)
NMe_2	+0.35	-0.96	-1.31
Phenyl	+0.60	-0.83	-1.43
Δ^a	0.25	0.13	0.12

[a]Shift in E_{cell} and redox potentials as substituents change from NMe_2 to phenyl

Table 1.3 Redox potentials of dimethylamino and aryl dithiadiazoles in DCM.

	Oxidation $E_{1/2}$ (V)	Reduction $E_{1/2}$ (V)	Oxidation E_{cell} (V)
NMe_2	+0.50	-0.95	-1.45
Phenyl	+0.78	-0.82	-1.60
Δ^a	0.28	0.13	0.15

[a]Shift in E_{cell} and redox potentials as substituents change from NMe_2 to phenyl

The disproportionation energies ξ_{cell} for 1,2,3,5-dithiadiazoles are reported as follows: -1.31 V and -1.43 V for NMe_2 and phenyl substituents, respectively, in CH_3CN and -1.45 V and -1.60 V for NMe_2 and phenyl substituents, respectively, in DCM. In CH_3CN, the oxidation potentials shift by 0.25 V in the more anodic region while the reduction potentials shift by 0.13 V in the less cathodic region. In DCM, the shift in oxidation potential moved up to 0.28 V while the reduction potential remained unchanged at 0.13 V. All these shifts coupled to NMe_2 having the least ξ_{cell} value are as a result of the strong electron donating influence of the substituent on the heterocyclic ring though it is obvious that it has less influence on the reduction potentials from the 0.13 V shift. Also the two dithiadiazoles experienced increased ξ_{cell} values as the solvent changed from CH_3CN to DCM. This is attributed to the ability of the more polar solvent to attract and combine with cationic solutes in it. Phenyl and dimethylamino derivatives of 1,2,3,5-dithiadiazoles were among five of its kind whose oxidation potentials in DCM solution gave a good linear correlation with gas-phase ionisation energies obtained from Ultraviolet-Visible

photoelectron spectroscopy (UV-PES).[26] Also, the phenyl derivative was among the five 1,2,3,5-dithiadiazoles whose half wave reduction potentials $E_{1/2}$ (red) gave a linear free-energy correlation with Hammett values σ_p.

1.3.2 1,3,2,4-Dithiadiazoles

The 0/+1 process for 1,3,2,4-dithiadiazolylium cation **7** possessing aryl substituents at the 5- position was reversible at -10°C.[36] The neutral radical generated in solution is unstable in solution so that it isomerises to the energetically stable 1,2,3,5-dithiadiazolyl on the time-scale of cyclic voltammetry (so that CVs at reasonable scan rates show peaks from both isomers).[73]

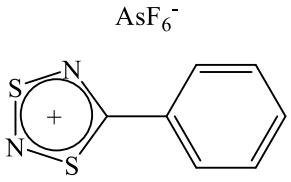

7

A set of 1,3,2,4-dithiadiazoles involving the aryl-substituted derivative gave a plot of $E_{1/2}$ (red) versus σ_p where the deviation from linearity was a little more than that of 1,2,3,5- but was not enough to distort the strong correlation between $E_{1/2}$ (red) and σ_p. Also ρ (the reaction constant that shows the effect of electronic influence on redox species) was greater in 1,3,2,4- compared to 1,2,3,5-dithiadiazoles.

Figure 1.5 LUMOs of 1,2,3,5- and 1,3,2,4-dithiadiazolylium cations (R = p-XC_6H_4). "Adapted from Aherne, C. M.; Banister, A. J.; Gorrell, I. B.; Hansford, M. I.; Hauptman, Z. V.; Luke, A. W.; Rawson, J. M., *J. Chem. Soc., Dalton Trans.* **1993,** 967-972. with permission of The Royal Society of Chemistry".

This is due to the formation of the 1,3,2,4-dithiadiazolyl radical via the partial occupation of the LUMO of the dithiadiazolylium cation resulting in some electron spin density on the heterocyclic carbon which push up the value of ρ. This is quite different from the 1,2,3,5-dithiadiazolylium

cation which has a LUMO with a nodal plane through the carbon atom of the heterocyclic ring. The nodal plane on the SOMO of 1,2,3,5-dithiadiazolyls prevents through-bond interactions between the aryl substituent and the heterocyclic ring.[36]

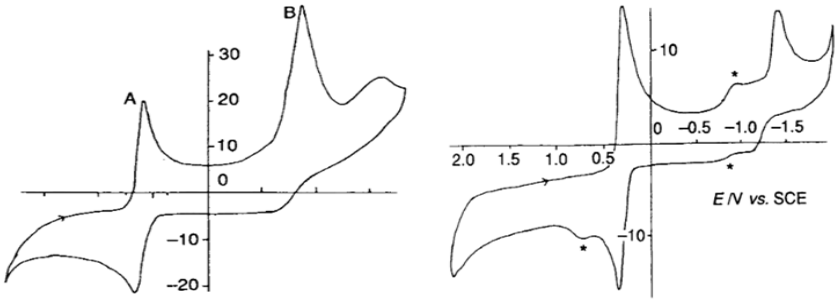

Figure 1.6 Cyclic voltammograms of 1,2,3,5- (left) and 1,3,2,4- (right) dithiadiazolyl at -10°C using 0.1 M $[NBu_4][BF_4]$ supporting electrolyte. Asterisks show peaks of 1,2,3,5-dithiadiazolyl ring system formed via the rearrangement of the 1,3,2,4-ring radical in solution. "Adapted from Aherne, C. M.; Banister, A. J.; Gorrell, I. B.; Hansford, M. I.; Hauptman, Z. V.; Luke, A. W.; Rawson, J. M., *J. Chem. Soc., Dalton Trans.* **1993,** 967-972. with permission of The Royal Society of Chemistry".

1.3.3 1,2,4,6-thiatriazine

Extensive studies have been carried out on symmetrical and asymmetrical 1,2,4,6-thiatriazines; most of which are synthesized using amidines or *N*-imidoylamidines as starting materials.[74-77] Certain symmetrical (phenyl-phenyl **8** and others)[74, 78-80] and asymmetrical (phenyl-trifluoromethyl **9** and others)[81] 1,2,4,6-thiatriazinyl radicals were made by chemical reduction of the 1-chloro-1,2,4,6-thiatriazines with triphenylantimony in oxygen-free DCM or CH_3CN (Scheme 1.4).[74, 81] The symmetrical radical **8** undergoes reduction using sodium in liquid ammonia to form the anion **10** which on acidification with ammonium chloride affords the protonated anion **11** which can be trapped by H^+ in the imine form.[82]

In the solid state, the radicals are capable of forming cofacial diamagnetic dimers **12/12a** that are linked by S••••S contacts though it was a little surprising that the presence of the bulky CF_3 group in the asymmetrical 1,2,4,6-thiatriazinyl radicals was not enough to suppress dimer formation (Scheme 1.3).[74, 79, 81-82] Oxidation of 3,5-diaryl-1,2,4,6-thiatriazinyl dimer with nitrosyl hexafluorophosphate gives the cation **13**.[82]

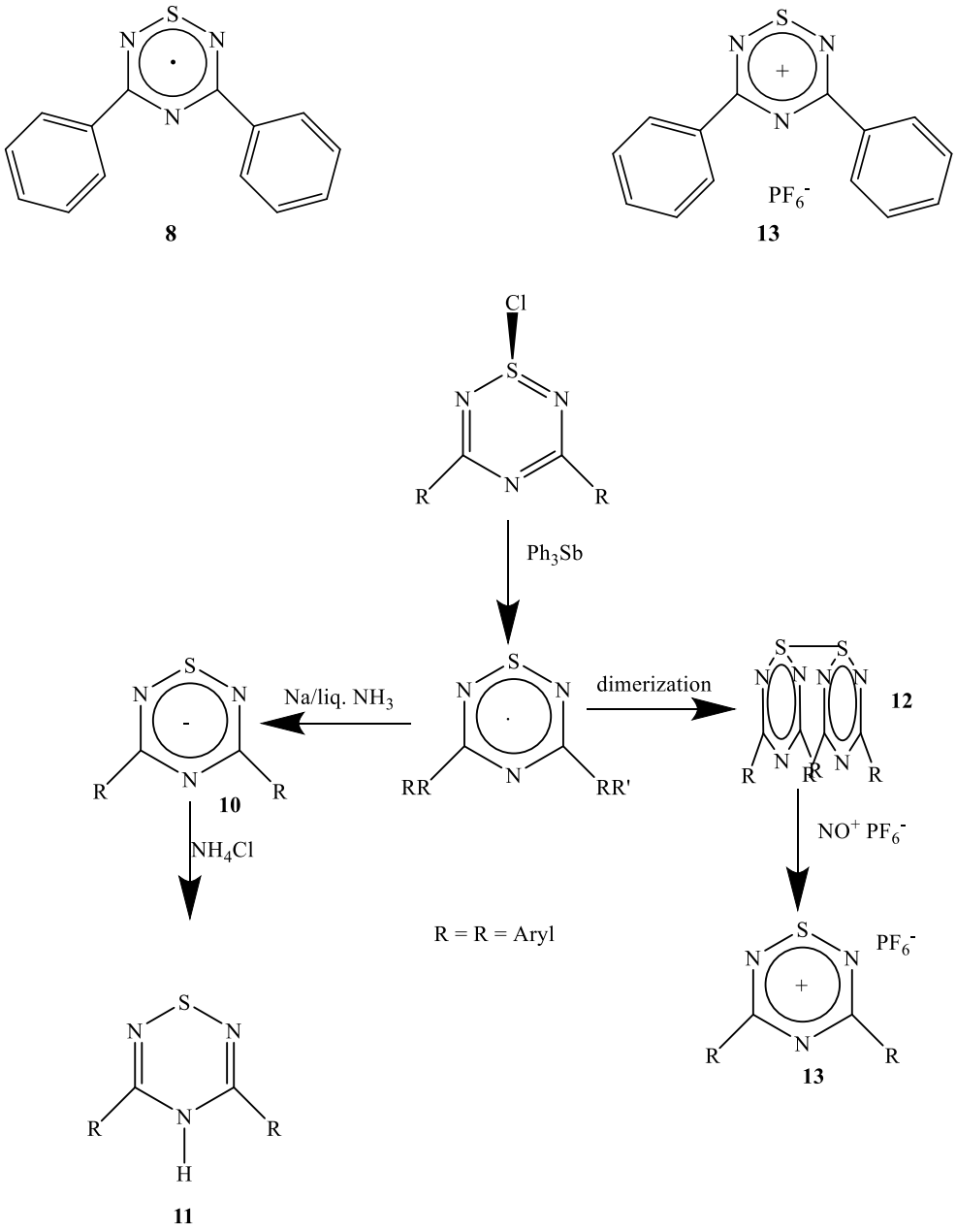

Scheme 1.3 Preparation of cationic, neutral, anionic and imide species of 1,2,4,6-thiatriazines. Circles in the heterocyclic rings indicate delocalization π-electrons.

1.3.3.1 Electrochemical studies of 1,2,4,6-thiatriazines

The cyclic voltammetry experiments on asymmetrical 1,2,4,6-thiatriazinyls reveal that there was the appearance of redox processes at more positive potentials as the solution becomes more concentrated with 1,2,4,6-thiatriazinyls analyte. This behaviour was confirmed to be due to monomeric units in equilibrium with the dimer via digital simulation of CVs. Coupled with these

was a colour change from pale yellow to deep brown as concentration of the analyte in solution increases.[81]

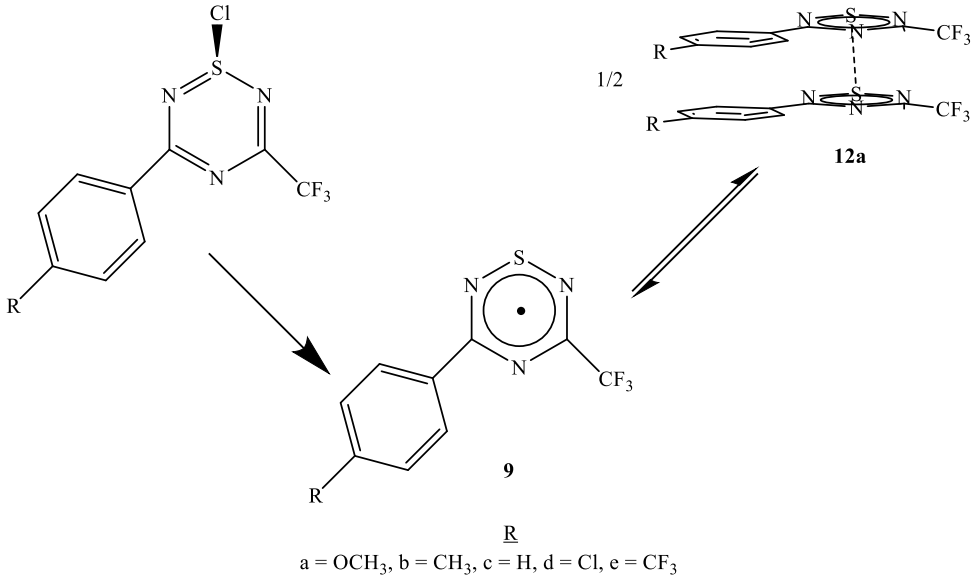

Scheme 1.4 Synthesis of asymmetrical thiatriazines

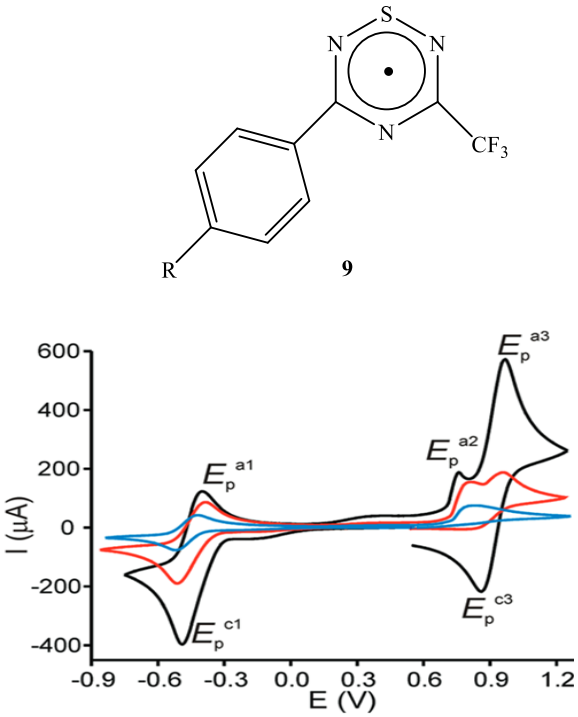

Figure 1.7 Overlapping CVs of **9** in CH_3CN solution containing $[NBu_4][PF_6]$ at lowest concentration (blue), medium (red) and highest concentration (black) "Adapted with permission from Boeré, R. T.; Roemmele, T. L.; Yu, X., *Inorg. Chem.* **2011,** *50*, 5123-5136. Copyright (2011) American Chemical Society."

Electrochemical studies equally reveal the influence of substituents, inductive effects and dimer formation on the nature of the redox processes and hyperfine splitting constants displayed by 1,2,4,6-thiatriazinyls. This is as a result of the heterocyclic carbon atoms' contribution (possession of a node) to the π-SOMO so that there is a weak communication through the π system via the substituents.[79, 81]

For thiatriazinyls **8** and **13** with two phenyl substituents at the 3- and 5- positions, the formation of -1/0 and 0/+1 processes are dependent on concentration of the thiatriazine in solution. The greater the concentration of the analyte in solution, the greater the tendency for an all monomeric radical cyclic voltammogram to disappear gradually with the simultaneous emergence of the monomeric radical-dimer equilibria and finally the appearance of stable dimer processes in solution.[83] It must be noted that these results are supported by EPR measurements.[77]

1.3.3.2 EPR and theoretical studies of 1,2,4,6-thiatriazines

EPR experiments on a yellow solution of **8** gave a spectrum indicating equal hyperfine coupling constant of 0.397 mT on the three nitrogen atoms in the heterocyclic ring. The *g* value of the radical was higher than that of free electron by 0.0036, suggestive of considerable spin density on the sulphur atom which is heavy enough to incite a spin-orbital coupling phenomenon while the remaining is equally distributed among the three nitrogen atoms. The nature of the spin distribution is reflected in the large coefficient of the sulphur orbital and the almost equal coefficients at the chemically equivalent nitrogen atoms.[74, 82] For the asymmetrical 1,2,4,6-thiatriazinyl radical **9**, its π-SOMO displayed the highest coefficient on the sulphur orbital just as in **8** while the remaining is spread out on three nitrogen atoms and a small fraction of the coefficient on fluorine atoms as well as phenyl carbon atoms. A more complex splitting pattern was observed to have evolved from coupling of the unpaired electron to three non-equivalent N nuclei in the heterocyclic ring bearing different hyperfine coupling constants in addition to three equivalent fluorine atoms of the CF_3 group directly attached to the heterocyclic ring having equal hyperfine coupling constants which are likely to have resulted from spin polarisation. The CF_3

group caused further splitting of the EPR signals into quartet suggesting rotational averaging of the three fluorine nuclei. Though, the hyperfine splitting constants a_F are small but they are quite similar to the a_F values reported for 3,5-bis (trifluoromethyl)-1,2,4,6-thiatriazinyl.[79-80] Due to the complex nature of the spectrum, contributions from computational calculations helped in allotting the hyperfine splitting constants to the non-equivalent N.[81]

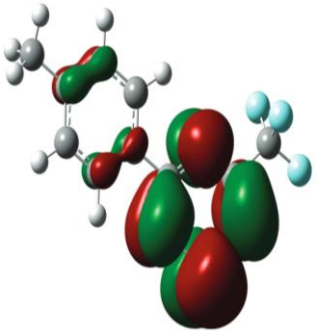

Figure 1.8 A representation of the π-SOMOs of asymmetrical 1,2,4,6-thiatriazinyl radicals. "Adapted with permission from Boeré, R. T.; Roemmele, T. L.; Yu, X., *Inorg. Chem.* **2011,** *50*, 5123-5136. Copyright (2011) American Chemical Society".

Boeré and co-workers on two occasions reported the degeneracy of symmetry-nonequivalent nitrogen nuclei for 3,5-bis-(4-methoxyphenyl)-1,2,4,6-thiatriazinyl wherein the three nitrogen atoms in the heterocyclic ring possess similar hyperfine coupling constant value of 0.3927 mT.[79-80]

Table 1.4 Voltammetric data for 9a-9e in CH_3CN

compounds	CH_3CN				
	E_P^{a1} (V)	E_P^{c1} (V)	E_P^{a3} (V)	E_P^{c3} (V)	E_{cell} (V)
9a	-0.51	-0.64	0.76	0.62	1.27
9b	-0.51	-0.60	0.81	0.71	1.32
9c	-0.48	-0.60	0.89	0.74	1.36
9d	-0.45	-0.55	0.90	0.78	1.34
9e	-0.42	-0.51	0.96	0.85	1.38

R= (a = OCH_3, b = CH_3, c = H, d = Cl, e = CF_3)

Table 1.5 Voltammetric data for 9a-9e in DCM

compounds	DCM				
	E_P^{a1} (V)	E_P^{c1} (V)	E_P^{a3} (V)	E_P^{c3} (V)	E_{cell} (V)
9a	-0.55	-0.66	0.78	0.66	1.33
9b	-0.54	-0.66	0.86	0.74	1.40
9c	-0.52	-0.64	0.92	0.78	1.43
9d	-0.47	-0.63	0.98	0.79	1.44
9e	-0.44	-0.55	1.01	0.87	1.44

R = (a = OCH_3, b = CH_3, c = H, d = Cl, e = CF_3)

Cyclic voltammetry studies were carried out on five different asymmetrical 1,2,4,6-thiatriazines (9a-9e) in CH_3CN and DCM containing 0.1 and 0.4 M $[^nBu_4N][PF_6]$ supporting electrolyte. The potential and E_{cell} values were all reported versus ferrocene on a platinum working electrode at a scan speed of 200 mV/s and at a temperature of 20 $\pm$ 2 ^oC. The E_{cell} values were calculated from E_n - E_m where $E_n = [E_p^{a3} + E_p^{c3}]/2$ and $E_m = [E_p^{a1} + E_p^{c1}]/2$ respectively (Tables 1.4 and 1.5). The E_{cell} values from 9a-9e as the R substituents on the aromatic ring change from electron donating to electron withdrawing (the CF_3 on the C3 position remaining unchanged all through the experiment) are 1.27, 1.32, 1.36, 1.34 and 1.38 V in CH_3CN and 1.33, 1.40, 1.43, 1.44 and 1.44 V, respectively, in DCM. These give a potential range of 0.11 V in both solvents as the R substituents change from electron donating to electron withdrawing. The average E_{cell} values are 1.33 $\pm$ 0.04 V and 1.41 $\pm$ 0.05 V in CH_3CN and DCM, respectively. For a typical monomeric thiatriazinyl neutral radical, the redox processes are strongly influenced by the inductive nature of R in similar magnitude in the two solvents.[81]

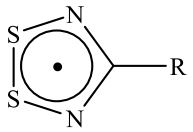

6 = NMe_2

a = CH_3, b = Ph, c = 2-furyl, d = H, e = Cl, f = CF_3

The same substituent effect has been observed in the electrochemical studies of dithiadiazolyls where the changes in potentials are probed as the substituents on 1,2,3,5-dithiadiazolyls are changed from electron donating to electron withdrawing. The tables (Tables

1.6 and 1.7) below show a summary of the voltammetric data comprising redox potentials and disproportionation potentials for the dithiadiazolyls at a platinum electrode in CH_3CN containing 0.1 M $[^nBu_4N][PF_6]$ supporting electrolyte referenced to SCE such that $\xi_{1/2}$ = +0.38 V for $[Cp_2Fe]^{+/0}$. Results were also generated at a platinum electrode in DCM containing 0.5 M $[^nBu_4N][PF_6]$ supporting electrolyte referenced to SCE such that $\xi_{1/2}$ = +0.48 V for $[Cp_2Fe]^{+/0}$. $\xi_{1/2}$ is derived from $-\{\xi^{ox} - \xi^{red}\}$ but in order to make justifiable comparisons, absolute values of the ξ_{cell} will be used. The disproportionation potential for compounds 6 – 6f in CH_3CN and DCM gave average values of 1.42 $\pm$ 0.06 and 1.61 $\pm$ 0.06 V respectively. On a conclusive note, thiatriazinyls have lower cell potential values compared to dithiadiazolyls showing that the effects of substituents is much more prominent in thiatriazinyl rings than in dithiadiazolyl ring systems. Also the non-reversibility of about seven redox processes in dithiadiazolyls could be a major factor affecting the disproportionation energies.[26]

Table 1.6 Voltammetric data for 1,2,3,5-dithiadiazolyls in CH_3CN

Compounds	CH_3CN		
	$\xi_{1/2}^{ox}$ (V)	$\xi_{1/2}^{red}$ (V)	$/\xi_{cell}/$(V)
6	+0.35	-0.96	1.31
6a	+0.59	-0.94	1.53
6b	+0.60	-0.83	1.43
6c	+0.63	-0.79	1.42
6d	+0.65	-0.83	1.48
6e	+0.83	-0.63	1.46[a]
6f	+0.91	-0.42	1.33[a]

[a] ξ_{cell} values were not obtained from reversible processes.
R = (a = CH_3, b = Ph, c = 2-furyl, d = H, e = Cl, f = CF_3)

The electronic studies of 1,2,4,6-thiatriazinyl radicals and dimers revealed manifold fascinating structural characteristics. The molecular orbitals of the dimer were characterised to possess weak π-orbital interaction from two radicals that are capable of cofacially approaching each other.[74, 82] Interestingly, the S••••S links in the dimer of **8** are not as strong as the S-S bond in a typical disulphide molecule. This is attributed to the fast rate at which dimer dissociates into its

constituent radical units in solution confirming the vulnerability of the dimer to dissociation in solution.

Table 1.7 Voltammetric data for 1,2,3,5-dithiadiazolyls in DCM

Compounds	DCM		
	$\xi_{1/2}^{ox}$ (V)	$\xi_{1/2}^{red}$ (V)	/ξ_{cell} /(V)
6	+0.50	-0.95	1.45[a]
6a	+0.78	-0.88	1.66
6b	+0.78	-0.82	1.60
6c	+0.84	-0.81	1.65[a]
6d	+0.86	-0.81	1.67[a]
6e	+1.04	-0.64	1.68[a]
6f	+1.11	-0.48	1.59[a]

[a] ξ_{cell} values were not obtained from reversible processes.
R = (a = CH_3, b = Ph, c = 2-furyl, d = H, e = Cl, f = CF_3)

The S••••S distance of 2.64 (2) Å in the dimer of **9** is much longer than those in normal disulphides[81] but lies within the range of 3,5-diaryl-1,2,4,6-thiatriazinyl **8** and 3,5-bis (dimethylamino)-1,2,4,6-thiatriazinyl with short contacts of 2.666 (3)[74] and 2.5412 (8)[81] Å, respectively. Symmetrical and asymmetrical 1,2,4,6-thiatriazinyls have similar bond lengths except for the S-N bonds adjacent the carbon attached to the CF_3 group which on the average are longer than those observed in symmetrical 1,2,4,6-thiatriazinyls.[81]

Boeré and co-workers[81] carried out thorough studies on the electronic structures of asymmetrical 1,2,4,6-thiatriazinyls using UB3LYP / 6-31G (d) hybrid DFT calculations. The outcome of the calculations showed the unpaired electron to occupy a π-SOMO which is delocalised over the heterocyclic ring system (Figure 1.8). The figure shows sulphur possessing the largest coefficient while substantial electron spin density is repository on the three nitrogen atoms and the carbon atoms in the heterocyclic core bearing far less electron spin density. However, small coefficients still exist on the fluorine atoms of the CF_3 group directly attached to the heterocyclic core as well as on the carbon atom of the phenyl substituents. Each of the five 1,2,4,6-thiatriazinyls subjected to EPR and theoretical studies showed three different values for a_N

except for 5-(p-methoxyphenyl)-3-trifluoromethyl-1,2,4,6-thiatriazinyls which gave two identical a_N values out of three. The hyperfine splitting constants of the five asymmetrical 1,2,4,6-thiatriazinyls are found to lie between those of 3,5-bis (trifluoromethyl)-1,2,4,6-thiatriazinyl and 3,5-bis (trichloromethyl)-1,2,4,6-thiatriazinyl where a_{N4} was found to be 40% larger than a_{N2} and a_{N6}. Despite this trend, the value of a_{N6} rises while the rest decrease as the remote para substituents become more electron donating due to the greater spin density residing on the N=S=N area of the heterocyclic ring. The decrease in the values of a_{N2} and a_{N4} sum up to 1.190 (5) for the five set of asymmetrical 1,2,4,6-thiatriazinyl compounds. Also, the variation in a_N values aligns with Hammet σ (p) coefficients.

1.3.4 1,2,3- and 1,3,2-dithiazoles

1,2,3 and 1,3,2-dithiazolium ions $[(RC)_2NS_2]^+$ are 6π-electron heterocycles, isoelectronic with dithiadiazolium rings $[RCN_2S_2]^+$ through the substitution of the N atom in the ring by the RC group.[14] These ring systems are focused on due to the 7π-electron dithiazolyl radicals formed from the cations via a one-electron electrochemical or chemical reduction using reducing agents such as Ph_3Sb, sodium dithionite or Zn/Cu couple.[12]

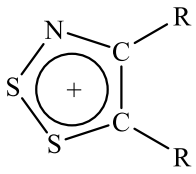

1,2,3-

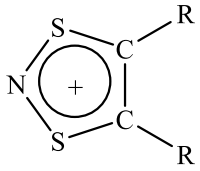

1,3,2-

Dithiazolyls are members of the thiazyl family that have attracted much attention due to their potential application as molecular conductors, molecular magnets and magnetic switches.[84-85] The magnetic properties of 1,3,2-dithiazolyl radicals have attracted much more attention. Methylbenzo-[86] **15** and naphthaleno-[87] dithiazolyl **16** retain their paramagnetism at room temperature and quite a number of the dithiazolyl family exhibits polymorphism or bistability; the possibility of switching between two different polymorphs of the same compound.[87-88] The

uncommon bistability they possess has diverted attention to them as potentials for molecular switching devices.[9]

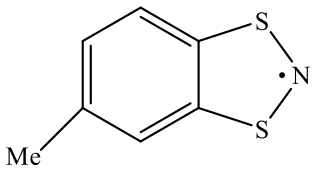

15

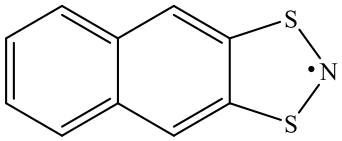

16

1.3.4.1 Electrochemical studies of dithiazoles.

4-Chloro-5-pentafluorophenyl-1,2,3-dithiazolyl radical **17,** a non-fused 1,2,3-dithiazole monomer has been characterized electrochemically at room temperature to give -1/0 and 0/+1 processes at -1.1 and +0.38 V, respectively.[89] It has the highest cell potential value of 1.5 V of all the compounds for which both processes have been determined and is also greater than 1.2 V for benzo-fused-1,2,3-dithiazolyl **28**. The cyclic voltammogram of the tricyclic **18** and its 2,1,3-isomer **19** form completely reversible waves for both 0/+1 and -1/0 processes. The reversibility of both waves is connected to the –N=S=N- group (thiadiazolopyrazine substituent) having a strong electron withdrawing effect on the redox properties of heterocyclic systems.[90]

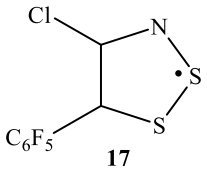

17

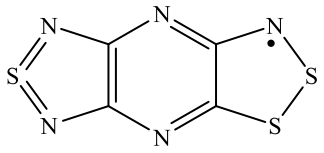

18

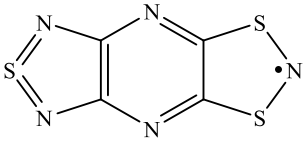

19

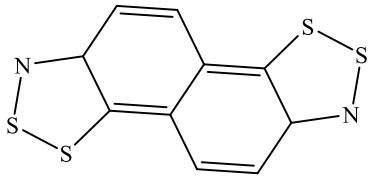

20

The comparison of fused 1,2,3-dithiazole with their non-fused counterpart show that the former display a much more diversified potential of their redox processes and E_{cell} values. This simply points at these systems having a tendency to be tuned into functional NRCs with appropriate

structural modifications and substituent effects. Interestingly, bifunctional 1,2,3-dithiazole **20** was observed to have much smaller E_{cell} value of 0.25 V between the +1/+2 and 0/+1 couples and this was attributed to the strongly quinoidal structure of the organic π-systems caused by substitution trends in these compounds. On the other hand, diamagnetic ground states are induced in these systems when the two 7π systems are coupled through the communicative quinoidal linkages. Bifunctional 1,2,3-dithiazoles are on this note different from bifunctional 1,2,3,5-dithiadiazoles in which there is a very weak communication across bridging backbones resulting in ground states with isolated doublets. This makes bifunctional 1,2,3-dithiazoles potential candidates for RICs rather than NRCs.[42-43]

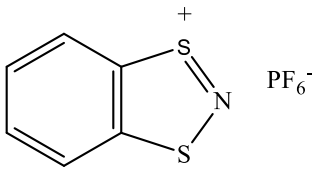

21

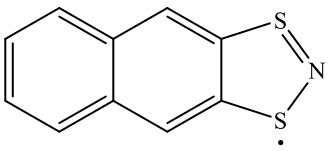

22

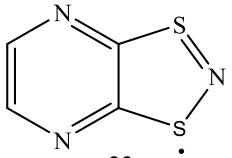

23

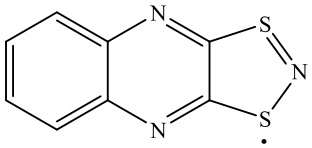

24

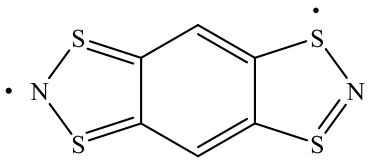

25

The redox orbital for the 1,3,2-dithiazolyl is a π-SOMO that lacks a low-lying σ-antibonding orbital. This is seen from the weaker strength of the S-S bonds compared to N-S and C-S bonds; a property not existing in the 1,2,3- isomers like **17** and **18**. 1,3,2- dithiazolylium cations form 7π-electron neutral radicals just like their 1,2,3- counterparts.[90-91]

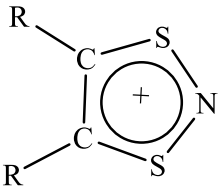

1,3,2-

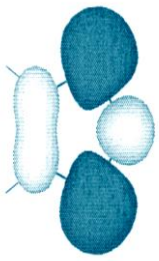

π-SOMO

Monofunctional 1,3,2-dithiazoles have potentials for making NRCs while the bifunctional counterparts face the problem of communication across the carbocyclic backbone resulting in spin-coupling. This way, they cannot function as NRCs except when couplings are impossible in the isolated rings. A high degree of redox tunabilily was displayed by 1,3,2-dithiazoles **21**, **22**, **23**, **24** as they gave cyclic voltammograms that reflected the effect of different fused substituents on redox potentials.[26, 90-91] Oakley reported both reversible 0/+1 and irreversible -1/0 processes of the afore-mentioned compounds being shifted by the same amount while the E_{cell} are significantly constant though there was a significant reduction in the case of the earlier mentioned isomeric 2,1,3-dithiazole **19** with the electron-withdrawing thiadiazolopyrazine substituent.[11]

Strong communication between the heterocyclic ring and the carbocyclic backbone makes bifunctional 1,3,2-dithiazolyl **25** susceptible to reversible oxidation to form to the radical monocation and then the dication.[37]

1.3.4.2 EPR studies of dithiazoles

Quite a number of EPR spectra of 1,2,3-dithiazolyl radicals have been reported.[12, 92] The *g*-values were all higher than for the free electron (g_e = 2.0023); an indication of a spin-orbit coupling that arises from a significant level of spin-density at sulphur.[93] The *g*-values observed for fused 1,2,3-dithiazolyl radicals were a little smaller compared to those for non-fused derivatives which are greater than 2.009. This is due to the reduction of the spin-orbit coupling caused by the ability of the fused derivatives to delocalise spin-density away from the sulphur atom. The N-hyperfine coupling varied inversely with substituents based on the correlation

observed between the Hammett parameter, σ_p for the para-substituents and the N-hyperfine interaction. The hyperfine coupling constant was noticed to drop as the level of delocalisation gets more extensive. This resulted in much larger coupling constants for the protons ortho and para to the heterocyclic nitrogen than the other H atoms, indicative of considerably more electron spin-density on the aromatic ring C atoms ortho and para to the heterocyclic N atom.

Comprehensive EPR studies on 1,3,2-dithiazolyl radicals (**22**-**25**) reported spectra that were observed as 1:1:1 triplets, triplet of triplets and quintet of triplets.

The 1:1:1 triplets were a result of coupling to the dithiazolyl ring nitrogen N in addition to weaker coupling to other elements in the fused substituents. Those fused to substituted aryl rings **28** showed small coupling constants a_N as well as small g values while on the contrary, others such as fused thiadiazolopyrazine-1,3,2-dithiazolyl radical **19** showed large g values with associated large a_N values. Those associated with low a_N and g values were due to the influence of the electron withdrawing effect of the fused aryl rings on the heterocyclic ring systems. The high a_N and g values of **19** are attributed to the considerable delocalisation of spin density into the second five membered 2,1,3-dithiazolyl ring in addition to the spin orbit coupling that is as a result of the substantial spin density on sulphur S.[92]

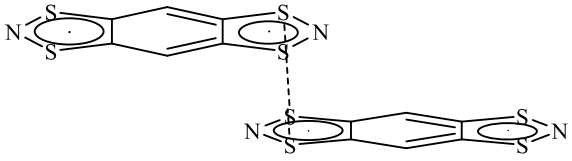

26

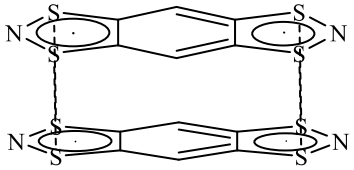

27

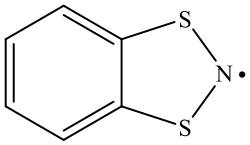

28

The EPR spectrum of benzo (bis -1,3,2-dithiazolyl) radicals **25** was reported by Barclay and co-workers as a triplet of triplets. This is also in alignment with delocalisation of unpaired

electron spin density over the two rings. They went further to show that the EPR spectrum is dependent on the nature of the sample and solvents used. The triplet of triplets in terms of the nature of sample were associated to non-interacting spins of species in solution; e.g. **26**$^{\bullet\bullet}$ while the solvent effect was linked to the size of the gap between the hyperfine interactions and intramolecular exchange bands (Fig. 1.9).[37]

The quintet of triplets' spectrum have been reported for **25** and just like the 1:1:1 triplets and triplet of triplets are in agreement with delocalisation of unpaired electron spin density to other attached rings. The extra triplet was confirmed to be due to the hyperfine interactions to protons on the benzo-bridge between the two 1,3,2-dithiazolyl rings. Further studies on the spectrum revealed dimers **26** with non-interacting radical centres that are largely due to two non-interacting doublets. Though, there is the possibility of association resulting in the diamagnetic dimer **27** which shows no assignable EPR signal.[37]

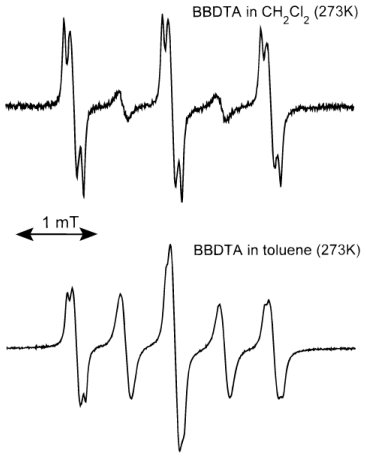

Figure 1.9 EPR spectra of **25** in methylene chloride (top) and toluene (bottom). "Adapted with permission from (Barclay, T. M.; Cordes, A. W.; de Laat, R. H.; Goddard, J. D.; Haddon, R. C.; Jeter, D. Y.; Mawhinney, R. C.; Oakley, R. T.; Palstra, T. T. M.; Patenaude, G. W.; Reed, R. W.; Westwood, N. P. C., *J. Am Chem. Soc.* **1997,** *119*, 2633-2641). Copyright © 1997, American Chemical Society".

1.3.4.3 Theoretical studies of dithiazoles

Theoretical calculations on the derivatives of 1,2,3-[12] and 1,3,2-[37, 89]dithiazolyl radicals have shown good agreement with reports of EPR studies in terms of the direction and extent of

delocalisation of unpaired electron spin density and significant coupling to certain nuclei in the radical ring systems. Output of theoretical calculations have also been used to account for changes in bond sizes; e.g. in benzo-fused 1,3,2- dithiazolyl radical **28** when it is derived from its cationic counterpart via reduction.

1.4 Goals of Thesis

The aim of this thesis is to have an in-depth understanding of the nature of electron transfer reactions and coupled chemical reactions that take place in symmetrical and unsymmetrical 1,2,4-dithiazolium salts. These redox experiments are aimed at confirming them as neutral or charged radical ring systems that have potentials as molecular conductors.

For the symmetrical 3,5-diaryl-1,2,4-dithiazolium perchlorate salt $\mathbf{3}^+$ and unsymmetrical 3-diethylamino-5-phenyl-1,2,4-dithiazolium salt $\mathbf{1}^+$, investigative studies take further steps from the electrochemical studies carried out by Uemachi and Hartung's groups, respectively, to examine the mechanism and kinetic parameters responsible for their redox behaviour via simulation of the cyclic voltammograms.

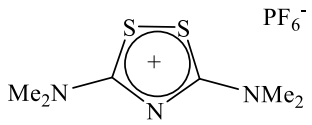

14

A symmetrical 1,2,4-dithiazolium salt with dimethylamino groups at the 3- and 5-positions **14** is synthesized and fully characterized by ^{1}H NMR, ^{13}C NMR, IR spectroscopy and X-ray diffraction experiments. Its redox behaviour just like others is probed using electroanalytical methods such as voltammetry in the form of cyclic and squarewave voltammetry, rotating disk electrode voltammetry coupled with simultaneous electrochemical electron paramagnetic resonance (SEEPR), DFT and simulation studies. The redox behaviour of all these 1,2,4-ring systems will be studied relative to those of isoelectronic thiazyl species with same substituents mentioned earlier in this review chapter.

1.5. References

1. Labes, M. M.; Love, P.; Nichols, L. F., *Chem. Rev.* **1979,** *79*, 1-15.

2. Banister, A. J.; Gorrell, I. B., *Adv. Mater* **1998,** *10*, 1415-1429.

3. Rawson, J. M.; Longridge, J. J., *Chem. Soc. Rev.* **1997,** *26*, 53-61.

4. Lang, J.-P.; Kawaguchi, H.; Tatsumi, K., *J. Chem. Soc., Dalton Trans.* **2002,** 2573-2580.

5. Chivers, T., Sulfur–Nitrogen Compounds. In *Encyclopedia of Inorganic Chemistry*, John Wiley & Sons, Ltd: 2006.

6. Ji, W.; Shi, S.; Du, H. J.; Ge, P.; Tang, S. H.; Xin, X. Q., *J. Phys. Chem.* **1995,** *99*, 17297-17301.

7. Oakley, R. T., Cyclic and Heterocyclic Thiazenes. In *Prog. Inorg. Chem.*, John Wiley & Sons, Inc.: **2007**; pp 299-391.

8. Banister, A. J.; Smith, N., *J. Chem. Edu.* **1982,** *59*, 1058-1062.

9. Chivers, T., *A Guide To Chalcogen-nitrogen Chemistry*. World Scientific Publishing Company, Incorporated: 2005.

10. Whangbo, M.-H.; Hoffmann, R.; Woodward, R. B., *Proc. Royal Soc.London A. Math.Phy. Sci.* **1979,** *366*, 23-46.

11. Boeré, R. T.; Roemmele, T. L., *Coord. Chem. Rev.* **2000,** *210*, 369-445.

12. Rawson, J. M.; McManus, G. D., *Coord. Chem. Rev.* **1999,** *189*, 135-168.

13. Cordes, A. W.; Haddon, R. C.; Oakley, R. T., *Adv. Mater* **1994,** *6*, 798-802.

14. Rawson, J. M.; Banister, A. J.; Lavender, I., The Chemistry of Dithiadiazolylium and Dithiadiazolyl Rings. In *Advances in Heterocyclic Chemistry*, Alan, R. K., Ed. Academic Press: 1995; Vol. Volume 62, pp 137-247.

15. Gregson, C. K. A.; Gibson, V. C.; Long, N. J.; Marshall, E. L.; Oxford, P. J.; White, A. J. P., *J. Am Chem. Soc.* **2006,** *128*, 7410-7411.

16. Lorkovic, I. M.; Duff, R. R.; Wrighton, M. S., *J. Am Chem. Soc.* **1995,** *117*, 3617-3618.

17. Al-Ahmad, S.; Boje, B.; Magull, J.; Rauchfuss, T. B.; Zheng, Y., *J. Am Chem. Soc.* **1995,** *117*, 1145-1146.

18. Sibert, J. W.; Forshee, P. B.; Lynch, V., *Inorg. Chem.* **2005,** *44*, 8602-8609.

19. Beer, P. D., *Chem. Soc. Rev.* **1989,** *18*, 409-450.

20. Liu, Z.; Yasseri, A. A.; Lindsey, J. S.; Bocian, D. F., *Science* **2003,** *302*, 1543-1545.

21. Krumova, K.; Cosa, G., *J. Am Chem. Soc.* **2010,** *132*, 17560-17569.

22. Pop, F.; Amacher, A.; Avarvari, N.; Ding, J.; Daku, L. M. L.; Hauser, A.; Koch, M.; Hauser, J.; Liu, S.-X.; Decurtins, S., *Chem. – A Eur. J.* **2013,** *19*, 2504-2514.

23. Bechgaard, K.; Parker, V. D.; Pedersen, C. T., *J. Am. Chem. Soc.* **1973,** *95*, 4373-4378.

24. MacLean, G. K.; Passmore, J.; Rao, M. N. S.; Schriver, M. J.; White, P. S.; Bethell, D.; Pilkington, R. S.; Sutcliffe, L. H., *J. Chem. Soc., Dalton Trans.* **1985,** 1405-1416.

25. Boeré, R. T.; Moock, K. H.; Parvez, M., *Z. Anorg. Allg. Chem* **1994,** *620*, 1589.

26. Boere, R. T.; Moock, K. H., *J. Am Chem. Soc.* **1995,** *117*, 4755-4760.

27. Geue Rodney, J.; Hanna John, V.; Höhn, A.; Qin, C. J.; Ralph Stephen, F.; Sargeson Alan, M.; Willis Anthony, C., In *Electron Transfer Reactions*, American Chemical Society: 1997; Vol. 253, pp 137-150.

28. Bullock, J. P.; Bond, A. M.; Boeré, R. T.; Gietz, T. M.; Roemmele, T. L.; Seagrave, S. D.; Masuda, J. D.; Parvez, M., *J. Am Chem. Soc.* **2013,** *135*, 11205-11215.

29. Brooks, W. V. F.; Burford, N.; Passmore, J.; Schriver, M. J.; Sutcliffe, L. H., *J. Chem. Soc., Chem. Commun.* **1987,** 69-71.

30. Molev, G.; Tumanskii, B.; Sheberla, D.; Botoshansky, M.; Bravo-Zhivotovskii, D.; Apeloig, Y., *J. Am Chem. Soc.* **2009,** *131*, 11698-11700.

31. Becker, M.; Förster, C.; Franzen, C.; Hartrath, J.; Kirsten, E.; Knuth, J. r.; Klinkhammer, K. W.; Sharma, A.; Hinderberger, D., *Inorg. Chem.* **2008,** *47*, 9965-9978.

32. Förster, C.; Klinkhammer, K. W.; Tumanskii, B.; Krüger, H.-J.; Kelm, H., *Angew. Chemie Int. Ed.* **2007,** *46*, 1156-1159.

33. Lee, V. Y.; Sekiguchi, A., *Acc. Chem. Res.* **2007,** *40*, 410-419.

34. Bryan, C. D.; Cordes, A. W.; Haddon, R. C.; Hicks, R. G.; Kennepohl, D. K.; MacKinnon, C. D.; Oakley, R. T.; Palstra, T. T. M.; Perel, A. S.; et al., *J. Am Chem. Soc.* **1994,** *116*, 1205-1210.

35. Sandman, D. J.; Zoski, G. D.; Burke, W. A.; Hamill, G. P.; Ceasar, G. P.; Baker, A. D., *J. Chem. Soc., Chem. Commun.* **1981,** 829-831.

36. Aherne, C. M.; Banister, A. J.; Gorrell, I. B.; Hansford, M. I.; Hauptman, Z. V.; Luke, A. W.; Rawson, J. M., *J. Chem. Soc., Dalton Trans.* **1993,** 967-972.

37. Barclay, T. M.; Cordes, A. W.; de Laat, R. H.; Goddard, J. D.; Haddon, R. C.; Jeter, D. Y.; Mawhinney, R. C.; Oakley, R. T.; Palstra, T. T. M.; Patenaude, G. W.; Reed, R. W.; Westwood, N. P. C., *J. Am Chem. Soc.* **1997,** *119*, 2633-2641.

38. Beekman, R. A.; Boeré, R. T.; Moock, K. H.; Parvez, M., *Can. J. Chem* **1998,** *76*, 85-93.

39. Cordes, A. W.; Haddon, R. C.; Oakley, R. T.; Schneemeyer, L. F.; Waszczak, J. V.; Young, K. M.; Zimmerman, N. M., *J. Am Chem. Soc.* **1991,** *113*, 582-588.

40. Cordes, A. W.; Haddon, R. C.; Hicks, R. G.; Oakley, R. T.; Palstra, T. T. M.; Schneemeyer, L. F.; Waszczak, J. V., *J. Am. Chem. Soc* **1992,** *114*, 5000-5004.

41. Cordes, A. W.; Haddon, R. C.; Hicks, R. G.; Kennepohl, D. K.; Oakley, R. T.; Schneemeyer, L. F.; Waszczak, J. V., *Inorg. Chem* **1993,** *32*, 1554.

42. Barclay, T. M.; Cordes, A. W.; Oakley, R. T.; Preuss, K. E.; Reed, R. W., *Chem. Mater.* **1999,** *11*, 164-169.

43. M. Barclay, T.; Wallace Cordes, A.; J. Burgess, I.; T. Oakley, R.; W. Reed, R., *Chem. Commun.* **1998,** 1939-1940.

44. Torroba, T., *J. Prakt. Chem.* **1999,** *341*, 99-113.

45. Argyropoulos; N.G., *Sci. of Synth.* **2004,** *13*, 29-71.

46. Neels, J.; Ziemer, B.; Meisel, M.; Leibnitz, P., *Z. Anorg. Allg. Chem.* **1986,** *542*, 123-130.

47. Hamed, A., Sedeak, M., Ismail, A.E.H., Stumpf, R., Fischer, H.,Jochims, J.C.,, *J. Prakt. Chem.* **1995** *337*.

48. Liebscher, J.; Hartmann, H., *Liebigs Ann.* **1977,** *1977*, 1005-1012.

49. Leistner, S., Wagner, G., Ackermann, M.,, *Z. chem.* **1977,** *17*, 223.

50. Agency of Industrial Sciences and Technology 1982.; JP 82 156 474., *Chem. Abstr.* **1983,** *98*, 126109j.

51. Hartmann, H., *In Houben-Weyl* **1994,** *E 8d*, 13.

52. Corsaro, A.; Compagnini, A.; Chiacchio, U.; Purrello, G., *Synthesis* **1984,** *1984*, 515-516.

53. Corsaro, A.; Compagnini, A.; Perrini, G.; Purrello, G., *J. Chem. Soc. Perkins Trans 1* **1984,** 897-900.

54. Hartmann, H.; Liebscher, J.; Czerney, P., *Tetrahedron* **1985,** *41*, 5371-5376.

55. Liebscher, J., Hartmann, H., (1977); DD 126 401., *Chem. Abstr.* **1978,** *88*, 62394g.

56. Köhler, R.; Sieler, J.; Richter, R.; Hoyer, E.; Beyer, L.; Maartmann-Moe, K., *Z. Anorg. Allg. Chem.* **1989,** *576*, 203-214.

57. Fernández, V.; Monge, A.; Gutierrez-Puebla, E.; Beyer, L.; Hartung, J.; Richter, R., *Z. Anorg. Allg. Chem.* **1990,** *586*, 79-86.

58. Peyronel, G.; Pignedoli, A.; Malavasi, W., *Spectrochim. Acta. Part A: Mol. Spec.* **1982,** *38*, 971-973.

59. Oliver, J. E.; Brown, R. T.; Fye, R. L.; Borkovec, A. B., *J. Agr. Food Chem.* **1973,** *21*, 753-755.

60. Oliver, J. E., *J. Org. Chem.* **1971,** *36*, 3465-3467.

61. Oliver, J. E.; Chang, S. C.; Brown, R. T.; Stokes, J. B.; Borkovec, A. B., *J. Med. Chem.* **1972,** *15*, 315-320.

62. Bailey, R. T., *J. Chem. Soc. A: Inorganic, Physical, Theoretical* **1970,** 1386-1389.

63. MacDonald, J. W.; McKinnon, D. M., *Can. J. Chem* **1967,** *45*, 1225-1229.

64. Raj, T.; Bhatia, R. K.; Sharma, R. K.; Gupta, V.; Sharma, D.; Ishar, M. P. S., *Eur. J. Med. Chem.* **2009,** *44*, 3209-3216.

65. Nihon, T. N., Seizo, K.K.,(1982); JP 82 183 769., *Chem. Abstr.* **1983,** *98*, 179388.

66. Hartung, J.; Rosenbaum, K.; Beyer, L.; Losada, J.; Fernandez, V., *J. Prakt. Chem.* **1991,** *333*, 537-544.

67. Uemachi, H.; Iwasa, Y.; Mitani, T., *Electrochim. Acta* **2001,** *46*, 2305-2312.

68. Pedersen, C. T.; Bechgaard, K.; Parker, V. D., *J. Chem. Soc., Chem. Commun.* **1972,** 430-431.

69. Sugimoto, K.; Uemachi, H.; Maekawa, M.; Fujiwara, A., *Cryst. Growth. Des.* **2012,** *13*, 433-436.

70. Hofmann, A. W., *Ber. Dtsch. Chem. Ges.* **1869,** *2*, 645-649.

71. Belluz, P. D. B.; Cordes, A. W.; Kristof, E. M.; Kristof, P. V.; Liblong, S. W.; Oakley, R. T., *J. Am Chem. Soc.* **1989,** *111*, 9276-9278.

72. Aherne, C. M.; Banister, A. J.; Hibbert, T. G.; Luke, A. W.; Rawson, J. M., *Polyhedron* **1997,** *16*, 4239-4245.

73. Aherne, C. M.; Banister, A. J.; Gorrell, I. B.; Hansford, M. I.; Hauptman, Z. V.; Luke, A. W.; Rawson, J. M., *J. Chem. Soc., Dalton Trans.* **1993,** 967.

74. Hayes, P. J.; Oakley, R. T.; Cordes, A. W.; Pennington, W. T., *J. Am. Chem. Soc.* **1985,** *107*, 1346-1351.

75. Cordes, A. W.; Hayes, P. J.; Josephy, P. D.; Koenig, H.; Oakley, R. T.; Pennington, W. T., *J. Chem. Soc., Chem. Commun.* **1984,** 1021-1022.

76. Boeré, R. T.; Tuononen, H. M.; Chivers, T.; Roemmele, T. L., *J. Organomet. Chem.* **2007,** *692*, 2683-2696.

77. Oakley, R. T.; Reed, R. W.; Cordes, A. W.; Craig, S. L.; Graham, S. B., *J. Am. Chem. Soc* **1987,** *109*, 7745-7749.

78. Geevers, J.; Hackmann, T.; Trompen, W. P., *J. Chem. Soc. C* **1970,** 875-878.

79. Boeré, R. T.; Roemmele, T. L., *Phosphorus, Sulfur, Silicon* **2004,** *179*, 875-882.

80. Boeré, R. T.; Oakley, R. T.; Reed, R. W.; Westwood, N. P. C., *J. Am. Chem. Soc* **1989,** *111*, 1180-1185.

81. Boeré, R. T.; Roemmele, T. L.; Yu, X., *Inorg. Chem.* **2011,** *50*, 5123-5136.

82. Boeré, R. T.; Cordes, A. W.; Hayes, P. J.; Oakley, R. T.; Reed, R. W.; Pennington, W. T., *Inorg. Chem.* **1986,** *25*, 2445-2450.

83. Boere, R. T.; Moock, K. H., *Unpublished data*.

84. Rawson, J. M.; Alberola, A.; Whalley, A., *J. Mater. Chem.* **2006,** *16*, 2560-2575.

85. Awaga, K.; Tanaka, T.; Shirai, T.; Fujimori, M.; Suzuki, Y.; Yoshikawa, H.; Fujita, W., *Bull. Chem. Soc. Jpn.* **2006,** *79*, 25-34.

86. McManus, G. D.; Rawson, J. M.; Feeder, N.; Palacio, F.; Oliete, P., *J. Mater. Chem.* **2000,** *10*, 2001-2003.

87. Barclay, T. M.; Cordes, A. W.; George, N. A.; Haddon, R. C.; Oakley, R. T.; Palstra, T. T. M.; Patenaude, G. W.; Reed, R. W.; Richardson, J. F.; Zhang, J., *J. Chem. Soc., Chem. Commun.* **1997,** 873-874.

88. Itkis, M. E.; Chi, X.; Cordes, A. W.; Haddon, R. C., *Science* **2002,** *296*, 1443-1445.

89. Awere, E. G.; Burford, N.; Haddon, R. C.; Parsons, S.; Passmore, J.; Waszczak, J. V.; White, P. S., *Inorg. Chem.* **1990,** *29*, 4821-4830.

90. Barclay, T. M.; Cordes, A. W.; Haddon, R. C.; Itkis, M. E.; Oakley, R. T.; Reed, R. W.; Zhang, H., *J. Am Chem. Soc.* **1999,** *121*, 969-976.

91. Barclay, T. M.; Cordes, A. W.; George, N. A.; Haddon, R. C.; Itkis, M. E.; Mashuta, M. S.; Oakley, R. T.; Patenaude, G. W.; Reed, R. W.; Richardson, J. F.; Zhang, H., *J. Am Chem. Soc.* **1998,** *120*, 352-360.

92. Harrison, S. R.; Pilkington, R. S.; Sutcliffe, L. H., *J. Chem. Soc., Faraday Trans. 1* **1984,** *80*, 669-689.

93. Barclay, T. M.; Cordes, A. W.; Goddard, J. D.; Mawhinney, R. C.; Oakley, R. T.; Preuss, K. E.; Reed, R. W., *J. Am Chem. Soc.* **1997,** *119*, 12136-12141.

Chapter Two

Methodology

2.1 Electroanalytical methods

Electroanalytical techniques are analytical chemistry techniques that study the behaviour of analytes by measuring the potentials and current in an electrochemical experiment.[1-2] These techniques include potentiometry, coulometry and voltammetry, amongst others. Potentiometry is used to determine the concentration of an analyte in solution between two electrodes whose potential is measured by the use of a high impendance voltmeter. The high impendance voltmeter allows negligible flow of current through the cell and since there is zero net current, no electrochemical reaction takes place and the system is in equilibrium. They occur in the form of potentiometric titrations which play important roles in the pharmaceutical and chemical sectors. [3-4] In coulometry, the current flowing through the cell is determined when a certain amount of analyte is modified into another form through a redox process. It has various forms and these include coulometric titrations.[5]

2.1.1 Voltammetry

In voltammetry, the behaviour of analytes in solution is studied either by keeping the potential across the electrodes unchanged or varying it in order to measure the current flow through the cell.[4] The resulting curves from these current values (vertical axis) versus the varied or fixed applied potentials (horizontal axis) are called voltammograms.[2, 6-7] The shapes of these curves hinge on the scan rates and on the nature of the mass transport in solution by which species are drawn to the electrode. [7-8]

Voltammetry experiments are carried out using a three-electrode system of working, reference and auxiliary electrodes (Fig. 2.1). The three-electrode system is combined with the potentiostat which supplies voltage to the working electrode relative to the reference electrode for accurate measurement.[9] The working electrode which often comes in contact with the analyte

supplies it with potential that will aid electron transport. Working electrodes are made from conducting materials such as glassy carbon, platinum, gold and silver.[9]

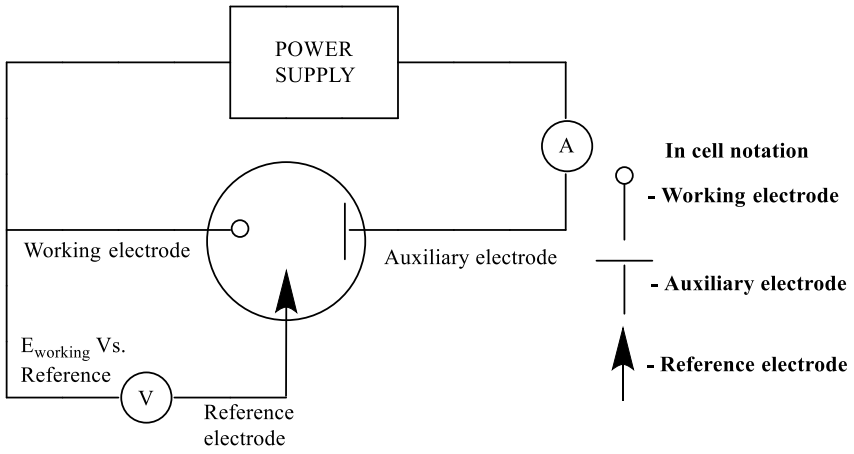

Figure 2.1 Basic components of a 3-electrode voltammetry cell.[24]

The potentiostat (power supply) supplies the potential while the potentiometer which is used to measure the potential between the working and reference electrodes possesses a high input impendance which allows negligible current to be drawn through the reference electrode. Hence the potential of the reference electrode is constant. Examples of the reference electrodes are the saturated calomel electrode (SCE) and Ag/Ag^{+} electrode.[8] The auxiliary electrode is introduced to support the reference electrode while simultaneously balancing charge at the working electrode. The auxiliary electrode possesses electrochemical properties that do not interfere with the functionality of the working electrode surface.[10] A feedback loop ensures that the potentiostat supplies a constant potential through the circuit. The major issue with aqueous reference electrodes in non-aqueous solvents is the variation in the measured potentials as solvents are changed. This is attributed to the different junction potentials in existence between systems. One method to reduce the junction potential of the reference electrodes is to carry out electrochemistry experiments using the same solvent. Another method with which the junction potentials could be minimized is to calibrate the reference electrodes using a well-defined redox couple as an internal standard in electrochemical experiments. Two conditions necessary to act as

a good reference redox couple are that it must be stable throughout the duration of the electrochemical measurements coupled with possessing a constant potential in the system under study. Avery good example of a reference redox couple for non-aqueous and controlled aqueous system is the ferrocene/ferrocenium Fc/Fc^+ couple which has been recommended by IUPAC. [11,12]

The internal standard acts as a reference potential standard in cases where the reference electrode alone is incapable of providing constant reference potential. The internal standard must possess a redox potential $E_{1/2}$ that is completely separated from the potential of the analyte under study. The $E_{1/2}$ of the reference electrode is recorded as 0V on the horizontal potential axis by adjusting the experimental potential scale.[13] This is similar to a system comprising three electrodes but with a pseudo-reference electrode (platinum or silver wire) coupled with the use of an internal standard for the redox potentials.[14-16]. The Fc/Fc^+ couple with 0.1 M of the ^{n}-NBu_4PF_6 shows up at 0.38V against SCE in acetonitrile (CH_3CN) solution and 0.48V in dichloromethane.[17] The advantages pseudo-reference electrodes have are not unconnected to the simplicity of their construction, small ohmic resistance effect, disappearance of the liquid junction potentials and the zero possibility of contamination of the bulk solution by molecules of the solvent or ions. Some of their disadvantages include the lack of thermodynamic equilibrium attributable to the adjacent phases lacking anions or cations which result in difficulty to calculate real potentials. Also, their polarizability results in shifts in their potential values due to the applied current density. In addition, their behaviour become doubtful once they are used outside the limited range of conditions such as temperature or pH.[18]

It is standard practice that the working electrode maintains its known dimensions and surface characteristics and that is why it is regularly cleaned with care (before and after use).[19]

In voltammetry experiments, supporting electrolytes are non-electroactive species added to the solvent for better charge transfer in solution via diffusion (eliminating the effect of migration). In electrochemical experiments, the current in the bulk solution is carried by ion migration while migration and diffusion are the means of mass transport near the surface of the

working electrode. The addition of excess supporting electrolyte to the solution drastically reduces the contribution of migration and also aid the reduction of resistance to flow of current.[7, 20]

Examples of voltammetric techniques include linear sweep, staircase, squarewave, cyclic, cathodic and anodic stripping, polarography, alternating current, and rotated electrode voltammetries, but only those that are applicable to this thesis will be discussed in this method chapter.

2.1.1.1 Squarewave voltammetry (SWV)

SWV is one of the methods classified under pulse voltammetry. Its invention by Ramaley and Krause[21] was extensively developed by Osteryoungs and co-workers.[22] In SWV, the potential values between the reference and working electrodes are swept linearly with time while taking measurements of the current at the working electrode.[23] There is the formation of potential waveform at the working electrode which consists of squarewave scans which are superimposed to form staircases. The staircase is the result of applying a square pulse to the linear scan (Fig. 2.2 right). The electrode is subjected to a number of measurement cycles whose diffusion components remain unchanged. When compared with squarewave polarography or ac polarography, a steady state of recurring current cycles which is a function of the extra cycles of potentials is attainable in SWV. This is due to the application of the squarewave about a stationary electrode whose potential value is changing.[24]

In addition, it is the best of all the pulse methods because it is able to suppress background currents such that fitting to theoretical models is done with better accuracy compared to cyclic voltammetry. Moreover, it possesses sensitivity that is slightly higher than that of differential pulse voltammetry coupled with faster scan times and improved application to extensive list of electrodes and systems.[24] This has led to improved output of the current signal which is a result of the faster decay rate of the capacitive charging current compared to the faradaic current.[25]

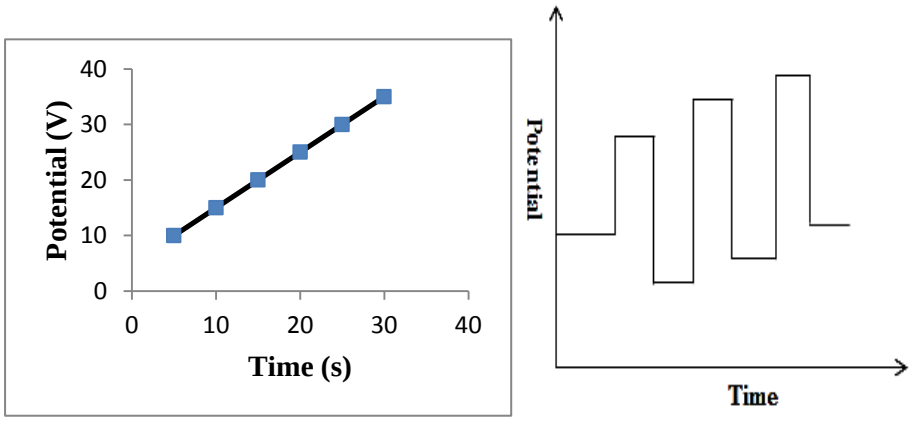

Figure 2.2 Graphs of LSV (left) and SWV (right)

2.1.1.2 Cyclic voltammetry

Cyclic voltammetry (CV) is one of the most commonly used electrochemical measurements to probe the properties of analytes in solution coupled with their redox kinetic and thermodynamic behaviour.[7] From this type of measurement, the plot of potential applied to the working electrode against time gives a direct proportion linear graph whose slope is the scan rate (Figure 2.3). The forward scan before the reversal potential is typically the linear sweep voltammetry (Fig. 2.2 left).[24] The working electrode's potential gets reversed at the attainment of the set potential for the background scan to be completed.

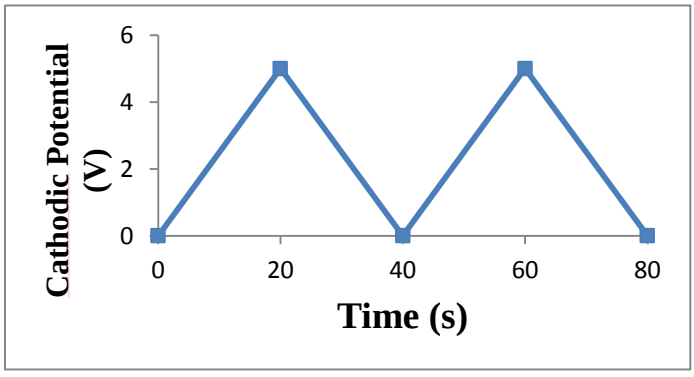

Figure 2.3. CV waveform

In cyclic voltammetry experiments, the nature of processes obtained determines the nature of parameters that can be extracted. For instance, thermodynamics parameters are obtained if a redox experiment is reversible (fast heterogenous electron exchange) while kinetic potentials

and supporting parameters are the results of irreversible (slow heterogenous electron exchange) processes.

Quite a number of equations developed from electrochemical theories have been used to explain the dynamics of voltammetric relationship between experimental and theoretical electrochemical results. These include the Butler-Volmer and Nernst equations[7] which are relevant to simple thermodynamics and kinetic redox events. The Nernst equation (Eqn. 2.1) named after the German physicist Walther Nernst showed the redox equilibria of an electron-transfer as being established from thermodynamics parameters. This is an equation that holds true when the rate of heterogenous electron-transfer is fast enough to set up a dynamic equilibrium at the phase boundary resulting in reversible processes. This means that the equation no longer holds when electrochemical kinetics from irreversible processes form the bulk of response from the analyte under study.[7, 26-27]

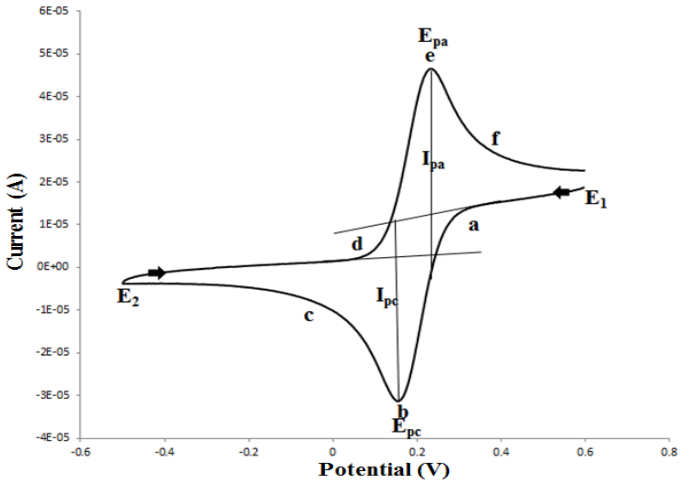

Figure 2.4. Reversible cyclic voltammogram showing cathodic (i_{pc}) and anodic (i_{pa}) currents respectively.

The cyclic voltammogram shows the effect of basic potential step experiments on the interface between a solid electrode and an unstirred (diffusion-controlled) solution containing an electroactive species. It basically reflects the processes that occur between potentials E_1 and E_2 which represent the points where Faradaic processes do not occur and where mass-transfer is

limited respectively. The diffusion-controlled flow of electrons is required to support the active electrochemical processes at scan rates that are consistent with the potential values (between the working and reference electrodes) that are functionally related to the current.[24] When the potential is sufficiently positive to start reduction of the analyte, a cathodic current starts to build up at "a" due to the reduction process taking place at the electrode. The current increases gradually and peaks at "b" The logarithmic relationship between E and the ratio of the reduced to the oxidized species (Eqn. 2.1) is as a result of the rapid rate of change in the region where $E = E^{\ominus}$ (where the ratio of the reduced to the oxidized species equals 1). The current then drops from "b" to "c" showing that the solution around the electrode is depleted of the reduced species as it is being gradually converted to the oxidized species via electrolysis. On reaching the reversal potential E_2, the scanning is switched to move in the opposite direction producing a reversal current that has the same shape as the forward scan for virtually the same reasons. An in-depth understanding of these redox processes coupled with the change in concentration that occurs in solution beside the electrode is best explained by the Nernst equation for reversible systems.

$$E = E^{\ominus}_{ox,red} + \frac{0.059\ V}{1} \log \frac{\text{activity of reduced sp.}}{\text{activity of oxidized sp.}} \qquad \text{eqn. 2.1}$$

Where $E^{\ominus}$ represents the standard reduction potential of the redox couple.[28]

These redox peaks or processes always have very similar shapes and from them, thermodynamic information about the analyte could be obtained.[13] Other information that could be extracted from CV experiments is the current flux with respect to diffusion of species to the electrode surface. This relationship is described by the Cottrell equation (Eqn. 2.2), named after its discoverer, Frederick Gardner Cottrell.

$$i = \frac{nFAc\sqrt{D}}{\sqrt{\pi t}} \qquad \text{eqn. 2.2}$$

Where *i* = current in Amperes, n = number of electrons required for electron transfer, F = Faraday's constant in Coulomb per mole, A = area of the electrode in cm^2, c = initial

concentration of the redox active analyte in mol/cm^3, D = diffusion coefficient for analyte in cm^2 per second and t = time in second. The linearity of the plot of current against square root of scan rates (t) is a strong indication that a redox event is diffusion-controlled while deviation from linearity indicates non-diffusion controlled redox events.[13] For reversible processes, Equation 2.3 [6] below holds when one mole of electron is transferred (n=1) with E_{pc} and E_{pa} representing the cathodic and anodic potentials respectively.

$$\left|E_{pc} - E_{pa}\right| = \frac{57\ \text{mV}}{n} \qquad \text{eqn. 2.3}$$

Also, the ratio of the cathodic and anodic peak currents should be very close to unity ($i_{pc}/i_{pa} = 1$). This ratio can be distorted in the presence of a homogenous chemical process following the heterogenous electron transfer resulting in quasi-reversible or irreversible waves. This way, the ratio of the peak currents becomes less than or greater than 1. From an analysis of the disagreement in these ratios, it becomes possible in principle to use a method such as simulation to extract kinetic information from the lineshape of the cyclic voltammograms rather than rely on the peak heights of the processes.[13] The Butler–Volmer equation is a fundamental equation that investigates the kinetics of electrochemical reactions. It does this by showing the nature of the electron transfer that takes place at the interface of the working electrode[7] followed by chemical reactions as long as the mass transport system in solution is diffusional and not convectional or migrational.[2] It is shown in Equation 2.4 and in the more compact form in Equation 2.5.[29]

$$I = A \,.\, i_0 .\{\exp\left[\frac{\alpha_a n F}{RT}\left(E - E_{eq}\right)\right] - \exp\left[\frac{\alpha_c n F}{RT}\left(E - E_{eq}\right)\right\} \qquad \text{eqn. 2.4}$$

$$f_e = k_s\left\{[A]_{x=0}\, e\left[\frac{-\alpha F}{RT}(E-E^0)\right] - [B]_{X=0}\, e\left[\frac{(1-\alpha)F}{RT}(E-E^0)\right]\right\} \qquad \text{eqn. 2.5}$$

where f_e represents the flux of electrons to the solution from the electrode; k_s is the standard rate constant, α is the transfer coefficient, F is Faraday constant, R is the gas constant, T is the temperature in Kelvin, E is the applied potential between the working and reference electrodes and E^0 is the formal potential in Volts.

2.1.1.3 Electrochemical and Chemical Reversibility.

It is a common observation to have heterogenous electron transfer steps (E) accompanied by homogenous chemical reaction steps (C) in cyclic voltammetry experiments.[24] If species A undergoes a one-electron reduction to give an electroactive species B and this in turn undergoes a first-order solution-phase chemical reaction to give C, then the equations can be written as:

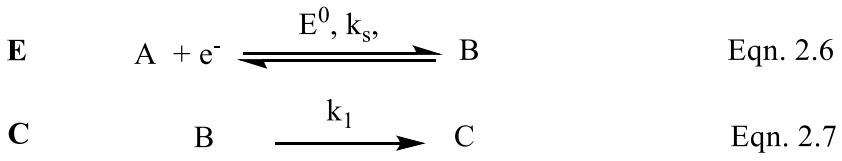

where E_f^0 is the formal potential of the reduction process in volts (V), k_s is the electron transfer rate constant, k_1 is the chemical rate constant and α is the transfer coefficient. The combination of these two reactions forms the EC mechanism. From this, it is also possible to build electrode reaction mechanisms from diverse combination of E and C steps associated with different levels of reversibility.[24]

Reversibility in electrochemical reactions is related to the heterogenous kinetics at the surface of the working electrode. An electron transfer reaction that is "fast" in both directions is said to be electrochemically reversible and is interpretable using the Nernst equation (Eqn. 2.1). From this type of reaction, equilibrium is attained at each potential applied on the time scale of the electrochemical experiment. Hence, a process that is electrochemically reversible under certain conditions such as carrying out cyclic voltammetry at a slow scan rate may be irreversible at faster scan rates or under hydrodynamic conditions such as convection. Electochemical irreversibility is used to describe slow heterogenous electron transfer kinetics which is no longer in equilibrium and does not agree with the Nernstian equation.[24]

Chemical reversibility is related to the stability of the electroactive species formed from electron transfer steps. For example, if the chemical step associated with the consumption of B is fast such that equilibrium is maintained on the time scale of the voltammetric experiment, then

the process is chemically reversible. It is characterized by small or even zero K_c from equal or almost equal forward k_f and backward k_b rate constants. Chemical irreversibility on the other hand occurs when the chemical consumption of B is slow such that equilibrium is no longer maintined on the time scale of the voltammetric experiment. Also, it is characterized by high K_c that results from high forward rate constant k_f and very low back rate constant k_b. From earlier discussion on EC mechanisms, it helps a great deal to discuss the nomenclature of existing EC mechanisms:[24]

CE mechanism: The electroactive species B generated via the chemical step C undergoes an electron transfer step at the electrode.[30] This type of reaction mechanism is evident when metal complexes are subjected to reduction (Eqns. 2.8-2.9).

$$A \rightleftharpoons B \qquad \text{Eqn. 2.8}$$

$$B + ne^- \rightleftharpoons C \qquad \text{Eqn. 2.9}$$

EC mechanism: In this reaction pattern, the electron transfer step results in B which reacts with species around it in solution such as the solvent to form a non-electroactive species C at the reductive potential of A (Eqns 2.10-2.11). There are cases where the chemical step is a dimerization reaction designated as EC_2 (Eqn. 2.12). This is a common occurrence when B is a radical and is capable of forming a dimer from the two approaching unpaired electrons. Also, there are situations where an electron transfer step is followed by two different chemical steps to form the ECC mechanism (Eqns. 2.13-2.14).

$$A + ne^- \rightleftharpoons B \qquad \text{Eqn. 2.10}$$

$$B \rightleftharpoons C \qquad \text{Eqn. 2.11}$$

$$B \rightleftharpoons 2B \qquad \text{Eqn. 2.12}$$

$$B \rightleftharpoons C \qquad \text{Eqn. 2.13}$$

$$C \rightleftharpoons D \qquad \text{Eqn. 2.14}$$

EE mechanism: This is a consecutive two one-electron transfer whereby the electroactive product from the first electron transfer step undergoes a second electron transfer step at potentials more or less anodic than that of the first (Eqns. 2.15-2.16). Interestingly, there are cases in the EE where the second electron transfer steps are thermodynamically more feasible than the first. This is attributed to the structural changes associated with the electroactive species B from the first electron transfer step which results in a shift of its standard potential to promote a second electron transfer step. Valuable considerations are given to standard potentials of electron transfer steps and also the possibility of solution phase electron transfer reactions via the disproportionation of B or its reverse reaction (comproportionation). EE mechanisms have high tendencies to be followed by chemical steps that are reversible or irreversible to form the EEC mechanism.[24]

$$A + e^- \underset{}{\overset{E^0_1}{\rightleftharpoons}} B \qquad \text{Eqn. 2.15}$$

$$A + e^- \underset{}{\overset{E^0_2}{\rightleftharpoons}} B \qquad \text{Eqn. 2.16}$$

Square schemes: This is a mechanism that involves the coupling of two one-electron transfers with two chemical steps in a cyclic manner.[24, 30] This is a common phenomenon when the product of a reduction electron transfer step undergoes unavoidable structural changes (Scheme 2.1).

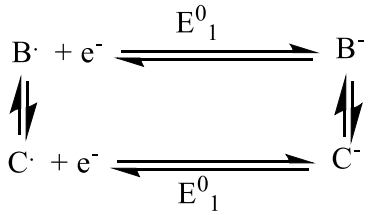

Scheme 2.1 Square scheme mechanism for electrochemical reactions

2.1.1.4 Rotating Disk Electrode (RDE)

The rotating disk electrode (RDE) is a convective working electrode system utilized in steady-state hydrodynamic techniques. Hydrodynamic techniques are subcategories of electroanalytical methods in which the analyte solution exhibits a laminar flow across the

working electrode. This result in a steady-state current called the limiting current I_l which can be accounted for by the solution flow (convection) rather than by diffusion. The RDE which is the working electrode rotates and stirs the solution to flow in order to attain a well-controlled flux or mass-transfer that would result in reliable outcomes. This type of working electrode is used in electrochemical experiments when probing the transport kinetics and mechanisms of redox reactions. One of the advantages of hydrodynamic techniques is that the effect of capacitive charging is comparably small as a result of the low scan rates and steady-state conditions used during the experiment. Often, the RDE method is used to reliably determine the number (n) of electrons transferred and also the diffusion coefficients (D) in redox reactions.[2]

The rotating disk electrode consists of a disk of the working electrode material (glassy carbon or platinum) embedded in a non-conducting mantle such as Teflon, epoxy resin or plastic. The mantle is directly attached to a motor by an adaptable rotating shaft or pulley arrangement which induces rotation at a frequency f (revolutions per second), though a much clearer illustration of the rotation rate is the angular velocity, ω (s^{-1}) where $\omega = 2\pi f$. The RDE is submerged into solution and is made to rotate around an axis passing through and perpendicular to the centre of the disk.[2] This rotation creates convection flows that are perpendicular to the electrode surface and then spread outwards from the surface. This way, the effect of diffusion on transfer measurements is reduced due to the fast mixing afforded by rotation which enables regular restoration of the redox-active species to the electrode surface.[31] In hydrodynamic experiments, the limiting current I_l produced via reduction or oxidation of redox-active species at the electrode surface is described by the Levich equation:

$$I_l = 0.62nFAC\nu^{-1/6}D^{2/3}\omega^{1/2} \qquad \text{eqn. 2.17}$$

where I_l is the limiting current in Ampere, n is the number of transferred electrons per molecule, F is the Faraday's constant in Coulombs per mole of electron, A is the electrode surface area in cm^2, C is the concentration of the analyte in mole per cm^3, D is the diffusion coefficient in cm^2/s,

ν is the kinematic viscosity of the solution in cm^2/s and ω is the angular velocity of the rotating disk in s^{-1}. In practice, the viscosity of the pure solvent is always used in place of that of the mixture of solvent, analyte and electrolyte.[2]

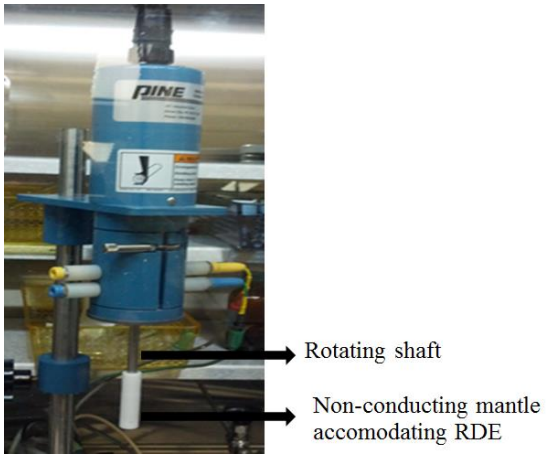

Figure 2.5 Rotating disk electrode mounted on a rotator

2.2 Simulation

Dynamic simulation is defined as the imitation of the behaviour of a system with respect to time.[32] First and foremost, it requires the development of a model (the algorithms and equations used to come up with the behaviour of the system being modeled) of the physical process under study. This is followed by carrying out the simulation via computers (computer simulations) or the use of softwares to fit the data set of the system into its model or vice versa.

The most common treatment of any electrochemical problem is based on the fast implicit finite difference (FIFD) algorithm which makes use of the discretization of space and time. Space discretization is fundamentally dividing the space close to the surface of the electrode into volume elements. The thickness of this volume elements increase with increase in distance from the surface of the electrode in the presence of an exponentially expanding space grid. The result of this is a more reliable set of concentration profiles that are strongly associated with reaction layers produced by homogenous chemical steps.

The simulation procedure starts with attempts to create models that will closely imitate the experimental cyclic voltammograms. The first step is to enter all constant values such as charge transfer coefficient $\alpha = 0.5$ (for Butler-Volmer formalism), the diffusion coefficient of the salt under study, the area of the electrode used for the experiment, the initial, set and final potentials as recorded in the experimental CV, the temperature at which the experimental CVs were obtained and the scan rates at which each run was carried out. This is followed by the adjusment of the potentials and their corresponding electron transfer rate constants until a model CV closely similar to the experimental CV is obtained. If a good replica of the experimental CV is obtained, then the simulation can start. But, if on the other hand, the model is having difficulty in closely imitating the experimental CV, then there might be the need to introduce a following chemical step. The chemical steps would have their forward and backward chemical rate constants in addition to the equilibrium constants adjusted alongsides the potentials and their corresponding rate constants to get a model that will imitate the experimental CV.

Simulation could help to converge the fits as well as optimize important parameters such as k_{s1}, k_{s2}, and D as well as reliable estimates of the equilibrium constants K_c and forward and backward chemical rate constants k_f and k_b, respectively. The optimization of the simulated CV response is regarded as successful when the experimental and simulated peak heights and positions overlay reasonably well on each other (Fig. 2.6) This would help to come up with reasonable predictions about the behaviour of the system under study.[32] In chemistry, simulation is applicable to various areas of which electrochemistry is one.[33]

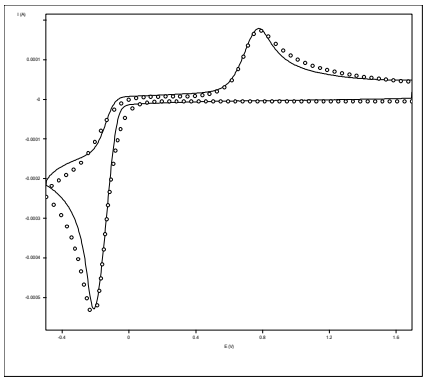

Figure 2.6 Reasonable overlay of theoretical and experimental CV

2.2.1 **Digital simulation in electrochemistry**.

Digital simulation has become a very useful tool to researchers of theoretical and experimental electrochemistry. It is a method whereby a numerical model of the electrochemical experiment is set up inside a computer followed by allowing the model to develop via a set of differential equations.[34] This results in the extraction of numerical representation of concentration profiles, potential values (transient or steady-state) and current functions.[24] Digital simulation of electrochemical experiments was pioneered by Stephen Feldberg[30] who is still at work developing the field till date. A lot of simulators exist as tools for electrochemical researchers and they include Digisim, ELSIM, EASIEST, CVSIM. Digisim developed by Feldberg and Rudolph employs fast implicit finite difference (FIFD) algorithm to solve complex electrochemical problems with reasonable speed and accuracy.[35]

Electron transfer between an electrode and analyte has played prominent roles in charge transport processes of bulky biological structures,[36-37] electronics,[38-39] and macromolecules.[40-42] Through simulation of electrochemical processes, the relationship between important variables was attained at the interfacial level [40, 43-45] while in some cases, the successful extraction of reasonable parametric values was made possible.[46-47]

2.3 Electron Paramagnetic Resonance Spectroscopy

Electron paramagnetic resonance (EPR) is a spectroscopic technique for studying chemical species that possess unpaired electrons. Its fundamental principles are similar to those of nuclear magnetic resonance (NMR), however EPR signals come from the magnetic properties of the unpaired electrons with spin value of ½ while NMR signals come from the magnetic properties of the atomic nuclei.[48]

If an electron in an atom is subjected to an external magnetic field with strength B_0, its magnetic moments are aligned in such a way that they spin in the same direction as the direction of the field ($m_s = -\frac{1}{2}$) or they oppose it ($m_s = +\frac{1}{2}$). From this, the energy generated becomes equation 2. 18 which is called the Zeeman splitting.

$$E = m_s g_e \mu_B B_0 \qquad \text{eqn. 2.18}$$

Where g_e is the g-factor of the electron with a value of 2.0023.[49] This results in an energy difference $\Delta E = g_e \mu_B B_0$ between the two states for free unpaired electrons from splitting of the (2s+1) = 2 Zeeman levels.[48]

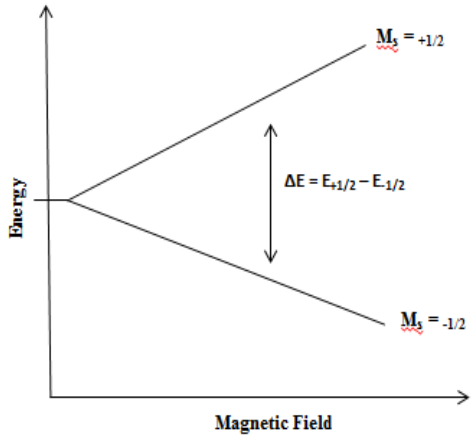

Figure 2.7. Splitting of the energy levels in relation to the magnetic field strength.

This is equivalent to the lifting of the degeneracy of the electron spin energy levels when electrons are placed in a magnetic field and described by the spin Hamiltonian.

$$\hat{H} = g\mu_B B \hat{S}_z \qquad \text{eqn. 2.19}$$

As long as the resonant condition $h\nu = \Delta E$ holds, unpaired electrons can move between two spin states by absorbing or emitting a photon of energy of energy $h\nu$ necessary to cause a transition from one energy level to another. For most experiments, the frequency is kept constant while the magnetic field is varied so that resonance can occur. Most EPR spectrometers are built in such a way that they transmit electromagnetic energy through a sample to a detector. They contain microwave generators which are responsible for the transmission in the 9-10 GHz region. So, as the magnetic field is increased, the energy gap between $m_s = +\frac{1}{2}$ and $m_s = -\frac{1}{2}$ energy states is increased until it equals that of the microwave at that constant frequency. At this stage of resonance, absorption will continue to occur as long as the number of electrons in the lower energy level outweighs that in the upper energy level due to the Maxwell-Boltzmann distribution. This net absorption is transmitted to the detector and is in turn processed and converted to a spectrum (Figure 2.8).[48] Lines in EPR spectra are recorded as dispersion signals which are first derivative of the absorption signals. Dispersion signals have better resolution than absorption signals and this makes interpretation of spectra less challenging.[50] Continuous wave EPR spectrometers use the automatic frequency control (AFC) to lock the resonator frequency. This reduces the distortion of signals via frequency shifts that result from changes in resonator temperature or change in sample position or properties. Since dispersion signals result from change in the resonating frequency, therefore they are vulnerable to being distorted while trying to use the AFC to lock the resonating frequency. Also, the dispersion signals are most times noisier than the absorption signals due to the greater sensitivity of the quadrature detection channel to phase noise.

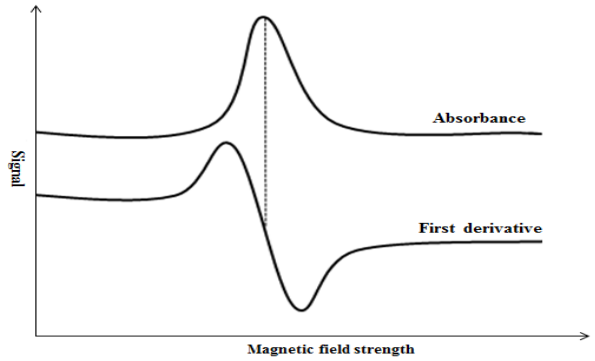

Figure 2.8. First derivative relationship between dispersion signal and absorption curve. [51]

Apart from interacting with an external magnetic field, unpaired electrons are sensitive to the magnetic moments of nuclei of atoms in their local environment. This produces a local magnetic field at the electron. The Zeeman splitting which corresponds to the ΔE is dependent on the quantum number M_s which is related to the Landé splitting energy "g" by the equation $/\mu/= g\mu_B\sqrt{m(m+1)}$. There can be the perturbation of the electronic energy when there is interaction between unpaired electron and close magnetic nuclei with spin quantum number $I > 0$. This results in an additional term to the spin Hamiltonian equation which gives useful spectral and chemical information. This additional term is referred to as the hyperfine splitting constant A_o.

$$\hat{H} = g\mu_B B\hat{S}_z + \Sigma_o A_o \hat{I}_o \cdot \hat{S}_o \qquad \text{eqn. 2.20}$$

2.3.1 Hyperfine coupling constant

The interaction between the electron and surrounding nuclei is termed the hyperfine interaction.[48] First, line shapes of EPR signals are changed as unpaired electrons interact with their environment. The hyperfine interaction or coupling which is analogous to J-coupling in NMR results when an atom with a non-zero nuclear spin interacts with an unpaired electron. This results in splitting of EPR single line signals into doublets, triplets and multiplets. It gives details of the number and types of magnetic nuclei that have interacted with the free unpaired electron.

The number of lines expected from coupling patterns is determined by 2NI + 1 where N = number of magnetically equivalent nuclei and I = nuclear spin.

There are two types of hyperfine coupling depending on whether the interaction is independent or dependent on the orientation of the sample in a magnetic field. The former interaction is isotropic hyperfine coupling and it is determined by the Fermi contact interaction between an electron and an atomic nucleus when the electron is inside the nucleus. This results in free reorientation of the nuclei and observed parameters are estimated from the average values obtained via rotational motion of molecules. The latter is called anisotropic hyperfine interaction and it is based on dipolar interactions whereby the orientation of the nuclei and dipole moments are fixed. The orientation produces different types of interactions and the observed parameters are dependent on the orientation of the molecule with respect to the magnetic induction. Isotropic hyperfine coupling are represented by 'A_o' while the anisotropic part of the hyperfine coupling is represented by 'δA'.[52]

2.3.2 *g* value

The g value which is located at the midpoint of the signal gives a measure of the effect of the electronic environment on the spin of the free unpaired electron. When an electron with degenerate quantum states in its atomic orbitals is placed in a magnetic field, the degeneracy is lifted. It is closely similar to the chemical shifts in NMR spectroscopy which are also dependent on interaction of magnetic field with the nuclei under consideration.[53] The electron does not only respond to the magnetic field in which it is placed but also to local magnetic fields of atoms in its immediate environment. This leads to the effective field strength B_{eff} as given by (Eqn. 2.21) with σ being the local fields of surrounding atoms.

$$B_{eff} = B_0(1-\sigma) \qquad \text{eqn. 2.21}$$

Substituting (Eqn. 2.18) into the resonance equation gives: $h\nu = g_e\mu_B B_{eff} = g_e\mu_B B_0(1-\sigma)$

$g_e(1-\sigma) = g$. Therefore, the final resonance equation reduces to Eqn. 2.22.

$$h\nu = g\mu_B B_0 \qquad \text{eqn. 2.22}$$

If g derived from above is not equal to that of a free electron g_e, then the ratio of magnetic moment to magnetic moment for the unpaired electron has changed considerably from that of the free electron.[48, 54] This means the electron must have gained or lost angular momentum through spin-orbit coupling since it possesses a constant spin magnetic moment.[55]

2.3.3 Application of EPR

EPR spectroscopy has applicability in biology, chemistry and physics, for the detection and identification of free radicals and paramagnetic centers both in the liquid and solid states. The combination of EPR with quantum chemical calculations in biochemistry and chemistry has led to the determination of electronic and geometrical structures of free radicals.[48]

2.3.4 EPR Spectroelectrochemistry

Spectroelectrochemistry is simply "in situ" spectroscopy during electrochemical reactions. It is a scientifically reliable technique that helps to identify the identity of the products of the chemical or electrochemical reversible step of a one-electron transfer. EPR spectroscopy has been applied successfully in the past to clarify processes at different interfaces; e.g solid/liquid interfaces [56-57] whereas *in situ* EPR spectroscopy, experiments are carried out on diamagnetic species and EPR signals emerge on electrogeneration. These experiments yield information that include locating the redox active centre of the compound and the contribution of the nuclei in the compound to the occupation of the molecular orbital. Moreover, the designs for EPR electrochemistry have been faced with challenges such as the nature of the solvent, (CH_3CN has high dielectric constant which is not suitable for EPR studies) shape of cell (cylindrical shaped tubes do not favour EPR studies) and inability of redox products to be stable at room temperature without undergoing decomposition. These challenges have all been addressed by introducing modifications to the designs. For example, flat cells with small pathlengths have been used in place of cylindrical cells. Also, the designs possess the capacity to carry out experiments at low temperature thus preventing decomposition of the redox product at room temperature.[58]

The combination of electrochemistry with spectroscopic measurements such as optical spectroscopy has made identification of redox products and intermediates easier via the determination of justifiable mechanism and evaluation of kinetic parameters for redox processes that lack thermodynamic phenomena. EPR combined with electrochemistry at first had the initial challenge of having the desired process at the detection zone of the spectrometer due to the high resistance of the thin cell used for radical generation in the microwave cavity. This was corrected by generating the radicals outside the microwave cavity followed by allowing the solution to flow into the cavity at a known speed are identified with ease when the electrochemical experiment is combined with techniques such as infrared, ultraviolet-visible, and electron paramagnetic resonance spectroscopy.[59]

2.3.5 Simultaneous electrochemical EPR (SEEPR)

In time past, electroanalytical studies and radical generation experiments are performed separately. This is attributed to factors such as uncompensated solution resistance, uncertain control over the working electrode potential due to the poor positioning of the reference electrode and the current-resistance (iR) drop along the length of the bulk solution. However, some designs have been developed to permit the monitoring of both EPR and electrochemical response of a free radical system. This is referred to as simultaneous electrochemical electron paramagnetic resonance (SEEPR) spectroscopy. Bard[59] designed one of the earliest in situ EPR electrochemical flat cell containing two tungsten rods placed parallel along the edges of the cell to act as auxiliary electrodes. The working and reference electrodes are Teflon-coated platinum wire mesh and silver wire, respectively. This design offers the advantage of allowing the simultaneous measurement of CVs and recording of EPR signal intensity coupled with the probing of the decomposition of electro-generated radicals.

Work in the Boeré lab makes use of a modification of the design pioneered by Neudeck and Kress.[60] The design utilizes a large surface area gold micromesh working electrode to maximize the intensity of EPR signals coupled with its commercial availability and optical

transparency to permit simultaneous EPR. This electrode material is fragile but laminating it with a thin copper wire which extends out of the cell cavity stabilizes and insulates it. The reference electrode is a Teflon-coated silver wire placed close to the working electrode. This design gives reasonable signal-to-noise ratios in addition to high sensitivity and retention of good performance for in situ EPR electrochemical processes.

This design is very sensitive and works well for voltammetry by allowing simultaneous recording of undistorted CV measurements and also the generation of sufficient amount of radicals. It also favours EPR scans resulting in signals with high signal-to-noise ratios. This cell is fixed inside a Bruker EMX Plus/10 instrument operating at X-band frequencies (9.8GHz) at 19 ± 2^{o}C. Variable temperature (VT) experiments are performed using the ER4141 VT accessory. On inserting the electrochemical cell into the EPR cavity, it is connected to the potentiostat via non-magnetic leads. The CV studies are then initiated to determine the exact potential for the reduction process against the reference electrode in this cell. Then controlled potential electrolysis experiments were carried out with the potential set a little beyond (~ 0.01 V) the cathodic peak potential (Fig. 2.9)

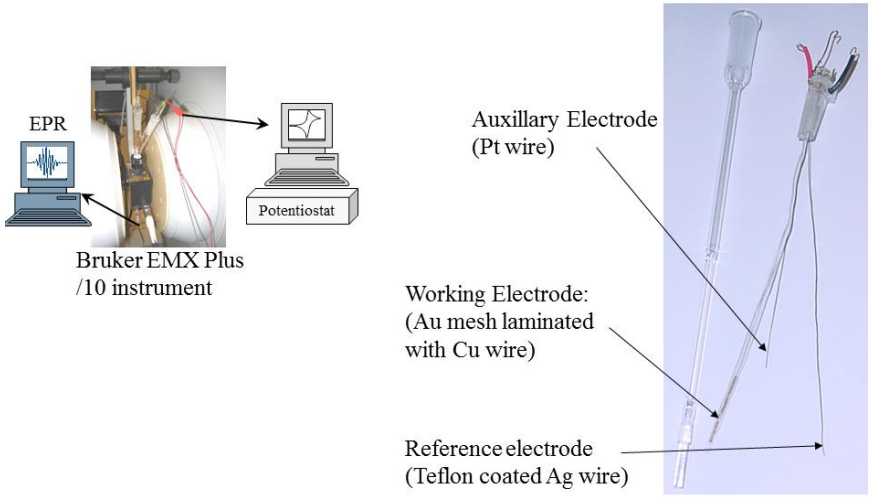

Figure 2.9 Basic components of a SEEPR experiment in the Boeré Lab

2.4 Density Functional Theory

2.4.1 Introduction

Density functional theory (DFT) is a quantum mechanical modelling method that probes structural and electronic properties of atoms, molecules, crystals and complex extended systems such as glasses and liquids in response to structural, electrical and magnetic perturbations. Its scientific recognition started in the 90s when electron density dependent functionals were used to determine the properties of multi-electron systems.[61] Quantum mechanical methods used by chemists include semi-empirical, ab initio and DFT methods. Semi-empirical methods are faster than ab initio or DFT but they are time consuming in terms of developing parameters before running a calculation. There has been great improvement in the speed and accuracy of ab initio and DFT calculations due to the development and introduction of new algorithms and more appropriate basis functions.

The driving force behind DFT calculations is the determination of molecular energy from electron density rather than from wave functions. DFT methods use linear combination of atomic orbitals-molecular orbital (LCAO-MO) approximation in all its calculation:

$$\psi_i = \Sigma_\mu C_{\mu i} \phi_\mu \qquad \text{eqn. 2.23}$$

Where ψ_i represents the molecular orbital, ϕ_u the atomic orbital and $C_{\mu i}$ is the coefficient of the *μth* atomic orbital in the *ith* molecular orbital. Atomic orbitals are represented by x, y, and z coordinates of the electron which shares close resemblance with valence orbitals of isolated atoms. These atomic orbitals are referred to as Slater type orbitals (STOs)[62] while their complete set is termed basis set. Other types of orbitals are the Gaussian type orbitals (GTOs)[63] which have been used in place of STOs because the latter consume time and encounter difficulties when carrying out multi-centre integrals.[64] Due to their improved computational efficiency, GTOs have become more common basis sets for DFT and ab initio Hatree-Fock (HF) calculations.

DFT was first explained by the Thomas-Fermi model though its application was short-lived because it shows some errors in the exchange energy due to the approximate representation of the kinetic energy functional term in addition to the absolute negligence of the electron correlation effect.

In 1964, Hohenberg and Kohn (H-K) published a theorem wherein they demonstrated that the ground state properties of complicated multi-body problem of N electrons with 3N special coordinates can be substituted by functionals of electron density containing only 3 variables. A second H-K theorem proved that the correct ground state electron density is capable of minimizing the energy of the system. In general, the two H-K theorems provide proofs that there is the existence of one-to-one mapping relationship between electron density functional and system properties.[65]

The Kohn-Sham (K-S) theorem[66] was published in 1965 to specifically answer the question of relationship between electron density and system properties. It simplifies the multi-body problem of interacting electrons in a static external potential into a problem of non-interacting electrons in an effective potential which comprises the external potential and the effect of coloumbic exchange and correlation interaction between the electrons. One major difficulty with the K-S theorem is modelling the exchange and correlation interaction. However, the remedy to this problem is making use of the simplest approximation which is the local-density approximation (LDA)[67] which derives the exact exchange energy from the uniform electron gas model or the Thomas-Fermi model and the correlation energy from parameters that fit the uniform electron gas model.

The equations derived from the K-S theorem are very similar to the closed shell (restricted Roothnaan equation) and open shell (unrestricted Pople-Nesbet equation) Hartree-Fock systems. The open shell system of the HF theory involves two Fock matrices F^{α} and F^{β} as shown below.

$$F^{\alpha}_{\mu\nu} = H^{\alpha}_{\mu\nu} + \Sigma_{\lambda\sigma} P^{T}_{\lambda\sigma} (\mu\nu \mid \lambda\sigma) - P^{\alpha}_{\lambda\sigma} (\mu\lambda \mid \nu\sigma) \qquad \text{eqn. 2.24}$$

$$F_{\mu\nu}^{\beta\alpha} = H_{\mu\nu}^{\beta\alpha} + \sum_{\lambda\sigma} P_{\lambda\sigma}^{T}(\mu\nu \mid \lambda\sigma) - P_{\lambda\sigma}^{\alpha}(\mu\lambda \mid \nu\sigma) \qquad \text{eqn. 2.25}$$

The last term in equation 2.13 is the Coloumb energy while that in equation 2.14 is the exchange energy with correlation energy (difference between HF energy of a single determinant wave function and the exact energy defined as zero). The fundamental equation of DFT as put forward by K-S replaced the exchange and coloumb terms in equations 2.23 and 2.24 with a new exchange-correlation potential and equivalent matrix F^{xc}.

$$F_{\mu\nu}^{\alpha} = H_{\mu\nu}^{\alpha} + \Sigma_{\lambda\sigma} P_{\lambda\sigma}^{T}(\mu\nu \mid \lambda\sigma) - F_{\mu\nu}^{XC\alpha} \qquad \text{eqn. 2.26}$$

$$F_{\mu\nu}^{\beta\alpha} = H_{\mu\nu}^{\beta\alpha} + \sum_{\lambda\sigma} P_{\lambda\sigma}^{T}(\mu\nu \mid \lambda\sigma) - F_{\mu\nu}^{XC\beta} \qquad \text{eqn. 2.27}$$

From these fundamental equations, it was concluded that the operating principle of DFT is developing accurate functionals that describe either the exchange or correlation functional or both. In most cases, describing the total exchange-correlation energy is a result of adding an exchange functional to a correlation functional. Slater orbital theorem simplified the calculation of the exchange energy using LDA or local spin density approximation (LSDA) analytical format. On the contrary, LDA analyses for correlation functionals are complex; however obtaining these functionals depend on numerical results from Monte Carlo simulations of the uniform electron gas. The LDA correlation functionals are then obtained by fitting the numerical results into an analytical functional.[68-71]

2.4.2 Exchange-Correlation Functionals

The shortage of exchange and correlation functionals is one of the major setbacks for DFT. The exchange and correlation energy is the difference between the exact sum of the energy of a system and the classical Hartree energy. Therefore, in order to determine the quality of results from DFT calculations, emphasis is laid on the closeness of the approximate exchange and correlation energy to the exact value of the energy. One of such functionals is the local-density

approximation (LDA) which gives allowance for some approximations when extraction of physical quantities from calculations is the ultimate goal.

$$E_{XC}^{LDA}[n] = \int \epsilon_{XC}(n) n\left(\underset{r_i}{\rightarrow}\right) d^3r \qquad \text{eqn. 2.28}$$

There is also the local spin-density approximations (LSDA) which incorporates electron spin as a modification of the LDA.[61]

$$E_{XC}^{LSDA}[n_\uparrow n_\downarrow] = \int \epsilon_{XC}(n_\uparrow, n_\downarrow) n\left(\underset{r_i}{\rightarrow}\right) d^3r \qquad \text{eqn. 2.29}$$

Some exchange functionals of Tao, Perdew, Staroverov and Scuseria (TPSS),[72] generalized gradient approximation (GGA: an approximation that recognises electron densities in molecules as a variable that possess gradient i.e. larger values near a nucleus and zero at large distance from nucleus)[73] and meta-GGA[74] all embrace further terms such as density and electronic operators in their expanded format. Some of these functionals have the problem of finding it hard to express their exchange part of the energy but this has been replaced by the introduction of Hybrid functionals whose exchange energy is calculated from Hartree-Fock theory.[75] One popularly used functionals that was able to reduce to LDA in the electron-gas limit is the revised Perdew–Burke–Ernzerhof exchange model. [76] Unfortunately, its usage became obsolete because it was unable to satisfy the energy requirements for gas-phase molecular calculations. A very popular functional known as BLYP; Becke for exchange and Lee, Yang and Parr for correlation came into existence. Another widely used hybrid functional is B3LYP; Becke three parameter hybrid functional uses the exchange energy from Becke's exchange functional combined with the exact exchange from Hartree–Fock theory. These parameters define the hybrid functional based on the exchange and correlation components specifying how much of the exact Hartree-Fock exchange functionality is mixed in.[77-78] Hybrid functionals provide the strategy to improve the molecular properties of matter such as bond lengths, atomization energies and vibrational frequencies.[79]

2.5 References

1. Skoog, D. A.; West, D. M.; Holler, F. J., *Fundamentals of analytical chemistry*. Saunders College Pub.: 1988.

2. Bard, A. J.; Faulkner, L. R., *Electrochemical Methods: Fundamentals and Applications*. Wiley: 2000.

3. Liptak, B. G., *Analytical Instrumentation*. Taylor & Francis: 1994.

4. Cazes, J., *Analytical Instrumentation Handbook, Third Edition*. Taylor & Francis: 2004.

5. Webster, J. G., *The Measurement, Instrumentation, and Sensors: Handbook*. CRC Press: 1999.

6. Nicholson, R. S.; Shain, I., *Anal. Chem.* **1964,** *36*, 706-723.

7. Heinze, J., *Angew. Chem., Int. Ed. Engl* **1984,** *23*, 831-847.

8. Kissinger, P.; Heineman, W. R., *Laboratory Techniques in Electroanalytical Chemistry, Second Edition, Revised and Expanded*. Taylor & Francis: 1996.

9. Tissue, B. M., *Basics of Analytical Chemistry and Chemical Equilibria*. Wiley: 2013.

10. Otles, S., *Handbook of Food Analysis Instruments*. Taylor & Francis: 2008.

11. Gritzner G.; Kuta, J., *Pure Appl. Chem.* **1984,** *56*, 461-466.

12. Butovskiy, M. V.; Balázs, G.; Bodensteiner, M.; Peresypkina, E. V.; Virovets, A. V.; Sutter, J.; Scheer, M., *Angew. Chemie Int. Ed.* **2013,** *52*, 2972-2976.

13. Zoski, C. G., *Handbook of Electrochemistry*. Elsevier: 2007.

14. Moock, K. H.; Macgregor, S. A.; Heath, G. A.; Derrick, S.; Boere, R. T., *J. Chem. Soc., Dalton Trans.* **1996,** 2067-2076.

15. Beekman, R. A.; Boeré, R. T.; Moock, K. H.; Parvez, M., *Can. J. Chem* **1998,** *76*, 85-93.

16. Boeré, R. T.; Moock, K. H.; Derrick, S.; Hoogerdijk, W.; Preuss, K.; Yip, J., *Can. J. Chem.* **1993,** *71*, 473-486.

17. Boeré, R. T.; Moock, K. H.; Parvez, M., *Z. Anorg. Allg. Chem.* **1994,** *620*, 1589-1598.

18. Inzelt, G., Pseudo-reference Electrodes. In *Handbook of Reference Electrodes*, Inzelt, G.; Lewenstam, A.; Scholz, F., Eds. Springer Berlin Heidelberg: 2013; pp 331-332.

19. Boeré, R. T.; Bond, A. M.; Chivers, T.; Feldberg, S. W.; Roemmele, T. L., *Inorg. Chem.* **2007,** *46*, 5596-5607.

20. Wang, J., *Analytical Electrochemistry*. Wiley: 2006.

21. Ramaley, L.; Krause, M. S., *Anal. Chem.* **1969,** *41*, 1362-1365.

22. Osteryoung, J., *Acc. Chem. Res.* **1993,** *26*, 77-83.

23. Lovrić, M., Square-Wave Voltammetry. In *Electroanalytical Methods*, Scholz, F., Ed. Springer Berlin Heidelberg: 2010; pp 121-145.

24. Bard, A. J.; Faulkner, L. R., *Electrochemical Methods: Fundamentals and Applications*. 2001.

25. Chen, A.; Shah, B., *Anal. Met.* **2013,** *5*, 2158-2173.

26. Stock, J. T.; Chemistry, A. C. S. D. O. T. H. O.; Orna, M. V.; Chemistry, A. C. S. D. O. A.; Meeting, A. C. S., *Electrochemistry: past and present*. American Chemical Society: 1989.

27. Oldham, K.; Myland, J.; Bond, A., *Electrochemical Science and Technology: Fundamentals and Applications*. Wiley: 2011.

28. Kissinger, P. T.; Heineman, W. R., *J. Chem. Edu.* **1983,** *60*, 702-706.

29. Bockris, J. O. M.; Reddy, A. K. N.; Gamboa-Aldeco, M., *Modern Electrochemistry*. Kluwer Academic/Plenum Publishers: 2000.

30. Feldberg, S. W.; Auerbach, C., *Anal. Chem.* **1964,** *36*, 505-509.

31. Burgess, K. S. D.; Kable, J. W.; Justice, J. B., *Electroanal.* **1999,** *11*, 337-343.

32. Banks, J., *Discrete-event system simulation*. Prentice Hall: 2001.

33. Nann, T.; Heinze, J., *Electrochem. Commun.* **1999,** *1*, 289-294.

34. Britz, D., *Digital Simulation in Electrochemistry*. Springer: 2005.

35. Deng, Z.-X.; Lin, X.-Q.; Tong, Z.-H., *Chin. J. Chem.* **2004,** *22*, 719-726.

36. McLendon, G., *Acc. Chem. Res.* **1988,** *21*, 160-167.

37. Williams, R. J. P., *Mol. Phys.* **1989,** *68*, 1-23.

38. Mirkin, C. A.; Ratner, M. A., *Annu. Rev. Phys. Chem.* **1992,** *43*, 719-754.

39. Blake, A. J.; Champness, N. R.; Crew, M.; Hanton, L. H.; Parsons, S.; Schröder, M., *J. Chem. Soc., Dalton Trans.* **1998,** 1533-1534.

40. Becka, A. M.; Miller, C. J., *J. Phys. Chem.* **1992,** *96*, 2657-2668.

41. Porter, M. D.; Bright, T. B.; Allara, D. L.; Chidsey, C. E. D., *J. Am Chem. Soc.* **1987,** *109*, 3559-3568.

42. Bilewicz, R.; Majda, M., *J. Am Chem. Soc.* **1991,** *113*, 5464-5466.

43. Becka, A. M.; Miller, C. J., *J. Phys. Chem.* **1993,** *97*, 6233-6239.

44. Miller, C.; Cuendet, P.; Graetzel, M., *J. Phys. Chem.* **1991,** *95*, 877-886.

45. Chidsey, C. E. D., *Science* **1991,** *251*, 919-922.

46. Laviron, E., *J. Electroanal. Chem. Interfac. Electrochem.* **1979,** *101*, 19-28.

47. Bard, A. J.; Faulkner, L. R., *Electrochemical Methods; J. Wiley and Sons: New York* **1980**.

48. Lund, A.; Shimada, S.; Shiotani, M., *Principles and Applications of ESR Spectroscopy*. Springer: 2011.

49. Odom, B.; Hanneke, D.; D'Urso, B.; Gabrielse, G., *Phys. Rev. Lett.* **2006,** *97*, 030801-030804.

50. Rieger, P. H.; Chemistry, R. S. o., *Electron Spin Resonance: Analysis and Interpretation*. Royal Society of Chemistry: 2007.

51. Heckmann, P. H.; Träbert, E., *Introduction to the Spectroscopy of Atoms*. North-Holland: 1989.

52. Weil, J. A.; Bolton, J. R., *Electron Paramagnetic Resonance: Elementary Theory and Practical Applications*. Wiley: 2007.

53. Fabian, G., *Magn. Res. Chem.* **1995,** *33*, 80-80.

54. Zimmerman, M. R.; Whitehead, N., *New Applications of Electron Spin Resonance: Dating, Dosimetry and Microscopy*. World Scientific: 1993.

55. Barclay, T. M.; Cordes, A. W.; Goddard, J. D.; Mawhinney, R. C.; Oakley, R. T.; Preuss, K. E.; Reed, R. W., *J. Am Chem. Soc.* **1997,** *119*, 12136-12141.

56. Gale, R. J., *Spectroelectrochemistry: theory and practice*. Plenum Press, cop.: 1988.

57. Webster, R. D.; Bond, A. M.; Coles, B. A.; Compton, R. G., *J. Electroanal. Chem.* **1996,** *404*, 303-308.

58. Kaim, W.; Klein, A., *Spectroelectrochemistry*. Royal Society of Chemistry: 2008.

59. Goldberg, I. B.; Bard, A. J., *J. Phys. Chem.* **1971,** *75*, 3281-3290.

60. Neudeck, A.; Kress, L., *J. Electroanal. Chem.* **1977,** *437*.

61. Koch, W.; Holthausen, M. C., *A chemist's guide to density functional theory*. 2001; Vol. 2.

62. Slater, J. C., *Phys. Rev.* **1930,** *36*, 57-64.

63. Gill, P. M. W., Molecular integrals Over Gaussian Basis Functions. In *Advances in Quantum Chemistry*, John, R. S.; Michael, C. Z., Eds. Academic Press: 1994; Vol. Volume 25, pp 141-205.

64. Barone, V.; Bencini, A.; Totti, F.; Uytterhoeven, M. G., *Int. J. Quant. Chem.* **1997,** *61*, 361-367.

65. Hohenberg, P.; Kohn, W., *Phys. Rev.* **1964,** *136*, B864-B871.

66. Kohn, W.; Sham, L. J., *Phys. Rev.* **1965,** *140*, A1133-A1138.

67. Wu, C. D.; Hu, A.; Zhang, L.; Lin, W. B., *J. Am. Chem. Soc.* **2005,** *127*, 8940-8941.

68. *Hyperchem 8.0.8 Hypercube, Inc., Gainesville* **2002,** *FL 32601*.

69. Parr, R. G.; Pearson, R. G., *J. Am Chem. Soc.* **1983,** *105*, 7512-7516.

70. Bond, A. M., *Broadening Electrochemical Horizon*. Oxford University Press, New york: 2001.

71. Jensen, F., *Introduction to Computational Chemistry*. Wiley: 2006.

72. Goll, E.; Ernst, M.; Moegle-Hofacker, F.; Stoll, H., *J. Chem. Phy.* **2009,** *130*, 234113.

73. Perdew, J. P.; Chevary, J. A.; Vosko, S. H.; Jackson, K. A.; Pederson, M. R.; Singh, D. J.; Fiolhais, C., *Phys. Rev. B* **1992,** *46*, 6671-6687.

74. Kossmann, S.; Kirchner, B.; Neese, F., *Mol. Phys.* **2007,** *105*, 2049-2071.

75. Uemara, T.; Kitagawa, K.; Horike, S.; Kawamura, T.; Kitagawa, S., *Chem. Commun.* **2005,** 5968-5970.

76. Pan, L.; Olson, D. H.; Ciemnolonski, L. R.; Heddy, R.; Li, J., *Angew. Chem., Int. Ed.* **2006,** *45*, 616-619.

77. Fujita, M.; Kwon, Y. J.; Washizu, S.; Ogura, K. J., *J. Am. Chem. Soc.* **1994,** *116*, 1151-1152.

78. Becke, A. D., *Phys.Rev. A* **1988,** *38*, 3098-3100.

79. Perdew, J. P.; Ernzerhof, M.; Burke, K., *J. Chem. Phy.* **1996,** *105*, 9982-9985.

Chapter Three

Results and Discussion

3.1 Synthesis and spectroscopic studies

3.1.1 Synthesis and spectroscopic studies of 3,5-diphenyl-1,2,4-dithiazolium perchlorate.

Bright-yellow coloured 3,5-diphenyl-1,2,4-dithiazolium perchlorate **3**$^{+}$ **(**Scheme 3.1**)** is prepared by the one-pot oxidation of thiobenzamide with hydrogen peroxide in formic and perchloric acids.[1] Its recrystallization from concentrated acetic acid afforded a yield of 64 (±1) % (*the error of ± 1 is applicable to all the yields reported in this thesis*) and infrared analysis on the purified salt confirmed a Cl-O stretch at 1060 cm^{-1}. Its composition was further confirmed by X-ray crystallography and elemental analysis (see section 6.18 and 6.16 respectively for details). The crystal structure of the salt is being reported for the first time. It could equally be made following Corsaro and co-workers' synthetic route.[2]

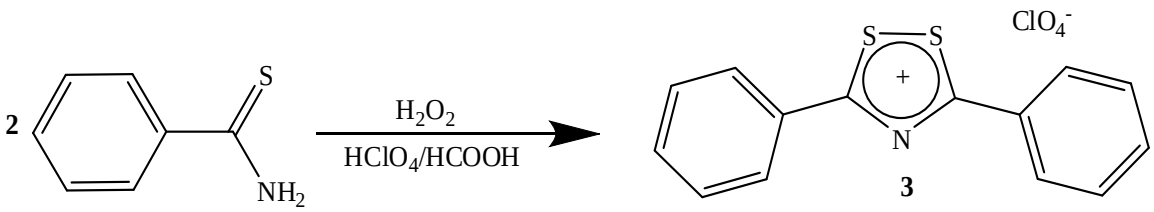

Scheme 3.1 One-pot synthesis of **3**$^{+}$ via oxidation of thiobenzamide

3.1.2 Synthesis and spectroscopic studies of 3-diethylamine-5-phenyl dithiazolium perchlorate salt

3-Diethylamine-5-phenyl dithiazolium perchlorate **1**$^{+}$ **(**Scheme 3.2**)** was prepared by the oxidation of 3-diethylamine-5-phenyl thiourea using hydrogen peroxide in an acetic acid / perchloric acid mixture.[3] Crystals of the salt were grown from acetic acid to afford a yield of 26 %. The replacement of oxygen in 3-diethylamine-5-phenyl thiourea was carried out by the intramolecular extraction of sulphur before ring cyclization (Scheme 3.2). This is presumed to have had an effect on the yield. The ^{1}H NMR spectra of 3-diethylamine-5-phenyl thiourea showed aromatic doublet for ortho-protons at 7.85 ppm, triplet for meta-protons at 7.49 ppm and multiplets at 7.60 ppm for para-protons. There were also non-aromatic doublets for the methylene

protons at 4.14 and 3.62 ppm and multiplets for methyl protons at 1.37 ppm. There is a singlet at a chemical shift of 8.34 ppm for the proton of the N-H group.[4] Also, IR spectrum of $\mathbf{1}^+$ showed a sharp Cl-O stretch at 1069 cm^{-1}. Its composition was further confirmed by X-ray crystallography and elemental analysis (section 6.18 and 6.16 respectively).

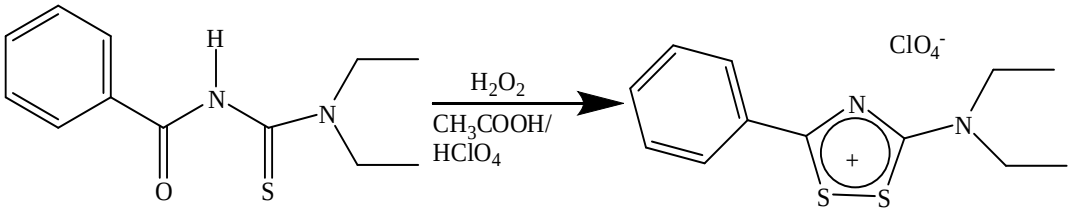

1

Scheme 3.2 Synthesis of $\mathbf{1}^+$ via the oxidation of N-benzoyl-N,N'-diethylthiourea.

3.1.3 Synthesis and spectroscopic studies of 3,3,5,5-tetramethyl dithiazolium hexafluorophosphate.

3,3,5,5-tetramethyl dithiazolium hexafluorophosphate salt $\mathbf{14}^+$ **(**Scheme 3.3**)** was prepared by the metathesis reaction of its chloride salt with potassium hexafluorophosphate in anhydrous methanol.[5] The starting material is the dimethylthiocarbamoyl chloride which forms the isothiocyanate after being refluxed with potassium thiocyanate in acetone. The isothiocyanate filtrate that has been separated from the KCl residue is converted to the dithiourea following the addition of dimethylamine. The dithiourea in the presence of HCl and H_2O_2 (oxidizing agent) undergo oxidative coupling with cyclization to form the 3,3,5,5-tetramethylamino-dithiazolylium chloride monohydrate salt. It was recrystallized from 95% ethanol to afford a yield of 81 %. IR analysis of needle-shaped crystals show symmetric and anti-symmetric stretches of PF_6^- at 744 and 822 cm^{-1} respectively. Its identity and composition were further confirmed by X-ray crystallography and elemental analysis (section 6.18 and 6.16 respectively).

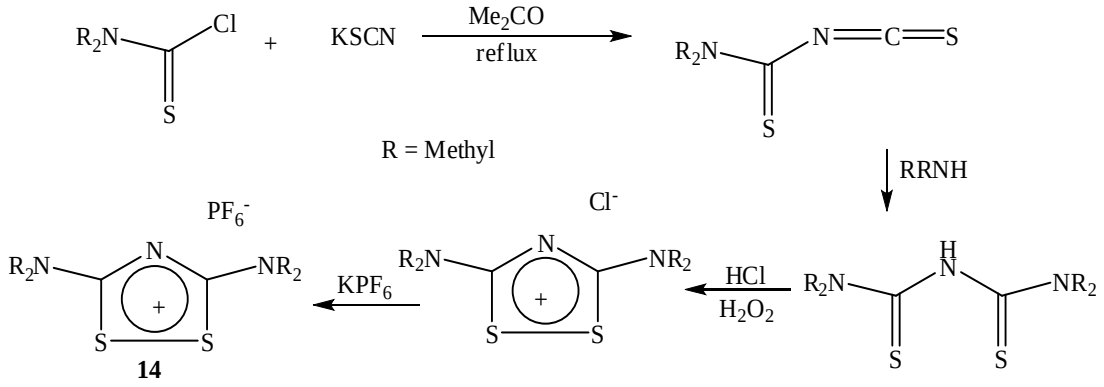

Scheme 3.3 Synthetic route to **14**$^{+}$ starting from dimethyl thiocarbamoyl chloride.

3.2 Crystallographic studies

3.2.1 Crystallographic studies of 3,5-diphenyl-1,2,4-dithiazolium perchlorate.

The cation **3**$^{+}$ [$C_{14}H_{10}NS_2$] possesses a flat NC_2S_2 ring (r.m.s deviation = 0.01 Å) with two phenyl rings that are almost coplanar [the dihedral angle between the mean planes are 4.7 (2) and 8.7 (2)˚ for the two phenyl rings]. This is contrary to the NC_2S_2 ring with two o-tolyl substituents (3c) lying 29.11(9)˚ out of the plane due to the steric hindrance of the methyl groups at the para-positions of the aryl substituents.[6] See crystal data and refinement details in Tables 6.1-6.3.

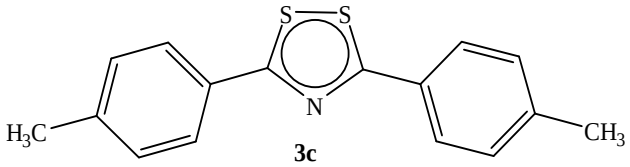

3c

The cation is located at a crystallographic two-fold rotation axis through N1 and the midpoint of S1-S2 bond.[7] The [ClO_4^-] anion makes short O····S contacts that are less than the van der Waals radii of 3.32 Å [O····S = 3.183 (6), O····S = 3.097 (5) Å] (Figure 3.2). The cation-anion pair as found in the crystal lattice possesses much shorter contacts from the anion O atom to the S atoms of the cation. Stacking in dimer structure is displayed through short inter-ring C····S, C····C, C····O interactions] and other lateral extensions into planes via short H-bonds between phenyl H and [ClO_4^-] O atoms [O····H = 2.676 (5), O····H = 2.551 (5), O····H = 2.652 (5), O····H = 2.605 (6) and O····H = 2.689 (5) Å] (Figure 3.4**)**. The separation between the arrays of dimer pairs coincides

with the representative minimum distance for off-centre parallel stacking of electron-rich aromatic systems (Figure 3.3).[8] It consists of a symmetry glide plane parallel to the *ac* plane and perpendicular to the *ab* plane. The geometry of the phenyl substituents is usual with ring C-C bonds in the range 1.375 (6)-1.395 (6) Å. A Cambridge Structural Database search gave twenty-one hits including compounds with the same cationic ring unit. These include the diphenyl derivative with the $P_4NS_9^-$ **3d** counteranion[9] which has essentially the same ring geometry as $\mathbf{3}^+$ and the hydrobromide[7] and hydroiodide[10] of thiuret, with two -NH_2 substituents.

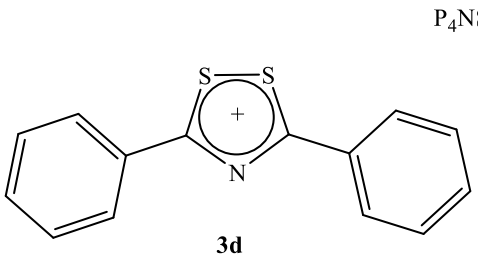

3d

All the interatomic bond lengths of **3** are not different from the mean bond lengths obtained from $\mathbf{3}^+$, $\mathbf{3a}^+$ and $\mathbf{3b}^+$ within experimental uncertainty at the 99% confidence level (Table 3.1) despite the nature of the short contact between the O atoms of the low-coordinating perchlorate counter-anion and the S of the central heterocyclic cation in $\mathbf{3}^+$.

While carrying out experiments for this thesis, I also prepared and characterized 1,2,4-dithiazolylium salts with triiodide $\mathbf{3a}^+$ and tetrabromido ferrate (III)[8] $\mathbf{3b}^+$ counter-anions, respectively (Table 3.1). The former was made by the oxidation of thiobenzamide using iodine in glacial acetic acid. Dark-orange crystals of the salt were recrystallized from nitromethane/ether solvent mixture in a yield of 80%. The 1,2,4-dithiazolium salt with tetrabromido ferrate (III) counter-anion was unexpectedly formed as tiny red-orange prisms during the synthesis of 3,5-diphenyl-1,2,4-dithiazolium perchlorate salt. The source of the tetrabromido ferrate (III) counter-anion was strongly suspected to be the rust that got digested by the perchloric acid making the ferric aquo ion readily available for the highly nucleophilic bromide ion.[8]

Table 3.1 Selected interatomic distances (Å) for 3 and literature dithiazolium salts.

Distance,	I_3^-(**3a**)	$FeBr_4^-$(**3b**)	ClO_4^-	Mean(sd)[a]
S2-S1	2.020 (1)	2.019 (1)	2.007 (2)	2.015(7)
S1-C1	1.718 (3)	1.732 (2)	1.726 (5)	1.725(7)
C1-N1	1.324 (4)	1.328 (3)	1.319 (6)	1.324(5)
N1-C2	1.323 (4)	1.324 (4)	1.318 (5)	1.322(3)
C2-S2	1.719 (3)	1.729 (3)	1.720 (5)	1.723(6)

[a] Mean (± standard deviation from the mean). Statistical analyses including the standard error are in the appendix **A.25.** $3b^+$ is from ref. 8

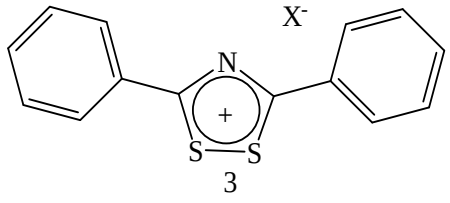

3

X^- = (a) I_3^- (b) $FeBr_4^-$

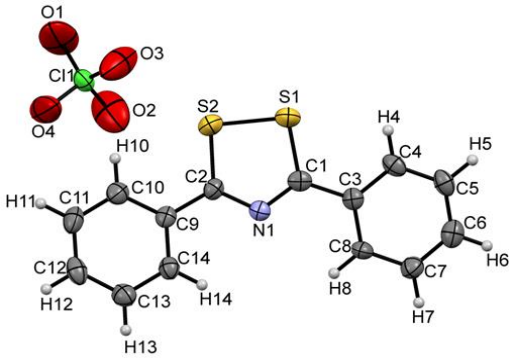

Figure 3.1 Molecular structure of $\mathbf{3}^+$ as found in the crystal lattice (displacement ellipsoids drawn at 50 % probability)

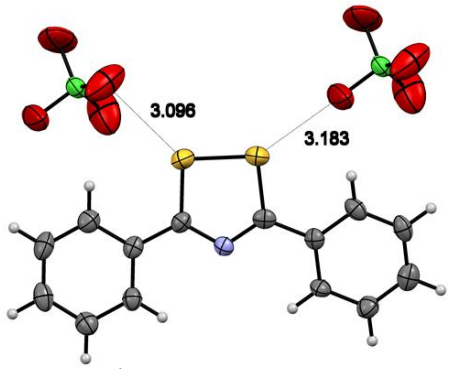

Figure 3.2 A view of $\mathbf{3}^+$ plotted with displacements ellipsoids drawn at the 50% probability level. Dotted lines indicate short cation-anion contacts.

3.2.2 Crystallographic studies of 3-diethylamine-5-phenyl-1,2,4-dithiazolium perchlorate.

The cation 3-diethylamino-5-phenyl-1,2,4-dithiazolium perchlorate salt **1**$^{+}$ $[C_{12}H_{15}N_2S_2][ClO_4]$ contains a flat NC_2S_2 ring with a phenyl ring that is consistently co-planar with the central heterocyclic ring (Figure 3.5). The amino substituents up to the nitrogen-methylene bonds are co-planar as well. The extended contacts show a dimer of two monomeric rings connected through short inter-ring interactions [C····C = 3.347 Å and C····C = 3.393 Å which are less than the vdW radius by 0.053 and 0.007 Å, respectively] (Figure 3.6**)** via π-stacking. These represent the minimum contacts for short off-centre parallel stacking; a common phenomenon in aromatic ring systems (Fig. 3.9).[10] See crystal data and refinement details in Tables 6.1-6.3.

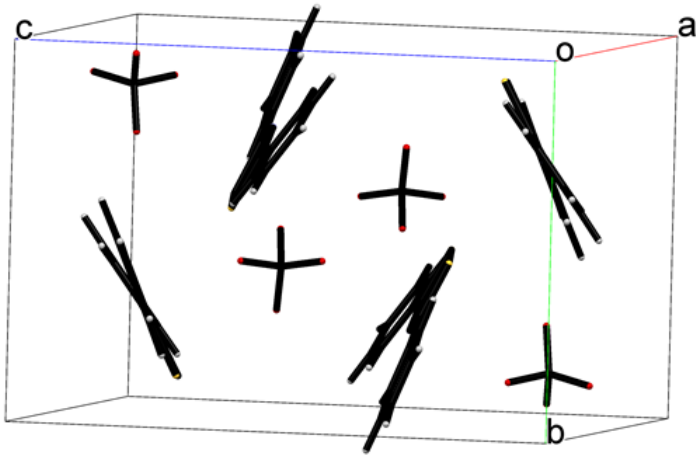

Figure 3.3 Packing patterns for **3**$^{+}$ showing separation between arrays of dimer pairs

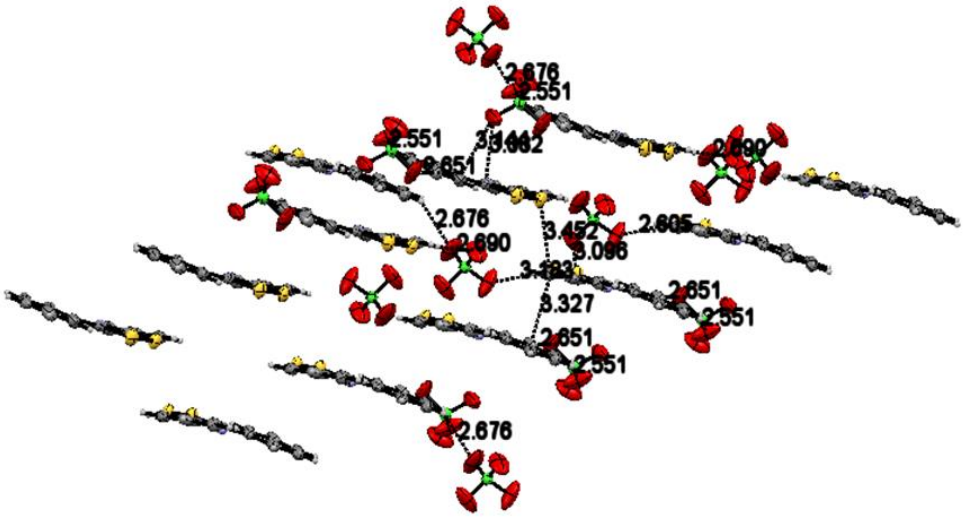

Figure 3.4 An array of dimer components in $\mathbf{3}^{+}$ showing minimum distance for off-centre parallel stacking of electron-rich aromatic rings.

In the structure of $\mathbf{1}^{+}$, the [ClO_4^-] anion O atom makes a short contact with the S of the central heterocyclic ring [O····S = 3.133 (2) Å] and also bridges through short contacts between counteranion O atoms and ring and amino alkyl hydrogen atoms [O····H = 2.423 (2), O····H = 2.498 (1), O····H = 2.520 (1), O····H = 2.529 (2), O····H = 2.598 (1), O····H = 2.602 (1), O····H = 2.648 (1), and O····H = 2.684 (2) Å] (Figure 3.7**)**. The packing shows a dimer located at the centre of the cell and two other parallel components of the other dimer located on faces *ab* and *bc* respectively.

Table 3.2 Selected interatomic distances (Å) for 1 and literature dithiazolium salts

Distance,	$CoCl_4^-$(1a)	$Cu_2Cl_6^{2-}$(1b)	ClO_4^-	Mean(sd)[a]
S2-S1	2.036 (2)	2.044 (2)	2.044 (8)	2.041(5)
S1-C1	1.730 (4)	1.734 (5)	1.738 (2)	1.734(4)
C1-N1	1.304 (4)	1.300 (7)	1.300 (3)	1.301(2)
N1-C2	1.346 (4)	1.351 (6)	1.351 (2)	1.349(3)
C2-S2	1.749 (4)	1.754 (3)	1.751 (2)	1.759(3)

[a] Mean (± standard deviation from the mean). Statistical analyses including the standard error are in the appendix **A.26**. Compounds 1a and 1b are from Ref 11.

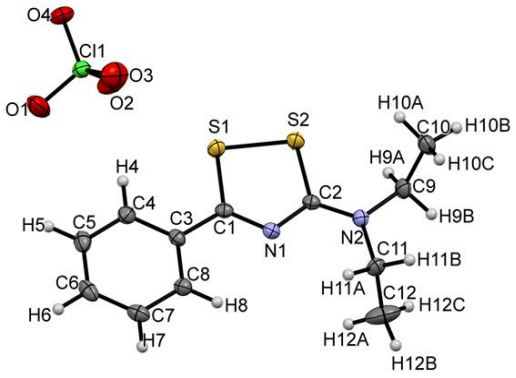

Figure 3.5 Molecular structure of $\mathbf{1}^{+}$ as found in its crystal lattice (displacement ellipsoids drawn at 50% probability)

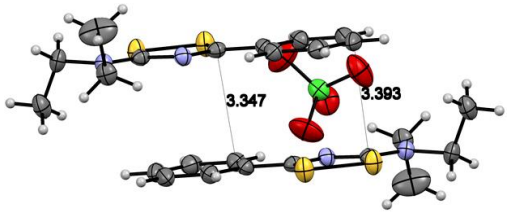

Figure 3.6 Parallel dimer components in $\mathbf{1}^{+}$ showing minimum distance for off-centre parallel stacking of electron rich aromatic rings via C····C contacts.

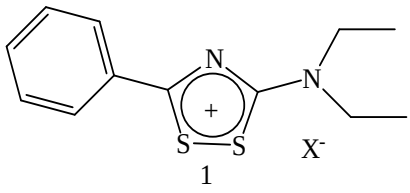

1

X^{-} = (a) $CoCl_4^{-}$ (b) $Cu_2Cl_6^{2-}$

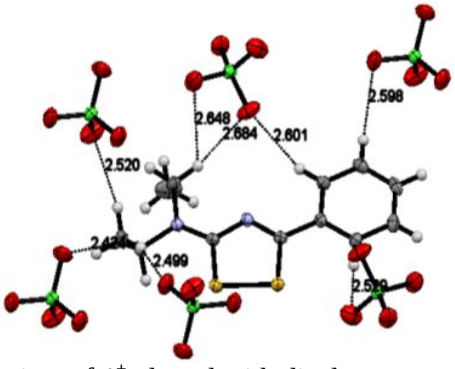

Figure 3.7 A view of $\mathbf{1}^{+}$ plotted with displacement ellipsoids drawn at the 50% probability level. Dotted lines indicate short anion-cation O····H contacts.

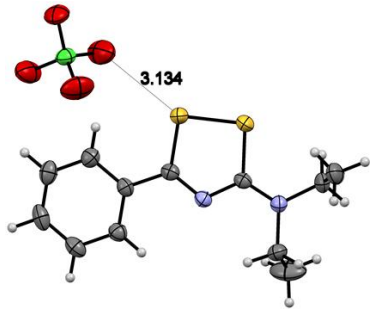

Figure 3.8 A view of $\mathbf{1}^+$ plotted with displacement ellipsoids drawn at the 40% probability level. Dotted lines indicate short anion-cation contacts.

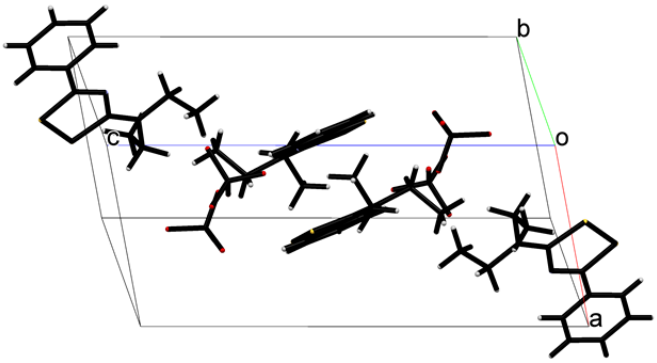

Figure 3.9 Packing pattern of 1^+ showing location of heterocyclic ring at the centre and faces of cell.

Salts with the same central heterocyclic cation but different counteranions [$CoCl_4^-$ and $Cu_2Cl_6^{2-}$][11] were found in the Cambridge Structural Database (Table 3.2). All bond lengths of **1** are the same as the mean bond length obtained from $\mathbf{1}^+$, $\mathbf{1a}^+$ and $\mathbf{1b}^+$ within experimental uncertainty at the 99% confidence level (Table 3.2). The central heterocyclic cation still retains its structural features despite the electron donating diethyl amino group, the asymmetric nature of the cationic ring[6] and the short contacts between the O atoms of the low-coordinating perchlorate counter-anion and the S of the central heterocyclic cation in addition to the mean value of 2.563 Å for O···H contacts which is less than the vdW radii of 2.720 Å.

3.2.3 Crystallographic studies of 3,3,5,5-tetramethyl dithiazolium hexafluorophosphate.

The cation $\mathbf{14}^+$ **(**Figure 3.10**)** contains a flat central NC_2S_2 ring with two amino groups that are almost coplanar with the exception of the methyl hydrogen atoms which lie out of the plane. The hexafluorophosphate counter-anion possesses large thermal ellipsoids that result from

positional disorder and these are indicative of the weakness of the anion-cation contacts. The pair of dimer consists of two monomeric rings that are rotated by about 90˚ to each other (Figures 3.12 and 3.13). See crystal data and refinement details in Tables 6.1-6.3.

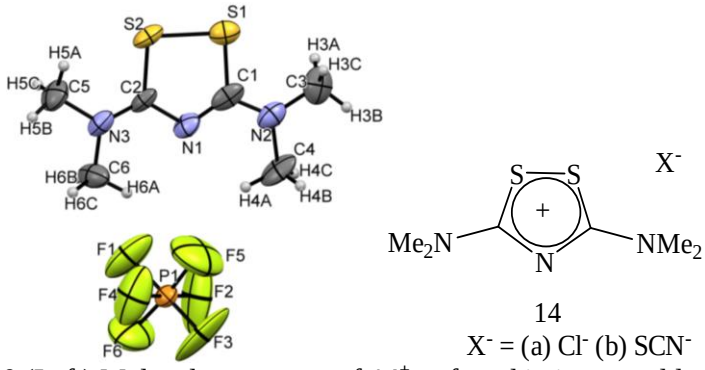

Figure 3.10 (Left) Molecular structure of **14**$^{+}$ as found in its crystal lattice (displacement ellipsoids drawn at 50% probability). (Right) **14a**$^{+}$ **(Thesis)** and **14b**$^{+}$ [12]

The [PF_6^-] anion makes short F····S contacts [F····S = 2.916 (1) Å] (Figure 3.11**)** and also bridges via shorter H····acceptor (F) contacts in the range 2.276 (7)-2.644 (6) Å and donor (C)-H contacts 0.980 (2) and 0.980 (3) Å (Figure 3.14**)** to amino-alkyl hydrogen atoms of a second cation aligned parallel to the first by stacking. Coupled with the F····S and F····H contacts are longer S····H contacts [2.970 (8) Å] (Figure 3.11**)** which add stability to the structural moiety.

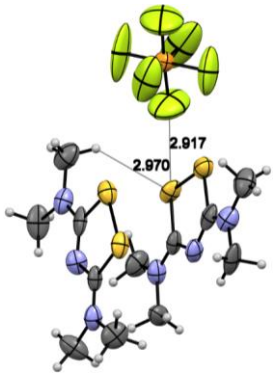

Figure 3.11 Cation-anion interactions via short S····H and S····F contacts.

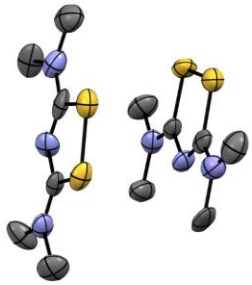

Figure 3.12 Parallel dimer showing 90˚ alignment difference between monomers.

Table 3.3 Selected interatomic distances (Å) for 14 and literature dithiazolium salts.

Distance, Å	Cl^- [a](**14a**)	PF_6^-	SCN^-(**14b**)	Mean(sd)[b]
S2-S1	2.053 (5)	2.063 (5)	2.057(1)	2.058(5)
S1-C1	1.762 (1)	1.760 (1)	1.758(4)	1.760(2)
C1-N1	1.329 (2)	1.320 (2)	1.324(5)	1.324(5)
N1-C2	1.332 (2)	1.380 (1)	1.328(5)	1.350(29)
C2-S2	1.767 (1)	1.750 (1)	1.768(4)	1.762(10)

[a] Crystals of the chloride were obtained as a monohydrate. [b] Mean (± standard deviation from the mean). Statistical analyses including the standard error are in the appendix **A.27.** 14b[12]. , 14a was prepared in the Boeré lab (see section 6.2.8)

All the interatomic bond lengths of **14** are not different within experimental uncertainty at the 99% confidence level from the mean bond length obtained from $\mathbf{14}^+$, $\mathbf{14a}^+$ and $\mathbf{14b}^+$ (Table 3.3). This is indicative of the bonds remaining intact despite the large size of the thermal ellipsoids of PF_6^- which are indicative of weak anion-cation contacts.

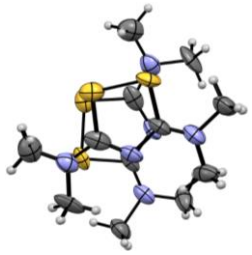

Figure 3.13 parallel arrays of dimer components showing 90˚ rotational motion displacement.

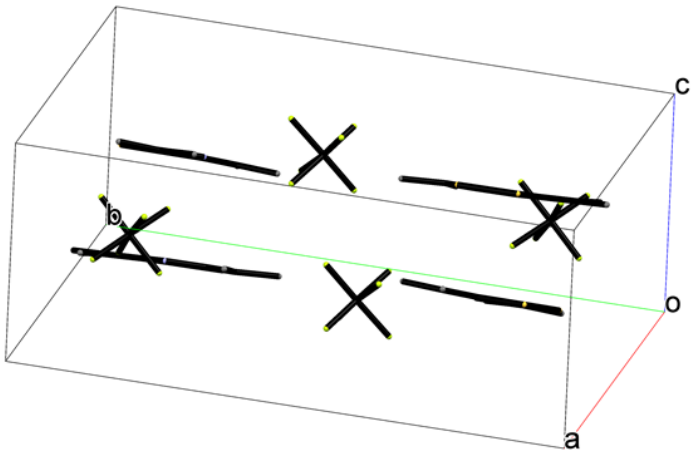

Figure 3.14 Packing pattern (viewed from *b* axis) showing parallel alignment of flat central NC_2S_2 ring.

3.3 Electrochemical studies

The candidacy of dithiadiazolylium, trithiadiazolylium, 1,2,3- and 1,3,2-dithiazolylium salts as building blocks for the design of molecular conductors is inspired by their one-electron reduction to form the corresponding stable radicals. This is in addition to their ability to tune the redox behaviour of the sulphur-nitrogen ring systems via change in substituents coupled with the small dimerization energy that results from delocalization of unpaired electron density. All these peculiar properties motivated the electrochemical studies of 1,2,4-dithiazolylium salts.

Representative cyclic voltammograms (CVs) of $\mathbf{3}^+$, $\mathbf{1}^+$ and $\mathbf{14}^+$ **(**Figures 3.15, 3.16, and 3.17**)** in acetonitrile and dichloromethane containing 0.1 and 0.4 M $[^nBu_4N][PF_6]$ as supporting electrolyte and on a platinum electrode are reported herein. The CVs were obtained over a scan rate range of 50-20,000 mVs^{-1}. All the data (Tables 3.4-3.6) in this section are reported versus the formal potential, $E^{0/+/0}_{Fc}$, for ferrocenium / ferrocene (F_c^+/F_c) redox couple, which is used as a secondary internal standard. All potential measurements are estimated to be ± 0.01 V for accuracy. The three dithiazolium salts (**DTAs**) are very soluble in acetonitrile while 1 and 14 are also soluble in dichloromethane and **3** shows fair solublility. All cyclic voltammograms show uniform behaviour via electrochemically irreversible E_p^{c1} reduction processes with strong offset reoxidation waves E_p^{a1} (Figure 3.18). The cyclic voltammograms showed dependence on scan

rates. As the scan rates increased, the reduction and reoxidation processes moved towards the negative and positive ends of the redox window, respectively. This resulted in increased ΔE_p values from scan rates of 100-20000 mVs^{-1}; [$\mathbf{3}^+$ = 1.17-1.46 V in CH_3CN., 1.17-1.57 V in CH_2Cl_2, $\mathbf{1}^+$ = 0.54-1.13 V in CH_3CN., 0.77-1.60 V in CH_2Cl_2 and $\mathbf{14}^+$ = 0.53-1.09 V in CH_3CN., 0.43-1.25 V in CH_2Cl_2].

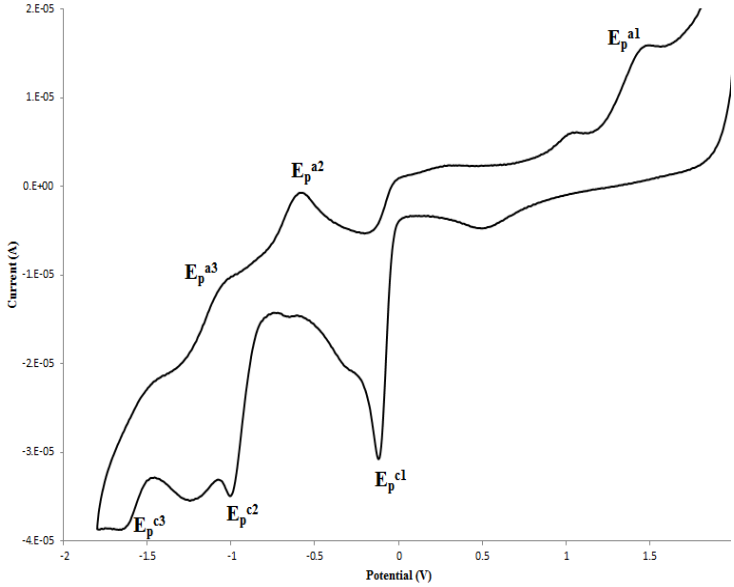

Figure 3.15 Cyclic voltammogram (nominal) of $\mathbf{3}^+$ in CH_2Cl_2 solution (0.4 M $[^nBu_4N][PF_6]$ at a scan rate of 200 mVs^{-1} on a platinum electrode. Potential value estimate = ± 0.01 V

On scanning through a potential range of 1 V to -2 V, $\mathbf{3}^+$ recorded E_p^{c1}, E_p^{c2} and E_p^{c3} reduction processes that could correspond to the formation of neutral radicals, anions and dianions, respectively, coupled with offset reoxidation processes E_p^{a1}, E_p^{a2} and E_p^{a3}, respectively (Figure 3.15). DTAs $\mathbf{1}^+$ and $\mathbf{14}^+$ on the other hand recorded only the E_p^{c1} and E_p^{a1} processes within the same potential window of 1 V to -2 V (Figures 3.16 and 3.17). The E_p^{c1} and E_p^{a1} processes are used to study the three DTAs since they are common to the CVs of the three target compounds.

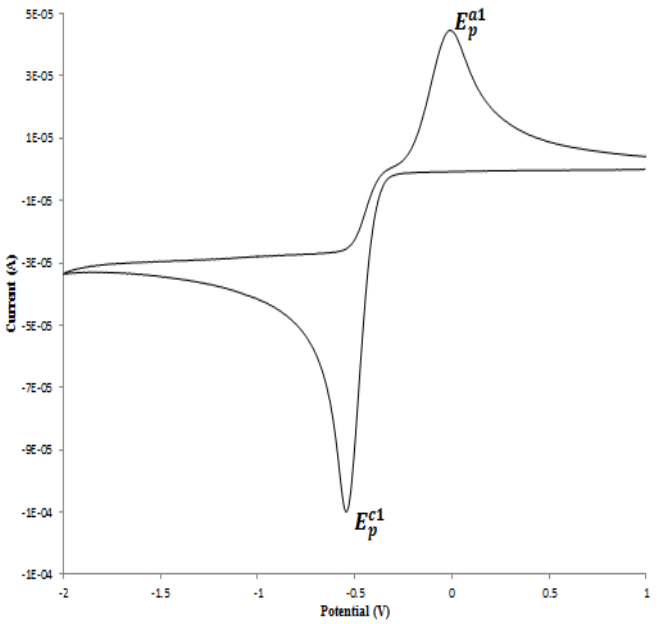

Figure 3.16 Cyclic voltammogram (nominal) of $\mathbf{1}^+$ in CH_3CN solution 0.1 M [$^nBu_4N$][PF_6] at a scan rate of 200 mVs^{-1} on a platinum electrode. Potential value estimate = ± 0.01 V

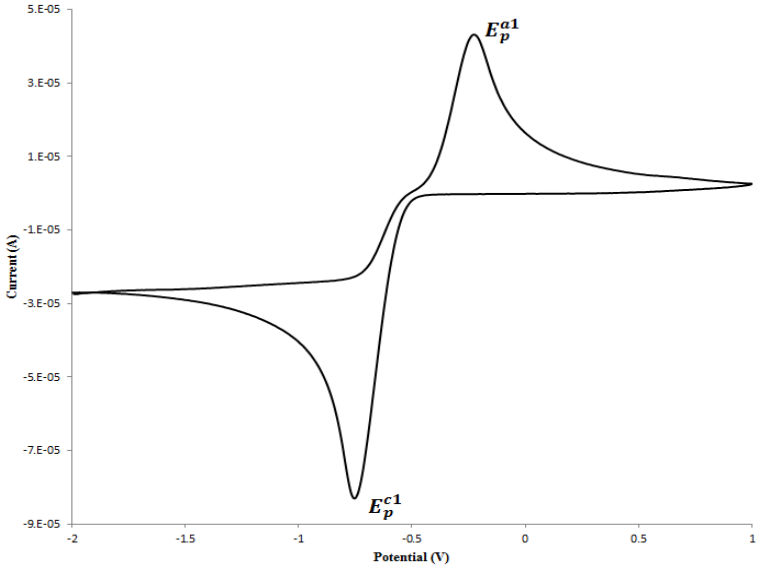

Figure 3.17 Cyclic voltammogram (nominal) of $\mathbf{14}^+$ in CH_2Cl_2 solution (0.4 M [$^nBu_4N$][PF_6] at a scan rate of 200 mVs^{-1}. Potential value estimate = ± 0.01 V

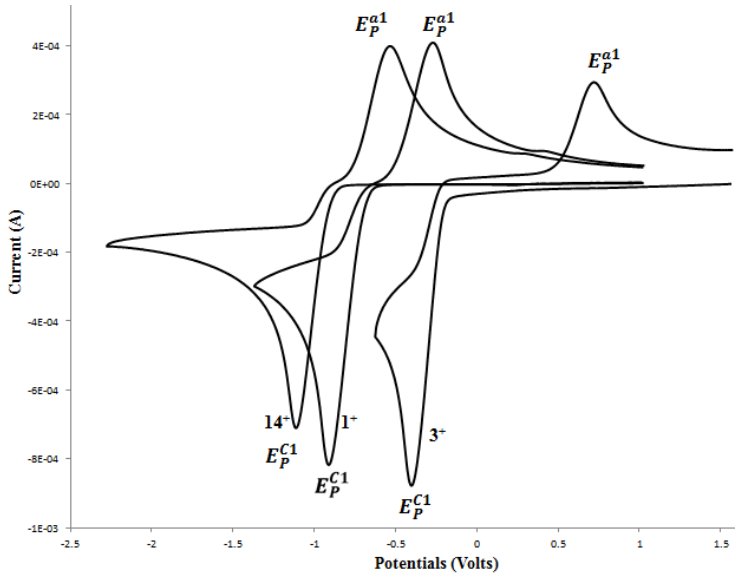

Figure 3.18 Overlapping cyclic voltammograms (referenced to F_c^+/F_c) of $\mathbf{3}^+$, $\mathbf{1}^+$,and **14** in CH_3CN solution containing (0.1 M $[^nBu_4N][PF_6]$ at a scan rate of 200 mVs^{-1} on a platinum electrode. Potential value estimate = ± 0.01 V

The three compounds showed potentials that are solvent dependent. In $\mathbf{3}^+$, there was an average of ≈ 0.06 V solvent dependence with acetonitrile being more anodic for the offset reoxidation processes. For the reduction processes, there was an average of $\approx$ 0.02 V solvent dependence with acetonitrile being less cathodic. In $\mathbf{1}^+$, there was an average of $\approx 0.19\,V$ solvent dependence with acetonitrile being more anodic then dichloromethane for the offset reoxidation process while there was an average of $\approx 0.14\,V$ with acetonitrile being less cathodic for the reduction processes. $\mathbf{14}^+$ displayed an average of $\approx 0.19\,V$ solvent dependence with acetonitrile being more cathodic than dichloromethane for the reductive process while the offset reoxidation processes showed an average of $\approx 0.18\,V$ with dichloromethane being less anodic than acetonitrile. At scan rates of 200 mVs^{-1}, the cyclic voltammetric response of $\mathbf{14}^+$ gave the lowest anodic-cathodic peak-to-peak separation of 0.52 V in both acetonitrile and dichloromethane while $\mathbf{3}^+$ gave the highest of 1.17 V in both acetonitrile and dichloromethane. $\mathbf{1}^+$ was in between with peak-to-peak difference of 0.60 V and 0.81 V in acetonitrile and dichloromethane respectively (Eqn. 3.1). They all have peak-to-peak separation much larger than the Nernstian value for reversible reactions as represented below.

$$\Delta E_p = E_{pc} - E_{pa} = \frac{58}{n}\, mV \text{ at all scan rates at } 25^{o}\text{C} \qquad \text{Eqn. 3.1}$$

The peak-current ratio $i_{pc}/i_{pa} \neq 1$ coupled with increasing peak-to-peak separation as scan rates increase further confirmed them as irreversible processes (Figure 3.19). The cathodic peak currents were observed to be much larger than the anodic peak currents for the corresponding offset reoxidation processes (Figure 3.18). Perhaps, this suggests that more than one electron was transferred during the redox processes. The cathodic peak voltages all shift towards more negative values as the R substituents attached to the 1,2,4-dithiazolium central rings change from aryl to alkylamino groups. This is a reflection of the difference in the electron donating influence of aryl and alkylamino groups on the electrochemical response of 1,2,4-dithiazolium ring systems (Fig. 3.18). The anodic peak potentials for **3** increased by average of ~ 0.04 V and 0.07 V as the scan rates increased from 200-20,000 mVs^{-1} in acetonitrile and dichloromethane respectively (Table 3.4). On the contrary, the anodic peak voltages $\mathbf{1}^{+}$ and $\mathbf{14}^{+}$ all reduced as scan rates increase (Tables 3.5-3.6). The anodic potentials of $\mathbf{1}^{+}$ had an average reduction of 0.04 V and 0.05 V in acetonitrile and dichloromethane, respectively, as the scan rates increase from 100-20,000 mVs^{-1}. The anodic potentials of $\mathbf{14}^{+}$ reduced by averages of ~ 0.02 and 0.05 V in acetonitrile and dichloromethane, respectively, as scan rates increased from 100-20,000 mVs^{-1}. These occurrence are attributable to the presence of one and two electron-donating alkyl-amino substituents respectively around the 1,2,4-dithiazolium central cationic ring.

Table 3.4 Voltammetry data (vs $Fc^{0/+}$) for 3^+ in CH_2Cl_2 and CH_3CN Solutions containing (0.4 and 0.1 M [$^nBu_4N$][PF_6] respectively.[a]

Scan	E_a(V)[b]	E_c(V)[c]	ΔE(V)[d]
200	0.77 / **0.73**	-0.40 / **-0.44**	1.17 / **1.17**
400	0.77	-0.42	1.19
800	0.80	-0.43	1.23
1000	0.91 / **0.71**	-0.45 / **-0.47**	1.36 / **1.18**
2000	0.85 / **0.75**	-0.46 / **-0.48**	1.31 / **1.23**
4000	0.87	-0.49	1.36
5000	**0.89**	**-0.56**	**1.45**
8000	0.87	-0.52	1.39
10000	0.87 / **0.84**	-0.54 / **-0.52**	1.41 / **1.36**
20000	0.87 / **0.95**	-0.59 / **-0.62**	1.46/ **1.57**

[a] All potentials are measured in DCM (**bold**) and acetonitrile versus $E^{0/}_{Fc0/+}$,the redox couple of ferrocene/ferrocenium. [b] E_a = anodic peak potential. [c] E_c = cathodic peak potential. [d] $\Delta E = E_a - E_c$. Potential value estimate = ± 0.01 V

Table 3.5a Voltammetry data for 1^+ in CH_3CN solution (0.1 M [$^nBu_4N$][PF_6]).[a]

Scan rate(mV/s)	E_a(V)[b]	E_c(V)[c]	ΔE(V)[d]
100	-0.34	-0.88	0.54
200	-0.30	-0.90	0.60
500	-0.28	-0.93	0.65
800	-0.26	-0.96	0.70
1000	-0.24	-0.97	0.73
5000	-0.15	-1.06	0.91
10000	-0.13	-1.12	0.99
20000	-0.06	-1.19	1.13

[a] All potentials are measured in acetonitrile versus $E^{0/}_{Fc0/+}$,the redox couple of ferrocene/ ferrocenium. [b] E_a = anodic peak potential. [c] E_c = cathodic peak potential. [d] $\Delta E = E_a - E_c$. Potential value estimate = ± 0.01 V

Table 3.5b Voltammetry data for 1^+ in CH_2Cl_2 solution (0.4 M [$^nBu_4N$][PF_6]).[a]

Scan rate(mV/s)	E_a(V)[b]	E_c(V)[c]	ΔE(V)[d]
100	-0.23	-1.00	0.77
200	-0.19	-1.00	0.81
400	-0.14	-1.02	0.88
800	-0.08	-1.06	0.98
1000	-0.05	-1.08	1.03
2000	-0.01	-1.13	1.12
4000	0.05	-1.19	1.24
8000	0.11	-1.27	1.38
10000	0.13	-1.30	1.43
20000	0.20	-1.40	1.60

[a] All potentials are measured in acetonitrile versus $E^{0/}_{Fc0/+}$,ferrocenium. [b] E_a = anodic peak potential. [c] E_c = cathodic peak potential. [d] $\Delta E = E_a - E_c$. Potential value estimate = ± 0.01 V

Table 3.6a Voltammetry data (vs $Fc^{0/+}$) for 14^+ in CH_3CN solution (0.1 M [$^nBu_4N$][PF_6]).[a]

Scan rate(mV/s)	E_a(V)[b]	E_c(V)[c]	ΔE(V)[d]
100	-0.55	-1.08	0.53
200	-0.52	-1.10	0.52
400	-0.49	-1.13	0.64
800	-0.46	-1.17	0.71
1000	-0.45	-1.19	0.74
2000	-0.41	-1.24	0.83
4000	-0.36	-1.29	0.93
8000	-0.33	-1.37	1.04
10000	-0.35	-1.40	1.05
20000	-0.41	-1.50	1.09

[a] All potentials are measured in dichloromethaneversus $E^{0/}_{Fc0/+}$,the redox couple of ferrocene/ ferrocenium. [b] E_a = anodic peak potential. [c] E_c = cathodic peak potential. [d] ΔE = E_a - E_c. Potential value estimate = ± 0.01 V

Table 3.6b Voltammetry data (vs $Fc^{0/+}$) for 14^+ in CH_2Cl_2 solution (0.4 M [$^nBu_4N$][PF_6]).[a]

Scan rate(mV/s)	E_a(V)[b]	E_c(V)[c]	ΔE(V)[d]
50	-0.50	-0.93	0.43
100	-0.46	-0.94	0.48
200	-0.43	-0.95	0.52
400	-0.37	-0.92	0.55
500	-0.35	-0.93	0.58
1000	-0.25	-0.94	0.59
2000	-0.27	-1.04	0.77
5000	-0.19	-1.11	0.92
10000	-0.12	-1.19	1.07
20000	-0.05	-1.30	1.25

[a] All potentials are measured in dichloromethaneversus $E^{0/}_{Fc0/+}$,the redox couple of ferrocene/ ferrocenium. [b] E_a = anodic peak potential. [c] E_c = cathodic peak potential. [d] ΔE = E_a - E_c. Potential value error = $\pm$ 0.01 V

At all the scan rates with which cyclic voltammetry were carried out on $\mathbf{3}^+$, $\mathbf{1}^+$ and $\mathbf{14}^+$, the reduction peak potentials of **3** were the closest to 0 V. This is followed by $\mathbf{1}^+$ while $\mathbf{14}^+$ is furthest from the origin of the redox window. The potential difference of the anodic peak potentials from 0 V is reverse of what was experienced by the cathodic peak voltages with $\mathbf{14}^+$ being the closest and $\mathbf{3}^+$ being the furthest (Figures 3.18 and 3.19).

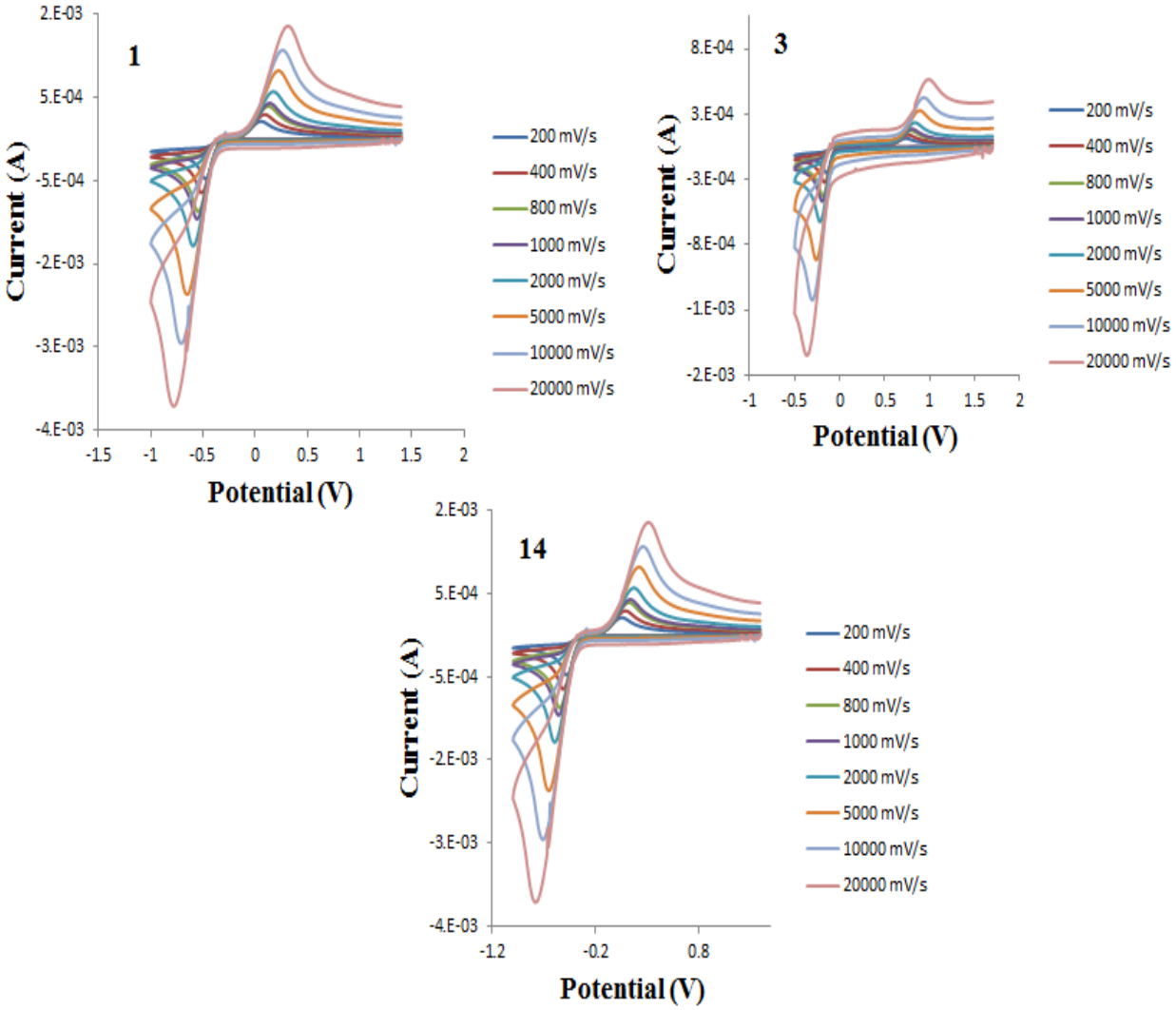

Figure 3.19 Plots showing dependence of potentials on change in scan rates.

From Table 3.7, it is obvious that compound **3** which was prepared and characterized in the Boeré lab for this thesis and the one made by Uemachi and co-workers[1] are closely similar in terms of potentials but completely different with the appearance of a reverse peak for Uemeachi's (Figure 3.18 and Figure 1.4). We confirmed its composition by X-ray crystallography while the Uemachi group on the other hand characterized it via IR and Raman spectroscopy. The discrepancies in these two CVs made us go further to carry out cyclic voltammetry on **1** and **14** and coincidentally, the cyclic voltammograms all gave very similar responses (irreversible reduction E_p^{c1} processes coupled with offset reoxidized E_p^{a1} processes). Though, while they used n-Bu_4NClO_4 as the electrolyte, we used n-Bu_4NPF_6 but the effect of electrolyte was presumed negligible as they were

only meant to ensure sufficient conductivity in the test solution. For Uemachi and co-workers' voltammograms (Fig. 1.4). These strange differences between our voltammogram and Uemachi's were the driving force behind the use of other investigative efforts to find mechanisms from which kinetic parameters for the redox behaviour of compound **3** could be derived.

Table 3.7 Voltammetry data for compounds 3, 1, 14 and comparative compounds.

Comp	E_p^{c1}(V)	E_p^{a1}(V)	$/\Delta E^1$	E_p^{c2}(V	E_p^{a2}(V	E_p^{c3}(V)	E_p^{a3}(V)
3 [Thesis]	-0.32	0.84	1.16	-1.19	-0.74	-1.87	-1.58[a,b]
3[Uemachi]	-0.15	-0.06	0.09	-1.07	-0.45	-1.53	-1.32[a,c]
1 [Thesis]	-0.93	-0.39	0.54[d]	-	-	-	-
1 [Hartung]	-0.85	-0.50	0.35[f,]	-	-	-	-
14[Thesis]	-1.21	-0.68	0.53[h]	-	-	-	-

[a]Potentials are reported at a scan rate of 100 mV/s on glassy carbon working electrode in DCM solution containing 0.4 M [^{n}Bu$_4$N][PF$_6$] for thesis and 0.1 M [^{n}Bu$_4$N][ClO$_4$] in CH$_3$CN solution for Uemachi, T = 20 $\pm$ 2 ^{o}C. [b]Reported potentials are referenced vs. F_c/F_c^+ in DCM, T = 20 $\pm$ 2 ^{o}C. [c]Potentials are referenced vs. Ag/Ag$^+$ on a platinum or glassy carbon working electrode at room temperature. [d]Potentials are reported at a scan rate of 100 mV/s on glassy carbon working electrode in CH$_3$CN solution containing 0.1 M [^{n}Bu$_4$N][PF$_6$], T = 20 $\pm$ 2 ^{o}C. [e]Potentials are reported at a scan rate of 200 mV/s on glassy carbon working electrode in CH$_3$CN solution containing 0.1 M [^{n}Bu$_4$N][PF$_6$], T = 20 $\pm$ 2 ^{o}C. [f]Potentials are recorded vs. F_c/F_c^+ at a scan rate of 200 mV/s in CH$_3$CN solution containing 0.1 M [^{n}Bu$_4$N][PF$_6$].[g]Hartung et. al. reported a single 2e$^-$ process at a formal potential of -0.675 V vs ferrocene. [h]Potentials are reported at a scan rate of 200 mV/s on glassy carbon working electrode in DCM solution containing 0.4 M [^{n}Bu$_4$N][PF$_6$], T = 20 $\pm$ 2 ^{o}C.

Hartung and co-workers[11] reported electrochemically irreversible, but chemically reversible processes for **1**. They reported a single two-electron reduction process to form the anion with a ΔE of 0.35 V which occurred at a formal potential of 0.675 V (mean of E_p^{c1} and E_p^{c1} in Table 3.7) versus ferrocene / ferrocenium redox couple. They gave unconvincing evidence as to the nature of the processes and that is why the simulation of the whole voltammograms is necessary to derive a meaningful mechanism and extract justifiable kinetic data.

3.4 SEEPR spectroscopic studies

The reduction of **3**$^+$, **1**$^+$, and **14**$^+$ was carried out in a spectroelectrochemical cell in CH$_3$CN and CH$_2$Cl$_2$ (0.1 M ^{n}Bu$_4$NPF$_6$ and 0.4 M ^{n}Bu$_4$NPF$_6$) respectively at room temperature (19 ± 2 ^{o}C) and at reduced temperatures (EPR experiments at low temperature have been proved to help trap reaction intermediates that cannot be studied at higher temperatures because of their

short lifetime in addition to restricting the studied molecule to a certain environment). The sole objective is to ascertain the formation of neutral radicals at the potentials where the reduction processes E_p^{c1} occured. By using the controlled electrolysis experiment with the cathodic peaks being adjusted by ≈ ± 0.1 V relative to the original potential observed in the cyclic voltammetry experiment, no EPR signals were detected for the three DTAs presumably owing to their very short lifetimes or the inability to form stable neutral radicals. The three DTAs each had strongly offset reoxidation waves while $\mathbf{3}^+$ was the only one that had at least one process other than the E_p^{c1} process (Figure 3.18) within the redox window of the solvent in the negative potential region. $\mathbf{1}^+$ and $\mathbf{14}^+$ on the other hand had just one irreversible process E_p^{c1} within the solvent limit though there was the suspicion that there could be some other processes in the more negative region beyond the solvent limit since DFT revealed bond scission especially in $\mathbf{14}^+$ at the neutral, anion and dianionic redox states. Scans were not run in the negative potential direction because of the possibility of interference from the redox processes of the electrolytes and solvents.

3.5 Computational studies

The SOMOs are π*-orbitals for $\mathbf{3}^{\bullet}$ and $\mathbf{1}^{\bullet}$ while a strongly σ*-orbital is present in $\mathbf{14}^{\bullet}$ (Figure 3.23). This is an indication that there is a huge possibility of having the -1/0 process that may involve S-S bond scission coupled with twisting in the ring if the π*-orbitals or σ* especially got populated. This is very evident in the acceptor orbitals of $\mathbf{14}^{\bullet}$ and in its representative geometric structures (Figure 3.20).

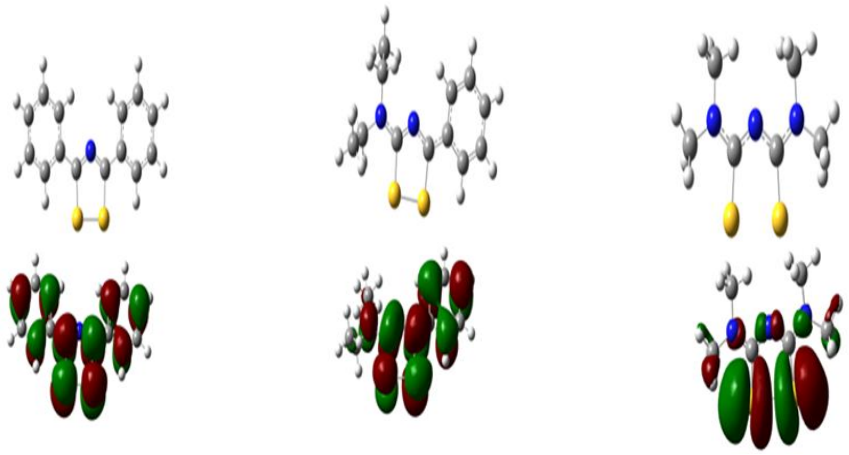

Figure 3.20 Representative geometrical structures of **3**$^{\bullet}$, **1**$^{\bullet}$, and **14**$^{\bullet}$ respectively (Up). and Molecular orbitals for **3**$^{\bullet}$, **1**$^{\bullet}$, and **14**$^{\bullet}$ respectively (Down).

DFT calculations reveal the possibility of S-S scission upon 3e^{-} reduction that could result from bond weakening due to twists to form the disulphide species (dianion) of **3**, sulphide thioketone (anion) of **1** and neutral, anion and dianion of **14**. The confirmation for the S-S cleavage coupled with a twist in the ring in dianion species **3**$^{2-}$ is a result of the strongly S-S antibonding σ orbital (as B3LYP level of DFT calculation shows the balance in energy to favour the indicated σ orbital (LUMO as the true representative of the dianionic species) (Figure 3.21) which has a greater tendency to cause bond cleavage than the antibonding π orbital (Figure 3.22). This shows that the strength of the S-S bonds in the dianions are a reflection of the nature of the LUMO.

S2-S1 bonds get weakened from **3** to **1** to **14** resulting in bond lenthening; a phenomenon connected to having SOMOs that are π* with respect to S-S bond in **3**$^{\bullet}$ and **1**$^{\bullet}$ but σ* with respect to S-S bond in **14**$^{\bullet}$. The increase in the length of the S-S bonds as the cations are gradually transformed to dianions was more in **14**$^{2-}$ (2.09 to 3.82 Å) compared to **3**$^{2-}$ (2.05 to 2.78 Å); suggestive of the greater strength of the antibonding LUMO of **14** compared to that of **3**. The same trend is seen in the anionic species but with **1**$^{-}$ in the lead followed by **14**$^{-}$ and **3**$^{-}$ respectively. This could be attributed to the populated σ* orbitals.

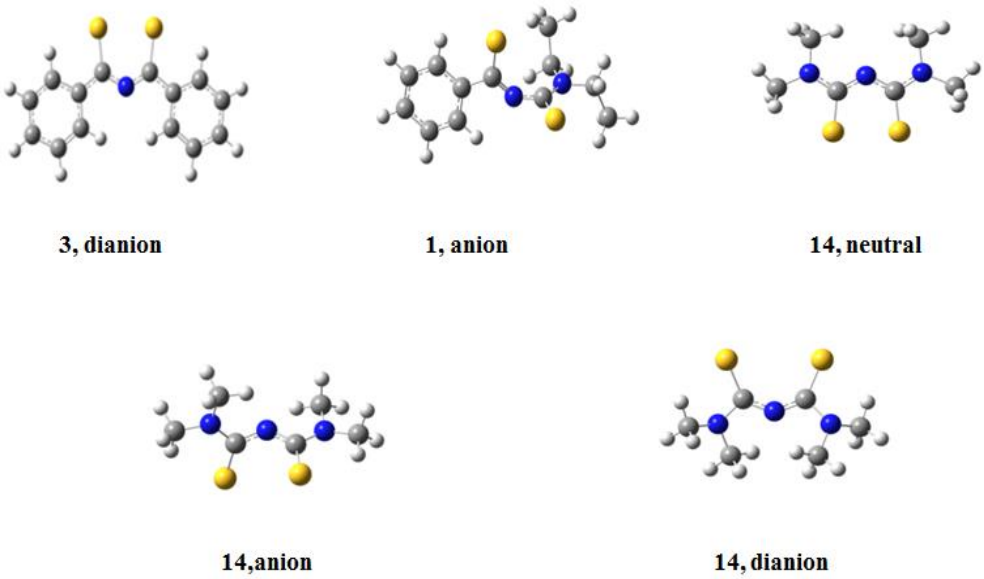

Figure 3.21 Representative geometrical structures of **3**, **1** and **14** showing S-S scission coupled with twists in the rings.

Figure 3.22 (a) σ* and (b) π* orbitals of **3** with close energies 0.12230 a.u (3.3 eV) and 0.08212 a.u (2.23 eV).

The opposite bond angles ∠S4C1C17 in the radical shows a slight difference for **14**$^{\bullet}$ (119.7 °) but drops to 118.8 ° (σ* molecular orbitals). In all the three compounds, the S-S bonds are weakened resulting in the lengthening of the bonds as electrons are added to the antibonding LUMO molecular orbitals with **1** experiencing the highest increase from 2.08 $Å_{cation}$ to 4.02 $Å_{anion}$ (it is obvious that the huge increase or decrease can be meaningless as well as complicated for rings with twisted geometries compared to planar or pseudo-planar geometries). The ∠S5C2N3 and ∠S4C1N3 bond angles in the dianionic species both increased tremendously from 116.8 ° to 122.9 ° in **3**$^{2-}$ and from 118.6 ° to 132.9 ° in **14**$^{2-}$. This is slightly connected to the antibonding orbitals coupled with the amine N substituents attachment in **14**$^{+}$.

The CVs of $\mathbf{3}^{+}$, $\mathbf{1}^{+}$ and $\mathbf{14}^{+}$ all point to the fact that the peak potentials are kinetically controlled rather than possessing thermodynamic tendencies due to changes they undergo with respect to scan rates. The couple could have been irreversible because the electron transfer reaction is followed by a chemical step or the electron transfer reactions possess a very slow rate transfer constants. Figures 3.23, 3.24 and 3.25 below are graphs showing the effects of scan rates on the kinetically controlled peak voltages.

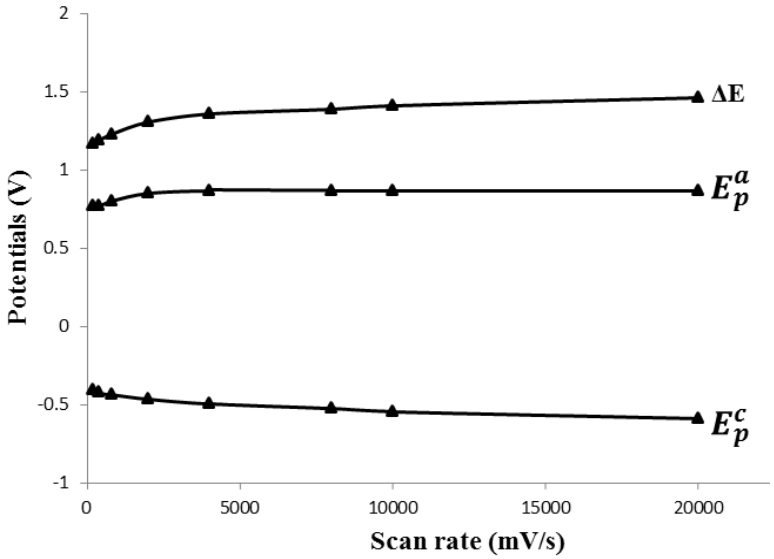

Figure 3.23 Plot of scan rates against voltages (vs $Fc^{0/+}$) for $\mathbf{3}^{+}$ in CH_3CN solution containing (0.1 M $[^nBu_4N][PF_6]$ on a platinum electrode. Potential value error = $\pm$ 0.01 V

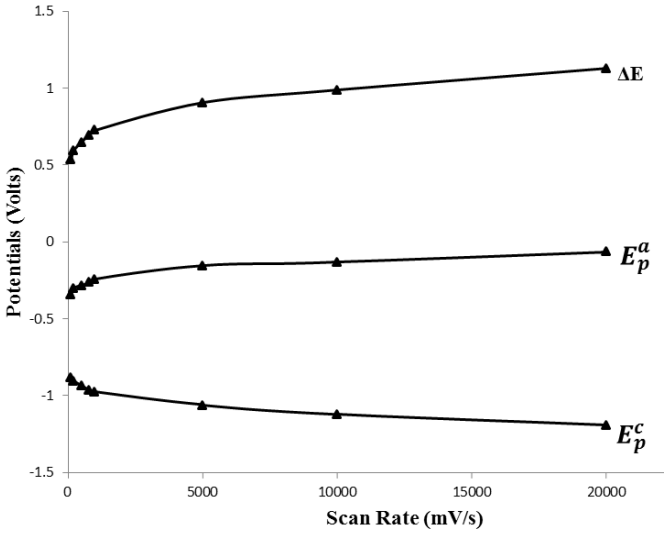

Figure 3.24 Plot of scan rates against voltages (vs $Fc^{0/+}$) for $\mathbf{1}^{+}$ CH_3CN solution containing (0.1 M $[^nBu_4N][PF_6]$ on a platinum electrode. Potential value error = $\pm$ 0.01 V

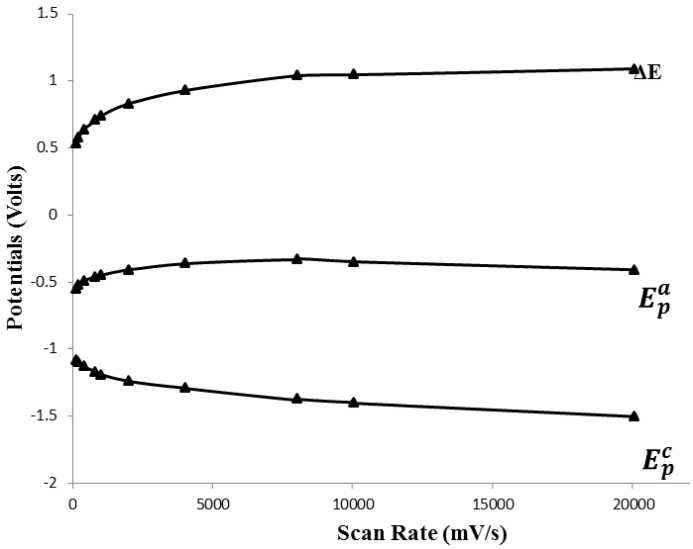

Figure 3.25 Plot of scan rates against voltages (vs $Fc^{0/+}$) for **14**$^{+}$ in CH_3CN solution containing (0.1 M [$^{n}Bu_4N$][PF_6]on a platinum electrode. Potential value error = $\pm$ 0.01 V

Table 3.8 Calculated energies of molecular orbitals of 3 in eV.[a]

	Cation	Neutral	Anion	Dianion
HOMO (eV)	-10.61	-6.53	-2.72	0.81
LUMO (eV)	-7.35	-4.35	-0.27	2.18
$\lvert\Delta\rvert$ (eV)[b]	3.26	2.18	2.45	1.37

[a] Computed from Gaussian W03 package. [b] HOMO-LUMO gap.

Table 3.9 Calculated energies of molecular orbitals of 1 in eV.[a]

	Cation	Neutral	Anion
HOMO (eV)	-7.53	-6.53	-1.69
LUMO (eV)	-5.71	-3.81	-1.60
$\lvert\Delta\rvert$ (eV)[b]	1.82	2.72	0.09

[a] Computed from Gaussian W03 package. [b] HOMO-LUMO gap.

Table 3.10 Calculated energies of molecular orbitals of 14 in eV.[a]

	Cation	Neutral	Anion
HOMO (eV)	-10.61	-6.00	-1.09
LUMO (eV)	-6.00	-4.90	-0.82
$\lvert\Delta\rvert$ (eV)[b]	4.61	1.10	0.27

[a] Computed from Gaussian W03 package. [b] HOMO-LUMO gap.

The electron spin density in the SOMO of neutral **3**$^{\bullet}$ was delocalized on the central ring more than on the substituents. There have been suggestions that other radicals with N in their rings are able to impede dimerization.[13] In the SOMO of **3**$^{\bullet}$, N on the central heterocyclic ring is a

node (Figure 3.20**)**; a phenomenon observed in the electrochemical investigations of 1,2,3,5-dithiadiazolyls[14] and is expected to have little or no effect on the electronic behaviour of the system. Therefore, there is the possibility that the electronic properties of the dithiazolium salt[15] are based on inductive effects from N.[14] **14**$^{\bullet}$ shows the same behaviour of having similar nodal pattern at N unlike **1**$^{\bullet}$ which lacks a node at N.

The LUMO of **3** got raised from -7.35 to -4.35 eV (Table 3.8). The electronic distribution, in turn, decreases the energy gap between the singly occupied molecular orbital (SOMO) of the neutral species and the HOMO of the cationic specie (-3.26 to -2.16 eV). **1** showed a drop in its LUMO energy from -5.71 to -3.81 eV. This is not enough to facilitate a decrease in the HOMO-LUMO gap, rather there was an increase from 1.82 to 2.72 eV (Table 3.9). **14** had its LUMO lowered on the energy scale from -6.00 to -4.90 eV and equally had a decrease in the HOMO-LUMO gap from 4.61 to 1.10 eV making it the compounds with the lowest HOMO-LUMO gap of the three compounds from the DFT data (Table 3.10).

3.6 CV and RDE experiments on Ferrocene, 3^+, 1^+, and 14^+.

CV measurements on solutions of **3^+, 1^+, and 14^+**were carried out to ascertain the nature of the mass transport in terms of what controls it. For CV measurements of these compounds in acetonitrile (**3** and **14**) and dichloromethane **1**, the square root of the scan rates $\nu^{1/2}$ within the range of 0.32-2.83 $V^{1\backslash2}$ $s^{-1\backslash2}$ were tabulated with the anodic and cathodic peak currents I_p^a and I_p^c respectively (Table 3.11). In both cases, straight line graphs were obtained suggesting that the mass transport in the solutions was diffusion-controlled. The peak currents of CVs were obtained under the Nernstian conditions as given by the equation $I_p = (2.69 \times 10^5)n^{3/2}AD^{1/2}C\nu^{1/2}$ where I_p is the peak current, n is the number of transferred electrons and is taken to be 1.0, A is the surface area of the electrode in cm^2, D is the diffusion coefficient in cm^2/s, C is the concentration in mol/cm^3 and ν is the scan rate in V/s.

Table 3.11 Cathodic and anodic peak currents for 3, 1 and 14 in CH_3CN solution containing 0.1 M [$^nBu_4N$][PF_6] on a glassy carbon electrode to determine diffusion-controlled mass transport.

Scan rate ν	$\sqrt{\nu}$	(**3**) 5 mM (*μA)		(**1**) 5 mM (*μA)		(**14**) 5 mM (*μA)	
V/s	$\sqrt{V/s}$	I_p^c [a]	I_p^a [b]	I_p^c	I_p^a	I_p^c	I_p^a
0.10	0.32			57.24	9.60	167.83	47.3
0.20	0.45	60.20	7.67	82.24	21.51	229.01	74.13
0.40	0.63	88.90	14.1	113.49	39.53	311.54	99.46
0.80	0.89	117.61	20.10	156.38	58.55	414.29	121.14
1.00	1.00	136.16	22.77	176.28	70.13	454.29	177.70
2.00	1.41	197.76	33.23	236.65	93.11	597.34	215.16
4.00	2.00	259.16	53.72	319.41	132.41	798.94	286.13
8.00	2.83	349.55	73.23	425.49	170.1	1017.96	349.48

[a] I_p^c = Cathodic peak currents. [b] I_p^a = Anodic peak currents

In the determination of the surface area of the rotating glassy carbon electrode in acetonitrile solution, ferrocene whose diffusion coefficient is known was used as the analyte. Concentrations of 2.5, 5.0 and 10.0 mM solutions of ferrocene were used for the RDE experiments. After carrying out linear scans, the limiting currents I_l were determined (Figure 3.26) and their inverse values (I_l^{-1}) were plotted versus the reciprocal of the square root of the angular velocities ($\omega^{-1/2}$) in the range 500-2000 rpm (Figure 3.27). This resulted in a Koutecky-Levich graph which is a straight line with slope equal to $0.62nFAC\nu^{-1/6}D^{2/3}$. Solving for A using the Levich equation resulted in a mean value of 1.65 (6) × 10^{-1} cm^2 (Table 3.12). These values are trusted to a very large extent compared to the areas obtained using CV outside of the glovebox [Tables A.2 and A.3 wherein the area was found to be 8.1 (6) × 10^{-2} cm^2]. This is attributed to the fact that the solutions outside the glovebox are purged regularly thus resulting in gradual evaporation of the solvent. This affects the concentrations of the solution which in turn decreases the accuracies of the peak currents (Table A.2).

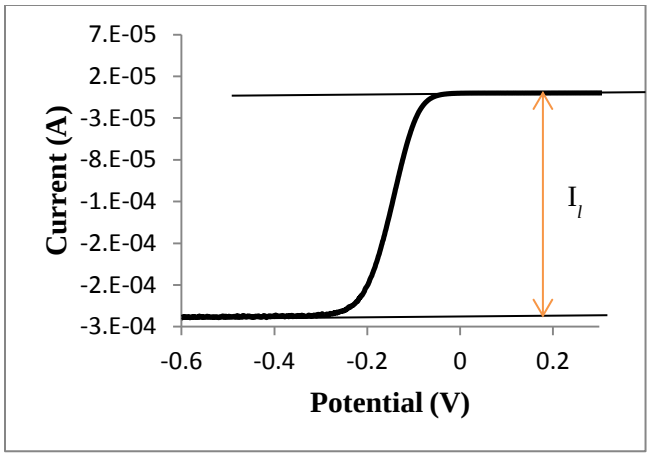

Figure 3.26 Scheme representing the determination of I_l from RDE experiments

For all the experiments, a value of 4.4×10^{-3} cm^2/s[16] was used in the Levich equation for the kinematic viscosity ν of acetonitrile at 25 ^oC. The diffusion coefficients (Ds) were determined by carrying out RDE measurements on acetonitrile solutions of **3^+, 1^+, and 14^+.** The Ds were determined in order to use them as parameters in the simulation of experimental CVs.

Concentrations of 2.5, 5.0, 7.5, and 10 mM of **3^+, 1^+, and 14^+**were used for the RDE experiments. On carrying out linear scans, the limiting currents I_l were obtained from angular frequencies in the range of 500-2500 rpm.

Table 3.12 Areas of electrode determined via RDE measurements at different concentrations in CH_3CN solution containing 0.1 M [$^nBu_4N$][PF_6] under a dry atmosphere of N_2 on a glassy carbon electrode at T = 22 ^oC.

Conc. (mM)	Area (cm^2)
2.5	0.162
5.0	0.171
10.0	0.161
Mean	0.165
Standard deviation (SD)	0.0055
Mean (SD)	$1.7\ (6) \times 10^{-1}$

Koutecky-Levich straight line graphs are obtained by plotting the reciprocal of the limiting currents against the reciprocal of the square root of the angular frequencies.

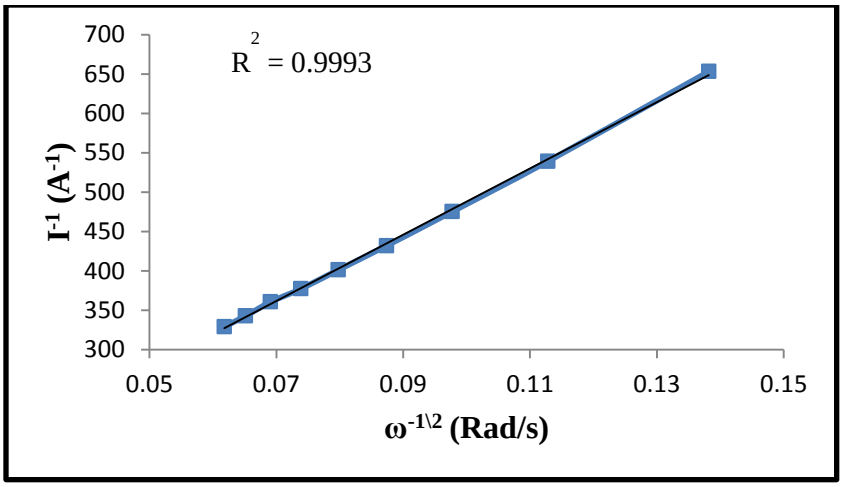

Figure 3.27 Typical straight line plots of the Levich currents against the reciprocal of the square-root of the angular velocities for test solutions in CH_3CN solution containing 0.1 M $[^nBu_4N][PF_6]$ on a glassy carbon electrode.

The slope of the straight line = $0.62nFAC\nu^{-1/6}D^{2/3}$. Solving for D for the three compounds using a constant value (1.65×10^{-1} cm^2) for A results in D values of 8.48 (2) $\times 10^{-6}$, 4.51 (4) $\times 10^{-5}$, and 4.30 (2) $\times 10^{-5}$ cm^2/s for $1e^-$ transfers and 2.99 (7) $\times 10^{-6}$, 1.58 (1) $\times 10^{-5}$, and 1.51 (8) $\times 10^{-5}$ cm^2/s for $2e^-$ transfers for **3**, **1** and **14,** respectively, (Tables 3.13 and 3.14). All the potentials for the different concentrations of the three DTAs were all measured versus the formal potential $E^{0/}_{Fc0/+}$ of Fc^+/Fc redox couple (Fc = ferrocene), which was used as an internal standard having a potential value of zero.

Table 3.13 Diffusion coefficient (D) values for solutions of 3, 1, and 14 in CH_3CN[f]

	(D) cm^2/s [$1e^-$ transfer]		
Conc.(mM)	**3**	**1**	**14**
2.5[a]	8.58E-06	4.08E-05	4.37E-05
5.0[b]	8.24E-06	4.74E-05	4.48E-05
7.5[c]	-	4.71E-05	4.05E-05
10.0[d]	8.60E-06	-	-
MEAN	8.48E-06	4.51E-05	4.30E-05
SD[e]	2.04E-07	3.76E-06	2.21E-06
Mean(sd)	8.5(2)	4.5(4)	4.3(2)

[a] Actual concentrations were 2.47, 2.46 and 2.48 mM respectively for **3^+, 1^+, and 14^+.**
[b] Actual concentrations were 5.01, 4.99 and 5.01 mM respectively for **3^+, 1^+, and 14^+.**
[c] Actual concentrations were 7.47 mM respectively for **1^+ and 14^+.**
[d] Actual concentration was 10.03 mM respectively for **3^+.**
[e] Standard deviation.
[f] Standard errors associated with concentrations range from 0.2-1.6 %.

Table 3.14 Diffusion coefficient (D) values for solutions of 3, 1, and 14 in CH_3CN[f]

	(D) cm^2/s [$2e^-$ transfer]		
Conc.(mM)	**3**	**1**	**14**
2.5[a]	2.98E-06	1.42E-05	1.53E-05
5.0[b]	2.92E-06	1.67E-05	1.59E-05
7.5[c]	-	1.66E-05	1.42E-05
10.0[d]	3.06E-06	-	-
MEAN	2.99E-06	1.58E-05	1.51E-05
SD[e]	6.67E-08	1.44E-06	8.28E-07
Mean(sd)	3.0(7)	1.6(1)	1.5(8)

[a] Actual concentrations were 2.47, 2.46 and 2.48 mM respectively for **3^+, 1^+, and 14^+.**
[b] Actual concentrations were 5.01, 4.99 and 5.01 mM respectively for **3^+, 1^+, and 14^+.**
[c] Actual concentrations were 7.47 mM respectively for **1^+ and 14^+.**
[d] Actual concentration was 10.03 mM respectively for **3^+.**
[e] Standard deviation.
[f] Standard errors associated with concentrations range from 0.2-1.6 %.

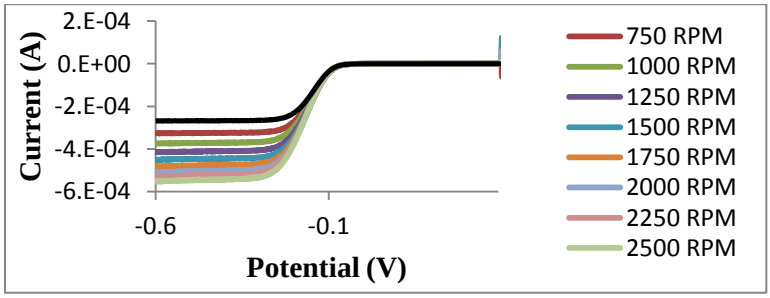

Figure 3.28 Typical RDE curves at a glassy carbon electrode for the reduction of DTAs from 2.5 mM solutions in CH_3CN containing 0.1 M [^{n}Bu$_4$N][PF_6] at ν = 100 mV/s on a glassy carbon electrode at different rotation speeds.

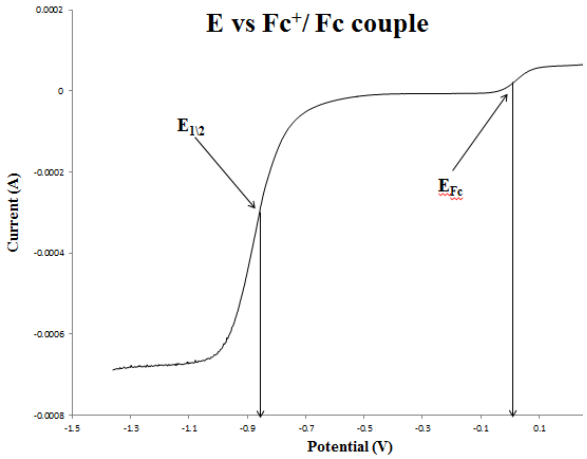

Figure 3.29 Scheme showing the determination of $E_{1/2} = (E_p^a + E_p^c)/2$ V versus $E^{0/}_{Fc0/+}$. $E_{1/2}$ is ≈ -0.86 V for 2.5 mM of **1^+** (Table 3.5a)

3.7 Conclusion

In conclusion, the analyses (electrochemical, computational and spectroelectrochemical) carried out on $\mathbf{3}^{+}$, $\mathbf{1}^{+}$, and $\mathbf{14}^{+}$ have shown their inabilities to generate neutral radicals via electrochemical reduction. This calls for an indepth mechanistic study to explain the factors responsible for the line-shapes of the cyclic voltammograms.

3.8 References

1. Uemachi, H.; Iwasa, Y.; Mitani, T., *Electrochim. Acta* **2001,** *46*, 2305-2312.

2. Corsaro, A.; Compagnini, A.; Perrini, G.; Purrello, G., *J. Chem. Soc. Perkins Trans 1* **1984,** 897-900.

3. Köhler, R.; Sieler, J.; Richter, R.; Hoyer, E.; Beyer, L.; Maartmann-Moe, K., *Z. Anorg. Allg. Chem.* **1989,** *576*, 203-214.

4. Rodríguez-Fernández, E.; García, E.; Hermosa, M. R.; Jiménez-Sánchez, A.; Mar Sánchez, M.; Monte, E.; Criado, J. J., *J. Inorg. Biochem.* **1999,** *75*, 181-188.

5. Oliver, J. E.; Chang, S. C.; Brown, R. T.; Stokes, J. B.; Borkovec, A. B., *J. Med. Chem.* **1972,** *15*, 315-320.

6. Clegg, W.; Elsegood, M. R. J.; Banister, A. J.; Hibbert, T. G., *Acta Crystallogr. Sect. C* **1996,** *52*, 2148-2150.

7. Peyronel, G.; Pignedoli, A.; Malavasi, W., *J. Cryst. Spect. Res.* **1982,** *12*, 481-488.

8. Shotonwa, I. O.; Boere, R. T., *Acta Crystallogr. Sect. E* **2013,** *69*, m95.

9. Neels, J.; Ziemer, B.; Meisel, M.; Leibnitz, P., *Z. Anorg. Allg. Chem.* **1986,** *542*, 123-130.

10. Rodesiler, P. F.; Amma, E. L., *Acta Crystallogr. Sect. B* **1971,** *27*, 1687-1692.

11. Hartung, J.; Rosenbaum, K.; Beyer, L.; Losada, J.; Fernandez, V., *J. Prakt. Chem.* **1991,** *333*, 537-544.

12. Diveley, W. R. US 3166564 19650119, **1969**

13. Boeré, R. T.; Roemmele, T. L., *Coord. Chem. Rev.* **2000,** *210*, 369-445.

14. Boeré, R. T.; Bond, A. M.; Chivers, T.; Feldberg, S. W.; Roemmele, T. L., *Inorg. Chem.* **2007,** *46*, 5596-5607.

15. Boeré, R. T.; Roemmele, T. L.; Yu, X., *Inorg. Chem.* **2011,** *50*, 5123-5136.

16. Stewart, S. G.; University of California, B., *Determination of Transport Properties and Optimization of Lithium-ion Batteries*. University of California, Berkeley: 2007.

Chapter Four

4.1 Simulation of cyclic voltammograms

Analyte concentrations and thermodynamic properties of redox couples are simply obtainable via cyclic voltammetry while the extraction of kinetic and mechanistic information from electrochemical-chemical systems is a much more difficult task. This is because the early stages of carrying out the extraction involve postulating an electrochemical-chemical mechanism based on the shape of an experimental voltammogram that results from various factors such as scan rate dependence, peak voltages and separation, peak currents and some other non-electrochemical details. The simulation of postulated mechanism that is based on values from physical and chemical parameters must match reasonably well with the experimental voltammogram which is a function of temperature, concentrations, electrode geometry, heterogenous electron transfer rate parameters, chemical reaction rate and equilibrium constants and scan rates. There is also the possibility of other alternate mechanisms fitting reasonably well with the experimental voltammogram.[1]

In order to obtain mechanisms behind the electrochemical behaviour of $\mathbf{3}^+$, $\mathbf{1}^+$, and $\mathbf{14}^+$ followed by the extraction of kinetic data for their reduction and offset oxidation couples, digital simulations of the CV responses were carried out. The potentials (E^0) of the CVs obtained from digital simulation were referenced to the correction factor of ferrocene as obtained from cyclic voltammetry to get the true values that reflect the behaviour of $\mathbf{3}^+$, $\mathbf{1}^+$, and $\mathbf{14}^+$ in solution. All the simulations utilized carefully measured values for the analyte concentration, temperature, electrode area A (Table 3.12) and diffusion coefficient D. The values for D (Tables 3.13 and 3.14) for $\mathbf{3}^+$, $\mathbf{1}^+$, and $\mathbf{14}^+$ were obtained from rotating disk electrode (RDE) voltammetry experiment and the D values were either the same or different for the reduction and offset oxidation processes depending on the number of electron transferred during the reaction. All interfacial electron transfer for heterogenous processes were described by the Butler-Volmer formalism[2] with the charge-transfer coefficient $\propto$ taken to be 0.5 all through the simulation

procedure. All the CV simulations obtained for the three compounds over a scan rate range of 0.05-2.0 Vs^{-1} at one to three concentrations were carried out to determine justifiable EC (Electron transfer and Chemical steps) [3] mechanisms and use their extracted parameters to explain the shape and nature of the experimental cyclic voltammograms (see section 2.1.1.3 for details of EC mechanisms). For the heterogenous electron transfer described by the Butler-Volmer formalism, the standard heterogenous rate constants k_s for the reduction and offset oxidation potentials were extracted while the equilibrium constants K_{eq} and the forward chemical rate constant k_f were obtained for the follow-up chemical reaction.[4] The mechanisms considered herein possess relatively low or high K_{eq} values that determine the appearance of current plateaus or peaks; a phenomenon that is indicative of steady state or diffusion controlled conditions. The following abbreviations will be adhered to all through the discussion on CV simulation in this chapter: Cat – cation, Rad – radical, An – closed anion, openAn – open anion, Dim – dimer and Dim^+ - positively charged dimer.

4.2 Model systems used in the simulation of cyclic voltammograms

Based on previously reported behaviour of C,N,S cations and on the claims of Uemachi and Hartung for CVs of $\mathbf{3}^+$ and $\mathbf{1}^+$**,** respectively, two basic models are being considered as suitable mechanisms responsible for the reduction processes and offset reoxidation processes in $\mathbf{3}^+$, $\mathbf{1}^+$, and $\mathbf{14}^+$. The first showed that the observed reduction process involves a two close-sequence $1e^-$ reduction of the cation to anion followed by a chemical step to convert the anion into the open anion system (E_1E_2C). The second model involves the formation of a dimer from the neutral radical that was formed from the $1e^-$ reduction of the cation. This is followed by a rapid chemical step to consume the radical since none of it was detected in the SEEPR experiments ($E_1C_2E_2C_{2'}$).

A postulate involving a direct $2e^-$ reduction (E) of the 3.09 mM $\mathbf{3}^+$ to form the closed anion was modelled (Eqn. 4.1). The model reflects a very slow heterogenous irreversible charge transfer to the closed anion **An** as indicated by the standard rate constants of $k_s = 2.27 \times 10^{-10}$ cm/s at $E^0 = 0.29$ V (Fig. A.39). The parameters for this mechanism were optimized but a good fit

could not be obtained, therefore it was discarded as one of the mechanisms to be considered for the reduction and offset oxidation processes.

$$Cat + 2e^- \underset{}{\overset{k_s}{\rightleftharpoons}} An \qquad \text{Eqn. 4.1}$$

4.2.1 Model 1: The Open Anion model

The simulated cyclic voltammograms obtained for the reduction and offset oxidation processes in **3** over a scan rate range of 0.05-2.0 Vs^{-1} at concentrations of 3.09, 5.89, and 9.80 mM gave products that were in accordance with the E_1E_2C (Eqns. 4.2-4.4).

$$Cat + e^- \underset{}{\overset{k_{s1}}{\rightleftharpoons}} Rad \qquad \text{Eqn. 4.2}$$

$$Rad + e^- \underset{}{\overset{k_{s2}}{\rightleftharpoons}} An \qquad \text{Eqn. 4.3}$$

$$An \underset{k_b}{\overset{k_f}{\rightleftharpoons}} OpenAn \qquad \text{Eqn. 4.4}$$

For the E_1E_2C mechanism (Eqns. 4.2-4.4) which represents two slow consecutive one-electron transfer reactions followed by a first order chemical reaction, it was discovered that the E^0 and k_s values for the electron transfer reactions are correlated i.e. any two values of E_1^0 and E_2^0 (Table 4.1) are associated with a particular set of k_{s1} and k_{s2} values though the relative values cannot be predicted by merely looking at the data from the electron transfer reactions. Moreover, the difference of 0.1 V between the E^0 values with E_2^0 being more negative than E_1^0 in addition to the chemical step helps to prevent the shapes of the processes from changing into double humps (the alternate E_1^0 being more negative than E_2^0 or $E_1^0 = E_2^0$ are less chemically reasonable for this system).

Table 4.1. Potentials used for simulation of CVs using the Open Anion model.[a]

Compounds	E_1^0 (V)	E_2^0 (V)
3[b]	-0.04	-0.14
	-0.02	-0.12
	0.03	-0.07
1[c]	-0.71	-0.81
14[d]	-0.95	-1.05
	-0.94	-1.04
	-0.96	-1.06

[a] The potential (E^0) values are reported vs F_c/F_c^+ at a scan rate of 200 mV/s in CH_3CN solution containing 0.1 M [$^nBu_4N$][PF_6]. [b] The potentials are for concentrations of 3.09 (3%), 5.89 (2%), and 9.80 (2%) mM investigated during simulation. [c] The potentials are for 3.13 (4%) mM. [d] The potential values are for 2.97 (1%) mM, 5.95 (1%) mM, and 10.02 (0.2%) mM concentrations investigated during simulation.

Table 4.2 Parameters used for the CV simulation based on the Open Anion model [a]

Compound	E_1^0 (V)[b]	E_2^0 (V)[b]	k_{s1} cm/s	k_{s2} cm/s	K_{eq}	k_f s^{-1}
3	-0.03(1)	-0.11(4)	5 (8)$\times10^{-6}$	6 (7) $\times10^{-5}$	4 (4) $\times10^{3}$	7 (6) $\times10^{9}$
1	-0.707	-0.807	4 $\times10^{-4}$	2×10^{-2}	1×10^{4}	1×10^{10}
14	-0.95(1)	-1.05(1)	4 (4) $\times10^{-3}$	4 (6) $\times10^{-3}$	1 (4) $\times10^{4}$	1×10^{10}

[a] k_s values were obtained from the average of optimized k_s values obtained for each concentration of the E_1E_2C mechanism (Eqns. 4.2-4.4) ., k_f values of 10^{10} s^{-1} were fixed for **1** and **14** in order to achieve reasonable fit. See details in Table A.37. [b] Potentials E_1^0 and E_2^0 were obtained from the mean and standard deviation of potentials in Table 4.1.

The E_1E_2C mechanism (E_2^0 being more negative than E_1^0) is favoured over E_1E_2 (reversal of E_1E_2C) because DFT calculations revealed that the open anionic ring is much more stable than the closed anionic ring (by 66 KJmol^{-1} from -3651991.0 and -3651925.1 KJmol^{-1}, respectively.) as a result of its lower potential energy (Fig. 4.1) provided that the ring-opening chemical step imposes a large conformational change on the mechanism. This is dependent on the gas phase calculations reflecting the behaviour of the system in solution. At concentrations of 3.09, 5.89, and 9.80 mM for $\mathbf{3}^+$, there are high k_f values of 10^{10}, 10^8, and 10^{10} s^{-1}, respectively, which point at the limited chemical reversibility of the An / OpenAn reaction on the time scale of the CV experiment. Their limited chemical reversibilities reasonably explain why the current peaks observed on the return scan are smaller than those in the forward scan.

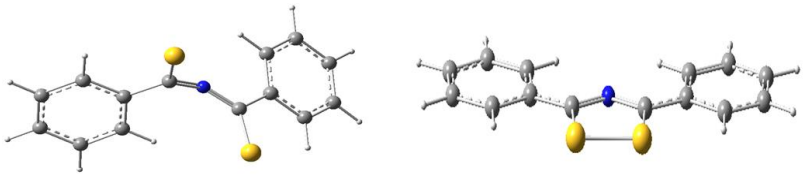

Figure 4.1 Open anion of **3** more stable than its closed anion by 66 KJ mol^{-1} **.**

It is a general electrochemical observation that a one-electron transfer reaction following another one-electron transfer reaction should be more energetic thus resulting in a much higher difference in potential than the observed theoretical 0.1 V difference. Much large difference could be attributed to factors which may include adsorption of the analyte to the electrode surface or that the product formed on the time scale of the experiment is unstable.[5] The small potential difference of 0.1 V could be due to the effect of the following chemical step in offering a lower energetic route for the conversion of the anion to the open anion. From an equilibrium viewpoint, K_{eq} values of ≈ 8100, 1900, and 620 (Table A.37) derived from k_f values mentioned earlier are relatively high enough to shift the equilibrium to the right leading to the rapid consumption of the closed anion. For the E_1E_2C mechanism, k_{s1}, k_{s2}, and D were optimized using DigiElch and the optimization of the simulated CV response was regarded as successful when the experimental and simulated peak heights and positions overlay reasonably well on each other (Fig.4.2). Estimates for the rate constants k_{s1} and k_{s2} are 5 (8)$\times 10^{-6}$ cm/s and 6 (7) $\times 10^{-5}$ cm/s and the k_f is 7 (6) $\times 10^{9}$ s^{-1} (Table 4.2). D was optimized before adjustments were made to the parameters of the chemical reaction resulting in a final value of 2.72 $\times$ 10^{-6} cm^2/s for the Cat, Rad and An and 2.83 $\times$ 10^{-6} cm^2/s for the open An (Table 4.3). These optimised D values are considered valid for the $2e^-$ transfer reactions (Table 3.14).

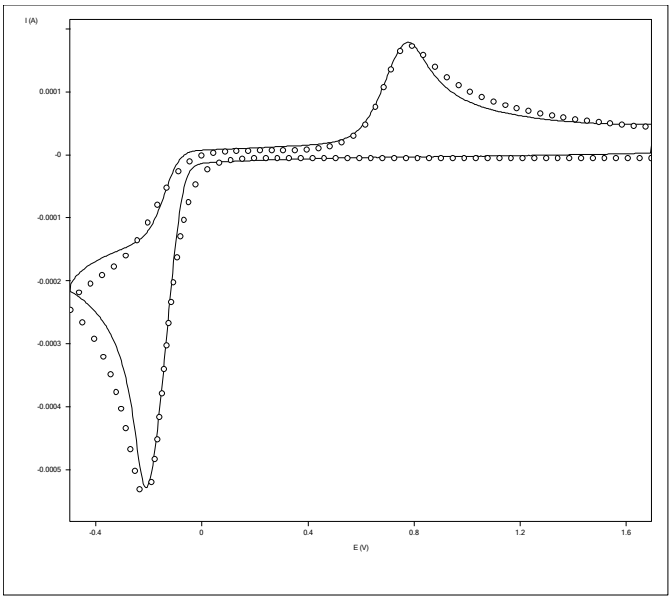

Figure 4.2. Representative fit of experimental (−) and theoretical (◦◦◦◦) CVs for **3** using the E_1E_2C mechanism. See details in A.28, A.30, and A.32

Table 4.3 Diffusion coefficient values from the optimization of E_1E_2C model[a]

	Diffusion coefficient D cm^2/s			
Compound	Cation	Radical	Anion	Open anion
3	2.72×10^{-6}	2.72×10^{-6}	2.72×10^{-6}	2.83×10^{-6}
1	1.82×10^{-5}	1.82×10^{-5}	1.82×10^{-5}	1.82×10^{-5}
14	1.46×10^{-5}	1.46×10^{-5}	1.46×10^{-5}	1.46×10^{-5}

[a] Values were obtained on optimization using DigiElch

The observation of E^0 values with 0.1 V difference in the closely-spaced sequential E_1E_2C mechanism is a strong indication that the two electron transfer processes both took place at close time scale of the electrochemical experiment. The two processes must have overlapped resulting in the big reduction processes (Fig. 3.19). The offset oxidation processes are presumed to be delayed reversal processes due to high K_{eq} values for chemical steps that result from high k_f and low k_f resulting in a difficult backward reaction.

4.2.2 Model 2: The Dimerization Model

The second mechanism employed is the $E_1C_2E_2C_2$, (Eqns. 4.5-4.8) involving two irreversible electron transfer reactions where the first represents the reduction of the monomeric cation and the second for the oxidation of the dimer. The intermediate chemical step is the dimerization reaction. The EC_2E is followed by a second chemical step. The current response on

the ECE is dependent on the nature of the redox potentials of the two one-electron transfer reactions and the rate of the chemical steps. In the three concentrations considered for the simulation of this mechanism, the redox potential of the second reduction process is positive of that of the first by an approximate average of 0.78 V (Table 4.4) which is the exact opposite of the inversion of potentials observed in the open-anion model.

Table 4.4 Potentials used for simulation of CVs using the Dimerization model.

Compd.	E_1^0	E_2^0
3 3.09 mM	-0.44	0.33
5.89 mM	-0.41	0.36
9.80 mM	-0.32	0.45
1 3.13 mM	-0.90	-0.31
14[a]		

[a] The potential values are for 2.97 mM, 5.95 mM, and 10.02 mM concentrations investigated during simulation.

$$Cat + e^- \underset{}{\overset{k_{s1}}{\rightleftharpoons}} Rad \qquad \text{Eqn. 4.5}$$

$$Rad + Rad \underset{k_{b1}}{\overset{k_{f1}}{\rightleftharpoons}} Dim \qquad \text{Eqn. 4.6}$$

$$Dim^+ + e^- \underset{}{\overset{k_{s2}}{\rightleftharpoons}} Dim \qquad \text{Eqn. 4.7}$$

$$Dim^+ \underset{k_{b2}}{\overset{k_{f2}}{\rightleftharpoons}} Cat + Rad \qquad \text{Eqn. 4.8}$$

The first chemical step C_2 is a dimerization reaction involving the chemical combination of two radicals to form the dimer Dim (Eqn. 4.6) which undergoes a one-electron oxidation to form the positively charged dimer (Dim^+) upon the reversal of the scan direction (Reversal of Eqn. 4.7). The chemical step that follows the E_2 is a dissociation reaction of Dim^+ to form the neutral radical and cationic species (Eqn. 4.8). On running through the reaction chain of electron transfers and chemical reaction steps, it was obvious that the electroactive cationic species that participated in the first electron transfer reaction (E_1., Eqn. 4.5) also showed up in the second chemical step ($C_{2'}$**.,** Eqn. 4.8) revealing a cyclic process. Another peculiar occurrence in the mechanism is that the neutral radical species exist as "spectator" molecules in solution without any contribution to the equilibrium balance. Due to these occurrences, we employed the "square

scheme"[6-7] mechanism (Scheme 4.1). In order to come up with the very reasonable fit between the model CV for the $E_1C_2E_2C_2$, mechanism and the experimental CV, k_{s1}, k_{s2}, k_{f1}, and k_{f2} were fine-tuned while K_{eq1} and K_{eq2} were randomly fixed at 10^8 and 1.92×10^5, respectively, thus making the chemical reaction strongly product-favoured for all the scan rates that were probed. On carrying out optimization of the simulated CV responses using DigiElch, a fit was obtained when the experimental peak heights and positions overlaid those of the simulated (Fig. 4.3).

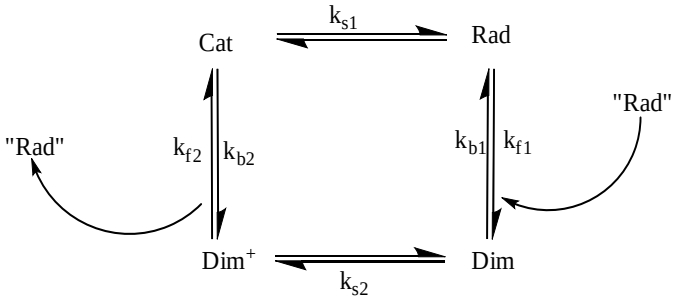

Scheme 4.1 "Square Scheme" for the $E_1C_1E_2C_2$ mechanism

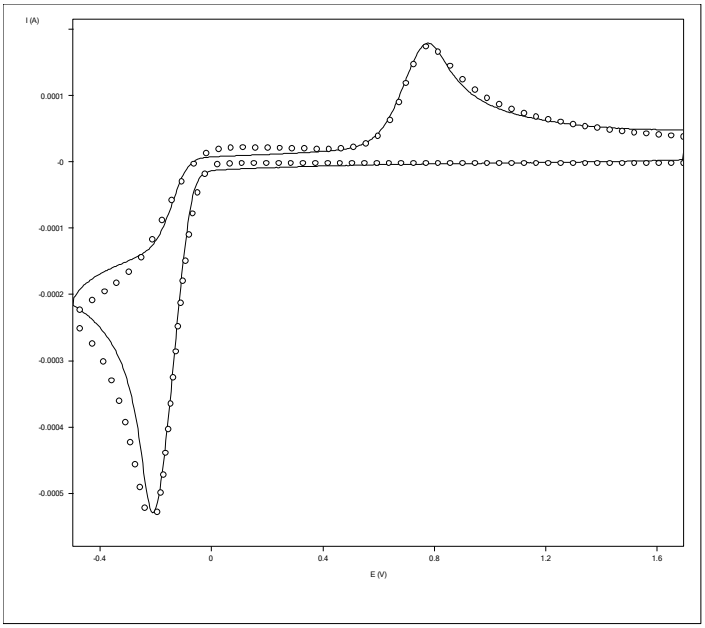

Figure 4.3 Representative fit of experimental (−) and theoretical (◦◦◦◦) CVs for **3** using the $E_1C_2E_2C_2$, mechanism. Full sets of fits are in A.29, A.31 and A.33

Values for the heterogenous charge transfer rate constants k_s and chemical reaction rate constants k_f were all determined from fitting CVs that were obtained at three different concentrations measured over a scan rate range of 0.05-2.0 Vs^{-1} and these resulted in estimates of 2 (1) $\times 10^{-2}$

cm/s, 7 (6) $\times 10^{-4}$ cm/s, 4.5 (3) $\times 10^{8}$ s^{-1} and 91 (27) s^{-1} for k_{s1}, k_{s2}, k_{f1}, and k_{f2}, respectively (Table 4.5). Optimized diffusion coefficient D values yielded 1.06 $\times$ 10^{-5} cm^2/s for the Cat and Rad while 8.73 $\times$ 10^{-6} cm^2/s was the result for the two dimeric species (Table 4.6). These optimised D values satisfy the $1e^-$ transfer reactions (Table 3.13).

Table 4.5 Parameters used for the CV simulation based on the $E_1C_2E_2C_2$, mechanism [a,b]

Compd	E_1^{0c}	E_2^{0c}	k_{s1} cm/s	k_{s2} cm/s	k_{f1} s^{-1}	k_{f2} s^{-1}
3	-0.39(6)	0.39(6)	0.02 (1)	7.2 (6))$\times 10^{-4}$	4.5(3) $\times 10^{8}$	91(27)
1	-0.91	-0.31	3.31×10^{-2}	3.63×10^{-3}	7.2×10^{9}	2.6×10^{9}
14						

[a] k_s values were obtained from the average of optimized k_s values obtained for each concentration of the E_1E_2C (Eqns. 4.5-4.8). K_{eq1} and K_{eq2} values of **3** were kept at 10^8 and $1.92(7)\times 10^5$ to get reasonable fit., K_{eq1} and K_{eq2} values of **1** were kept at 10^{10} and 1.81 to get reasonable fit. [c] Potentials (E_1^0 and E_2^0) were obtained from the mean and standard deviation of potentials in table 4.4.

Table 4.6 Diffusion coefficient values from the optimization of $E_1C_2E_2C_2$, model[a]

	Diffusion coefficient D cm^2/s			
Compound	Cation	Radical	Dimer	$Dimer^+$
3	1.06×10^{-5}	1.06×10^{-5}	8.73×10^{-6}	8.73×10^{-6}
1	6.52×10^{-5}	6.52×10^{-5}	3.19×10^{-7}	3.19×10^{-7}
14				

[a] Values were obtained on optimization using DigiElch

The formation of the dimer (Eqn. 4.6) is a result of the combination of two SOMOs of degenerate energies to form a stable "pancake" dimer with paired electrons in the lower energy level (Scheme 4.2). The removal of an electron from one of the two SOMOs of the dimer to form the Dim^+ results in the loss of degeneracy leaving behind a much weaker bonded MO (Eqn. 4.7). It is presumed that the much reduced bond energy of the unstable Dim^+ is high enough to favour its dissociation into the neutral radical and cation (Scheme 4.2).

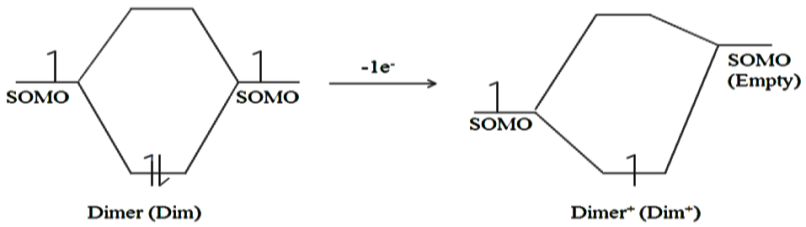

Scheme 4.2 Oxidation of Dimer MO to form $Dimer^+$ MO

The E^0 values of $E_1C_2E_2C_{2'}$ mechanisms are well spread out with peak separation of 0.60 and 0.78 V for **3** and **1,** respectively, as calculated from $E_2^0 - E_1^0$ (Table 4.5). These are indications that the reduction of the cation represents the first process while the oxidation processes represents the oxidation of the dimer radical to dimer cation. In the course of the electron transfer reaction, the neutral species formed therein had undergone some structural changes which to an extent agree with the electrochemical and chemical irriversibilities as seen from the simulation parameters. The much smaller oxidation processes are assumed to be as a result of the chemical irreversibility that aligns with high K_{eq} that result from high k_f and low k_b.

4.2.3 Application of Models to Simulation of CVs of 1.

The simulated cyclic voltammograms obtained for the redox processes of **1** over a scan rate range of 0.1-2.0 Vs^{-1} at a concentration of 3.13 mM gave products that were in accordance with E_1E_2C (Eqns. 4.2-4.4) and $E_1C_2E_2C_{2'}$ (Eqns. 4.5-4.8) mechanisms just as in **3**. In the E_1E_2C mechanisms, there are slight differences of its parameters (optimized and unoptimized) in comparison to those of **3**. For instance, the E^0 values of **1** -0.71 and -0.81 V (Table 4.2) shifted more into the negative region of the redox window compared to those of **3** [-0.03(1) and -0.11(4) V]. This is not unexpected as it is the outcome of the electron donor influence of diethylamino substituents on the 1,2,4-dithiazolium ring compared to the phenyl substituent.

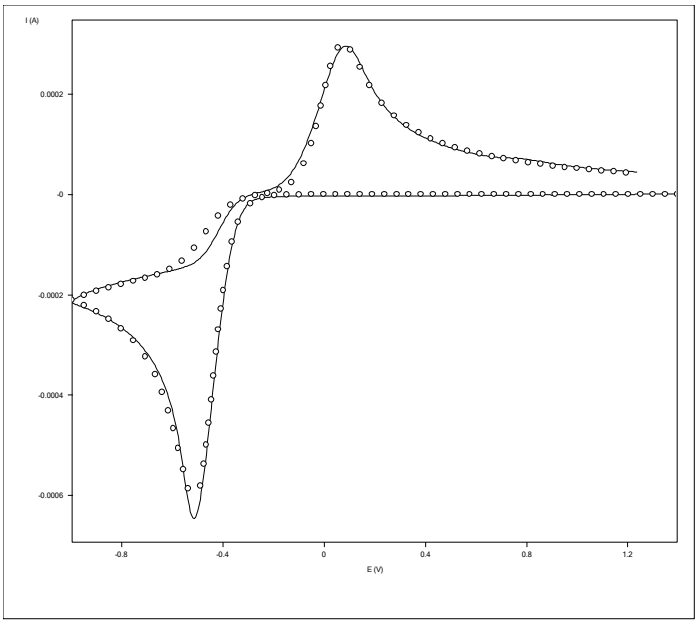

Figure 4.4 Representative fit of experimental (−) and theoretical (◦◦◦◦) CVs for **1** using the E_1E_2C mechanism. See details in A.34.

The optimization of parameters in order to get a reasonable fit between the experimental and simulated CVs (Fig. 4.4) resulted in a K_{eq} value of ≈ 12,000 (Table A.37) which is high enough to shift equilibrium to the right resulting in the rapid consumption of the electroinactive closed anion. Thus, it is merely providing a less energetic route for the interconversion of the closed An to OpenAn $\mathbf{1}^-$. Estimated values of the optimized parameters are $k_{s1} = 4\times10^{-4}$ cm/s, $k_{s2} = 2\times10^{-2}$ cm/s, and $K_{eq} = 1\times10^{4}$ (Table 4.2). Optimization of D carried out just as in **3** resulted in 1.82×10^{-5} cm^2/s for all the participating species (Table 4.3). It is noteworthy to mention that Hartung's[8] prediction of a direct $2e^-$ transfer reaction followed by a chemical step is close to our postulate of a sequential closely-spaced two $1e^-$ transfer processes followed by a chemical step from digital simulation of the experimental CVs.

The alternative mechanism for the CVs of **1** is still the $E_1C_2E_2C_2$, (Eqns. 4.5-4.8**)** and it has the same definition and simulation procedure as **3**. For the 3.13 mM concentration considered for this mechanism, the redox potential of the second reduction process is positive of that of the first by 0.60 V (Table 4.5) leading to the observation of two one-electron reduction process. The

only difference between these potentials and the E^0s for **3** is that the E^0s in **3** are less negative compared to those of **1** pointing at generation of more stable neutral radicals in **3** than in **1 (**though they weren't stable enough for detection via SEEPR on the time scale of the experiment).

In order to extract with parameters that justify the "square scheme" mechanism, K_{eq1} and K_{eq2} were fixed at 10^{10} and a very low 1.81, respectively, making the k_f and k_b (for the second chemical step) close enough to make the chemical process reversible over all the scan rates investigated (Table 4.5). Estimates for the optimized parameters are k_{s1} = 3.31×10^{-2} cm/s, k_{s2} = 3.63×10^{-3} cm/s, and k_{f1} = 7.2×10^{9} s^{-1} and k_{f2} = 2.6×10^{9} s^{-1} (Table 4.5). The optimization resulted in D values of 6.52×10^{-5} cm^2/s for Cat and Rad while Dim^+ and Dim had 3.19×10^{-7} cm^2/s (Table 4.6). The formation of Dim^+ from Dim follows the same pattern as **3 (**Scheme 4.2**)**.

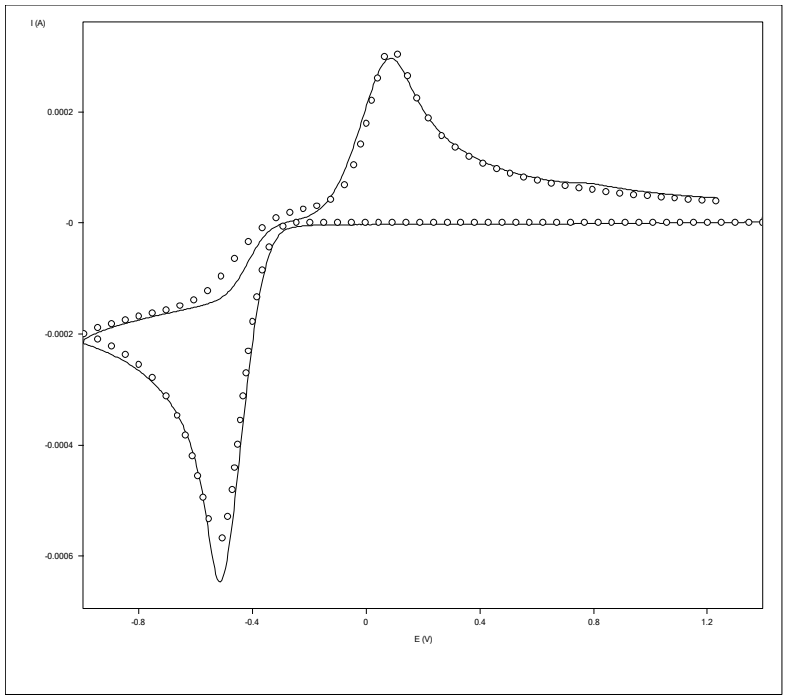

Figure 4.5 Representative fit of experimental (−) and theoretical (◦◦◦◦) CVs for **1** using the $E_1C_2E_2C_2$, mechanism. See details in A.35.

4.2.4 Application of Models to Simulation of CVs of 14.

The simulated CVs obtained for the redox couples of **14** at a scan rate range of 0.05-2.0

Vs^{-1} over three concentrations of 2.97 mM, 5.95 mM, and 10.02 mM were all in agreement with the earlier discussed E_1E_2C and $E_1C_1E_2C_2$ mechanisms. All the CV behaviour are quite similar to those of **3** and **1** except for few discrepancies that are worthy of discussion.

In the E_1E_2C mechanism, the average E^0 values of -0.95 (1) and -1.05 (1) in 2.97 mM, 5.95 mM, and 10.02 mM (Table 4.1) respectively are tuned most into the negative region of the redox window compared to **3** and **1** reflecting the stronger π-electron donor influence of the dimethylamino substituents compared to aryl or diethylamino on the dithiazolium ring. The average K_{eq} value of ≈ 10,700 (Table A.37) is enough to shift equilibrium to the right thus providing a much less energy for the interconversion of the close anion to the open anion **14**$^-$. Estimated values of the optimized parameters to obtain a reasonably good fit between simulated and experimental CVs (Fig. 4.6) are k_{s1} = 4 (4) $\times 10^{-3}$ cm/s, k_{s2} = 4 (6) $\times 10^{-3}$ cm/s, and K_{eq} = 1 (4) $\times 10^4$ (Table 4.2). D on optimization just as in **3** and **1** equals 1.46 $\times$ 10^{-5} cm^2/s (Table 4.3).

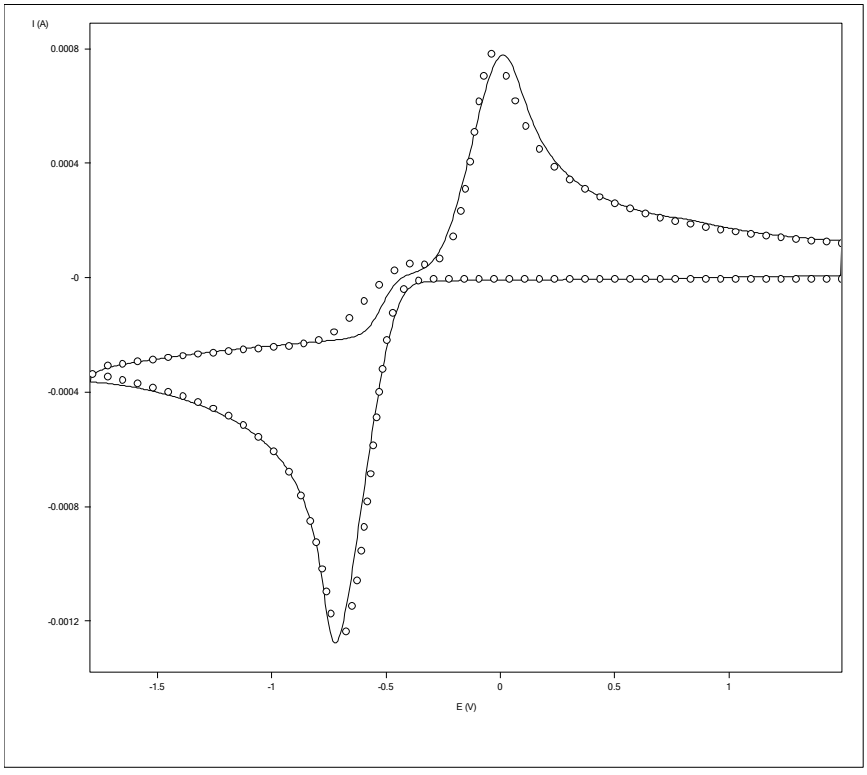

Figure 4.6 Representative fit of experimental (−) and theoretical (◦◦◦◦)CVs for **3** using the E_1E_2C mechanism. See details in A.36, A.37, and A.38.

4.3 Correlation of CV simulation and SEEPR experiments

It is recalled from Section 3.4 of this thesis that the reduction of **3**, **1**, and **14** in a spectroelectrochemical cell in CH_3CN and CH_2Cl_2 (0.1 M $^{n}Bu_4NPF_6$ and 0.4 M $^{n}Bu_4NPF_6$) respectively at room temperature $(19 \pm 2)℃$ and at ambient temperatures gave no EPR signals (non-detection of neutral radicals). This was also the case when the controlled electrolysis was carried out on the cathodic peaks with adjustment by $\approx \pm 0.01$ V of the experimental cathodic peak potentials observed from cyclic voltammetry experiments. This, we presumed, was due to short life times of the radicals or their inabilities to form stable neutral radicals. More light has been shed on this from the outcome of the simulation of the experimental CVs.

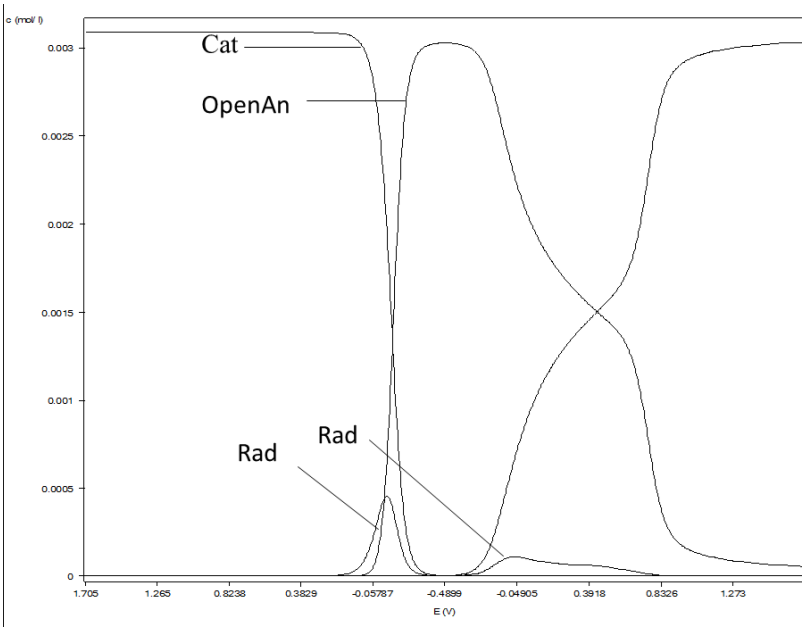

Figure 4.7a Concentration profiles for E_1E_2C and mechanism showing concentration of analyte adjacent electrode surface w.r.t. potentials.

From a detailed study of the concentration profiles of the two mechanisms obtained from DigiElch using a potential window that covers both reduction and offset oxidation couples (Fig. 4.7-4.9), the focus was on the concentrations of the species adjacent to the electrode surface (in the reaction and diffusion layers) with respect to distance (x) of the analyte (Fig. 4.8-4.9) under consideration (DTAs) and potentials (E) at which the processes occur (Fig. 4.7a-4.7b).

Though, merely looking at the details of the simulation from the two mechanisms proposed for the CVs, it is justified to conclude that the neutral radicals were very short-lived as a result of their rapid consumption in the electron transfers and follow-up chemical steps (Eqns. 4.2-4.8). On the other hand, on careful inspection of the potentials at which they were formed (Fig. 4.7), it was evident that very insignificant quantity of the neutral radicals formed at the electrode surface. For example, the E_1E_2C mechanism revealed that scans through the potential windows recorded low concentrations of the neutral radicals with ≈ 4.5 and 1.0×10^{-4} mol/L at potentials of -0.14 and -0.10 V, respectively (Fig 4.7b) while the $E_1C_2E_2C_2$, mechanism recorded much lower concentrations of ≈ 8.5 and 3.5×10^{-5} mol/L at potentials of -0.19 and -0.24 V, respectively, (Fig. 4.7b).

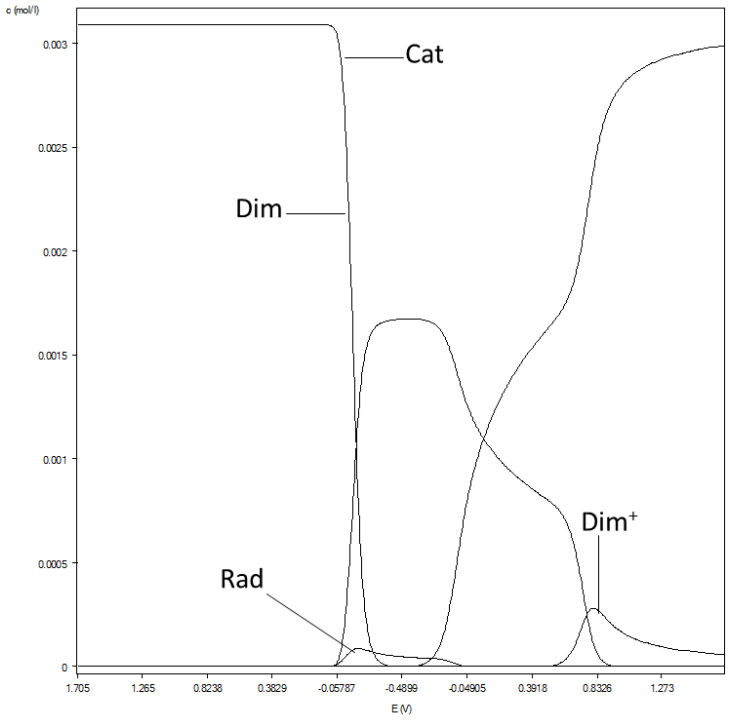

Figure 4.7b Concentration profiles for $E_1C_2E_2C_2$, mechanism showing concentration of analyte adjacent electrode surface w.r.t. potentials.

These concentrations which were constant for all the scans through the potential windows considered for the simulation were so small that they would go undetected in the SEEPR experiments. It is expected that radical concentrations of about 10^{-6} mol L^{-1} give highly intensed

EPR signals while the detection limits range from 10^{-6} to 10^{-9} mol L^{-1}.[9]Though, the concentrations from the simulations are higher than 10^{-6} mol L^{-1} but it is noteworthy that these concentrations sometimes do not reflect the real experimental values but give clues to what is happening during the experiment.

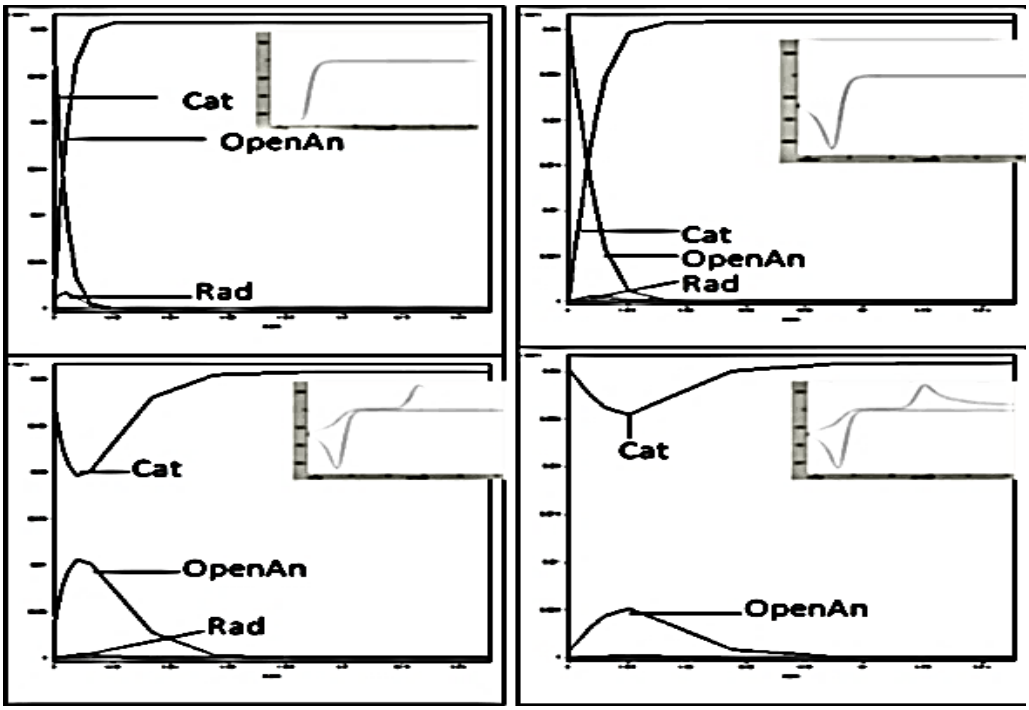

Figure 4.8 Concentration profiles for E_1E_2C mechanism showing concentration of analyte adjacent electrode surface w.r.t distance of analyte (x) from electrode surface.

As expected, the concentrations of the Cat species were high at the beginning of the forward scans and got depleted at the end of the forward scans. The concentrations gradually increased as the return processes approached and reached maximum at the end of the processes (Fig. 4.7-4.9**)**. In the E_1E_2C mechanism, the open anions were dominant at the beginning of the reduction processes and began to drop at the beginning of the offset oxidation process to a non-zero concentration (Fig. 4.8). The dimer concentration in the $E_1C_2E_2C_2$, mechanism was equally dominant through the forward scans and began to drop as it began the second process to a non-zero concentration (Fig. 4.9). A much smaller concentration of Dim^+ appeared at the start of the

second (offset-oxidation) processes and dropped to a very low but non-zero concentration at the end of the processes (Fig. 4.9) presumably owing to its earlier discussed instability.

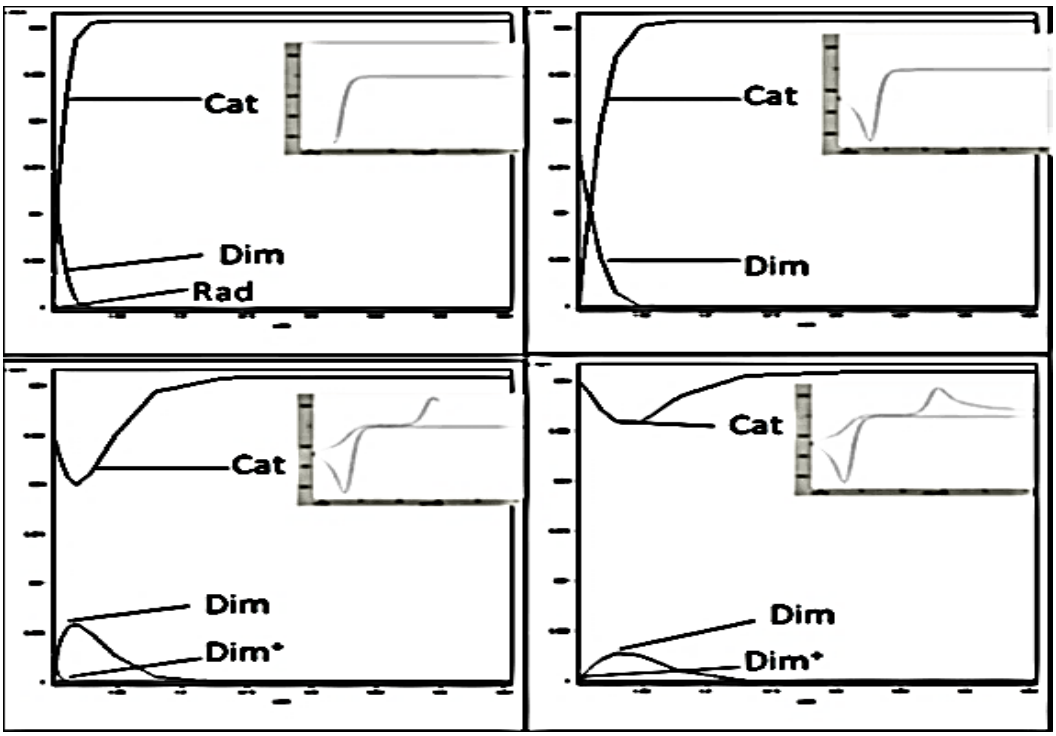

Figure 4.9 Concentration profiles for $E_1C_2E_2C_2$, mechanism showing concentration of analyte adjacent electrode surface w.r.t distance of analyte (x) from electrode surface.

4.4 Correlation of Redox Potentials with Gas Phase calculations

Data obtained from quantum calculations have been used to strengthen experimental electrochemical results.[10] DFT and ab initio methods have been explored in determining the most accurate molecular geometries for many heterocyclic compounds including C, N, S and binary S, N radicals. All calculations were carried out using the B3LYP, RB3LYP and UB3LYP functionals in conjunction with 6-31+G(2dp), 6-31+G(dp) and 6-31++G(3dfpd) basis sets due to the medium-sized nature of 1,2,4-dithiazolyl systems. Full geometry optimized calculations at the aforementioned levels of theory were performed on the cation, neutral and anion species of 1,2,4-dithiazolium derivatives coupled with the dianion of **3** and **14**. The energies of these optimized molecules were then used to define the theoretical redox reactions.

$$0/+1 \text{ process: } E_{cation} - E_{radical} = E_{oxidation}$$

-1/0 process: $E_{anion} - E_{radical} = E_{reduction}$

The calculated geometries of the triad of redox states were established to be local minima on the potential energy surface through full frequency calculations. The only exception was the full frequency calculation on the flat cation of **3** which gave an imaginary frequency indicative of saddle points between the degenerate ground states in the C1 point group. Moreover, full frequency calculations on the twisted cation and radicals of **3** gave a slightly lower energy compared to their flat counterparts. Relative to the twisted cation, the anion is the most stable followed by the neutral and dianion species respectively. A compilation of their energies coupled with those of **1** and **14** were used in deriving their $E_{oxidation}$ and $E_{reduction}$.

It was reported in Tables 3.4-3.6 and Figures 3.23-3.25 that kinetically controlled potentials vary with scan rates. With emphasis on the very slow electron transfer reactions that form the basis of the formation of the open anions and dimer species, the experimental potentials obtained in the limit of slow scanning (extrapolation to 0 mV/s) are reported herein with gas phase calculated potentials (Table 4.7).

Table 4.7 Calculated and Experimental 1st Reduction and Oxidation potentials of 3^+, 1^+, and 14^+.

Comp	3^+		1^+		14^+	
	Exp.	Calc.	Exp.	Calc.	Exp.	Calc.
1st Reduction (V)	-0.18	5.86	-0.40	5.23	-0.58	5.42
Oxidation (V)	0.63	-2.23	-0.74	-2.64	-0.65	-1.95
Cell Potential (V)[a]	0.81	8.09	0.34	7.87	0.07	7.37

[a] Cell potential = /1st Reduction - Oxidation/

It is expected that the ease with which electrons are added to **3^+, 1^+, and 14^+** should be dependent on the energy of the LUMO of the cationic species obtained from DFT calculations (Table 4.8 and Figure 4.11). Therefore, a plot of the LUMO energies versus the experimental potentials was obtained. A good correlation was obtained between them as shown in Figure 4.10 below.

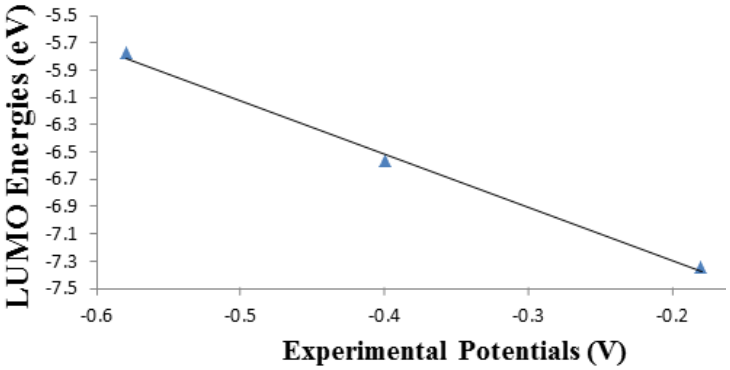

Figure 4.10 Plots of experimental potentials vs LUMO energies of $\mathbf{3}^{+}$, $\mathbf{1}^{+}$, and $\mathbf{14}^{+}$ as measured by cyclic voltammetry and DFT respectively (R = 0.998).

4.5 Conclusion

This chapter puts forward two models that offer sufficient reasons to why the shapes of the CVs of **3**, **1**, and **14** had longer processes in the forward scans than in the reverse scans. It also reasonably explains the factors responsible for the non-detection of neutral radicals via SEEPR experiments. One last question that deserves answers is "which of the two models better describes the behaviour of the CVs of $\mathbf{3}^{+}$, $\mathbf{1}^{+}$ and $\mathbf{14}^{+}$"? I hope to answer this question by investigating the "energy requirements" and "extent of fit between experimental and theoretical CVs" of the two models.

Table 4.8 Calculated energies of molecular orbitals of DTAs in eV[a]

Energy (eV)	3	1	14
LUMO+1	-	-5.81	-5.46
LUMO	-7.35	-6.57	-5.78
HOMO	-10.61	-10.57	-10.58
HOMO-1	-	-10.72	-10.96
HOMO-LUMO	3.26	4.00	4.80
LUMO+1 - LUMO	-	0.76	0.32

[a] Computed from Gaussian W03 package.

Table 4.9 Calculated energies for twisted 3^+ in eV[a]

LUMO+1 (eV)	LUMO (eV)	HOMO (eV)	HOMO-1 (eV)
-5.82	-7.23	-10.63	-10.79
	HOMO-LUMO (eV)	3.40	
	LUMO+1 – LUMO (eV)	1.41	

[a] Computed from Gaussian W03 package.

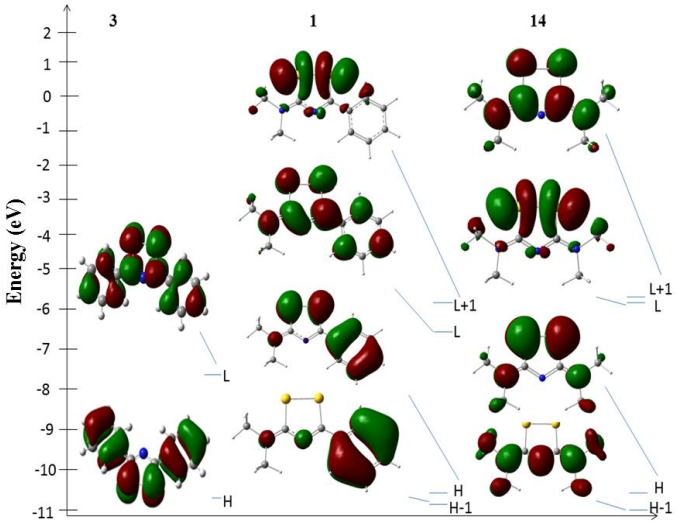

Figure 4.11 Molecular energy level diagrams for DTAs **3^+, 1^+, and 14^+**. H=HOMO and L=LUMO.

For the two models, it is of great importance to consider the nature of the orbitals involved in order to have the formation of the open anion and dimer. There are three major orbitals to be considered here; HOMO, LUMO and LUMO+1 (Fig.4.11). The LUMOs in **3** and **1** have π* character while that of **14** is σ*. The LUMOs+1 have σ* character in **3** and **1** while they are π* in **14**. It is also noticed that the HOMOs for **3**, **1**, and **14** all have π* character which somewhat explains the weakness of the S-S bonds even before the rings gain electrons. This is quite different from the HOMOs of 1,2,3,5-dithiadiazolyls[11-13] which possess π bonding character. Therefore the S-S bonds in 1,2,4-dithiazolylium rings are likely to be weaker than those in azoles

such as 1,2-dithiolane (C_3S_2). This reasonably explains why the addition of two electrons to the ring system (occupation of LUMOs) favours the lowest energy open anion structure in the gas phase at 0 K. The occupation of π* and σ* LUMOs of **3**, **1**, and **14** produce ring systems with additional antibonding character and the overall antibonding character is enough to induce ring opening even without populating σ* LUMO+1 **3** (Fig. 4.12) and **1** or π* LUMO+1 (**14**). Based on the antibonding of the LUMOs of **3**, **1**, and **14,** it is practicable to add an electron and still have the ring "closed". The S-S bonds open up while still retaining the planarity of the neutral radicals. However, the addition of a second electron into the LUMO whether π* or σ* (populated) lead to a preference for the open anion structure. Generally, putting electrons into the antibonding LUMOs especially for **3** and **1** "spontaneously" result in the opening of the ring to a twist structure while minimizing the anion geometry. For **14**, whose σ* LUMO shares a small band gap with LUMO+1 (1,2,3,5-dithiadiazolyls have small LUMO+1 – LUMO gap too)[11-13] will definitely undergo ring opening on populating the LUMO.

For the dimer models ($E_1C_2E_2C_{2'}$ mechanism), two possibilities are considered. First, **3** and **1** that possess π* orbitals (LUMO) will tend to form dimers via p orbitals of strong C-C bonds on adjacent rings. The result is a strongly distorted C-C π-dimer. Second, **14** which has a σ* character has the likelihood to form a disulphide structure which is common for S-S dimerized thiazyl radicals.[14-15]

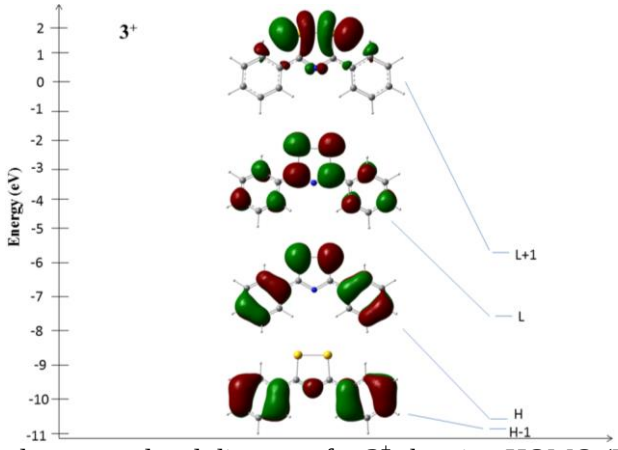

Figure 4.12 Molecular energy level diagrams for $\mathbf{3}^+$ showing HOMO (H) and LUMO (L).

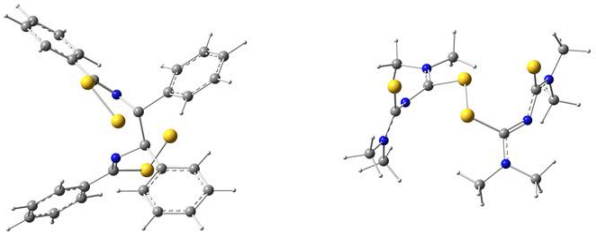

Figure 4.13 (Left) π-dimer formed via C-C bond with opened S-S bond. (Right) σ-dimer formed via S atom with opened S-S bond.

In terms of fits between experimental and theoretical CVs, the dimer models seem to fit better than the open anion models (Figures A.28-A.39)

4.6 References

1. Rudolph, M.; Reddy, D. P.; Feldberg, S. W., *Anal. Chem.* **1994,** *66*, 589A-600A.
2. Bard, A. J.; Faulkner, L. R., *Electrochemical Methods; J. Wiley and Sons: New York* **1980**.
3. Bard, A. J.; Faulkner, L. R., *Electrochemical Methods: Fundamentals and Applications*. 2001.
4. Nicholson, R. S.; Shain, I., *Anal. Chem.* **1964,** *36*, 706-723.
5. Compton, R. G.; Banks, C. E., *Understanding Voltammetry*. Imperial College Press: 2011.
6. Bott, A. W., *Current Separations* **1999,** *18:1*, 9-16.
7. Boeré, R. T.; Chivers, T.; Roemmele, T. L.; Tuononen, H. M., *Inorg. Chem.* **2009,** *48*, 7294-7306.
8. Hartung, J.; Rosenbaum, K.; Beyer, L.; Losada, J.; Fernandez, V., *J. Prakt. Chem.* **1991,** *333*, 537-544.
9. Bunce, N. J., *J. Chem. Edu.* **1987,** *64*, 907.
10. Boeré, R. T.; Roemmele, T. L.; Yu, X., *Inorg. Chem.* **2011,** *50*, 5123-5136.
11. Boeré, R. T.; Moock, K. H.; Parvez, M., *Z. Anorg. Allg. Chem.* **1994,** *620*, 1589-1598.
12. Boere, R. T.; Moock, K. H., *J. Am Chem. Soc.* **1995,** *117*, 4755-4760.
13. Boeré, R. T.; Roemmele, T. L., *Coord. Chem. Rev.* **2000,** *210*, 369-445.
14. Hicks, R., *Stable Radicals: Fundamentals and Applied Aspects of Odd-Electron Compounds*. Wiley: 2011.
15. Hicks, R. G., *Nat Chem* **2011,** *3*, 189-191.

Chapter five

5.1 Attempted Synthesis of trans-4,4'-dipyridylethylene (29)

The initial goal for preparing **29** was to utilize the terminal pyridine donors as bridging ligands on 1,3,2- dithiazole moieties in the synthesis of metal organic frameworks (MOFs) and cage complexes (Scheme 5.1). Focus on MOFs and cage complexes have attracted considerable interests because of their fascinating varieties of structural and molecular features[1-2] and the applicability of their porosities in the area of separation,[3] gas storage,[4] drug delivery,[5] and catalysis.[6]

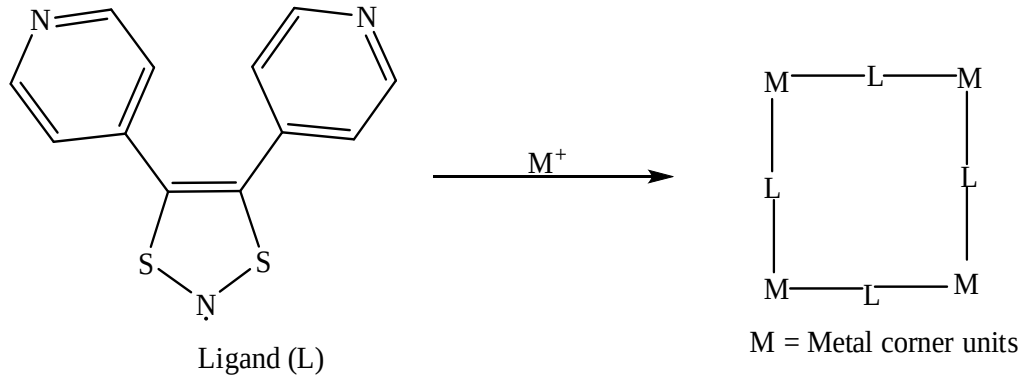

Scheme 5.1 Formation of MOFs and cages from 1,3,2-dithiazole ligand rings

5.2 Background

Crystal structures of rigid organic ligands containing two pyridine rings separated by one acetylene spacer have been studied via various applications in crystal engineering and supramolecular chemistry. It was utilized as an organic component in the formation of solid-state sulfa drug sulfadiazine (SDZ) co-crystals and salts employed in drug delivery and pharmaceutics.[7] Solution and solid-state discrete metallosupramolecular structures were made in stoichiometrically controlled fashion from the combination of **29** with heteroleptic complexation designs. Density functional theory (DFT) calculations were used to interpret structural information of these compounds.[8] Supramolecular silanol inclusion complexes as well as the peculiar stoichiometrically controlled co-crystalline motifs were synthesized via the interaction of **29**'s sp-carbon with the sulphur S of a fused 1,3-dithiole ring system.[9] It possesses sp^2-C-H•••N

hydrogen bonds that are crucial to the synthesis of discrete molecular complexes and 1D and 2D bimolecular networks.[10] Infinite, face-to-face, π-stacked solid-state supramolecular architectures were synthesized from the ligand of **29** and their stereochemical features were used as determinants for conducting, reactivity and crystalline properties.[11] Rigid ligands of **29** are used to synthesize solid-state crystalline complexes whose hydrogen bonds are connected to their electronic properties thus enabling them function in switchable devices.[12] Functional supramolecular architectures with potential applications as catalytic or molecular sieves were prepared from the ligands of **29** (Ciani & Proserpio, 1998).[13]

5.3 Results and discussion

The titled compound (**29**, Figure 5.1) was first prepared Tanner & Ludi (1980)[14] but we re-prepared it in the Boéré lab with slight synthetic modifications. It piqued our interest because of its unique unchanging bond angles and distances around and along the symmetrical C≡C bond and also due to the various literatures where they were reported as co-crystals. **29** crystallizes in the Fddd space group with 8 molecules per unit cell and sits on a special position with 222 site symmetry fitting the unique one-quarter of the molecule into the asymmetric unit.

In the structure of the title compound $C_{12}H_8N_2$, the pyridyl ring substituents C_5H_5N adopt an almost planar molecular geometry with bond angles of 121.13 (1) ˚ and 58.87 (7) ˚.

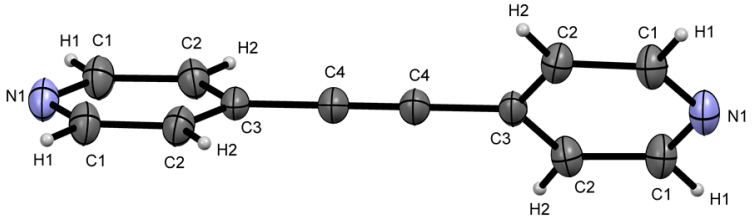

Figure 5.1 Molecular structure of **29** as found in the crystal lattice (displacement ellipsoids drawn at 50% probability)

In the crystal lattice of **29**, the N1-C1-C2-C3-C4-C4 planes are aligned parallel to one another while the opposite and symmetrical N1-C1-C2-C3 plane is inverted in successive lattices (Figure 5.3). These arrangements are all connected to form pairs via short intermolecular donor-

hydrogen N···H contacts of 2.472 (7) Å (Figure 5.2) and acceptor-hydrogen C-H bonds of 0.950 (1). This N•••H contact is longer than N•••H contacts reported for most discrete supramolecules having **29** as guest molecules except for that of 1,4-bis(4-pyridyl)butadiyne which is larger (2.551 Å).[15]The molecules are packed in such a manner that the pyridyl rings protrude at opposite ends of the cell axis. It possesses a C4-C4' bond distance of 1.189 (2) Å and a N•••H - C hydrogen bond angle of 159.42 (7) ˚ which is an indication of the level of tilt experienced by the pyridyl ring. One of the two pyridyl rings is twisted relative to the other by 58.87˚ to the plane of the pyridyl-C ≡ C bond; a phenomenon associated with the limited degree of conformational mobility in the molecule except for the rotation about the C2-C3 bond which rules out the possibility of it forming a polymeric solid. The angle is between 173.2 ˚ for sp-C-H•••N and 175.60 ˚ for sp^2-C-H•••N though it is higher than 147.41 ˚ reported for 1,4-bis(4-pyridyl)butadiyne whose lower value could be attributed to extensive conjugation.[15]

Figure 5.2 A view of **29** plotted with displacements ellipsoids drawn at the 50% probability level showing the N-H contacts.

Similar structures to **29 (29a, 29b, 29c and 29d)** have been reported by Neogi et al. (2012),[16] Zaman et al. (2000),[17] Dong et al. (1999)[18] and Dong et al. (1999)[19].

In the four structures, the trigonal planar angles on the two sides of the C≡C bonds are all the same within the limit of experimental error based on the 99% confidence level for the titled compounds and the four similar compounds; [58.87 (7)/ 121.13 (1) ˚]**, 29a** [58.79 (2)/120.99 (3), 58.71 (2)/ 120.22 (3) ˚]**, 29b** [59.09 (3)/ 121.01 (5), 59.19 (3)/ 121.18 (5)˚], **29c** [58.91 (3)/120.12 (4), 58.71 (3)/ 120.75 (4), 58.66 (3)/120.12 (4), 58.91 (3)/121.02 (5), 58.71 (3)/ 121.63 (5)˚] and **29d** [59.63 (6)/ 121.22 (9), 59.08 (6)/ 120.08 (9), 59.07 (6)/121.81 (9), 59.12 (6)/120.78 (9)].

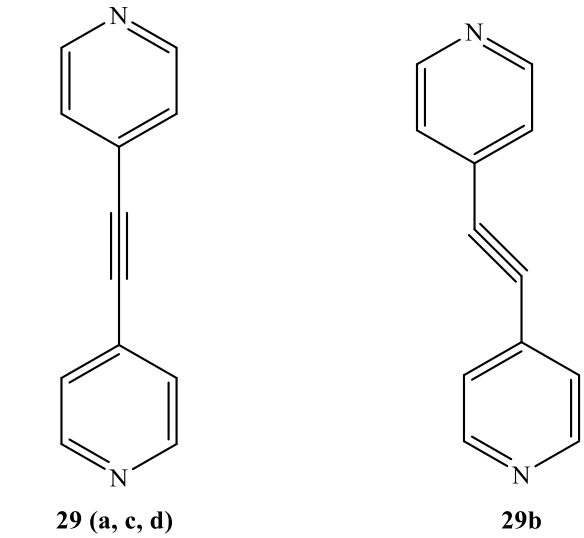

Figure 5.3 A view of **29** plotted with displacements ellipsoids drawn at the 50% probability level showing the N1-C1-C2-C3-C4-C4 planes aligned parallel to one another with the opposite and symmetrical N1-C1-C2-C3 plane being inverted in successive lattices.

Also, the C≡C bonds in **29c** and **29d** possess no short contacts from or to the sp hybridized C atoms. Apart from being similar to **30** in terms of having no short contacts, the C≡C bond distances of **29c** [1.188 (5), 1.188 (5), 1.182 (9) Å] agree with that of **29** [1.189 (2) Å] within the 99% confidence level while those of **29d** [1.173 (1), 1.173 (1), 1.178 (2) Å] dropped out significantly from the 99% confidence level . **29a** and **29b** on the other hand had one and two contacts on their sp hybridized C atoms, respectively, and these resulted in a significantly higher C≡C bond distance for the former [1.199 (5) Å though still within the experimental error limit] while that of the latter [1.186 (8) Å] was in agreement with that of **29**.

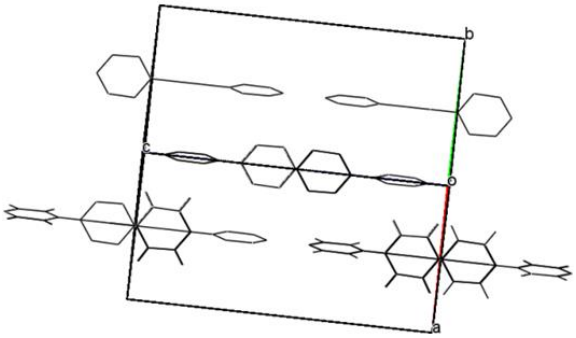

Figure 5.4 Packing pattern (viewed from b axis) showing parallel N1-C1-C2-C3-C4-C4 planes coupled with opposite and symmetrical N1-C1-C2-C3 plane being inverted in successive lattices.

5.4 References

1. Robin, A. Y.; Fromm, K. M., *Coord. Chem. Rev.* **2006,** *250*, 2127-2157.

2. Hill, R. J.; Long, D.-L.; Champness, N. R.; Hubberstey, P.; Schröder, M., *Acc. Chem. Res.* **2005,** *38*, 335-348.

3. Choi, H. J.; Suh, M. P., *J. Am Chem. Soc.* **2004,** *126*, 15844-15851.

4. Yang, S.; Lin, X.; Blake, A. J.; Thomas, K. M.; Hubberstey, P.; Champness, N. R.; Schroder, M., *Chem. Commun.* **2008,** 6108-6110.

5. Horcajada, P.; Serre, C.; Maurin, G.; Ramsahye, N. A.; Balas, F.; Vallet-Regí, M.; Sebban, M.; Taulelle, F.; Férey, G., *J. Am Chem. Soc.* **2008,** *130*, 6774-6780.

6. Kumagai, H.; Akita-Tanaka, M.; Inoue, K.; Kurmoo, M., *J. Mater. Chem.* **2001,** *11*, 2146-2151.

7. Elacqua, E.; Bučar, D.-K.; Henry, R. F.; Zhang, G. G. Z.; MacGillivray, L. R., *Cryst. Growth. Des.* **2012,** *13*, 393-403.

8. Neogi, S.; Lorenz, Y.; Engeser, M.; Samanta, D.; Schmittel, M., *Inorg. Chem.* **2013,** *52*, 6975-6984.

9. Beckmann, J.; Jänicke, S. L., *Eur. J. Inorg. Chem.* **2006,** *2006*, 3309-3309.

10. Dias, S. I. G.; Rabaca, S.; Santos, I. C.; Wallis, J. D.; Almeida, M., *CrystEngComm* **2010,** *12*, 3397-3400.

11. Sokolov, A. N.; Friščić, T.; Blais, S.; Ripmeester, J. A.; MacGillivray, L. R., *Cryst. Growth. Des.* **2006,** *6*, 2427-2428.

12. Zaman, M. B.; Tomura, M.; Yamashita, Y., *J. Org. Chem.* **2001,** *66*, 5987-5995.

13. Carlucci, L.; Ciani, G.; M. Proserpio, D., *Chem. Commun.* **1999,** 449-450.

14. Tanner, M.; Ludi, A., *Chimica* **1980,** *34*, 23-24.

15. Allan, J. R.; Barrow, M. J.; Beaumont, P. C.; Macindoe, L. A.; Milburn, G. H. W.; Werninck, A. R., *Inorg. Chim. Acta* **1998,** *148*, 85-90.

16. Neogi, S.; Schnakenburg, G.; Lorenz, Y.; Engeser, M.; Schmittel, M., *Inorg. Chem.* **2012,** *51*, 10832-10841.

17. Zaman, M. B.; Tomura, M.; Yamashita, Y., *Org. Letts* **2000,** *2*, 273-275.

18. Dong, Y.-B.; Layland, R. C.; Pschirer, N. G.; Smith, M. D.; Bunz, U. H. F.; zur Loye, H.-C., *Chem. Mater.* **1999,** *11*, 1413-1415.

19. Dong, Y.-B.; Layland, R. C.; Smith, M. D.; Pschirer, N. G.; Bunz, U. H. F.; zur Loye, H.-C., *Inorg. Chem.* **1999,** *38*, 3056-3060.

Chapter six

Experimental

6.1 General methods

6.1.1 Cyclic voltammetry

Dichloromethane CH_2Cl_2 and acetonitrile of BDH reagent grades were distilled in order to purify them. Acetonitrile was first distilled over P_2O_5 and then over CaH_2 while CH_2Cl_2 was purified by distilling it over CaH_2. Both solvents were purged with dry nitrogen before use. Electrochemical grade tetrabutylammonium hexafluorophosphate $[^nBu_4N][PF_6]$ (Fluka) was used as the supporting electrolyte and was kept in the desiccator.

Cyclic voltammograms (CVs) were obtained at room temperature 19 ± 2 ^oC in both acetonitrile and dichloromethane solvents containing 0.1 and 0.4 M $[^nBu_4N][PF_6]$ (Fluka), respectively, as the supporting electrolyte. These solvents were purged with dry nitrogen for 10-15 minutes before use and a blanket of argon gas covered the solutions during all experiments. The CVs were obtained using a computer-controlled potentiostat. The cell design uses the conventional three-electrode setup of working, reference and auxiliary electrodes. The working electrode is either a platinum or glassy carbon, the reference is a silver wire while the auxiliary is a platinum wire. The reference electrode was separated from the bulk solution by a fine porous frit. Initial background scans were carried out to determine the size of the electrochemical window. The CVs were obtained over scan rates of 50 – 20000 mV/s. The potentials reported versus the operative formal potential $E^{0/}_{Fc0/+}$ for the Fc^+/Fc redox couple (Fc = ferrocene), which was used as an internal standard. The working electrodes were polished with 0.05 micron alumina paste on a clean polishing surface, rinsed with distilled water and acetone, and dried with tissue paper before use and sometimes during experiments.

6.1.2 Computational details

Full geometry optimizations were performed at the B3LYP / 6-31G (dp), B3LYP 6-311++G3 (df,pd), and UB3LYP / 6-311++G3 (df,pd) levels of theory for the three redox states (cation, neutral and anion) of the compounds under study. The structures at the three redox states and two as dianion species were first optimized at the MM+ molecular mechanics force field level in Hyperchem Professional (molecular modeling system) and then transferred into the Gaussian program package GaussView 4.1.2 or GaussView 5.0.9 for the density functional theory (DFT) calculation set up. In most cases, the optimization was either done separately or combined with the frequency calculation at a time on the Gaussian W03 package. The results of the frequency calculations were used to correct the zero-point energies of all the species. Computational details such as molecular orbitals and geometrical structures from DFT calculations are compiled in the Appendix of this thesis.

6.1.3 Simulations of cyclic voltammetric responses

These were carried out using *DigiElch-Professional*, version 4.F (Build 3.008). The objective was to confirm that the suggested "EC" ($A + 2e \rightleftharpoons B$; $B \longrightarrow C$ (k_f)) and "EC_2" ($A + e \rightleftharpoons B$; $B + B \rightarrow B_2$ (k_f)) mechanisms were plausible explanations for the disappearance of the return peaks for the reduction processes and its eventual formation of strongly offset oxidation processes.[1]

6.1.4 Infrared Spectroscopy

IR spectra were obtained using the Bruker Alpha-P with diamond ATR modules via C-Opus software.

6.1.5 NMR spectroscopy

Spectra were acquired on a 300 MHz Bruker AVANCE II spectrometer and referenced relative to 0 ppm for tetramethylsilane (TMS) using deuterated chloroform, water or dimethyl sulphoxide (DMSO) as secondary reference.

6.1.6 Elemental analyses

These were carried out using an Elementar Americas Vario MicroCube instrument.

6.1.7 Mass spectroscopy

High resolution mass spectra were recorded at the Mass Spectrometry Facility, University of Lethbridge, Canada.

Table 6.1 Crystallographic Data and Refinement Parameters for **29**, **30**, **3b** and **14a**

Compounds	**29**	**30**	**3b**	**14a**
empirical formula	$C_6H_7IN_2S$	$C_{12}H_8N_2$	$C_{14}H_{10}Br_4FeNS_2$	$C_6H_{14}ClN_3OS_2$
M_r	266.10	180.20	631.84	243.77
Cryst size (mm^3)	0.31×0.23×0.18	0.34×0.17×0.11	0.22×0.13×0.07	0.378×0.105×0.078
cryst syst	Monoclinic	Orthorhombic	Monoclinic	Monoclinic
space group	*C*2/c	*Fddd*	$P2_1$/c	$P2_1$/c
a (Å)	18.7580(11)	9.5534(10)	10.6492(5)	8.2371(6)
b (Å)	7.7476(4)	12.6764(13)	11.4005(6)	19.1585(15)
c (Å)	24.1784(14)	15.8145(17)	15.8046(8)	7.0854(6)
α (deg)	90.00	90.00	90.00	90.00
β (deg)	101.1650(10)	90.00	96.4820(10)	100.9500(10)
γ (deg)	90.00	90.00	90.00	90.00
V ($Å^3$)	3447.3(3)	1915.2(3)	1906.51(17)	1097.79(15)
Z	16	8	4	4
D_c ($Mg·m^{-3}$)	2.051	1.250	2.201	1.475
μ (mm^{-1})	3.887	0.076	9.387	0.696
θ range	1.72-27.44	2.96-27.32	1.92-27.67	2.13-27.49
coll. reflns	19180	6353	27655	15062
obsd reflns	3923	542	4426	2522
no. of param	199	34	199	128
F(000)	2016	752	1196	512
T (K)	173(2)	173(2)	173(2)	173(2)
R1, wR2 [$I > \sigma 2(I)$]	0.0144, 0.0329	0.0360, 0.1061	0.0269, 0.0464	0.0233, 0.0571
R1, wR2 [all data]	0.0163, 0.0336	0.0432, 0.1128	0.0436, 0.0502	0.0292, 0.0602
GOF	1.075	1.121	1.019	1.070

[a] $wR2 = [\sum\{w (F_o^2 - F_c^2)^2\}/\sum w (F_o^2)^2]^{1/2}$; $R1 = \sum||F_o| - |F_c||/\sum|F_o|$. [b] $F_o > 4\sigma (F_o)$. [c] $GOF = [\sum\{w (F_o^2 - F_c^2)^2\}/(n - p)]^{1/2}$ where *n* = number of reflections and *p* = number of refined parameters.

6.1.8 Single Crystal X-Ray diffraction.

Selected crystals obtained via slow cooling method were mounted in Paratone™ on the ends of thin glass capillaries and cooled on the goniometer head to -100 °C with the Bruker low-temperature accessory attached to the APEX-II diffractometer. Mo Kα radiation (λ = 0.71073 Å) was used all through the diffraction experiment. Multi-scan absorption corrections were applied

to all the data sets and structures were solved using SHELX-M or SHELX-S, and refinements were conducted with full- matrix least-squares on F^2 using SHELXTL 6.14.[2] All hydrogen atoms were located on a difference map. C-bound H atoms were treated as riding, with C-H = 0.98 Å and U_{iso} = 1.5U_{eq} (C) for methyl, C-H = 1.00 Å and U_{iso} = 1.2U_{eq} (C) for methane, and C-H = 0.95 Å and U_{iso} = 1.2U_{eq} (C) for aromatic H atoms. Tables 6.1, 6.2 and 6.3 of crystallographic data and refinement parameters for compounds made during research in the Boeré lab are reported herein:

Table 6.2 Crystallographic Data and Refinement Parameters for **1**, **3**, **14** and **33**

Compounds	**1**	**3**	**14**	**33**
empirical formula	$C_{12}H_{15}ClN_2O_4S_2$	$C_{14}H_{10}ClNO_4S_2$	$C_6H_{12}F_6N_3PS_2$	$C_{12}H_{13}ClN_2O_5S_2$
M_r	350.83	355.80	335.28	364.81
Cryst size (mm^3)	0.462×0.11×0.088	0.236×0.068×0.021	0.41×0.06×0.02	0.23×0.14×0.08
cryst syst	Monoclinic	Monoclinic	Monoclinic	Orthorhombic
space group	$P2_1/n$	$P2_1/c$	$P2_1/c$	$P2_12_12_1$
a (Å)	7.4531(9)	8.9194(11)	9.344(3)	6.2825(5)
b (Å)	12.0752(15)	10.8047(14)	19.100(7)	12.7615(9)
c (Å)	17.090(2)	15.422(2)	7.383(3)	18.8809(14)
α (deg)	90.00	90.00	90.00	90.00
β (deg)	102.4960(10)	102.905(2)	101.815(5)	90.00
γ (deg)	90.00	90.00	90.00	90.00
V ($Å^3$)	1501.6(3)	1448.7(3)	1289.7(8)	1513.8(2)
Z	4	4	4	4
D_c ($Mg·m^{-3}$)	1.552	1.631	1.727	1.601
μ (mm^{-1})	0.548	0.568	0.595	0.552
θ range	2.08-27.51	2.32-27.76	2.13-26.45	1.93-27.69
coll. reflns	21613	20879	17204	22517
obsd reflns	3438	3375	2657	3543
no. of param	192	199	168	200
F(000)	728	728	680	752
T (K)	173(2)	173(2)	173(2)	173(2)
R1, wR2 [$I > \sigma 2(I)$]	0.0290, 0.0703	0.0679, 0.1461	0.1210, 0.2980	0.0403, 0.1060
R1, wR2 [all data]	0.0354, 0.0738	0.1561, 0.1840	0.2611, 0.3773	0.0499, 0.1102
GOF	1.036	1.001	1.042	1.048

[a] wR2 = $[\sum\{w (F_o^2 - F_c^2)^2\}/\sum w (F_o^2)^2]^{1/2}$; R1 = $\sum||F_o| - |F_c||/\sum|F_o|$. [b] $F_o > 4\sigma (F_o)$. [c] GOF = $[\sum\{w (F_o^2 - F_c^2)^2\}/(n - p)]^{1/2}$ where *n* = number of reflections and *p* = number of refined parameters.

Table 6.3 Crystallographic Data and Refinement Parameters for **3a**

Compound	**3a**
empirical formula	$C_{14}H_{10}I_3NS_2$
M_r	637.05
Cryst size (mm^3)	0.34×0.11×0.02
cryst syst	Orthorhombic
space group	Pbca
a (Å)	19.1157(14)
b (Å)	9.5849(7)
c (Å)	19.1625(14)
α (deg)	90.00
β (deg)	90.00
γ (deg)	90.00
V ($Å^3$)	3511.0(4)
Z	8
D_c ($Mg \cdot m^{-3}$)	2.410
μ (mm^{-1})	5.569
θ range	2.13-27.44
coll. reflns	41985
obsd reflns	4005
no. of param	181
F(000)	2336
T (K)	173(2)
R1, wR2 [$I > \sigma 2(I)$]	0.0288, 0.0637
R1, wR2 [all data]	0.0423, 0.0683
GOF	0.960

[a] wR2 = $[\sum\{w (F_o^2 - F_c^2)^2\}/\sum w (F_o^2)^2]^{1/2}$; R1 = $\sum||F_o| - |F_c||/\sum|F_o|$. [b] $F_o > 4\sigma (F_o)$. [c] GOF = $[\sum\{w (F_o^2 - F_c^2)^2\}/(n - p)]^{1/2}$ where *n* = number of reflections and *p* = number of refined parameters.

6.1.9 In Situ EPR Electrochemistry

In order to identify and characterize redox processes, detailed voltammetric and in situ EPR spectroelectrochemical investigations were carried out on target dithiazolium salts. Due to difficulties such as current-resistance (iR) drop along the volume of the solution and uncertainty in the control of the working electrode potential as a result of inadequate positioning of the reference electrode, electrochemical studies are usually performed separately from radical generation. This led to cell design that favour electrolysis inside an EPR resonant cavity.[3-6] This made electrochemists develop the concept of simultaneous electrochemical EPR (SEEPR)[7-8] by improving cell designs such that cyclic voltammograms can be measured in electrolytic cells within EPR cavities with a minimum amount of distortion.[9-10] Work in the Boere lab uses a cell

designed through the modification of a working electrode introduced by Neudeck and Kress.[11] This design makes use of a commercially available and optically transparent gold-micromesh working electrode with a large surface area to boost the intensities of the EPR signals. The electrode being fragile is stabilized and insulated by laminating the mesh together with a thin copper wire which extends out of the cell cavity. The reference electrode is a silver wire with a Teflon coating placed close to the working electrode. This design is very sensitive and works well for voltammetry by allowing simultaneous recording of undistorted CV measurements and also the generation of sufficient amount of radicals. It also favours EPR scans resulting in signals with high signal-to-noise ratios. This cell is fixed inside a Bruker EMX Plus/10 instrument operating at X-band frequencies (9.8GHz) at 19 ± 2 ^{o}C. Variable temperature (VT) experiments were performed using the ER4141 VT accessory. On inserting the electrochemical cell into the EPR cavity, it is connected to the potentiostat via non-magnetic leads. The CV studies were then initiated to determine the exact potential for the reduction process against the reference electrode in this cell. Then controlled potential electrolysis experiments were carried out with the potential set a little beyond (~ 0.01 V) the cathodic peak potential.

6.1.10 Melting point determination

Melting points were determined on an electrochemical MEL-TEMP 3.0 apparatus (capillaries) and are uncorrected.

6.2 Synthetic Details

Caution: *Perchloric acid and perchlorate salts are potentially explosive. The salts should be handled with care in the pure form and all reactions involving both salt and acid should be carried out in special fume hoods designed for them.*

6.2.1 Synthesis of 3,3,5,5-tetramethyl-1,2,4-dithiazolium chloride monohydrate 14a[12]

A mixture of dimethylthiocarbamoyl chloride (1.24 g, 10 mmol) and potassium thiocyanate (KSCN) (0.97 g, 10 mmol) in acetone (15.00 ml) was refluxed for fifteen minutes. After this, it was cooled and filtered. Dimethylamine (1.27 mL, 10 mmol) was added in drops to the yellow

filtrate at room temperature. The resulting dithiobiuret was oxidized in-situ first by the addition of concentrated HCl (0.82 mL) followed by the addition of H_2O_2 (1.03 mL) to the cold dithiobiuret solution in acetone. This resulted in a white precipitate that was filtered and washed with acetone. The filtrate also produced an orange precipitate. The recrystallization of the white precipitate from 95% ethanol afforded 1.05 g (55 %). CAS [1007-22-3]. IR (KBr): 3438m, 3368m, 3261w, 1629m, 1572s, 1456w, 1433m, 1420w, 1399w, 1380s, 1332m, 1243m, 1206w, 1145m, 1136m, 1060m, 920m, 899m, 747m, 634m, 616s, 535m, 492m, 442m, 424m cm^{-1}. Melting point = 242 - 247 ˚C (Literature melting point = 246 ˚C).[12]

6.2.2 Synthesis of 3,3,5,5-tetramethyl-1,2,4-dithiazolium hexafluorophosphate 14

3,3,5,5-tetramethyl-1,2,4-dithiazolium hexafluorophosphate salt was obtained via a metathesis reaction between the chloride salt[12] (0.10 g, 0.5 mmol) above with potassium hexafluorophosphate (0.10 g, 0.5 mmol) in methanol (10.00 mL) for one hour.[13] This resulted in a colourless solution which gave a white precipitate on evaporating under vacuum using the rotary evaporator. Its re-crystallization from 95% ethanol afforded 0.12 g (81 %) of the target salt.

IR (KBr): 1631w, 1576s, 1458w, 1422w, 1403w, 1381s, 1327m, 1244w, 1212w, 1135m, 1057m, 899w, 878w, 822s, 744m, 637m, 554s, 469w, 445w, 422m cm^{-1}. Mass spectrum (m/e): 190 ($((CH_3)_2NCSSNCN(CH_3)_2^+$, 100%), 147 ($((CH_3)_2NCSSNCH)^+$, 11.37%), 120 ($((CH_3)_2NCSS)^+$, 9.82%), 102 ($(CH_3)_2NCNS^+$, 4.56%), 88 ($((CH_3)_2NCS^+$, 50.48%). Elemental analysis: calculated (found): 21.49 (21.60) % C, 3.61 (3.26) % H, 12.53 (12.80) % N (Hydrogen is off the prescribed 0.3% limit. This could be due to a lot of factors such as the poor combustion of the PF_6^- counteranion etc. Melting point = 243 - 246 ˚C.

6.2.3 Synthesis of 3,3,5,5-tetramethyl-1,2,4-dithiazolium tetrafluoroborate

3,3,5,5-tetramethyl-1,2,4-dithiazolium tetrafluoroborate salt was obtained by carrying out a metathesis reaction between the chloride salt[12] (0.10 g, 0.45 mmol) prepared as above with silver tetrafluoroborate (0.09 g, 0.45 mmol) in chloroform (10.00 mL) for one hour.[14] This resulted in a colourless solution with white precipitate of AgCl which was filtered off. The

resulting filtrate gave a white precipitate on evaporating under vacuum using the rotary evaporator. Yield = 0.10 g (83 %). IR (KBr): 1623w, 1576s, 1383m, 1332m, 1030s, 904w, 832w, 749m, 642s, 604m, 565m, 533w, 522w, 482w, 443w, 421s, 405w, 389w cm^{-1}.

6.2.4 Synthesis of 3,5-diphenyl-1,2,4-dithiazolium tetrabromidoferrate (III) 3b[15]

This was formed via a two-stage reaction scheme. The first was the Willgerodt-Kindler reaction[16-17] of benzaldehyde (14.00 mL, 137 mmol), morpholine (17.00 mL, 196 mmol) and sulphur (6.40 g, 200 mmol). The mixture of these three compounds was heated under reflux on the steam bath. This resulted in an exothermic reaction that made the mixture boil. After three hours of heating, the resulting dark brown oil (which actually solidified on cooling) was dissolved in boiling ethanol (270.00 mL) and the hot solution filtered from a small insoluble residue. The filtrate on cooling afforded 22.4 g (82 %) of golden-yellow needles of thiobenzomorpholide. IR (KBr): 2938w, 2971w, 2918w, 2864w, 1573m, 1494s, 1460m, 1425m, 1386s, 1352m, 1317s, 1289m, 1254s, 1224s, 1203w, 1169w, 1154w, 1110s, 1072w, 1060m, 1022s, 1008w, 990m, 907m, 870s, 757s, 693s, 675w, 661w, 617w, 604w, 579s, 407m cm^{-1}.

The second stage[18] involves using the thiobenzomorpholide formed in stage one to undergo a reaction with a bromine solution to form an adduct. Bromine in 10.00 mL chloroform was added dropwise to a stirred ice-cooled solution of thiobenzomorpholide (4.14 g, 20 mmol) in 40.00 mL of chloroform. Gradually, the colour of the resulting suspension changed to reddish orange. This was stirred further for 30 minutes at $0^{o}C$. Thiobenzamide (2.74 g, 20 mmol) in 30.00 mL chloroform was added dropwise to the suspension and stirred for another 30 minutes. 30.00 mL of concentrated $HClO_4$ was added and the mixture was stirred for 15 minutes after which the yellow aqueous layer was separated from the deep red organic layer. The inorganic phase was cooled to a temperature of $-4^{o}C$ resulting in the precipitation of a mixture of crystalline tiny red prisms and yellow powdered plates of the perchlorate salt. The tiny red-orange prisms were confirmed by X-ray diffraction experiment to be 3,5-diphenyl-1,2,4-dithiazolium tetrabromidoferrate (III) salt, CAS [1434738-28-9]. The source of the iron was presumed to be

rust that was digested by the perchloric acid making the ferric aquo ion readily available by the highly nucleophilic bromide ions from the adduct formation step. Melting point = 169.3 - 171.1 ˚C.

6.2.5 Synthesis of 3,5-diphenyl-1,2,4-dithiazolium perchlorate 3[18-19]

This was formed via a two-stage reaction scheme. The first was the Willgerodt – Kindler reaction of benzaldehyde (14.00 mL, 137 mmol), morpholine (17.00 mL, 196 mmol) and sulphur (6.40 g, 200 mmol). The mixture of these three compounds was heated under reflux on the steam bath. This resulted in an exothermic reaction that made the mixture boil. After three hours of heating, the resulting dark brown oil (which actually solidified on cooling) was dissolved in boiling ethanol (270.00 mL) and the hot solution filtered from a small insoluble residue. The filtrate on cooling afforded 22.4 g (82 %) of golden-yellow needles of thiobenzomorpholide. IR (KBr): 2938w, 2971w, 2918w, 2864w, 1573m, 1494s, 1460m, 1425m, 1386s, 1352m, 1317s, 1289m, 1254s, 1224s, 1203w, 1169w, 1154w, 1110s, 1072w, 1060m, 1022s, 1008w, 990m, 907m, 870s, 757s, 693s, 675w, 661w, 617w, 604w, 579s, 407m cm^{-1}.

The second stage[18] involves using the thiobenzomorpholide formed in stage one to undergo a reaction with denetal bromine to form an adduct. Bromine in 10.00 mL chloroform was added dropwise to a stirred ice-cooled solution of thiobenzomorpholide (4.14 g, 20 mmol) in 40.00 mL of chloroform. Gradually, the colour of the resulting suspension changed to reddish orange. This was stirred further for 30 minutes at $0^{o}C$. Thiobenzamide (2.74 g, 20 mmol) in 30.00 mL chloroform was added dropwise to the suspension and stirred for another 30 minutes. 30.00 mL of concentrated $HClO_4$ was added and the mixture was stirred for 15 minutes after which the yellow aqueous layer was separated from the deep red organic layer. The inorganic phase was cooled to a temperature of $-4^{o}C$ resulting in a mixture of tiny red crystal and yellow powdered plates of the perchlorate salt CAS [64502-69-8]. The recrystallization of the yellow powdered plates of the perchlorate salt from concentrated acetic acid afforded 3.27 g (64 %) of the crystals. IR (KBr): 1591m, 1499w, 1453m, 1402w, 1392m, 1346w, 1327m, 1258w, 1223w, 1205m,

1196m, 1184m, 1068s, 997m, 775s, 729w, 680s, 656s, 619s, 567m, 467m, 425w, 384w cm^{-1}. Mass spectrum (m/e): 256 ($PhCNSSCPh^+$, 100%), 153 $PhCSS^+$, 14.23%), 77 (Ph^+) 10.26%). Elemental analysis: calculated (found): 40.60 (40.35) % C, 3.07 (2.96) % H, 5.15 (5.09) % N. Melting point = 265 – 267 ˚C (Literature melting point = 266-267 ˚C).[18]

6.2.6 Synthesis of N, N'-(5-diethylamino-3-phenyl-1,2,4-dithiazolium perchlorate 1[20-21]

Benzoyl chloride (8.00 mL, 70 mmol) was added in drops to a solution of ammonium thiocyanate NH_4SCN (5.30 g, 70 mmol) in 30.00 mL of acetone. This solution was maintained at 60^oC with constant stirring for 1 hour. The resulting yellow suspension was treated with a solution of diethylamine (7.00 mL, 70 mmol) in 40.00 mL acetone (Me_2CO). The cooled mixture was added over 100.00 mL water resulting in the immediate formation of a yellow precipitate. This suspension was stirred overnight, filtered and washed with water. The crude N-benzoyl-N,N'-diethylthiourea[22] product was recrystallized from about 50.00 mL of 99 % ethanol to afford 9.90 g of the product (Yield = 60 %).

^1H NMR, (δ, $CDCl_3$); 8.34 ppm (s, 1H, NH), 7.85 ppm (d, 2H, J = 6 Hz), 7.60 ppm (m, 1H Ar.), 7.49 ppm (t, 2H, Ar), 4.04 ppm (d, 2H methylene, J = 6 Hz), 3.62 ppm (d, 2H methylene, J = 6 Hz), 1.37 ppm (m, 6H)

Yellow crystalline N-benzoyl-N,N'-diethylthiourea (0.91 g, 4 mmol) from the above stage was added to a mixture of acetic acid (CH_3COOH) (4.00 mL) and perchloric acid ($HClO_4$) (0.80 mL). While the mixture was stirred, H_2O_2 (0.20 mL) was added in drops leading to an exothermic reaction. The resultant mixture was further heated to boiling point for 10-15 minutes and allowed to cool. This was followed by dilution of the mixture in ether resulting in the precipitation of light yellow solids. These were filtered off and recrystallized from acetic acid to afford 0.26 g (26 %), CAS [65407-92-3]. Mass spectrum (m/e): 251 ($PhCNS_2CN(CH_2CH_3)_2^+$, 100%), 223 ($PhCNS_2CNHCH_2CH_3)^+$, 8.68%), 168 ($PhCNS_2CNH)^+$, 8.01%), 104 ($PhCNH)^+$, 6.91%). Elemental analysis: calculated (found):41.08 (40.88) % C, 4.31 (4.12) % H, 7.98 (8.04) % N. Melting point = 146-147 ˚C (Literature melting point = 147-148 ˚C).[21]

6.2.7 Synthesis of N,-(5-morpholino-3-phenyl-1,2,4-dithiazolium perchlorate salt 33[20]

Benzoyl chloride (10.00 mL, 90 mmol) was added in drops to a solution of ammonium thiocyanate NH_4SCN (7.00g, 90 mmol) in 32.00 mL of acetone. This solution was maintained at 60^oC with constant stirring for 1 hour. The resulting yellow suspension was treated with a solution of morpholine (8.00 mL, 90 mmol) in 60 mL acetone (Me_2CO). The cooled mixture was added over 100.00 mL of water resulting in the immediate formation of a light yellow precipitate. This suspension was stirred overnight, filtered and washed with water. The crude N-(morpholinothiocarbamoyl) benzamide product was recrystallized from about 50.00 mL of dichloromethane (CH_2Cl_2) and this afforded a yield of 12.18g [Yield = 70 %]. ^1H NMR, (δ, $CDCl_3$); 8.67 ppm (s, 1H, NH), 7.85 ppm (d, 2H Ar., J = 9 Hz), 7.62 ppm (t, 1H Ar.), 7.50 ppm (t, 2H, Ar.), 4.23 ppm (s, 2H methylene), 3.83 ppm (d, 2H methylene), 3.65 ppm (m, 6H). Yellow crystalline N-(morpholinothiocarbamoyl) benzamide (1.00 g, 4 mmol) from the above stage was added to a mixture of acetic acid (CH_3COOH) (4.00 mL) and perchloric acid ($HClO_4$) (0.85 mL). While the mixture was stirred, H_2O_2 (0.25 mL) was added in drops leading to an exothermic reaction. The resultant mixture was further heated to boiling point for 10-15 minutes and allowed to cool. This was followed by dilution in ether resulting in the precipitation of light yellow solids. These were filtered off and recrystallization from acetic acid to afford 0.51 g (48 %) of the salt CAS [65459-17-8]. IR (KBr): 3165, 3105, 1587, 1500, 1485, 1444, 1427, 1390, 1305, 1278, 1234, 1211, 1183, 1073, 1056, 1029, 952, 929, 876, 867, 824, 775, 727, 687, 661, 654, 619, 589, 488, 452, 419 cm^{-1}. Melting point = 210-211 ˚C (Literature melting point = 210-211 ˚C).

6.2.8 Synthesis of 3,5-diphenyl-1,2,4-dithiazolium triiodide 3a[23]

Thiobenzamide (2.00g, 15 mmol) and iodine crystals (3.80 g, 15 mmol) in 20.00 mL glacial acetic acid were heated to boil for about 10 minutes. As the heating continues, the thiobenzamide and iodine dissolves in the acetic acid and a black-orange mass of precipitate began to form. The solution thickens up gradually and this necessitated adding extra 10.00 mL of glacial acetic acid. The black-orange precipitate was filtered off on cooling and recrystallized

from nitromethane-ether solvent mixture. This afforded 3.10 g (80 %) of needle-like black-orange crystals, CAS [64721-23-9]. IR (KBr): 3165w, 3105w, 1587m, 1500, 1485w, 1444m, 1427m, 1390m, 1305w, 1278w, 1234w, 1211w, 1183w, 1073w, 1056s, 1029w, 952m, 929m, 876m, 867w, 824m, 775w, 727w, 687w, 661w, 645w, 619s, 589m, 488w, 452m, 419s cm^{-1}. Melting point =177-180˚C (Literature melting point=177-179˚C).

6.2.9 Synthesis of protonated pyridine thioamide 29[23]

4-pyridine thioamide **29** (1.00 g, 10 mmol) and iodine (2.00 g, 10 mmol) in 7.00 mL glacial acetic acid were heated for about 10 minutes to the boil. Brownish colour of iodine in acetic acid changed to darkish red on adding 4-pyridine thioamide. Initially, there were undissolved lumps in the solution but they all soon disappeared by dissolving in solution upon the application of heat. Darkish brown precipitate was formed on cooling and this was filtered via a Buchner funnel. The precipitate was pumped on the Buchner funnel for a little while to get rid of acetic acid as much as possible before making efforts to recrystallize it. It was recrystallized from acetonitrile affording 2.17 g (84 %) of dark-brown needle-like crystals. ^{1}H NMR, (δ, DMSO); 9.07 ppm (d, 1H, 6.3 Hz), 9.00 ppm (d, 1H, 6.3 Hz), 8.67 ppm (d, 1H, J = 6.3 Hz), 8.36 ppm (s, 1H, J = 6.3 Hz), 5.28 ppm (br, 3H+HOD) IR (KBr): 3037w, 1633m, 1568w, 1473s, 1441m, 1328w, 1301m, 1273m, 1244m, 1207m, 1178m, 1153m, 1073m, 844s, 800m, 710s, 627m, 525s, 501s. Melting point = 153.6 – 153.8 ˚C.[24]

6.2.10 Synthesis of methylated pyridine thioamide[25]

Methyl iodide (0.57g, 4 mmol) was added in drops to 4-pyridine thioamide (0.50g, 4 mmol) in 5.00 mL of dry acetonitrile. The mixture was stirred for 30 minutes at room temperature and then heated for 10 minutes under reflux at 50^{o}C. While the methyl iodide was being added, the yellow colour of 4-pyridine thioamide in acetonitrile began to change to deep orange. The solution was allowed to cool at room temperature and then filtered using vacuum filtration. The precipitate was washed three times with cold acetonitrile before it was recrystallized from hot boiling 99 % ethanol which afforded a yield of 0.21g (35 %). CAS [749784-54-1]. The crystals

were kept in closed flasks as they had the tendency to absorb moisture (hygroscopic) if exposed to air. ^{1}H NMR, (δ, D_2O); 8.84 ppm (d, 2H Ar., J = 6.9 Hz), 8.23 ppm (d, 2H Ar., J = 6.9 Hz), 4.38 ppm (s, 3H, N-CH_3). Melting point = 219.3 – 220.9 ˚C (Literature melting point = 220 ˚C).[26]

6.2.11 Synthesis of Trans-4,4'-dipyridylethyne 29[27]

Trans-4, 4'-dipyridylethylene **29** (5.00 g, 27 mmol) are dissolved in 50.00 mL of concentrated HBr at 0^{o}C. 5.00 mL of bromine was added in drops while stirring was going on resulting immediately in an orange precipitate. After the addition of all the bromine, the reaction mixture was subjected to heat at 120^{o}C with mild stirring for 1 hour. It was then cooled to 0^{o}C and the perbrominated orange solid obtained was isolated by filtration. It is then converted to the white dibromide by treatment with 2 M NaOH. For the final dehydrobromination, a suspension of the dibromide in 20.00 mL of hot tertiary butanol is given in small quantities to a boiling solution of sodium (1.40g, 61 mmol) in 150.00 mL of absolute tertiary butanol. This mixture is refluxed for 30 minutes and then evaporated to about 80.00 mL. Excess of the butanolate is destroyed by adding about 10.00 mL of water. The solvent is now evaporated under reduced pressure to give a white precipitate. The white precipitate was extracted with ether three times and the ether solution is again evaporated to dryness leaving an orange precipitate behind. Recrystallizing the crude product from heptane afforded 3.63g (75 %) of pure 4, 4'- dipyridylethyne. CAS [73564-69-9] ^{1}H NMR, (δ, $CDCl_3$); 8.63 ppm (d, 4H, J = 6 Hz), 7.41 ppm (d, 4H, J = 6 Hz), J'= 1.5 Hz. Melting point = 113-116 ˚C (Literature melting point = 114 ˚C).[27]

6.3 References

1. Compton, R. G.; Banks, C. E., *Understanding Voltammetry*. Imperial College Press: 2011.
2. Sheldrick, G. M., *Acta Crystallogr. Sect. A* **2008,** *64*, 112-122.
3. Maki, A. H.; Geske, D. H., *J. Chem. Phy.* **1959,** *30*, 1356-1357.
4. Yokoyama, H.; Satoh, T.; Ohya-Nishiguchi, H.; Kamada, H.; Kasai, N.; Matsue, T., *Chem. Letts.* **1995,** *24*, 919-920.
5. Piette, L. H.; Ludwig, P.; Adams, R. N., *J. Am Chem. Soc.* **1962,** *84*, 4212-4215.

6. Compton, R. G.; Waller, A. M., *J. Electroanal. Chem. Interfac. Electrochem.* **1985,** *195*, 289-297.

7. Richter, R.; Kaiser, J.; Sieler, J.; Hartung, H.; Peter, C., *Acta Crystallogr. Sect. B* **1977,** *33*, 1887-1892.

8. Hinchley, S. L.; Morrison, C. A.; Rankin, D. W. H.; Macdonald, C. L. B.; Wiacek, R. J.; Cowley, A. H.; Lappert, M. F.; Gundersen, G.; Clyburne, J. A. C.; Power, P. P., *Chem. Commun.* **2000,** 2045-2046.

9. Fiedler, D. A.; Koppenol, M.; Bond, A. M., *J. Electrochem. Soc.* **1995,** *142*, 862-867.

10. Webster, R. D.; Bond, A. M.; Coles, B. A.; Compton, R. G., *J. Electroanal. Chem.* **1996,** *404*, 303-308.

11. Neudeck, A.; Kress, L., *J. Electroanal. Chem.* **1997,** *437*, 141-156.

12. Oliver, J. E.; Chang, S. C.; Brown, R. T.; Stokes, J. B.; Borkovec, A. B., *J. Med. Chem.* **1972,** *15*, 315-320.

13. Haque, R.; Iqbal, M.; Khadeer Ahamed, M.; Majid, A.; Abdul Hameed, Z., *Chem. Cent. J.* **2012,** *6*, 68-81.

14. Litschauer, M.; Puchberger, M.; Peterlik, H.; Neouze, M.-A., *J. Mater. Chem.* **2010,** *20*, 1269-1276.

15. Shotonwa, I. O.; Boere, R. T., *Acta Crystallogr. Sect. E* **2013,** *69*, m95.

16. Peak, D. A.; Stansfield, F., *J. Chem. Soc. Res.* **1952,** 4067-4075.

17. Penner, S. S.; Sherman, S., *J. Am Chem. Soc.* **1948,** *70*, 869-870.

18. Corsaro, A.; Compagnini, A.; Perrini, G.; Purrello, G., *J. Chem. Soc. Perkins Trans 1* **1984,** 897-900.

19. Uemachi, H.; Iwasa, Y.; Mitani, T., *Electrochim. Acta* **2001,** *46*, 2305-2312.

20. Köhler, R.; Sieler, J.; Richter, R.; Hoyer, E.; Beyer, L.; Maartmann-Moe, K., *Z. Anorg. Allg. Chem.* **1989,** *576*, 203-214.

21. Hartmann, H.; Liebscher, J.; Czerney, P., *Tetrahedron* **1985,** *41*, 5371-5376.

22. Rodríguez-Fernández, E.; García, E.; Hermosa, M. R.; Jiménez-Sánchez, A.; Mar Sánchez, M.; Monte, E.; Criado, J. J., *J. Inorg. Biochem.* **1999,** *75*, 181-188.

23. Liebscher, J.; Hartmann, H., *Liebigs Ann.* **1977,** *1977*, 1005-1012.

24. Shotonwa, I. O.; Boere, R. T., *Acta Crystallogr. Sect. E* **2014,** *70*, o340-o341.

25. Kosower, E. M., *J. Am Chem. Soc.* **1955,** *77*, 3883-3885.

26. Christ, W.; Rakow, D.; Strauss, S., *J. Heterocycl. Chem.* **1974,** *11*, 397-399.

27. Tanner, M.; Ludi, A., *Chimia* **1980,** *34*, 23-24.

Chapter seven

7.1 Conclusion

1,2,4-dithiazolium salts $\mathbf{3}^+$, $\mathbf{1}^+$, and $\mathbf{14}^+$, whose potential as molecular conductors are being investigated, are prepared by the oxidation of thiobenzamide, thiourea and dithiourea, respectively, using hydrogen peroxide in acids. They were characterized by IR, NMR, X-ray crystallography and elemental analyses. The flat central 6π dithiazolium cation rings NC_2S_2 all have almost coplanar substituents attached to them at the 3- and 5- positions. Cyclic voltammetry revealed electrochemically irreversible E_p^{c1}, E_p^{c2} and E_p^{c3} processes for **3** and E_p^{c1} processes for 1 and 14 while they all showed offset reoxidation waves, a phenomenon that indicates structural transformation in S-N compounds on exposure to reducing conditions. These processes were studied using density functional theory calculations with focus on the nature of orbitals present coupled with adequate description of the extent of occupation of the energy levels. The calculations also provide reasonable correlation between experimental and theoretical data. RDE voltammetry experiments on $\mathbf{3}^+$, $\mathbf{1}^+$ and $\mathbf{14}^+$ led to the determination of their diffusion coefficients. However, it was impossible to detect any dithiazolyl radical for the three compounds as well as extracting rate constants for the decay of electrochemically generated species after subjecting them to variable and room temperature SEEPR techniques. This is the first report for SEEPR studies of 1,2,4-dithiazolium cations. Digital simulation of experimental CVs found E_1E_2C and $E_1C_1E_2C_2$ to be reasonable mechanisms from which justifiable parameters such as potentials, electron transfer rate constants, equilibrium constants and chemical rate constants were extracted to give insight into the peculiar behaviour of the salts in solution. The two possible mechanisms also unravel the mystery behind the non-detection of neutral radicals during SEEPR experiments (due to rapid consumption as a result of their instability), an occurrence that limits their applicability as molecular conductors. The two were also compared from the perspective of "energy requirements" and "extent of fits" between experimental and theoretical CVs. In terms of

energy requirements, the open anion model (E_1E_2C) seems to be more favoured while in terms of fits between experimental and theoretical CVs, the dimer model ($E_1C_1E_2C_2$) is favoured.

7.2 Direction for future work

The use of phenyl and alkylamino groups as substituents has created an insight into the effect of substituent size on the stability of 3,5-substituted 1,2,4-dithiazole ring systems. Moreover, the cyclic voltammetry experiments showed that the presence of substituents of different sizes and orientations is able to tune the redox potential within a certain redox potential window. This tunability has the tendency to move peak-to-peak separation into the range acceptable for reversible electrochemical reactions in alignment with the Nernstian response. In order to achieve this feat, it is inevitable that bulkier groups be introduced at the 3- and 5-positions so that a track record is created to monitor the pattern of electrochemical responses as substituents change from less bulky to much bulkier groups. There are groups that come to mind in this instance based on their relevance in main group coordination chemistry. First, is the introduction of electron donating and withdrawing groups at the ortho, meta, and para positions of benzene that will enhance the electronic effects of resonance and inductive tendencies of the ring. Also, it is projected that the introduction of these groups into the aromatic ring will distort its orientation thus minimizing dimer formation considerably. Therefore, focus will be shifted to groups such as alkyl (methyl, ethyl, isopropyl), substituted amines, OH, OR, CF_3, halogens, -CN, and -NO_2 groups. For the alkylamino substituents, the aim is to use bulkier alkyl groups such as ethyl, isopropyl and t-butyl. It is hoped that electrochemical and the well-developed SEEPR studies coupled with simulation of electrochemical response of these compounds will help create a logical and reasonable trend for the redox changes that accompany 3,5-substituted 1,2,4-dithiazoles.

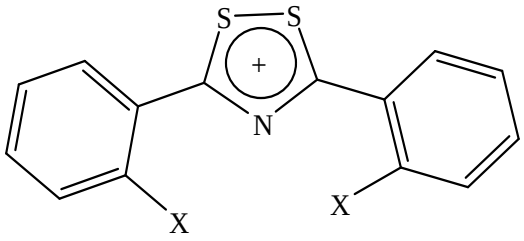

30

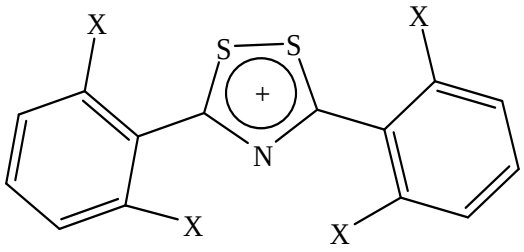

31

X = CH_3, C_2H_5, $CH(CH_3)_2$, -NHR, NR_2, -OH, -OR, CF_3, halogens, -CN, $-NO_2$
R = alkyl, (ethyl, isopropyl, t-butyl)

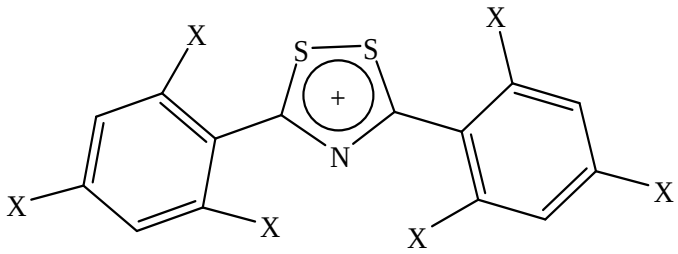

32

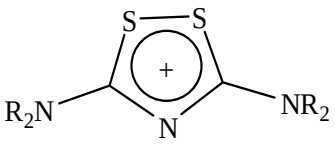

33

On a conclusive note, it is imperative to look into the precipitation of dimer by the use of reducing agents. This is inspired by the outcome of the dimer model derived from simulation studies. This will start with $\mathbf{3}^+$ since it shows other reduction and offset oxidation processes other than the irreversible E_p^{c1} and E_p^{a1} peaks. Afterwards, DTAs $\mathbf{1}^+$ and $\mathbf{14}^+$ will be studied for the precipitation of dimers though the success of the test cannot be vouched for as lone pairs of electrons on the substituents' nitrogen are somewhat capable of impeding dimer formation.

Appendix

Table A.1. Cathodic and anodic peak currents for **3**, **1** and **14** with scan rates to determine diffusion controlled current flow.

Scan rate,	$\sqrt{\nu}$	(68) 5 mM (*μA)		(69) 5 mM (*μA)		(70) 5 mM (*μA)	
		I_p^c [a]	I_p^a [b]	I_p^c	I_p^a	I_p^c	I_p^a
0.20	0.45	60.20	7.67	82.24	21.51	229.01	74.13
0.40	0.63	88.90	14.1	113.49	39.53	311.54	99.46
0.80	0.89	117.61	20.10	156.38	58.55	414.29	121.14
1.00	1.00	136.16	22.77	176.28	70.13	454.29	177.70
2.00	1.41	197.76	33.23	236.65	93.11	597.34	215.16
4.00	2.00	259.16	53.72	319.41	132.41	798.94	286.13
8.00	2.83	349.55	73.23	425.49	170.1	1017.96	349.48

[a] I_p^c =Cathodic peak currents. [b] I_p^a =Anodic peak currents. Current measurements error = $\pm$ 0.01 A

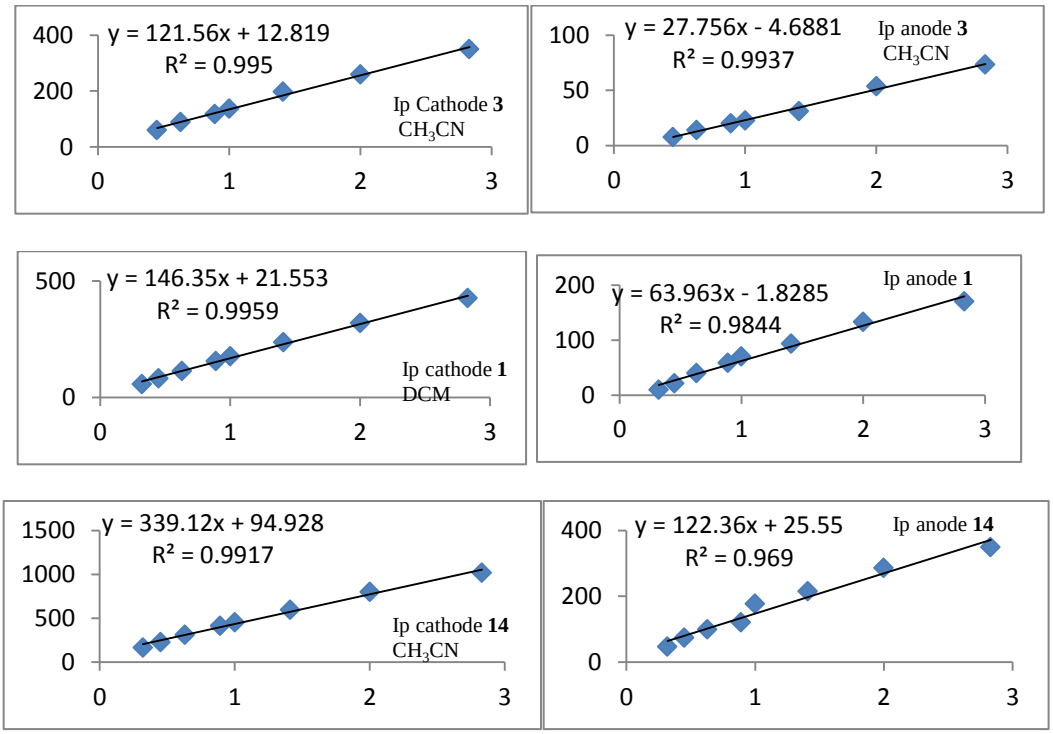

Figure A.1. Graphs of cathodic and anodic peak currents against the square root of scan rates.

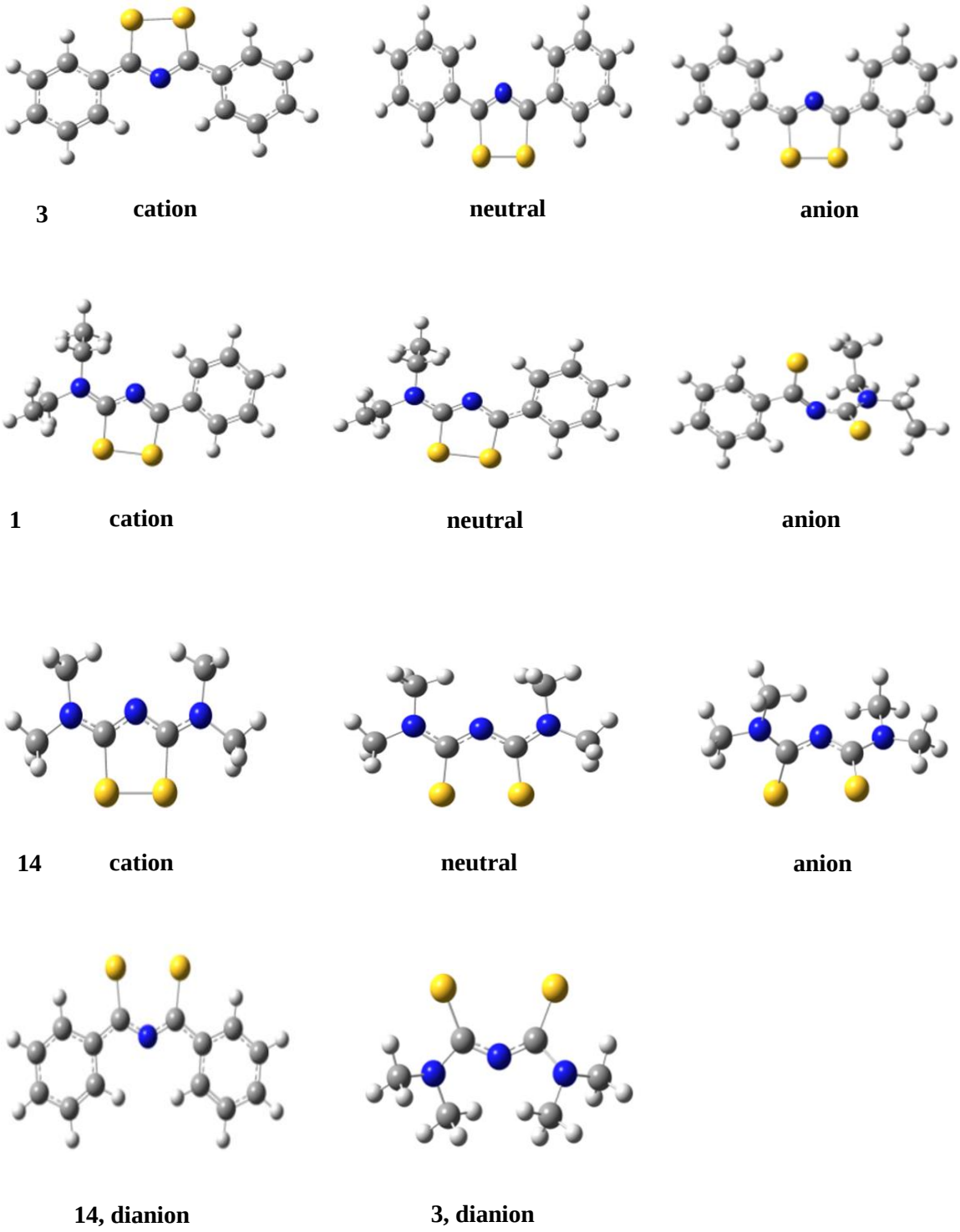

Figure A.2. Geometrical structures of **3**, **1** and **14** as obtained from DFT calculations.

3

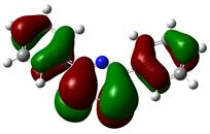

HOMO $^{-}$

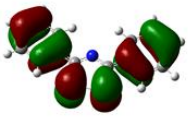

HOMO $^{+}$

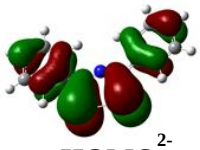

HOMO $^{2-}$

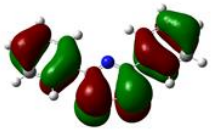

HOMO $^{\cdot}$

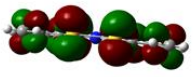

LUMO 1 $^{2-}$

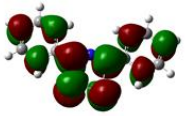

LUMO $^{-}$

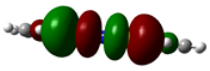

LUMO $^{2-}$

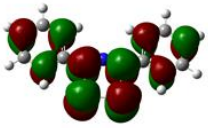

LUMO $^{\cdot}$

1

HOMO $^{-}$

HOMO $^{+}$

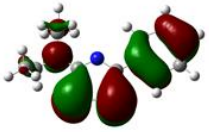

HOMO $^{\cdot}$

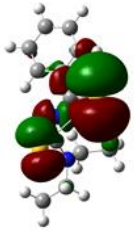

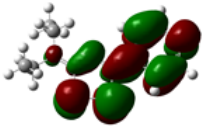

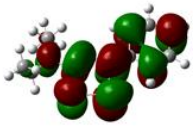

14

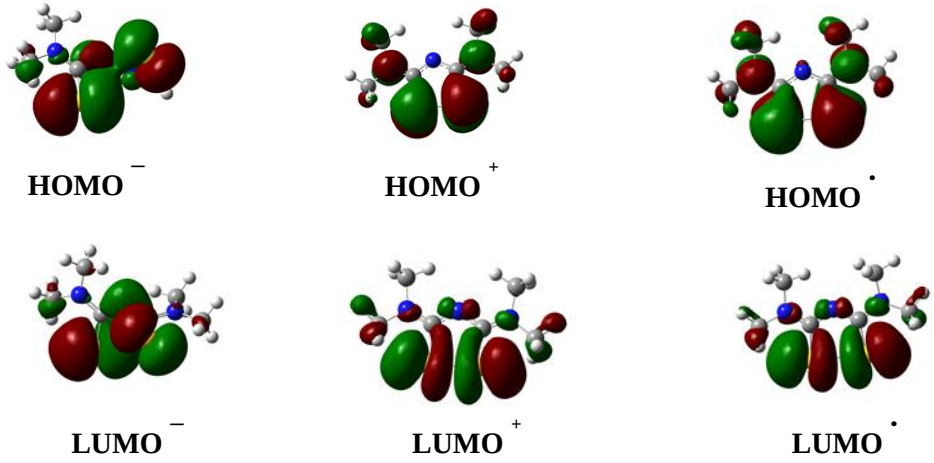

Figure A.3. Molecular orbitals of **3**, **1** and **14**.

Table A.2. Cathodic and anodic peak currents obtained from the electrochemistry of ferrocene in CH_3CN (0.4 M [$^nBu_4N$][PF_6]).[a]

Scan rate, ν (Vs^{-1})	$\sqrt{\nu}$	1mM (*μA)		2Mm (*μA)		3mM (*μA)	
		I_p^c [b]	I_p^a [c]	I_p^c	I_p^a	I_p^c	I_p^a
0.025	0.16	20.40	20.81	34.48	35.17	52.54	53.65
0.050	0.22	27.59	28.40	51.45	49.98	70.11	72.09
0.100	0.32	38.70	39.12	70.73	69.19	98.09	100.19
0.200	0.45	54.80	56.44	94.70	95.17	141.15	138.80
0.400	0.63	74.95	69.75	137.59	137.01	191.28	191.50
0.800	0.89	104.36	105.15	183.42	184.31	264.88	262.34

[a] Area of glassy carbon electrode determined from the equation $I_p = (2.69 \times 10^5)N^{1.5}AD^{0.5}\nu C$ where I_p is the peak current, N is the number of electron transferred, A is the area of the electrode, D is the diffusion coefficient, ν is the scan rate and C is the concentration of ferrocene in bulk solution. [b] I_p^c = cathodic peak currents. [c] I_p^a = anodic peak currents. Current measurements error = $\pm$ 0.01 A

Areas of working electrode: (8.9 + 8.7 +7.9 +7.9 +7.5 + 7.4) × $10^{-2}cm^2$

Table A.3. Cathodic and anodic peak currents obtained from the repeated electrochemistry of ferrocene in CH_3CN (0.4 M [$^nBu_4N$][PF_6]).[a]

Scan rate, ν (Vs^{-1})	$\sqrt{\nu}$	1mM		2Mm		3mM	
		I_p^c [b]	I_p^a [c]	I_p^c	I_p^a	I_p^c	I_p^a
0.100	0.32	44.40	44.11	85.46	85.43	144.85	144.58
0.200	0.45	60.63	60.13	116.25	115.69	190.76	191.30
0.400	0.63	86.93	86.19	161.58	161.10	265.00	265.65
0.800	0.89	118.46	118.99	223.55	223.05	359.55	360.98
1.000	1.00	132.49	132.91	247.03	247.29	395.81	394.68

[a] Area of glassy carbon electrode determined from the equation $I_p = (2.69 \times 10^5)N^{1.5}AD^{0.5}\nu C$ where I_p is the peak current, N is the number of electron transferred, A is the area of the electrode, D is the diffusion coefficient, ν is the scan rate and C is the concentration of ferrocene in bulk solution. [b] I_p^c = cathodic peak currents. [c] I_p^a = anodic peak currents. Current measurements error = $\pm$ 0.01 A

Areas of working electrode: (10.1, 10.2, 9.28, 9.29, 9.64, 9.63) × $10^{-2}cm^2$

Table A.4. Selected calculated bond lengths for **3**.[a]

Bond length (Å)	Cation	Neutral	Anion	Dianion
S2-S1	2.05	2.09	2.09	2.78
C1-N1	1.32	1.32	1.31	1.33
N2-C2	1.32	1.32	1.31	1.33
S1-C1	1.75	1.82	1.85	1.81
C2-S2	1.75	1.81	1.85	1.80

Table A.5. Selected calculated bond angles for **3**.[a]

Bond angles °	Cation	Neutral	Anion	Dianion
S5-C2-C6	120.1	119.5	119.3	119.2
S4-C1-C17	120.1	119.5	119.3	119.2
S5-C2-N3	116.8	116.6	114.9	122.9
S4-C1-N3	116.8	116.6	114.9	122.9

Angles have errors of $\pm$ 0.1 °

Table A.6. Selected calculated bond lengths for **1**.[a]

Bond length (Å)	Cation	Neutral	Anion
S2-S1	2.08	2.11	4.02
C1-N1	1.34	1.29	1.35
N2-C2	1.31	1.34	1.30
S1-C1	1.78	1.82	1.70
C2-S2	1.77	1.81	1.72

Table A.7. Selected calculated bond angles for **1**.[a]

Bond angles °	Cation	Neutral	Anion
S2-C5-N17	120.2	118.0	122.1
S1-C4-C6	118.8	119.7	119.8
S2-C5-N3	117.3	118.2	121.6
S1-C4-N3	118.1	116.1	126.7

Angles have errors of $\pm$ 0.1 °

Table A.8. Selected calculated bond lengths for **14**.[a]

Bond length (Å)	Cation	Neutral	Anion	Dianion
S2-S1	2.09	2.69	3.97	3.82
C1-N1	1.32	1.34	1.34	1.33
N2-C2	1.33	1.34	1.32	1.33
S1-C1	1.79	1.74	1.72	1.76
C2-S2	1.79	1.74	1.73	1.76

Table A.9. Selected calculated bond angles for **14**.[a]

Bond angles °	Cation	Neutral	Anion	Dianion
S2-C6-N4	117.9	118.4	120.7	114.8
S1-C7-N5	117.9	118.8	120.3	114.8
S2-C6-N3	118.6	124.9	124.5	132.9
S1-C7-N3	118.6	125.4	125.8	132.9

[a] Computed from Gaussian W03 package for **A.4 – A.9**
Angles have errors of $\pm$ 0.1 °

Table A.10. Cathodic and anodic peak potentials of **1** in acetonitrile solution containing 0.1 M [^{n}Bu$_4$N][PF$_6$].[a]

Scan rate(mV/s)	E_a(V)[b]	E_c(V)[c]	ΔE(V)[d]
100	-0.34	-0.88	0.54
200	-0.30	-0.90	0.60
500	-0.28	-0.93	0.65
800	-0.26	-0.96	0.70
1000	-0.24	-0.97	0.73
5000	-0.15	-1.06	0.91
10000	-0.13	-1.12	0.99
20000	-0.06	-1.19	1.13

[a] All potentials are measured in acetonitrile versus $E^{0/}_{Fc0/+}$,the redox couple of ferrocene/ ferrocenium. [b] E_a = anodic peak potential. [c] E_c = cathodic peak potential. [d] $\Delta E = E_a - E_c$. Potential measurements error = $\pm$ 0.01 V

Table A.11. Cathodic and anodic peak potentials of **14** in dichloromethane solution containing 0.4 M [$^{n}Bu_4N$][PF_6].[a]

Scan rate(mV/s)	E_a(V)[b]	E_c(V)[c]	ΔE(V)[d]
50	-0.50	-0.93	0.43
100	-0.46	-0.94	0.48
200	-0.43	-0.95	0.52
400	-0.37	-0.92	0.55
500	-0.35	-0.93	0.58
1000	-0.25	-0.94	0.59
2000	-0.27	-1.04	0.77
5000	-0.19	-1.11	0.92
10000	-0.12	-1.19	1.07
20000	-0.05	-1.30	1.25

[a] All potentials are measured in acetonitrile versus $E^{0/}_{Fc0/+}$,the redox couple of ferrocene/ ferrocenium. [b] E_a = anodic peak potential. [c] E_c = cathodic peak potential. [d] ΔE = E_a - E_c. Potential measurements error = $\pm$ 0.01 V

Table A.12. Parameters for RDE experiment on 2.5mM of **3**.[a]

RPM[b]	ω[c] (rad/s)	$\omega^{1/2}$	I_1	I_2	I_l [d](A)	$1/\omega^{1/2}$	$1/I_l$ (A^{-1})
500	52.35988	7.23601255	0	1.73E-04	1.73E-04	0.13819766	5.78E+03
750	78.53982	8.86226925	0	2.10E-04	2.10E-04	0.112837917	4.76E+03
1000	104.7198	10.2332671	0	2.40E-04	2.40E-04	0.097720502	4.16E+03
1250	130.8997	11.4411404	0	2.66E-04	2.66E-04	0.087403874	3.76E+03
1500	157.0796	12.5331414	0	2.90E-04	2.90E-04	0.079788456	3.45E+03
1750	183.2596	13.5373399	0	3.11E-04	3.11E-04	0.073869756	3.22E+03
2000	209.4395	14.4720251	0	3.29E-04	3.29E-04	0.06909883	3.04E+03
2250	235.6194	15.3499006	0	3.47E-04	3.47E-04	0.065147002	2.88E+03
2500	261.7994	16.1802159	0	3.63E-04	3.63E-04	0.061803872	2.75E+03

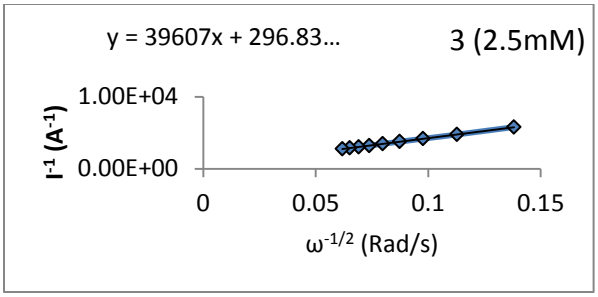

Figure A.4. Graph of I^{-1} vs $\omega^{-1/2}$ to determine diffusion coefficient from 2.5 mM of **3**

Slope	39607
$D^{2/3}$	4.19E-04
D	8.58331E-06 cm^2/s

Table A.13. Parameters for RDE experiment on 5.0mM of **3**.[a]

RPM[b]	ω[c] (rad/s)	$\omega^{1/2}$	I_1	I_2	I_l [d](A)	$1/\omega^{1/2}$	$1/I_l$ (A^{-1})
500	52.35988	7.23601255	0	3.41E-04	3.41E-04	0.13819766	2.93E+03
750	78.53982	8.86226925	0	4.13E-04	4.13E-04	0.112837917	2.42E+03
1000	104.7198	10.2332671	0	4.74E-04	4.74E-04	0.097720502	2.11E+03
1250	130.8997	11.4411404	0	5.26E-04	5.26E-04	0.087403874	1.90E+03
1500	157.0796	12.5331414	0	5.73E-04	5.73E-04	0.079788456	1.74E+03
1750	183.2596	13.5373399	0	6.11E-04	6.11E-04	0.073869756	1.64E+03
2000	209.4395	14.4720251	0	6.49E-04	6.49E-04	0.06909883	1.54E+03
2250	235.6194	15.3499006	0	6.82E-04	6.82E-04	0.065147002	1.47E+03
2500	261.7994	16.1802159	0	7.12E-04	7.12E-04	0.061803872	1.40E+03

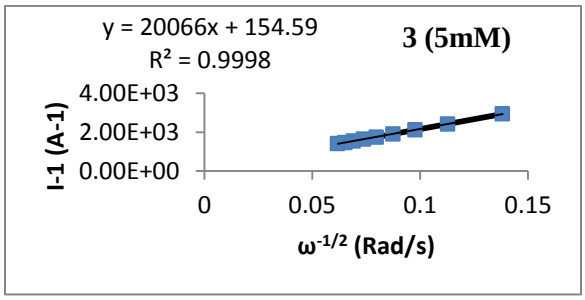

Figure A.5. Graph of I^{-1} vs $\omega^{-1/2}$ to determine diffusion coefficient from 5 mM of **3**

Slope	20066
$D^{2/3}$	4.08E-04
D	8.23968E-06 cm^2/s

Table A.14. Parameters for RDE experiment on 10mM of **3**.[a]

RPM[b]	ω[c] (rad/s)	$\omega^{1/2}$	I_1	I_2	I_l [d](A)	$1/\omega^{1/2}$	$1/I_l$ (A^{-1})
500	52.35988	7.23601255	0	7.36E-04	7.36E-04	0.13819766	1.36E+03
750	78.53982	8.86226925	0	8.97E-04	8.97E-04	0.112837917	1.11E+03
1000	104.7198	10.2332671	0	1.03E-03	1.03E-03	0.097720502	9.74E+02
1250	130.8997	11.4411404	0	1.14E-03	1.14E-03	0.087403874	8.74E+02
1500	157.0796	12.5331414	0	1.26E-03	1.26E-03	0.079788456	7.96E+02
1750	183.2596	13.5373399	0	1.36E-03	1.36E-03	0.073869756	7.36E+02
2000	209.4395	14.4720251	0	1.45E-03	1.45E-03	0.06909883	6.89E+02
2250	235.6194	15.3499006	0	1.54E-03	1.54E-03	0.065147002	6.51E+02
2500	261.7994	16.1802159	0	1.64E-03	1.64E-03	0.061803872	6.12E+02

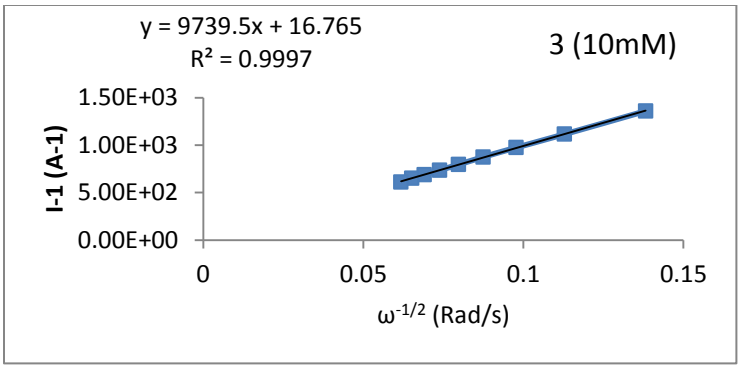

Figure A.6. Graph of I^{-1} vs $\omega^{-1/2}$ to determine diffusion coefficient from 10 mM of **3**

Slope	9739.5
$D^{2/3}$	4.20E-04
D	8.60204E-06 cm^2/s

Table A.15. Parameters for RDE experiment on 2.5mM of **1**.[a]

RPM[b]	ω[c] (rad/s)	$\omega^{1/2}$	I_1	I_2	I_l [d](A)	$1/\omega^{1/2}$	$1/I_l$ (A^{-1})
500	52.3598776	7.23601255	0	4.61E-04	4.61E-04	0.138198	2.17E+03
750	78.5398163	8.86226925	0	5.48E-04	5.48E-04	0.112838	1.83E+03
1000	104.719755	10.2332671	0	6.23E-04	6.23E-04	0.097721	1.61E+03
1250	130.899694	11.4411404	0	6.88E-04	6.88E-04	0.087404	1.45E+03
1500	157.079633	12.5331414	0	7.44E-04	7.44E-04	0.079788	1.34E+03
1750	183.259571	13.5373399	0	7.92E-04	7.92E-04	0.07387	1.26E+03
2000	209.43951	14.4720251	0	8.33E-04	8.33E-04	0.069099	1.20E+03
2250	235.619449	15.3499006	0	8.72E-04	8.72E-04	0.065147	1.15E+03
2500	261.799388	16.1802159	0	8.95E-04	8.95E-04	0.061804	1.12E+03

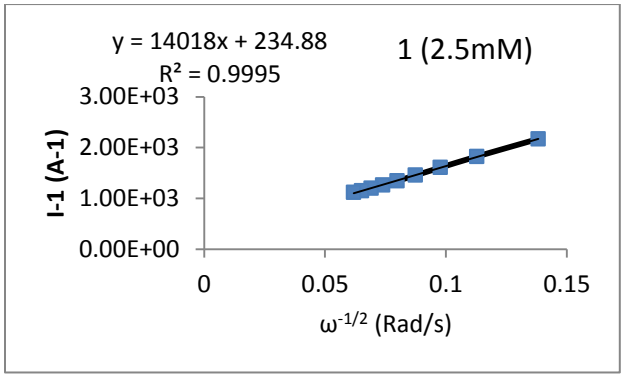

Figure A.7. Graph of I^{-1} vs $\omega^{-1/2}$ to determine diffusion coefficient from 2.5 mM of **1**

Slope	14018
$D^{2/3}$	1.18E-03
D	4.07646E-05 cm^2/s

Table A.16. Parameters for RDE experiment on 5mM of **1**.[a]

RPM[b]	ω[c] (rad/s)	$\omega^{1/2}$	I_1	I_2	I_l [d](A)	$1/\omega^{1/2}$	$1/I_l$ (A^{-1})
500	52.3598776	7.23601255	0	1.02E-03	1.02E-03	0.138198	9.78E+02
750	78.5398163	8.86226925	0	1.23E-03	1.23E-03	0.112838	8.12E+02
1000	104.719755	10.2332671	0	1.39E-03	1.39E-03	0.097721	7.19E+02
1250	130.899694	11.4411404	0	1.53E-03	1.53E-03	0.087404	6.56E+02
1500	157.079633	12.5331414	0	1.65E-03	1.65E-03	0.079788	6.08E+02
1750	183.259571	13.5373399	0	1.76E-03	1.76E-03	0.07387	5.68E+02
2000	209.43951	14.4720251	0	1.85E-03	1.85E-03	0.069099	5.39E+02
2250	235.619449	15.3499006	0	1.92E-03	1.92E-03	0.065147	5.20E+02
2500	261.799388	16.1802159	0	2.00E-03	2.00E-03	0.061804	5.00E+02

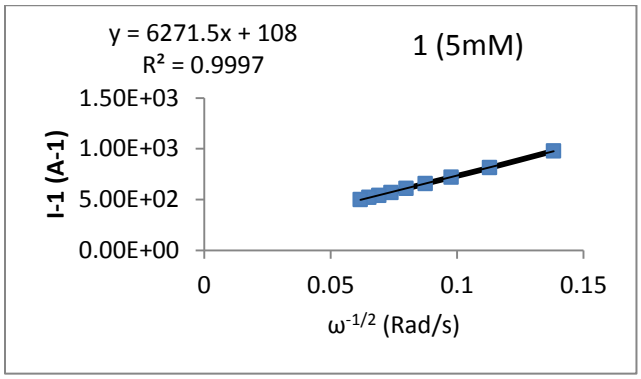

Figure A.8. Graph of I^{-1} vs $\omega^{-1/2}$ to determine diffusion coefficient from 5 mM of **1**

Slope	6271.5
$D^{2/3}$	1.31E-03
D	4.74406E-05 cm^2/s

Table A.17. Parameters for RDE experiment on 7.5mM of **1**.[a]

RPM[b]	ω[c] (rad/s)	$\omega^{1/2}$	I_1	I_2	I_l [d](A)	$1/\omega^{1/2}$	$1/I_l$ (A^{-1})
500	52.3598776	7.23601255	0	1.53E-03	1.53E-03	0.138198	6.53E+02
750	78.5398163	8.86226925	0	1.85E-03	1.85E-03	0.112838	5.39E+02
1000	104.719755	10.2332671	0	2.10E-03	2.10E-03	0.097721	4.75E+02
1250	130.899694	11.4411404	0	2.31E-03	2.31E-03	0.087404	4.32E+02
1500	157.079633	12.5331414	0	2.49E-03	2.49E-03	0.079788	4.01E+02
1750	183.259571	13.5373399	0	2.65E-03	2.65E-03	0.07387	3.77E+02
2000	209.43951	14.4720251	0	2.77E-03	2.77E-03	0.069099	3.61E+02
2250	235.619449	15.3499006	0	2.92E-03	2.92E-03	0.065147	3.43E+02
2500	261.799388	16.1802159	0	3.04E-03	3.04E-03	0.061804	3.29E+02

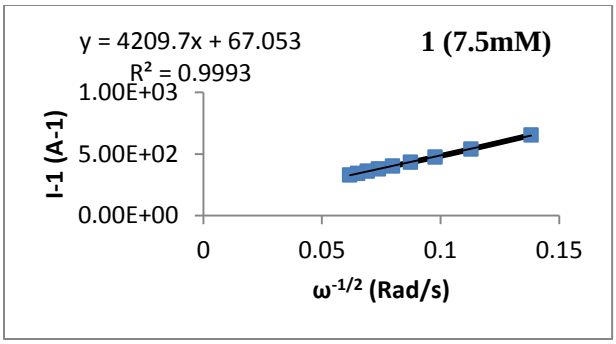

Figure A.9. Graph of I^{-1} vs $\omega^{-1/2}$ to determine diffusion coefficient from 7.5 mM of **1**

Slope	4209.7
$D^{2/3}$	1.30E-03
D	4.70978E-05 cm^2/s

Table A.18. Parameters for RDE experiment on 2.5mM of **14**.[a]

RPM[b]	ω[c] (rad/s)	$\omega^{1/2}$	I_1	I_2	I_l [d](A)	$1/\omega^{1/2}$	$1/I_l$ (A^{-1})
500	52.3598776	7.23601255	0	4.60E-04	4.60E-04	0.138198	2.17E+03
750	78.5398163	8.86226925	0	5.48E-04	5.48E-04	0.112838	1.82E+03
1000	104.719755	10.2332671	0	6.19E-04	6.19E-04	0.097721	1.62E+03
1250	130.899694	11.4411404	0	6.76E-04	6.76E-04	0.087404	1.48E+03
1500	157.079633	12.5331414	0	7.24E-04	7.24E-04	0.079788	1.38E+03
1750	183.259571	13.5373399	0	7.66E-04	7.66E-04	0.07387	1.31E+03
2000	209.43951	14.4720251	0	8.02E-04	8.02E-04	0.069099	1.25E+03
2250	235.619449	15.3499006	0	8.35E-04	8.35E-04	0.065147	1.20E+03
2500	261.799388	16.1802159	0	8.65E-04	8.65E-04	0.061804	1.16E+03

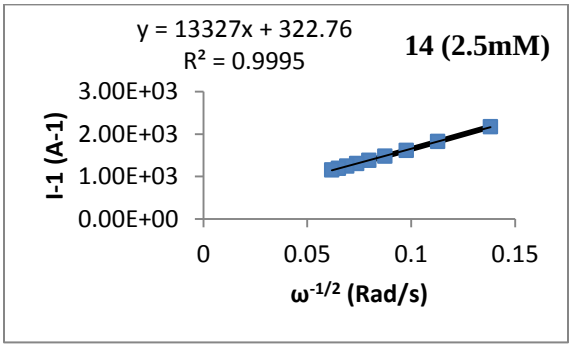

Figure A.10. Graph of I^{-1} vs $\omega^{-1/2}$ to determine diffusion coefficient from 2.5 mM of **14**

Slope	13327
$D^{2/3}$	1.24E-03
D	4.37101E-05 cm^2/s

Table A.19. Parameters for RDE experiment on 5mM of **14**.[a]

RPM[b]	ω[c] (rad/s)	$\omega^{1/2}$	I_1	I_2	I_l [d](A)	$1/\omega^{1/2}$	$1/I_l$ (A^{-1})
500	52.3598776	7.23601255	0	9.42E-04	9.42E-04	0.138198	1.06E+03
750	78.5398163	8.86226925	0	1.11E-03	1.11E-03	0.112838	9.03E+02
1000	104.719755	10.2332671	0	1.25E-03	1.25E-03	0.097721	8.01E+02
1250	130.899694	11.4411404	0	1.37E-03	1.37E-03	0.087404	7.29E+02
1500	157.079633	12.5331414	0	1.48E-03	1.48E-03	0.079788	6.78E+02
1750	183.259571	13.5373399	0	1.56E-03	1.56E-03	0.07387	6.40E+02
2000	209.43951	14.4720251	0	1.64E-03	1.64E-03	0.069099	6.10E+02
2250	235.619449	15.3499006	0	1.70E-03	1.70E-03	0.065147	5.89E+02
2500	261.799388	16.1802159	0	1.73E-03	1.73E-03	0.061804	5.78E+02

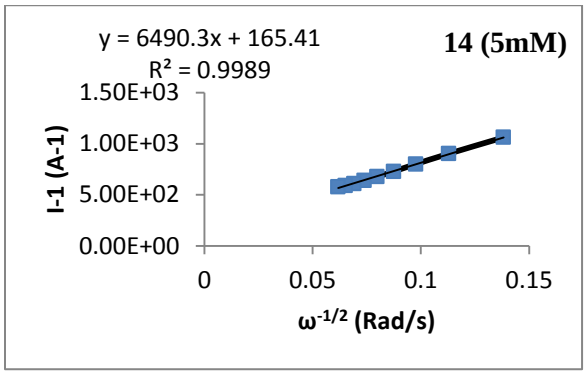

Figure A.11. Graph of I^{-1} vs $\omega^{-1/2}$ to determine diffusion coefficient from 5 mM of **14**

Slope	6490.3
$D^{2/3}$	1.26E-03
D	4.47924E-05 cm^2/s

Table A.20. Parameters for RDE experiment on 7.5mM of **14**.[a]

RPM[b]	ω[c] (rad/s)	$\omega^{1/2}$	I_1	I_2	I_l [d](A)	$1/\omega^{1/2}$	$1/I_l$ (A^{-1})
500	52.3598776	7.23601255	0	1.26E-03	1.26E-03	0.138198	7.96E+02
750	78.5398163	8.86226925	0	1.49E-03	1.49E-03	0.112838	6.72E+02
1000	104.719755	10.2332671	0	1.68E-03	1.68E-03	0.097721	5.96E+02
1250	130.899694	11.4411404	0	1.84E-03	1.84E-03	0.087404	5.44E+02
1500	157.079633	12.5331414	0	1.96E-03	1.96E-03	0.079788	5.09E+02
1750	183.259571	13.5373399	0	2.08E-03	2.08E-03	0.07387	4.81E+02
2000	209.43951	14.4720251	0	2.11E-03	2.11E-03	0.069099	4.74E+02
2250	235.619449	15.3499006	0	2.14E-03	2.14E-03	0.065147	4.66E+02

[a] All for tables **A.12 – A.20,** determination of diffusion coefficients from Levich equation: $I_l = (0.620)nFAD^{2/3}\omega^{0.5}\nu^{-1/6}C$ where I_l is the limiting current, n is the number of electrons transferred, F is the Faraday's constant, D is the diffusion coefficient, ω is the angular rotation rate of the electrode, ν is the scan rate and C is the concentration of the DTAs in solution. [b] RPM = Revolution per minute. [c] ω = angular rotation rate of the electrode. [d] I_l = limiting current.

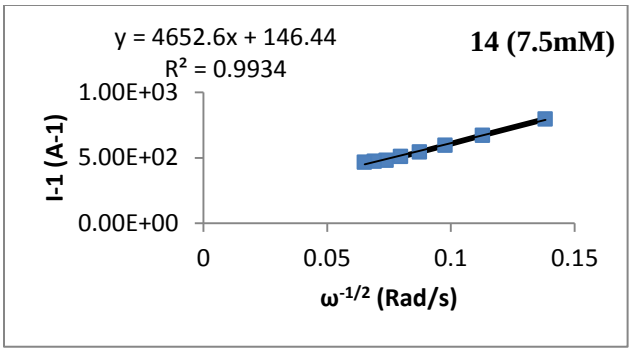

Figure A.12. Graph of I^{-1} vs $\omega^{-1/2}$ to determine diffusion coefficient from 7.5 mM of **14**

Slope	4652.6
$D^{2/3}$	1.18E-03
D	4.05353E-05 cm^2/s

Table A.21. Determination of electrode surface area via RDE experiment on 2.5mM Ferrocene.[a]

RPM[b]	ω[c] (rad/s)	$\omega^{1/2}$	I_1	I_2	I_l [d](A)	$1/\omega^{1/2}$	$1/I_l$ (A^{-1})
500	52.3598776	7.23601255	0	3.46E-04	3.46E-04	0.138198	2.89E+03
750	78.5398163	8.86226925	0	4.26E-04	4.26E-04	0.112838	2.35E+03
1000	104.719755	10.2332671	0	4.86E-04	4.86E-04	0.097721	2.06E+03
1250	130.899694	11.4411404	0	5.43E-04	5.43E-04	0.087404	1.84E+03
1500	157.079633	12.5331414	0	5.96E-04	5.96E-04	0.079788	1.68E+03
1750	183.259571	13.5373399	0	6.44E-04	6.44E-04	0.07387	1.55E+03
2000	209.43951	14.4720251	0	6.89E-04	6.89E-04	0.069099	1.45E+03

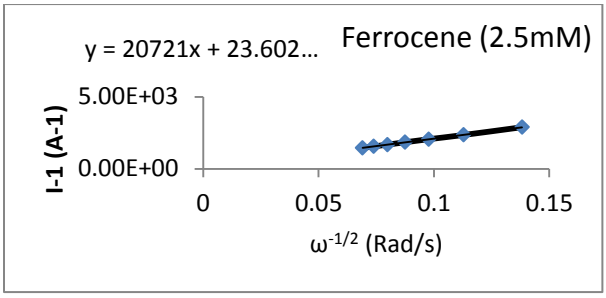

Figure A.13. Graph of I^{-1} vs $\omega^{-1/2}$ to determine electrode area in 2.5 mM ferrocene

Slope 2.5mM	20721
A	1.62E-01 cm^2

Table A.22. Determination of electrode surface area via RDE experiment on 5mM Ferrocene.[a]

RPM[b]	ω[c] (rad/s)	$\omega^{1/2}$	I_1	I_2	I_l [d](A)	$1/\omega^{1/2}$	$1/I_l$ (A^{-1})
500	52.3598776	7.23601255	0	7.28E-04	7.28E-04	0.138198	1.37E+03
750	78.5398163	8.86226925	0	8.87E-04	8.87E-04	0.112838	1.13E+03
1000	104.719755	10.2332671	0	1.02E-03	1.02E-03	0.097721	9.80E+02
1250	130.899694	11.4411404	0	1.14E-03	1.14E-03	0.087404	8.80E+02
1500	157.079633	12.5331414	0	1.24E-03	1.24E-03	0.079788	8.04E+02
1750	183.259571	13.5373399	0	1.34E-03	1.34E-03	0.07387	7.45E+02
2000	209.43951	14.4720251	0	1.43E-03	1.43E-03	0.069099	6.99E+02

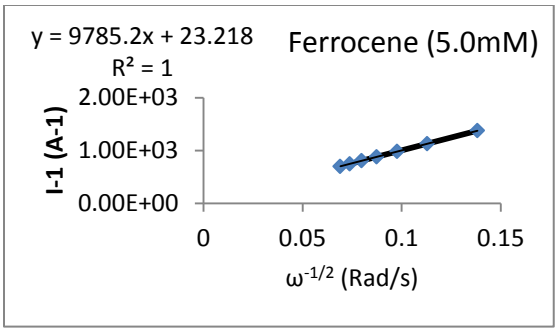

Figure A.14. Graph of I^{-1} vs $\omega^{-1/2}$ to determine electrode area in 5 mM ferrocene

Slope (5mM)	9785.2
A	1.71E-01 cm^2

Table A.23. Determination of electrode surface area via RDE experiment on 10 mM Ferrocene.[a]

RPM[b]	ω[c] (rad/s)	$\omega^{1/2}$	I_1	I_2	I_l [d](A)	$1/\omega^{1/2}$	$1/I_l$ (A^{-1})
500	52.3598776	7.23601255	0	1.40E-03	1.40E-03	0.138198	7.12E+02
750	78.5398163	8.86226925	0	1.72E-03	1.72E-03	0.112838	5.81E+02
1000	104.719755	10.2332671	0	1.97E-03	1.97E-03	0.097721	5.07E+02
1250	130.899694	11.4411404	0	2.21E-03	2.21E-03	0.087404	4.53E+02
1500	157.079633	12.5331414	0	2.43E-03	2.43E-03	0.079788	4.12E+02
1750	183.259571	13.5373399	0	2.64E-03	2.64E-03	0.07387	3.79E+02
2000	209.43951	14.4720251	0	2.84E-03	2.84E-03	0.069099	3.52E+02

[a] All for tables **A.21 – A.23,** determination of diffusion coefficients from Levich equation: $I_l = (0.620)nFAD^{2/3}\omega^{0.5}\nu^{-1/6}C$ where I_l is the limiting current, n is the number of electrons transferred, F is the Faraday's constant, D is the diffusion coefficient of ferrocene taken as 2.30E-05cm^2/s, ω is the angular rotation rate of the electrode, ν is the scan rate and C is the concentration of ferrocene in solution. [b] RPM = Revolution per minute. [c] ω = angular rotation rate of the electrode. [d] I_l = limiting current.

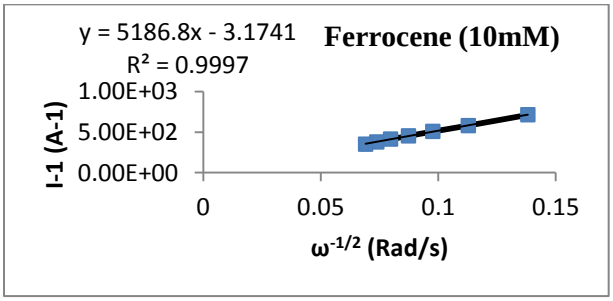

Figure A.15. Graph of I^{-1} vs $\omega^{-1/2}$ to determine electrode area in 10 mM ferrocene

	5186.8
A	1.61E-01cm^2

Table A.24a Statistical analysis of diffusion coefficient and surface area of electrode data[f]

	(D) cm^2/s [$1e^-$ transfer]			
Conc.(mM)		**3**	**1**	**14**
	2.5[a]	8.58E-06	4.08E-05	4.37E-05
	5.0[b]	8.24E-06	4.74E-05	4.48E-05
	7.5[c]	-	4.71E-05	4.05E-05
	10.0[d]	8.60E-06	-	-
MEAN		8.48E-06	4.51E-05	4.30E-05
SD[e]		2.04E-07	3.76E-06	2.21E-06
		8.5(2)	4.5(4)	4.3(2)

[a] Actual concentrations were 2.47, 2.46 and 2.48 mM respectively for **3**, **1**, and **14**.
[b] Actual concentrations were 5.01, 4.99 and 5.01 mM respectively for **3**, **1**, and **14**.
[c] Actual concentrations were 7.47 mM respectively for **1** and **14**.
[d] Actual concentration was 10.03 mM respectively for **3**.
[e] Standard deviation.
[f] Standard errors associated with concentrations range from 0.2-1.6 %.

Table A.24b Statistical analysis of diffusion coefficient and surface area of electrode data[f]

	(D) cm^2/s [$2e^-$ transfer]		
Conc.(mM)	**3**	**1**	**14**
2.5[a]	2.98E-06	1.42E-05	1.53E-05
5.0[b]	2.92E-06	1.67E-05	1.59E-05
7.5[c]	-	1.66E-05	1.42E-05
10.0[d]	3.06E-06	-	-
MEAN	2.99E-06	1.58E-05	1.51E-05
SD[e]	6.67E-08	1.44E-06	8.28E-07
	3.0(7)	1.6(1)	1.5(8)

[a] Actual concentrations were 2.47, 2.46 and 2.48 mM respectively for **3**, **1**, and **14**.
[b] Actual concentrations were 5.01, 4.99 and 5.01 mM respectively for **3**, **1**, and **14**.
[c] Actual concentrations were 7.47 mM respectively for **1** and **14**.
[d] Actual concentration was 10.03 mM respectively for **3**.
[e] Standard deviation.
[f] Standard errors associated with concentrations range from 0.2-1.6 %.

Table A.25. Selected interatomic distances for **3** and literature dithiazolium salts.

Distance, Å	I_3^-	$FeBr_4^-$	ClO_4^-	Mean(D)	Deviation
S2-S1	2.020 (1)	2.019 (1)	2.007 (2)	2.015(7)	0.007234
S1-C1	1.718 (3)	1.732 (2)	1.726 (5)	1.725(7)	0.007024
C1-N1	1.324 (4)	1.328 (3)	1.319 (6)	1.324(5)	0.004509
N1-C2	1.323 (4)	1.324 (4)	1.318 (5)	1.322(3)	0.003215
C2-S2	1.719 (3)	1.729 (3)	1.720 (5)	1.723(6)	0.005508

Table A.26. Selected interatomic distances for **1** and literature dithiazolium salts.

Distance, Å	$CoCl_4^-$	$Cu_2Cl_6^{2-}$	ClO_4^-	Mean(D)	Deviation
S2-S1	2.036 (2)	2.044 (2)	2.044 (8)	2.041(5)	0.0046188
S1-C1	1.730 (4)	1.734 (5)	1.738 (2)	1.734(4)	0.004
C1-N1	1.304 (4)	1.300 (7)	1.300 (3)	1.301(2)	0.0023094
N1-C2	1.346 (4)	1.351 (6)	1.351 (2)	1.349(3)	0.00288675
C2-S2	1.749 (4)	1.754 (3)	1.751 (2)	1.759(3)	0.00251661

Table A.27. Selected interatomic distances for **14** and literature dithiazolium salts.

Distance, Å	Cl^-	PF_6^-	SCN^-	Mean(D)	Deviation
S2-S1	2.053 (5)	2.063 (5)	2.057(1)	2.058(5)	0.005033
S1-C1	1.762 (1)	1.760 (1)	1.758(4)	1.760(2)	0.002
C1-N1	1.329 (2)	1.320 (2)	1.324(5)	1.324(5)	0.004509
N1-C2	1.332 (2)	1.380 (1)	1.328(5)	1.347(29)	0.028937
C2-S2	1.767 (1)	1.750 (1)	1.768(4)	1.762(10)	0.010116

Table A.28. Peak currents versus square root of scan rate to determine diffusion controlled experiment in 3.09 mM of **3.**

Scan rates V/s	$\sqrt{v}$	Ic (A)	Ia (A)
0.05	0.22	9.98E-05	2.32E-05
0.1	0.32	1.37E-04	2.32E-05
0.2	0.45	1.91E-04	2.32E-05
0.4	0.63	2.62E-04	2.32E-05
0.6	0.77	3.14E-04	2.32E-05
0.8	0.89	3.58E-04	2.32E-04
1.0	1.00	3.94E-04	2.32E-04
1.5	1.22	4.72E-04	2.32E-04
2.0	1.41	5.31E-04	2.32E-04

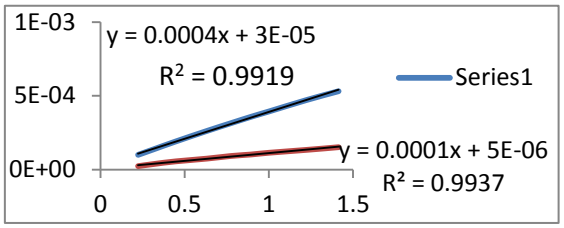

Figure A.16. Graph of currents vs. square root of scan rates (**for 3**) at a Platinum electrode of surface area 0.165cm^2 in CH_3CN solution containing 0.1 M [^{n}Bu$_4$N][PF_6].

Table A.29. Peak currents versus square root of scan rate to determine diffusion controlled experiment in 5.89 mM of **3.**

Scan rates V/s	$\sqrt{v}$	Ic (A)	Ia (A)
0.1	0.32	2.41E-04	5.02E-05
0.2	0.45	3.31E-04	8.49E-05
0.4	0.63	4.49E-04	1.38E-04
0.6	0.77	5.18E-04	1.64E-04
0.8	0.89	5.90E-04	1.90E-04
1.0	1.00	6.38E-04	2.10E-04
1.5	1.22	7.57E-04	2.46E-04
2.0	1.41	8.52E-04	2.68E-04

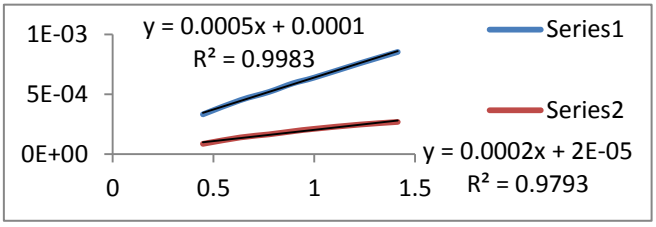

Figure A.17. Graph of currents vs. square root of scan rates (**for 3**) at a Platinum electrode of surface area 0.165cm^2 in CH_3CN solution containing 0.1 M [^{n}Bu$_4$N][PF$_6$].

Table A.30. Peak currents versus square root of scan rate to determine diffusion controlled experiment in 9.80 mM of **3.**

Scan rates V/s	$\sqrt{v}$	Ic (A)	Ia (A)
0.1	0.32	3.89E-04	8.95E-05
0.2	0.45	5.31E-04	1.48E-04
0.4	0.63	6.53E-04	2.21E-04
0.6	0.77	7.63E-04	2.60E-04
0.8	0.89	9.22E-04	3.15E-04
1.0	1.00	1.02E-03	3.38E-04
1.5	1.22	1.20E-03	3.95E-04
2.0	1.41	1.34E-03	4.42E-04

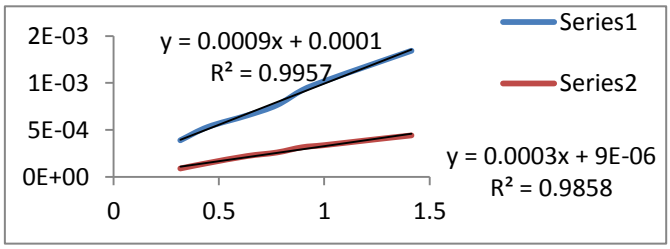

Figure A.18. Graph of currents vs. square root of scan rates (**for 3**) at a Platinum electrode of surface area 0.165cm^2 in CH_3CN solution containing 0.1 M [^{n}Bu$_4$N][PF$_6$].

Table A.31. Peak currents versus square root of scan rate to determine diffusion controlled experiment in 3.13 mM of **1.**

Scan rates V/s	$\sqrt{v}$	Ic (A)	Ia (A)
0.05	0.22	2.55E-04	8.27E-05
0.1	0.32	3.51E-04	1.45E-04
0.2	0.45	4.82E-04	2.18E-04
0.4	0.63	6.53E-04	3.03E-04
0.6	0.77	7.81E-04	3.59E-04
0.8	0.89	8.82E-04	4.04E-04
1.0	1.00	9.71E-04	4.41E-04
1.5	1.22	1.15E-03	5.23E-04
2.0	1.41	1.30E-03	5.85E-04
5.0	2.23	1.89E-03	8.38E-04

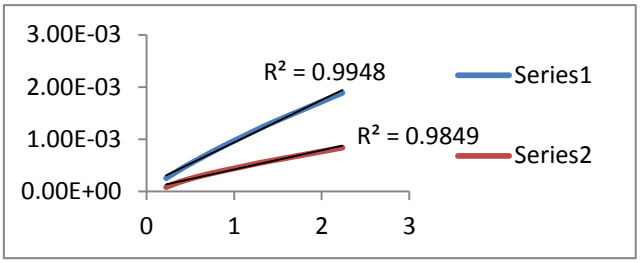

Figure A.19. Graph of currents vs. square root of scan rates (**for 1**) at a Platinum electrode of surface area 0.165cm^2 in CH_3CN solution containing 0.1 M [^{n}Bu$_4$N][PF$_6$].

Table A.32. Peak currents versus square root of scan rate to determine diffusion controlled experiment in 6.16 mM of **1.**

Scan rates V/s	$\sqrt{v}$	Ic (A)	Ia (A)
0.05	0.22	4.55E-04	1.97E-04
0.1	0.32	5.55E-04	2.60E-04
0.4	0.63	9.80E-04	4.67E-04
0.6	0.77	1.18E-03	5.57E-04
0.8	0.89	1.35E-03	6.38E-04
1.0	1.00	1.46E-03	6.71E-04

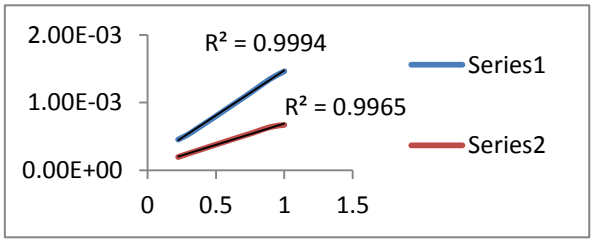

Figure A.20. Graph of currents vs. square root of scan rates (**for 1**) at a Platinum electrode of surface area 0.165cm^2 in CH_3CN solution containing 0.1 M [^{n}Bu$_4$N][PF$_6$].

Table A.33. Peak currents versus square root of scan rate to determine Diffusion controlled experiment in 9.92 mM of **1.**

Scan rates V/s	$\sqrt{v}$	Ic (A)	Ia (A)
0.05	0.22	7.23E-04	2.79E-04
0.1	0.32	9.62E-04	4.31E-04
0.2	0.45	1.35E-03	6.67E-04
0.6	0.77	1.96E-03	9.64E-04
0.8	0.89	2.20E-03	1.08E-03
1.0	1.00	2.39E-03	1.16E-03

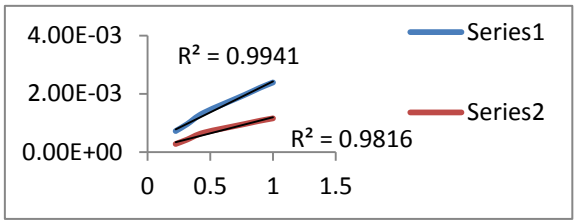

Figure A.21. Graph of currents vs. square root of scan rates (**for 1**) at a Platinum electrode of surface area 0.165cm^2 in CH_3CN solution containing 0.1 M [^{n}Bu$_4$N][PF$_6$].

Table A.34. Peak currents versus square root of scan rate to determine diffusion controlled experiment in 2.97 mM of **14.**

Scan rates V/s	$\sqrt{v}$	Ic (A)	Ia (A)
0.2	0.45	3.93E-04	2.15E-04
0.4	0.63	5.35E-04	2.99E-04
0.6	0.77	6.25E-04	3.59E-04
0.8	0.89	7.07E-04	4.14E-04
1.0	1.00	7.59E-04	4.50E-04
1.5	1.22	9.21E-04	5.48E-04
2.0	1.41	1.04E-03	6.15E-04

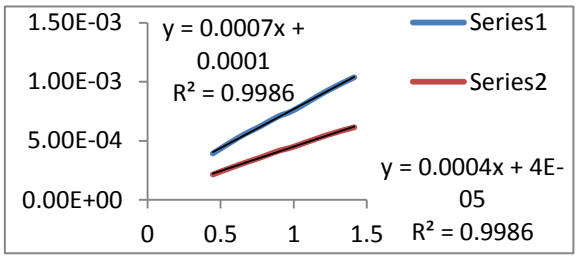

Figure A.22. Graph of currents vs. square root of scan rates (**for 14**) at a Platinum electrode of surface area 0.165cm^2 in CH_3CN solution containing 0.1 M [^{n}Bu$_4$N][PF$_6$].

Table A.35. Peak currents versus square root of scan rate to determine diffusion controlled experiment in 5.95 mM of **14.**

Scan rates V/s	$\sqrt{v}$	Ic (A)	Ia (A)
0.05	0.22	3.97E-04	1.97E-04
0.1	0.32	5.42E-04	2.96E-04
0.2	0.45	7.15E-04	4.08E-04
0.4	0.63	9.14E-04	5.61E-04
0.6	0.77	1.09E-03	6.70E-04
0.8	0.89	1.29E-03	7.92E-04
1.0	1.00	1.42E-03	8.75E-04
2.0	1.41	1.94E-03	1.20E-03

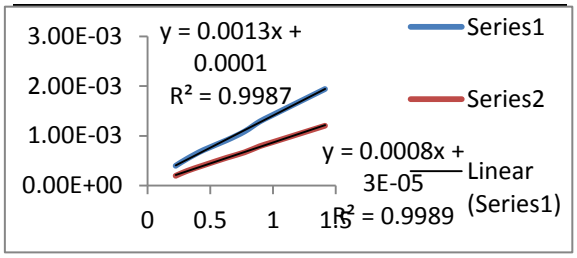

Figure A.23. Graph of currents vs. square root of scan rates (**for 14**) at a Platinum electrode of surface area 0.165cm^2 in CH_3CN solution containing 0.1 M [^{n}Bu$_4$N][PF$_6$].

Table A.36. Peak currents versus square root of scan rate to determine diffusion controlled experiment in 10.02 mM of **14.**

Scan rates V/s	$\sqrt{v}$	Ic (A)	Ia (A)
0.2	0.45	1.04E-03	5.64E-04
0.4	0.63	1.40E-03	8.07E-04
0.6	0.77	1.66E-03	9.83E-04
1.0	1.00	2.05E-03	1.26E-03
1.5	1.22	2.40E-03	1.50E-03
2.0	1.41	2.63E-03	1.66E-03

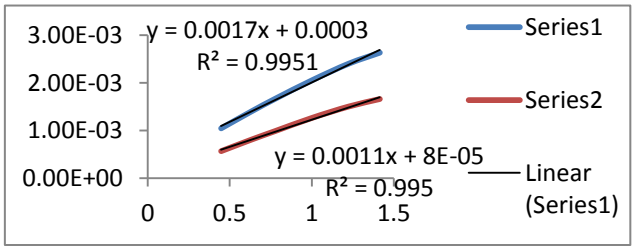

Figure A.24. Graph of currents vs. square root of scan rates (**for 14**) at a Platinum electrode of surface area 0.165cm^2 in CH_3CN solution containing 0.1 M [^{n}Bu$_4$N][PF$_6$].

Table A.37. Parameters for the formation of Open anion species of **3**, **1**, and **14** via the E_1E_2C mechanism

3

	$E^0$1	$E^0$2	K_{s1}	K_{s2}	K_{eq}	k_f
3.09	-0.04	-0.14	5.88E-06	1.42E-04	8113.6	1.00E+10
5.89	-0.02	-0.12	5.65E-06	2.98E-05	1944	1.00E+08
9.80	-0.03	-0.07	4.39E-06	7.59E-06	622.58	1.00E+10
mean	-0.0297	-0.11	5.31E-06	5.99E-05	3.56E+04	6.70E+09
S/deviation	0.01	0.04	8.00E-07	7.22E-05	3998.45	571576767
Mean(SD)	-0.03(1)	-0.11(4)	5(8)E-06	6(7)E-05	4(4)E+03	7(6)E+09

1

Conc (mM)	$E^0$1	$E^0$2	K_{s1}	K_{s2}	K_{eq}	k_f
3.13	-0.71	-0.81	4E-04	2E-02	11679	1.00E+10

14

Conc (mM)	$E^0$1	$E^0$2	K_{s1}	K_{s2}	K_{eq}	k_f
2.97	-0.95	-1.05	3.1E-03	4.8E-03	6552.9	1.00E+10
5.95	-0.94	-1.04	3.7E-03	3.6E-03	10287	1.00E+10
10.02	-0.96	-1.06	3.9E-03	4.1E-03	15334	1.00E+10
mean	-0.95	-1.05	3.6E-03	4.2E-03	10724.63	1.00E+10
s/deviation	0.0072	0.0072	0.00043	0.00057	4406.88	0
Mean(SD)	-0.95(1)	-1.05(1)	4(4)E-03	4(6)E-03	1(4)E+04	1.00E+10

SD-standard deviation

Table A.38. Parameters for the formation of dimer species of **3**, **1**, and **14** via the $E_1C_2E_2C_2$, Square scheme mechanism

3[a]

Conc (mM)	$E^0$1	$E^0$2	K_{s1}	K_{s2}	K_{f1}	k_{f2}
3.09	-0.44	0.33	3.64E-02	7.86E-04	1.16E+08	9.51E+01
5.89	-0.41	0.36	1.57E-02	6.69E-04	6.72E+08	115.27
9.80	-0.32	0.45	8.44E-03	7.19E-04	5.60E+08	62.04
mean	-0.39	0.38	2.02E-02	7.25E-04	4.49E+08	90.789
S/deviation	0.062	0.063	0.0145	5.89E-05	2.94E+08	26.870
Mean(SD)	-0.39(6)	-0.11(4)	0.02(1)	7.3(6)E-4	4(5)E+08	91(27)

[a] Keq1 is set at 10^8 for 3.09 mM, 5.89 mM, and 9.80 mM respectively to obtain the best reasonable fit.

1[b]

$E^0$1	$E^0$2	K_{s1}	K_{s2}	K_{f1}	K_{f2}
-0.90	-0.31	3.31E-02	3.62E-03	7.2E+09	2.6E+09

[a] Keq1 is set at 10^{10} for 3.13 Mm to obtain the best reasonable fit.

Table A.39. Dependence of cathodic peak currents on concentration for **3** [a]

Ic (A)	Conc. (mM)
1.37E-04	3.09
2.41E-04	5.89
3.89E-04	9.80

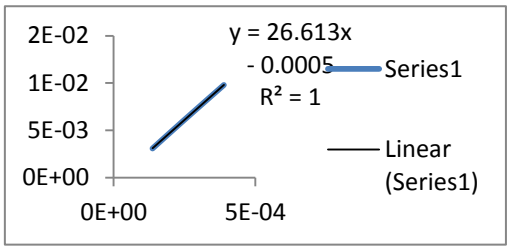

Figure A.25. Graph of cathodic peak currents vs. concentrations of **3**
[a] Data for **3** obtained at a platinum electrode, at a scan rate of 100 mV/s in CH_3CN solution containing 0.1 M [$^nBu_4N$][PF_6].

Table A.40. Dependence of cathodic peak currents on concentration for **1** [a]

Ic (A)	Conc. (mM)
3.51E-04	3.13
5.55E-04	6.16
9.62E-04	9.92

[a] Data for **1** obtained at a platinum electrode, at a scan rate of 100 mV/s in CH_3CN solution containing 0.1 M [$^nBu_4N$][PF_6].

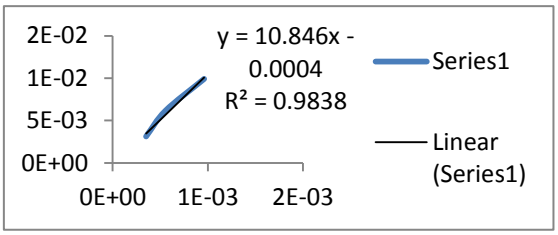

Figure A.26. Graph of cathodic peak currents vs. concentrations of **1.**

Table A.41. Dependence of cathodic peak currents on concentration for **14** [a]

Ic (A)	Conc. (mM)
3.93E-04	2.97
7.15E-04	5.95
1.04E-03M	10

[a] Data for **14** obtained at a platinum electrode, at a scan rate of 100 mV/s in CH_3CN solution containing 0.1 M [$^nBu_4N$][PF_6].

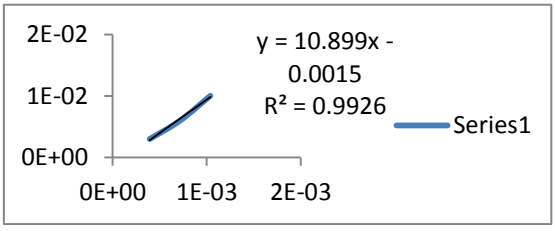

Figure A.27. Graph of cathodic peak currents vs. concentrations of **14.**

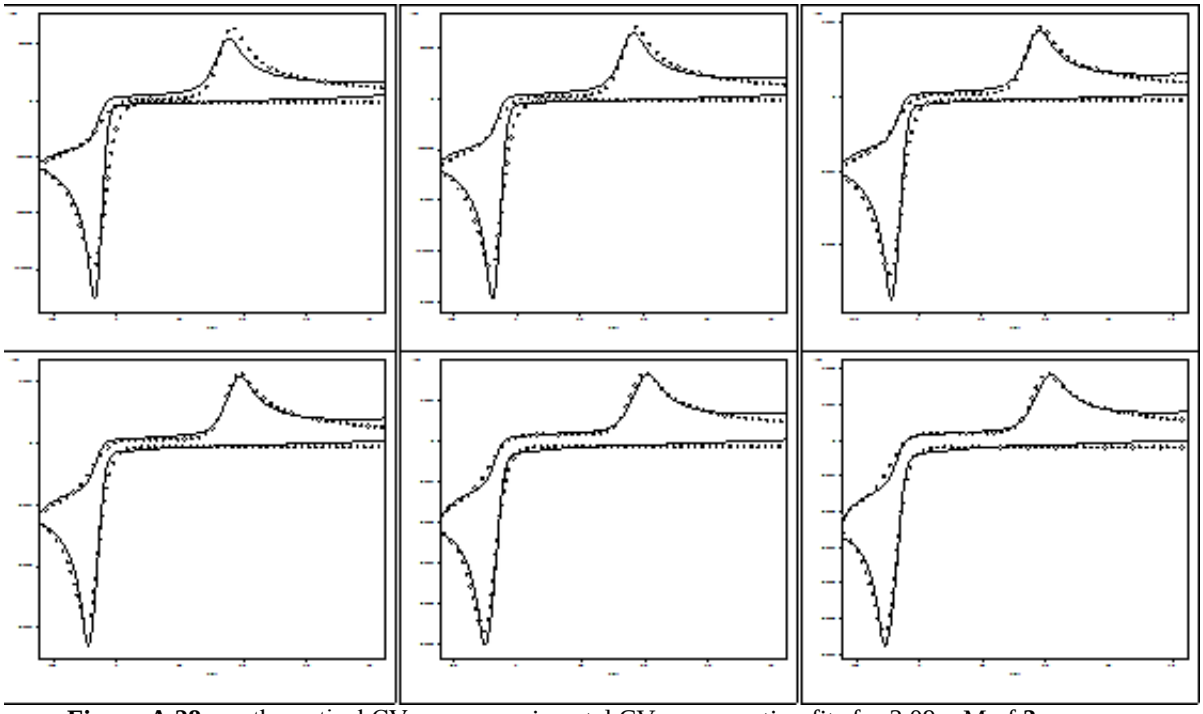

Figure A.28 ◦◦◦- theoretical CVs., ─- experimental CVs representing fits for 3.09 mM of **3** for the E_1E_2C mechanism. Left to right: ν = 100, 200, 400, 600, 1500, 2000 mV/s

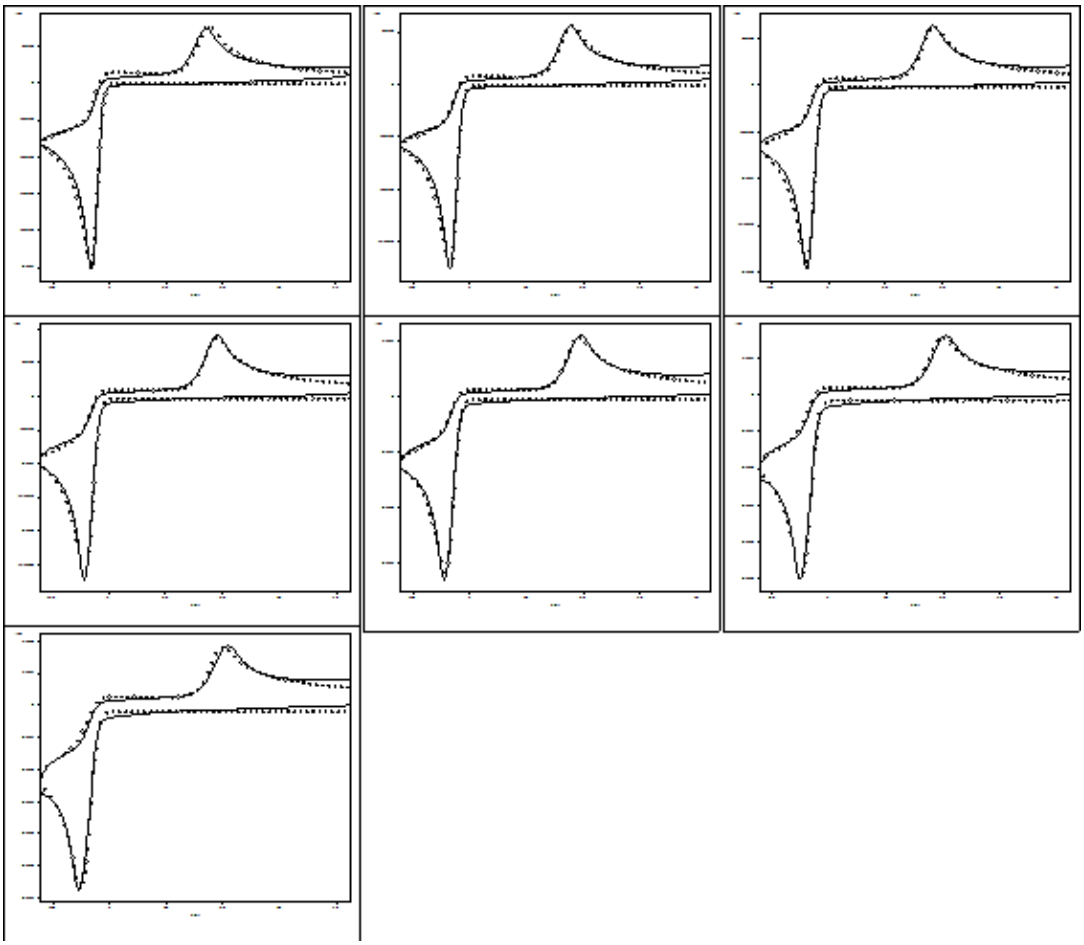

Figure A.29 ◦◦◦- theoretical CVs., ─- experimental CVs representing fits for 3.09 mM of **3** for the $E_1C_2E_2C_2$, mechanism. Left to right: ν = 50, 100, 200, 400, 600, 1500, 2000 mV/s

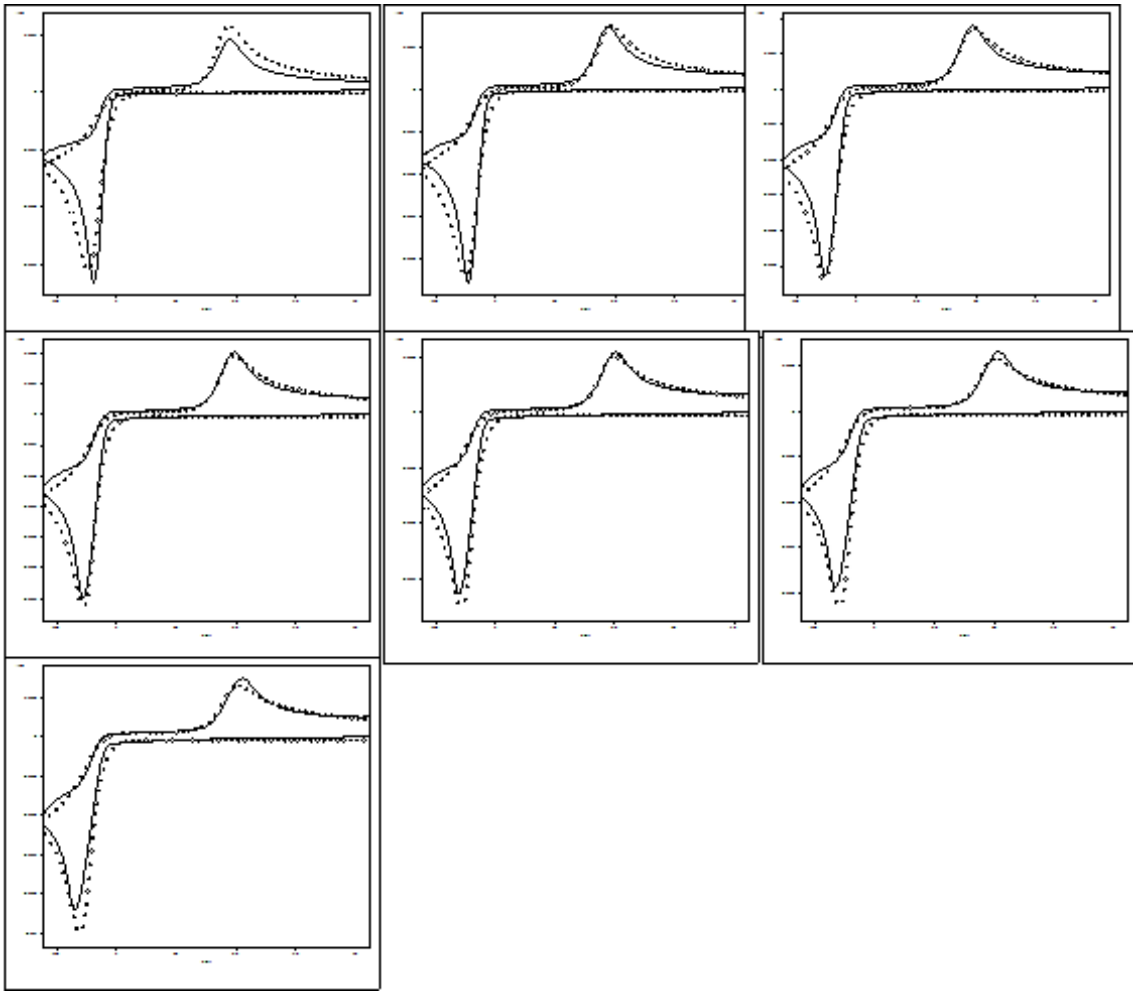

Figure A.30 ◦◦◦- theoretical CVs., ─- experimental CVs representing fits for 5.89 mM of **3** for the E_1E_2C mechanism. Left to right: ν = 200, 400, 600, 800, 1000, 1500, 2000 mV/s

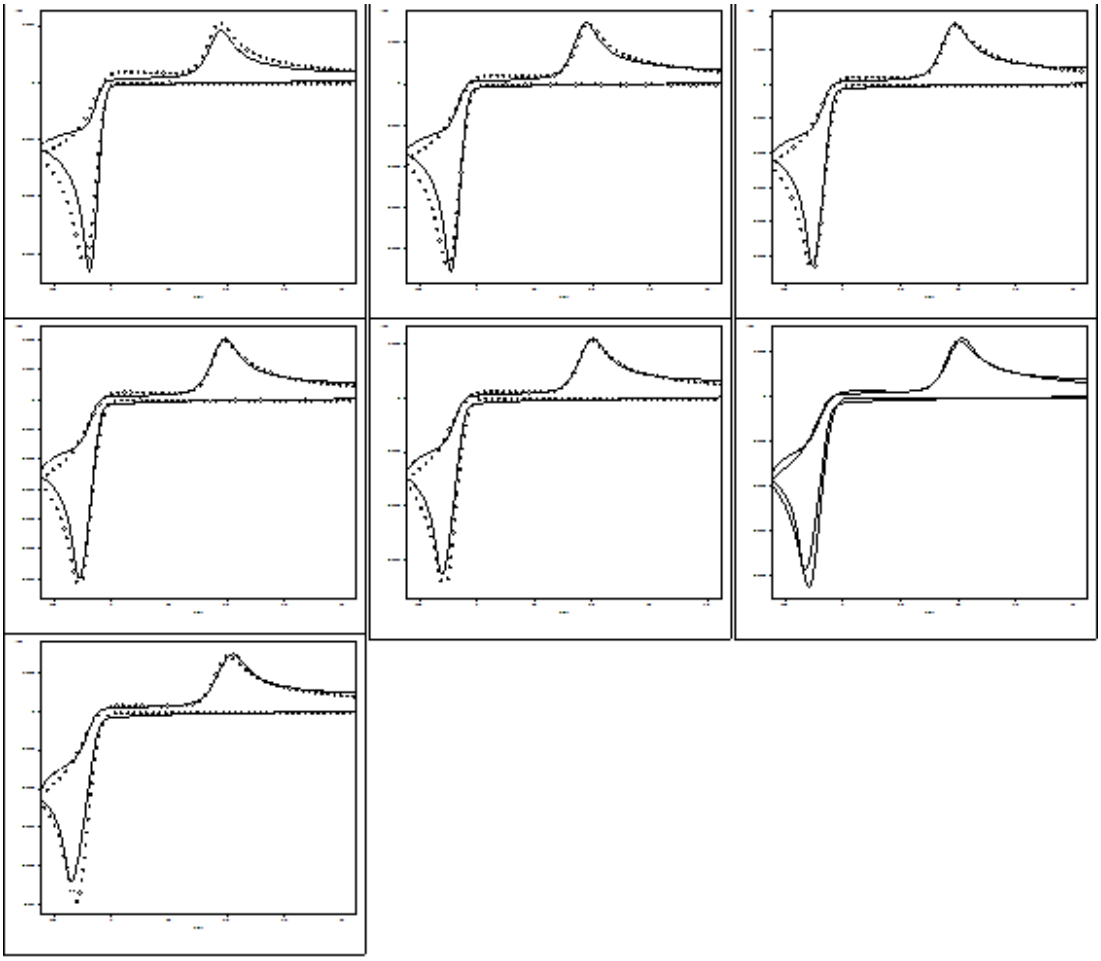

Figure A.31. ◦◦◦- theoretical CVs., —- experimental CVs representing fits for 5.89 mM of **3** for the $E_1C_2E_2C_2$, mechanism. Left to right: ν = 200, 400, 600, 800, 1000, 1500, 2000 mV/s

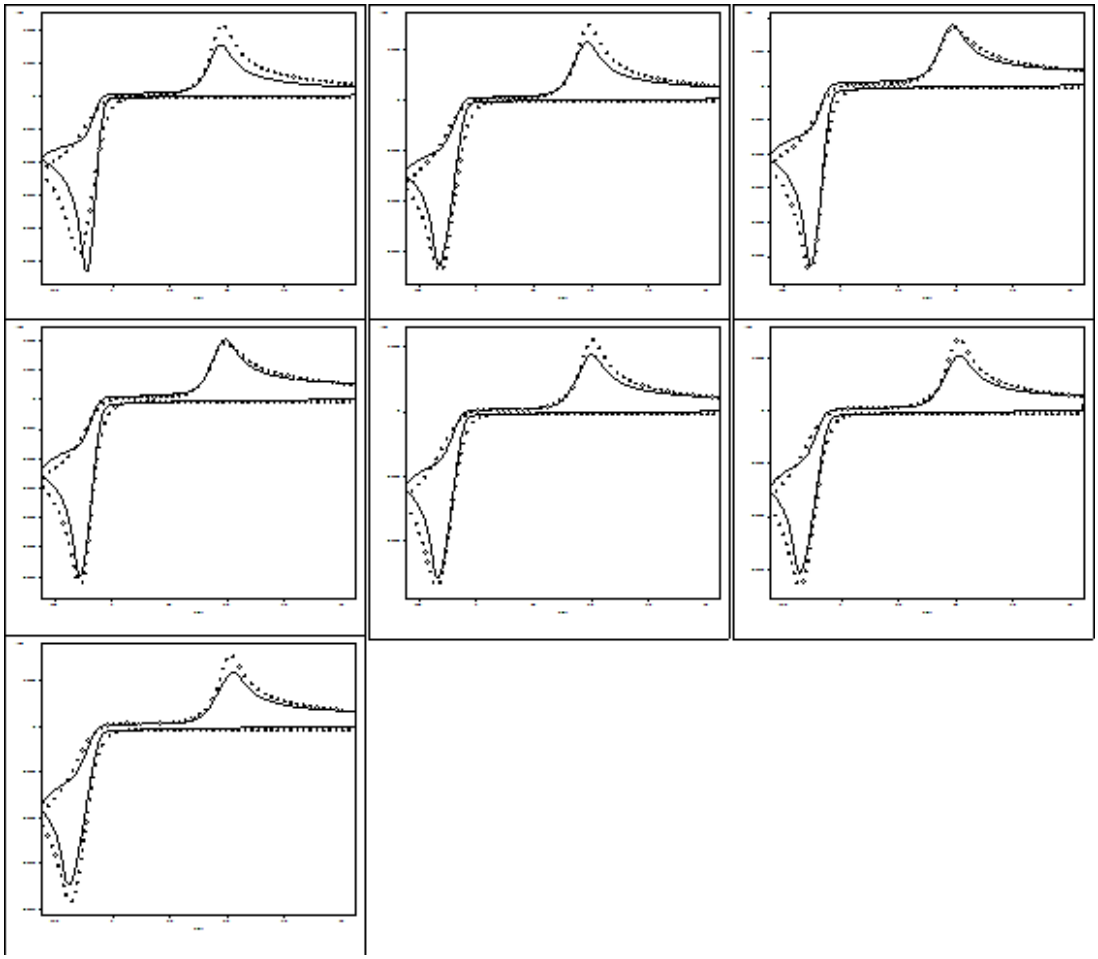

Figure A.32 ◦◦◦- theoretical CVs., ─- experimental CVs representing fits for 9.80 mM of **3** for the E_1E_2C mechanism. Left to right: ν = 200, 400, 600, 800, 1000, 1500, 2000 mV/s

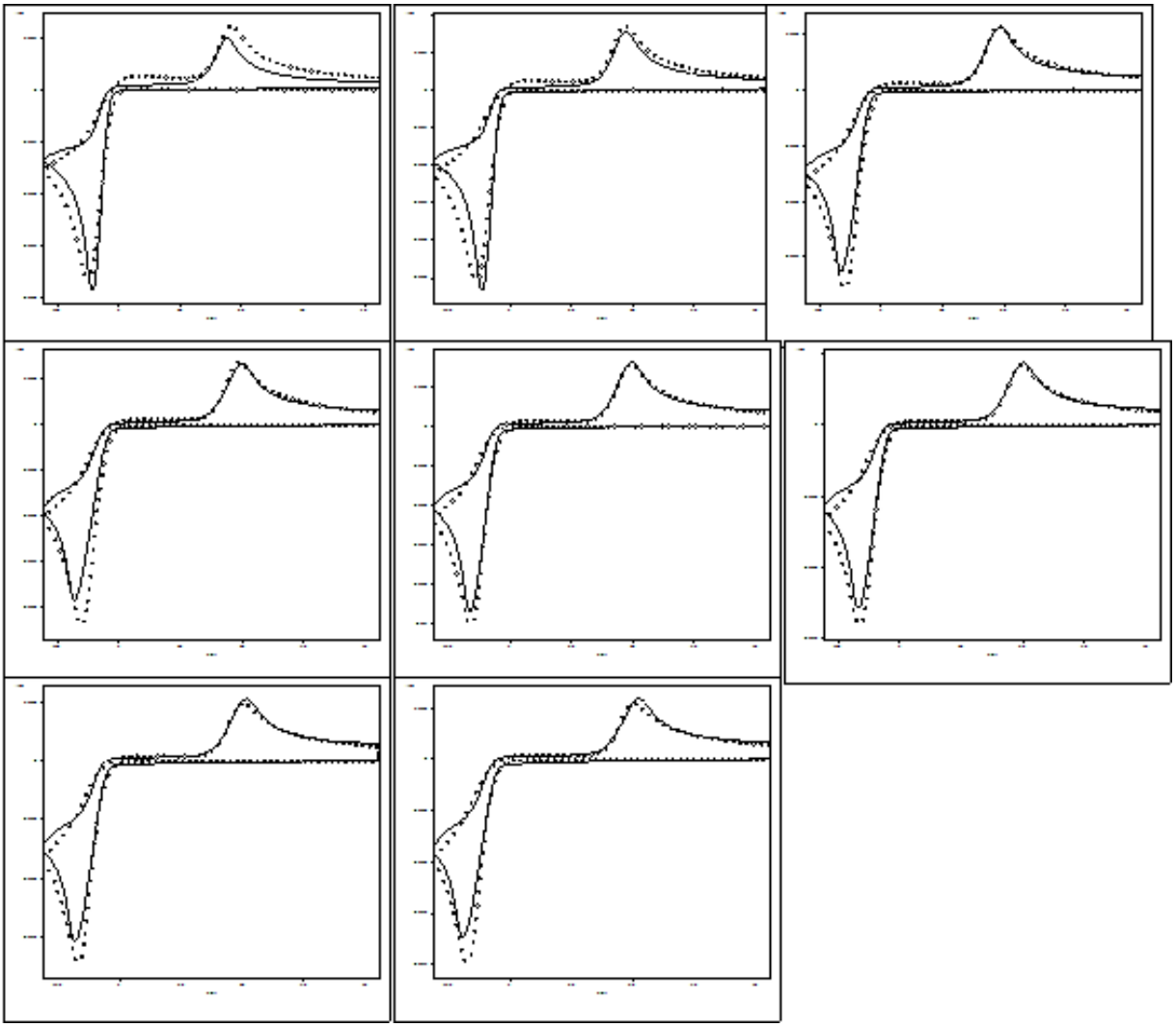

Figure A.33 ◦◦◦- theoretical CVs., ─- experimental CVs representing fits for 9.80 mM of **3** for the $E_1C_2E_2C_2$, mechanism. Left to right: ν = 100, 200, 400, 600, 800, 1000, 1500, 2000 mV/s

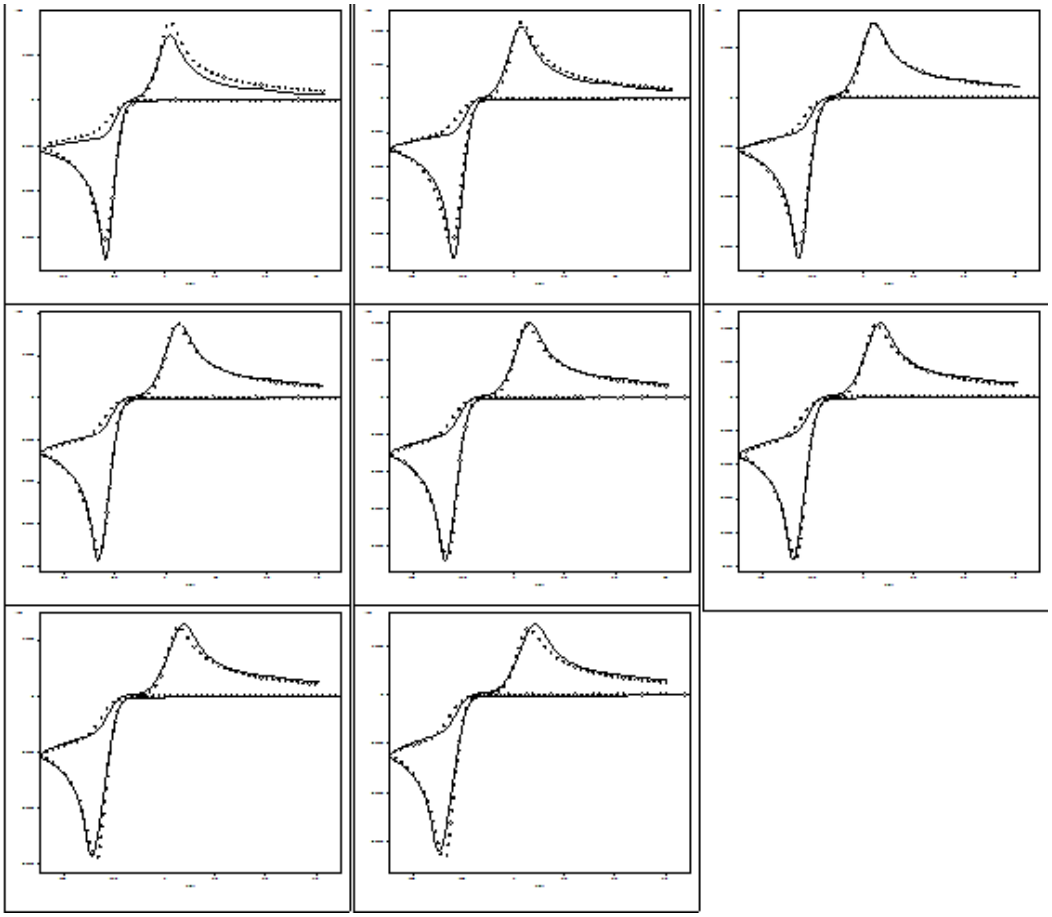

Figure A.34 ◦◦◦- theoretical CVs., ─- experimental CVs representing fits for 3.13 mM of **1** for the E_1E_2C mechanism. Left to right: ν = 100, 200, 400, 600, 800, 1000, 1500, 2000 mV/s

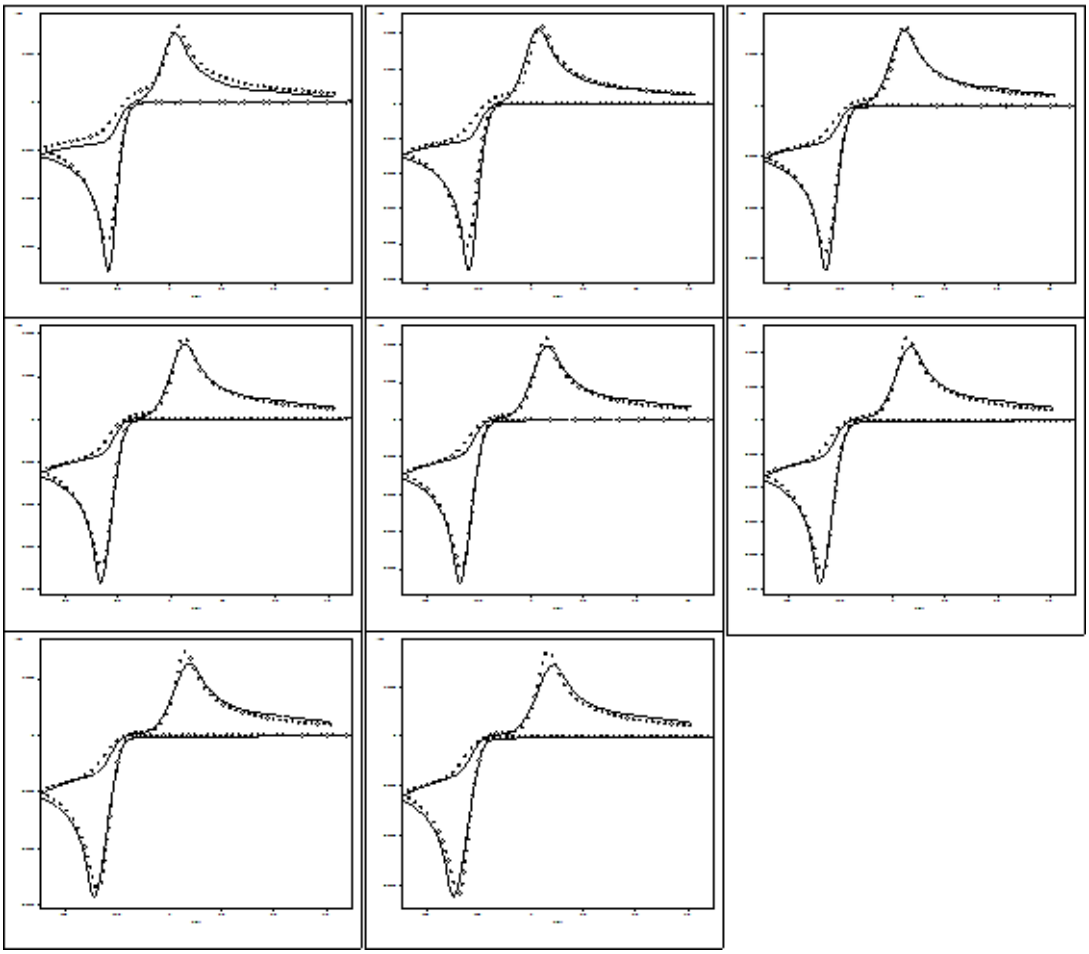

Figure A.35 ◦◦◦- theoretical CVs., ─- experimental CVs representing fits for 3.13 mM of **1** for the $E_1C_2E_2C_2$, mechanism . Left to right: ν = 100, 200, 400, 600, 800, 1000, 1500, 2000 mV/s

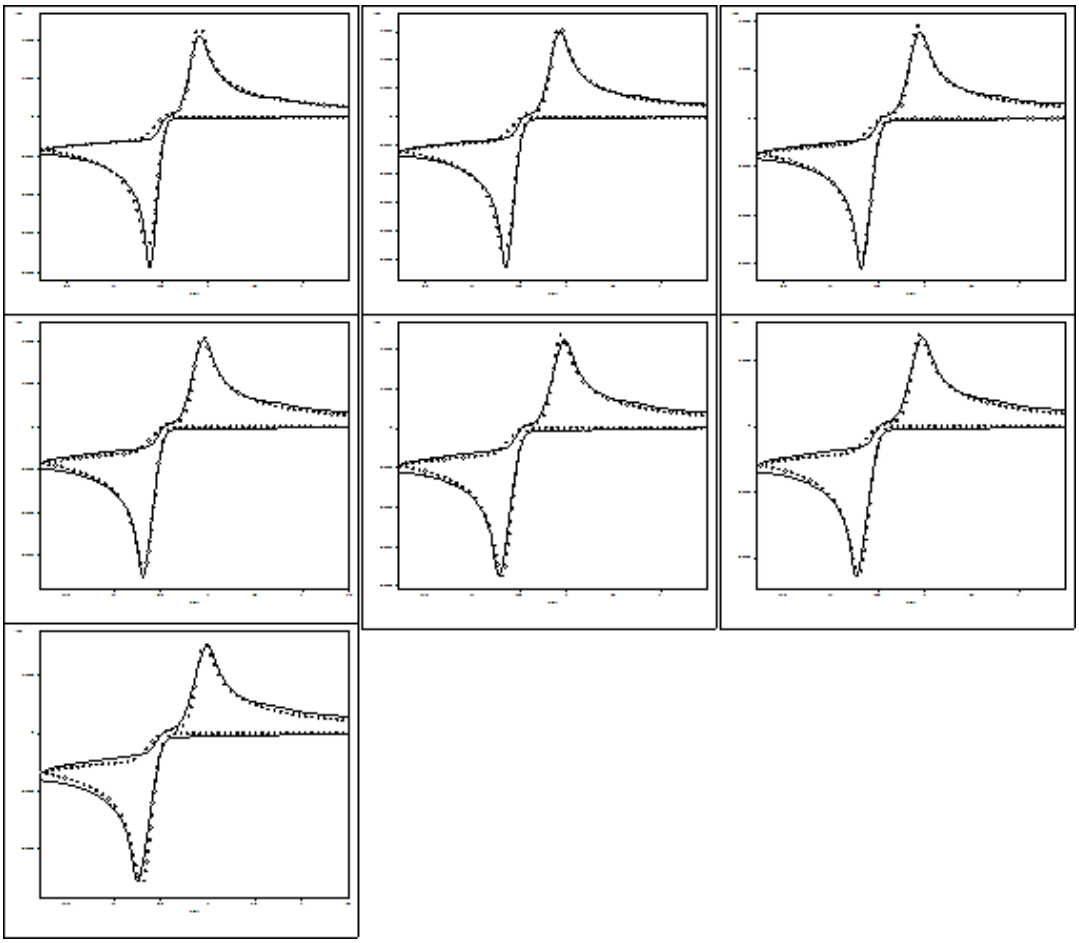

Figure A.36 ◦◦◦- theoretical CVs., ─- experimental CVs representing fits for 2.97 mM of **14** for the E_1E_2C mechanism . From left to right: ν = 200, 400, 600, 800, 1000, 1500, 2000 mV/s

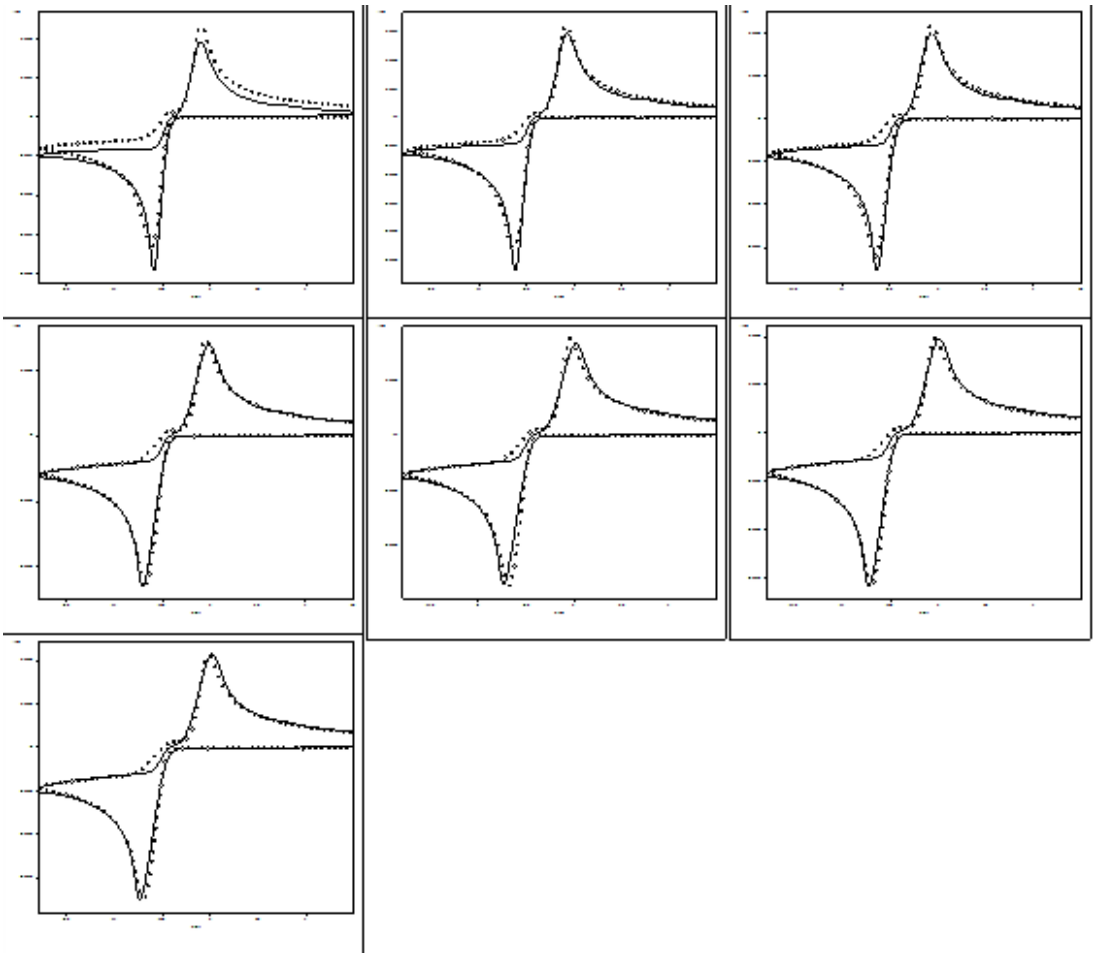

Figure A.37 ◦◦◦- theoretical CVs., ─- experimental CVs representing fits for 6.16 mM of **14** for the E_1E_2C mechanism . From left to right: ν = 50, 100, 200, 400, 600, 800, 1000 mV/s

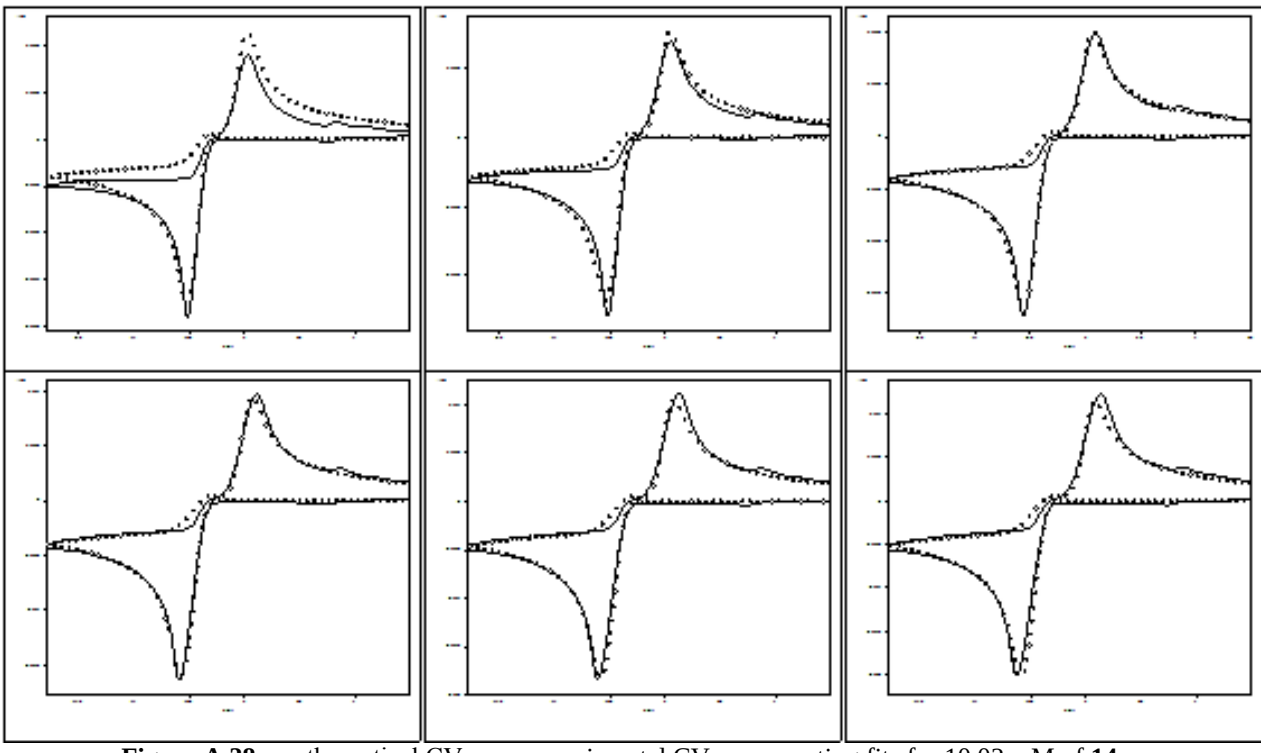

Figure A.38 ◦◦◦- theoretical CVs., ─- experimental CVs representing fits for 10.02 mM of **14** for the E_1E_2C mechanism . Left to right: ν = 100, 200, 400, 600, 800, 1000 mV/s

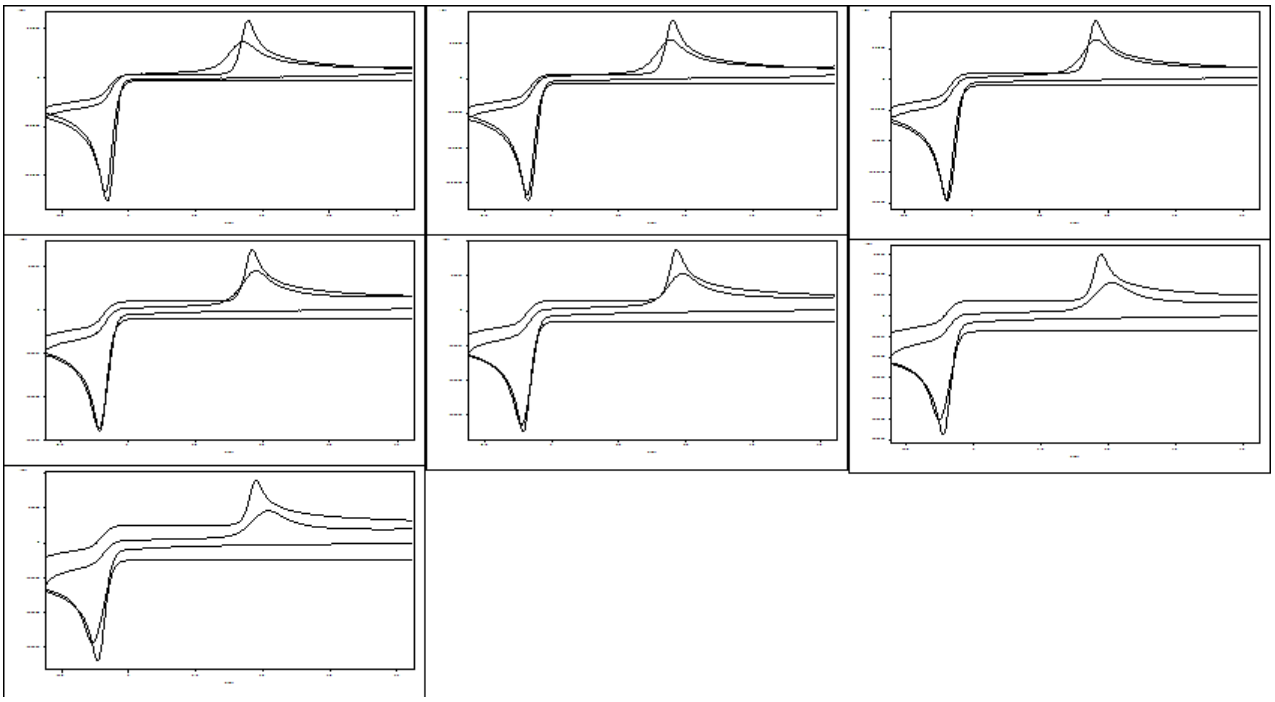

Figure A.39 Poor fits for 3.09 mM of **3** for the $2e^-$ E mechanism. From left to right: ν = 50, 100, 200, 400, 600, 1500, 2000 mV/s

Tables of atomic coordinates from DFT calculations.

Table A.42. (14) $_{neutral}$

Calculated energy (in atomic units) = -1196.50379916

Atom	Coordinates (Angstroms)		
	X	Y	Z
S	-1.32577300	-1.77726600	-0.03221100
S	1.36347700	-1.77006600	0.02498100
N	0.00754400	0.60917400	-0.00032700
N	2.28645500	0.73865000	-0.06139200
N	-2.28644000	0.71037300	0.06247000
C	1.17384000	-0.04184500	-0.01693000
C	-1.15765700	-0.04725100	0.01330200
C	3.62082100	0.15422400	0.01586700
H	3.71816200	-0.66826400	-0.69720600
H	3.83896700	-0.23731800	1.01723400
H	4.35515100	0.92259700	-0.23052900
C	2.14517500	2.19345400	0.00318900
H	1.41814200	2.53568400	-0.73455000
H	3.11449400	2.64673000	-0.20857500
H	1.80635200	2.52368200	0.99225300
C	-3.60996600	0.10096200	0.00894100
H	-3.83479700	-0.29781600	-0.98786200
H	-4.35097000	0.86287400	0.25889400
H	-3.68612100	-0.71771500	0.72861000
C	-2.23339700	2.16786400	-0.01362500
H	-1.21638900	2.49745900	0.17827300
H	-2.90734400	2.59644900	0.73496000
H	-2.54472500	2.52112100	-1.00554700

Table A.43. (14) $_{\text{cation}}$

Calculated energy (in atomic units)= -1196.30270869

Atom	Coordinates (Angstroms)		
	X	Y	Z
S	1.04709200	-1.67656100	0.01271900
S	-1.04723200	-1.67648900	-0.01247100
N	0.00003300	0.80498300	-0.00021700
N	-2.33263600	0.68046800	0.01940400
N	2.33267600	0.68037200	-0.01974400
C	-1.13225400	0.11544300	0.00740800
C	1.13227000	0.11536600	-0.00764100
C	-3.55334300	-0.13487800	0.01482900
H	-3.50450100	-0.90586800	0.79060100
H	-3.70891300	-0.60317300	-0.96296100
H	-4.40204100	0.51193800	0.23374200
C	-2.49439400	2.14266000	-0.02754600
H	-1.51739100	2.61687100	-0.05471300
H	-3.04061900	2.47208800	0.86025000
H	-3.06083700	2.41351200	-0.92274000
C	3.55344500	-0.13486300	-0.01513800
H	3.71080100	-0.60058300	0.96360000
H	4.40169800	0.51145100	-0.23730800
H	3.50331300	-0.90783100	-0.78884300
C	2.49446500	2.14253300	0.02796600
H	1.51748400	2.61672700	0.05623900
H	3.03994100	2.47254900	-0.86007000
H	3.06166800	2.41278800	0.92286100

Table A.44. (14) $_{anion}$

Calculated energy (in atomic units)= -1196.56531506

Atom	Coordinates (Angstroms)		
	X	Y	Z
S	-1.60560500	-1.47689900	-1.23134600
S	1.34670700	-1.32125100	1.41533800
N	0.03529900	0.42228700	-0.21265400
N	2.30373500	0.39757100	-0.45436800
N	-2.18300300	0.66760000	0.31075100
C	1.17355800	-0.13416900	0.17440700
C	-1.19523600	-0.09484700	-0.29911400
C	3.63556300	0.25990800	0.08958000
H	3.62271800	-0.53932000	0.83092900
H	3.97989600	1.19335600	0.57045700
H	4.34996100	0.01490700	-0.70961400
C	2.15940700	1.41758500	-1.47251100
H	1.20335800	1.29329900	-1.97798200
H	2.97696800	1.32399400	-2.19983800
H	2.19686100	2.44005400	-1.05553500
C	-3.59525200	0.39374700	0.17570600
H	-4.13435600	1.30787100	-0.11949400
H	-4.02639900	0.04362200	1.12683000
H	-3.72890200	-0.38134200	-0.57897700
C	-1.85615900	1.75070900	1.21606400
H	-0.77567700	1.87381500	1.24390700
H	-2.22430400	1.53801900	2.23138200
H	-2.32126200	2.69230700	0.88317700

Table A.45. (1) $_{\text{cation}}$

Calculated energy (in atomic units)= -1372.21416429

Atom	Coordinates (Angstroms)		
	X	Y	Z
S	0.55378700	-2.13793400	-0.34311500
S	-1.51509000	-1.88902800	-0.32094800
N	-0.15535600	0.38134000	0.06471700
C	0.86787300	-0.42266700	-0.03942200
C	-1.38365900	-0.13134100	-0.04854100
C	2.24364400	0.02775600	0.06756700
C	3.31163700	-0.88417700	0.11088600
H	3.12996300	-1.95247000	0.08768500
C	4.61440100	-0.42769200	0.20132500
H	5.43223000	-1.13476800	0.23735900
C	4.86907700	0.94220000	0.25268900
H	5.88929600	1.29695200	0.32390300
C	3.81702900	1.85550900	0.21576400
H	4.01958900	2.91756400	0.25647800
C	2.51062100	1.40707400	0.12672700
H	1.68940600	2.10842200	0.09414300
N	-2.46999400	0.60695000	0.04148100
C	-3.82095900	0.02664200	-0.08096000
H	-3.76518900	-0.84138600	-0.74242300
H	-4.43376700	0.76667700	-0.59607000
C	-4.43635000	-0.34388900	1.26669700
H	-3.84406300	-1.09682100	1.78743900
H	-5.43499200	-0.75132200	1.10485400
H	-4.53210500	0.52902800	1.91293500
C	-2.37658900	2.07199600	0.26568900
H	-1.49172800	2.26068700	0.86779500
H	-3.25136000	2.34351600	0.85652700
C	-2.33181100	2.85656800	-1.04101900
H	-1.43891900	2.61089000	-1.61642700
H	-2.30990300	3.92410000	-0.81758100
H	-3.20964800	2.66443400	-1.65941500

Table A.46. (1) neutral

Calculated energy (in atomic units)= -1372.39729629

Atom	Coordinates (Angstroms) X	Y	Z
S	0.55193800	-2.17421400	-0.35392700
S	-1.53643500	-1.91402300	-0.21815200
N	-0.18003500	0.38554100	-0.00800500
C	0.89139000	-0.42070300	-0.07207100
C	-1.37042100	-0.11521200	-0.06005500
C	2.24022000	0.02616000	0.05193400
C	3.33493700	-0.86814500	0.00294100
H	3.16158600	-1.93105800	-0.12477900
C	4.63568600	-0.40987600	0.12341300
H	5.45480800	-1.11864800	0.08401900
C	4.89832700	0.94894900	0.29358600
H	5.91760500	1.30320000	0.38519200
C	3.82889100	1.84642600	0.34348600
H	4.01986000	2.90543400	0.47592400
C	2.52480200	1.40306200	0.22634900
H	1.70178600	2.10362000	0.26575700
N	-2.50416200	0.62488100	0.02341100
C	-3.83714100	0.03844300	-0.07136900
H	-3.78072800	-0.86427900	-0.68486700
H	-4.46629500	0.73901300	-0.62712600
C	-4.47455900	-0.27840700	1.28283600
H	-3.87989200	-1.00855300	1.83382200
H	-5.47617900	-0.69074100	1.13773000
H	-4.56697900	0.61999700	1.89676000
C	-2.39752000	2.07770000	0.19875900
H	-1.53348600	2.27902200	0.83105000
H	-3.28703300	2.40183200	0.74362000
C	-2.27431600	2.83552800	-1.12232200
H	-1.36774000	2.53915700	-1.65090500
H	-2.22564100	3.91085100	-0.93372700
H	-3.13212300	2.64644700	-1.77196600

Table A.47. (1) $_{anion}$

Calculated energy (in atomic units)= -1372.50602529

Atom	Coordinates (Angstroms)		
	X	Y	Z
S	-0.63206200	1.71234700	1.57402500
S	2.01804800	-1.30435500	1.78094500
N	0.15402100	-0.41195400	0.08703300
C	-0.80400000	0.34245000	0.54731400
C	1.46404500	-0.45603100	0.41086100
C	-2.17618700	-0.06918900	0.06965600
C	-3.27913400	0.78258500	0.17568700
H	-3.12479600	1.75376400	0.62755300
C	-4.53362500	0.38823300	-0.27734100
H	-5.37388000	1.06844700	-0.18826500
C	-4.71627100	-0.87304400	-0.83874800
H	-5.69570500	-1.18247700	-1.18701800
C	-3.62695300	-1.73479700	-0.94228100
H	-3.75625500	-2.72381400	-1.36883100
C	-2.37198500	-1.33493400	-0.49717000
H	-1.51975600	-1.99689400	-0.57318200
N	2.32299800	0.08932200	-0.50347000
C	3.77063500	0.00460000	-0.35172600
H	3.99508500	-0.02420500	0.71331300
H	4.20039400	0.92173900	-0.76616400
C	4.37659300	-1.22181100	-1.03772100
H	3.97851700	-2.13000800	-0.58416800
H	5.46457900	-1.22403500	-0.92037400
H	4.15220500	-1.23618600	-2.10775400
C	1.83205300	0.79011600	-1.69049400
H	0.86627900	0.36195600	-1.95491500
H	2.52708600	0.57445400	-2.50921300
C	1.69619800	2.30241700	-1.49861200
H	1.00277600	2.51866200	-0.68453600
H	1.32027300	2.76441500	-2.41684400
H	2.66006900	2.76116500	-1.26059800

Table A.48. (3) $_{neutral}$

Calculated energy (in atomic units)= -1390.64479975

Atom	Coordinates (Angstroms)		
	X	Y	Z
C	-1.14394100	-0.41950900	-0.00000500
C	1.14394100	-0.41950900	0.00000500
N	0.00000000	0.23001800	0.00000000
S	-1.04788100	-2.23053500	0.00005400
S	1.04788100	-2.23053500	-0.00005700
C	2.44253400	0.22803200	0.00000300
C	3.64383000	-0.50980300	0.00029200
C	2.51954400	1.63857100	-0.00030700
C	4.87487700	0.13853300	0.00025600
H	3.61800100	-1.59605600	0.00057900
C	3.75276400	2.27693900	-0.00034000
H	1.59914000	2.21071400	-0.00053600
C	4.93808600	1.53355000	-0.00006400
H	5.78847700	-0.44837200	0.00048900
H	3.79256900	3.36231800	-0.00058800
H	5.89994200	2.03701700	-0.00009200
C	-2.44253400	0.22803200	-0.00000200
C	-3.64383000	-0.50980300	-0.00028700
C	-2.51954400	1.63857100	0.00030400
C	-4.87487700	0.13853300	-0.00025100
H	-3.61800100	-1.59605600	-0.00057200
C	-3.75276400	2.27693900	0.00033800
H	-1.59914000	2.21071400	0.00053000
C	-4.93808600	1.53355000	0.00006500
H	-5.78847700	-0.44837200	-0.00048100
H	-3.79256900	3.36231800	0.00058300
H	-5.89994200	2.03701700	0.00009400

Table A.49. (3) $_{\text{cation}}$

Calculated energy (in atomic units)= -1390.67248228

Atom	Coordinates (Angstroms)		
	X	Y	Z
C	1.13522900	0.42571300	0.00096500
C	-1.13523000	0.42571300	-0.00100800
N	-0.00000100	-0.24361200	-0.00002000
S	1.02262300	2.17305600	-0.01854000
S	-1.02262200	2.17305600	0.01851700
C	-2.43005100	-0.21684800	-0.00004000
C	-3.61764100	0.52396100	-0.12950300
C	-2.50000800	-1.61490800	0.14060200
C	-4.84140900	-0.11534700	-0.11522900
H	-3.58828500	1.59995300	-0.25587100
C	-3.72981100	-2.24633100	0.15537900
H	-1.58796700	-2.18415300	0.24339100
C	-4.89914400	-1.50123000	0.02847300
H	-5.75190600	0.45868400	-0.21975900
H	-3.78105900	-3.32096900	0.26692400
H	-5.85963600	-1.99986300	0.03888200
C	2.43005000	-0.21684800	0.00003000
C	3.61763500	0.52395900	0.12955800
C	2.50001300	-1.61490500	-0.14064600
C	4.84140400	-0.11534800	0.11530900
H	3.58827100	1.59994600	0.25595900
C	3.72981800	-2.24632500	-0.15539900
H	1.58797700	-2.18414800	-0.24348200
C	4.89914500	-1.50122600	-0.02843100
H	5.75189700	0.45868200	0.21988900
H	3.78107200	-3.32096000	-0.26697200
H	5.85963900	-1.99985800	-0.03881900

Table A.50. (3) $_{anion}$

Calculated energy (in atomic units)= -1390.94461963

Atom	Coordinates (Angstroms)		
	X	Y	Z
C	-1.14593000	-0.37993200	0.00356300
C	1.14593000	-0.37993200	-0.00356300
N	0.00000000	0.24786300	0.00000000
S	-1.02789800	-2.21081100	0.20073000
S	1.02789900	-2.21081100	-0.20073000
C	2.43077900	0.23804500	0.01565300
C	3.63039100	-0.51501200	0.01427600
C	2.56598000	1.65133900	0.02173900
C	4.87138600	0.10368500	0.01926900
H	3.57836600	-1.59702400	0.02274400
C	3.80790300	2.25267200	0.02631300
H	1.66653200	2.25210600	0.02332400
C	4.98362200	1.49149500	0.02512400
H	5.76618000	-0.50994600	0.02050400
H	3.86935100	3.33602700	0.03128600
H	5.95491700	1.97054500	0.02966500
C	-2.43077900	0.23804500	-0.01565300
C	-3.63039100	-0.51501200	-0.01427600
C	-2.56598000	1.65133900	-0.02173900
C	-4.87138600	0.10368500	-0.01926900
H	-3.57836600	-1.59702400	-0.02274400
C	-3.80790300	2.25267200	-0.02631300
H	-1.66653200	2.25210600	-0.02332400
C	-4.98362300	1.49149500	-0.02512400
H	-5.76618000	-0.50994600	-0.02050400
H	-3.86935100	3.33602700	-0.03128600
H	-5.95491700	1.97054500	-0.02966500

Table A.51. (14) dianion

Calculated energy (in atomic units)= -1196.39057305

Atom	Coordinates (Angstroms)		
	X	Y	Z
S	1.89262900	1.90802700	-0.24088400
S	-1.89271200	1.90797100	0.24087500
N	0.00000200	-0.19441900	0.00014900
N	-2.22826400	-0.71338200	-0.45550100
N	2.22841800	-0.71331400	0.45557700
C	-1.23081900	0.30401600	-0.06692800
C	1.23076300	0.30408500	0.06704300
C	-3.39284700	-0.83467900	0.39306900
H	-3.68300700	0.17668200	0.69307100
H	-3.21233300	-1.44177200	1.31332300
H	-4.22429600	-1.31858100	-0.15104300
C	-1.72611200	-2.00210100	-0.86357900
H	-0.87471700	-1.87065000	-1.53278100
H	-2.52724300	-2.55522900	-1.38826800
H	-1.37677700	-2.64875100	-0.02880000
C	3.39270200	-0.83459900	-0.39339000
H	3.21188000	-1.44174700	-1.31362500
H	4.22439800	-1.31850300	0.15039200
H	3.68273300	0.17676900	-0.69350300
C	1.72632800	-2.00203400	0.86370900
H	0.87511700	-1.87062700	1.53314400
H	2.52760400	-2.55522600	1.38814400
H	1.37677100	-2.64866700	0.02896000

Table A.52. (3) dianion

Calculated energy (in atomic units)= -1390.65962076

Atom	Coordinates (Angstroms)		
	X	Y	Z
C	-1.18778641	0.66949061	0.00006732
C	1.18778642	0.66949063	-0.00008385
N	0.00000001	0.07896704	-0.00001477
S	-1.39087048	2.46192464	0.00027559
S	1.39087047	2.46192467	-0.00027693
C	2.36243245	-0.17206129	0.00002589
C	3.69171782	0.35387487	-0.00019907
C	2.26708450	-1.59905386	0.00044215
C	4.81010399	-0.47359510	-0.00018506
H	3.81330746	1.43178920	-0.00035200
C	3.38802567	-2.41326758	0.00043681
H	1.27450708	-2.03446163	0.00077678
C	4.69151498	-1.87167023	0.00006488
H	5.80074570	-0.01746894	-0.00039846
H	3.25424545	-3.49540282	0.00072714
H	5.56929553	-2.51393962	0.00007706
C	-2.36243245	-0.17206130	-0.00003198
C	-3.69171780	0.35387487	0.00021437
C	-2.26708452	-1.59905386	-0.00045954
C	-4.81010397	-0.47359509	0.00021330
H	-3.81330742	1.43178920	0.00037403
C	-3.38802569	-2.41326757	-0.00044362
H	-1.27450711	-2.03446164	-0.00081086
C	-4.69151499	-1.87167021	-0.00004793
H	-5.80074570	-0.01746892	0.00044461
H	-3.25424546	-3.49540280	-0.00074329
H	-5.56929553	-2.51393959	-0.00005213